Dissertation zur Erlangung des Doktorgrades
der Fakultät für Chemie und Pharmazie
der Ludwig-Maximilians-Universität München

Novel Lithium Nitridophosphates and Their Capability as Lithium Ion Conductors

Eva-Maria Bertschler

aus

Feldkirch, Österreich

2017

Erklärung

Diese Dissertation wurde im Sinne von §7 der Promotionsordnung vom 28. November 2011 von Herrn Prof. Dr. Wolfgang Schnick betreut.

Eidesstattliche Versicherung

Diese Dissertation wurde eigenständig und ohne unerlaubte Hilfe erarbeitet.

München, 14.12.2017

.....

(Eva-Maria Bertschler)

Dissertation eingereicht am	18.12.2017
1. Gutachter:	Prof. Dr. Wolfgang Schnick
2. Gutachter:	Prof. Dr. Hubert Huppertz
Mündliche Prüfung am	06.02.2018

To my family

Imagination is more important than knowledge.

For knowledge is limited to all we now know and understand, while imagination embraces the entire world, and all there ever will be to know and understand.

Albert Einstein

Vielen herzlichen Dank

Mein ganz besonderer Dank gebührt Prof. Dr. Wolfgang Schnick für die Aufnahme in seinem Arbeitskreis und für die Möglichkeit meine Dissertation anzufertigen. Die vielfältigen Mittel und die Freiheit das Thema der Dissertation eigenständig zu entwickeln waren für die Anfertigung dieser Arbeit unverzichtbar. Außerdem bedanke ich mich für die vielen lehrreichen Fachgespräche und Anregungen. Außerdem bin ich sehr dankbar, dass er es mir ermöglichte, wertvolle Erfahrungen auf (inter)nationalen Tagungen sammeln zu können und meine Ergebnisse zu präsentieren.

Mein besonderer Dank gilt außerdem Herrn Prof. Dr. Hubert Huppertz für die Bereitschaft das Koreferat für diese Dissertation zu übernehmen, sowie für seine herausragenden Vorlesungen, die mich schließlich in den Arbeitskreis von Herrn Prof. Dr. Schnick führten.

Prof. Dr. Konstantin Karaghiosoff, Prof. Dr. Achim Hartschuh, Prof. Dr. Lena Daumann und Prof. Dr. Hans-Christian Böttcher danke ich für die Bereitschaft als Teil der Prüfungskommission für die mündliche Prüfung zur Verfügung zu stehen.

Bei Herrn Dr. Thomas Bräuniger bedanke ich mich für die zahlreichen Fachgespräche und Unterstützung bei der Interpretation der NMR Spektren.

Besondere Anerkennung verdient Dr. Constantin Hoch für seine Hilfsbereitschaft bei allen möglichen Fragestellungen. Vielen herzlichen Dank für die vielen Tipps, Anregungen und dein offenes Ohr.

Mein besonderer Dank gilt meinem Vorgänger Dr. Dominik Baumann, der mir vor allem zu Beginn meiner Promotion eine große Hilfe war.

Ebenso danke ich meinen Praktikanten Maximilian Lamoth, Katharina Maria Durner, Leonard Moser, Florian Grundner und Stephanie Schneider, die mich während meiner Zeit mit viel Einsatz unterstützt haben.

Außerdem möchte ich mich herzlich bei meinen Kooperationspartnern Christian Dietrich, Dr. Thomas Leichtweiß und Prof. Dr. Jürgen Janek von der Justus-Liebig-Universität Gießen für ihre Bemühungen bedanken. Durch ihren Beitrag konnte ich meine Proben bezüglich ihrer Lithium-Ionen-Leitfähigkeit und der Stabilität gegenüber Lithium Metall untersuchen.

Ich bedanke mich auch bei Herrn Prof. Dr. Oliver Oeckler und Markus Nentwig für die Möglichkeit meine Kristalle am ESRF (Microfokus) zu messen.

Herrn Christian Minke gilt besonderer Dank für die vielen sehr gewissenhaften Messungen am NMR-Spektrometer und seine Geduld mit meinen sehr empfindlichen Proben am Rasterelektronenmikroskop.

Herrn Tomas Miller danke ich für die Betreuung der Pulverdiffraktometer sowie für das Messen vieler Hochtemperatur-Pulverdiffraktogramme. Im Besonderen auch für die Bastelstunden am Cu-Stoe, um Messungen bei höheren Temperaturen zu ermöglichen.

Herrn Wolfgang Wünschheim danke ich für die Instandhaltung der Rechner und das Lösen so manchen Computerproblems.

Frau Olga Lorenz danke ich ganz herzlich für ihre organisatorische Tätigkeit und außergewöhnliche Hilfsbereitschaft bei allen Arten von Problemen.

Dr. Peter Mayer danke ich herzlich für die Messung vieler sehr kleiner Einkristalle, Frau Marion Sokoll danke ich für die Aufnahme der IR-Spektren.

Dem Pressenteam, darunter Florian Pucher, Herrn Dr. Dominik Baumann, Herrn Dr. Alexey Marchuk, Herrn Simon Kloß, Herrn Sebastian Vogel und Herrn Sebastian Wendl danke ich für die gute Zusammenarbeit.

Meinen ehemaligen und aktuellen Laborkollegen Florian Pucher, Dr. Dominik Baumann, Dr. Alexey Marchuk, Dr. Frank Tambornino, Dr. Matthias Wörsching, Simon Kloß, Philipp Bielec, Sebastian Vogel, Sebastian Wendl und Tobias Giftthaler danke ich für die unvergessliche Zeit im Labor D2.110 und die zahlreichen gemeinsamen Laborabende.

Meiner Nachfolgerin im Bereich der Lithium-Nitridophosphate Stephanie Schneider wünsche ich alles Gute und viel Spaß und Durchhaltevermögen für ihre Master- und Doktorarbeit.

Ich danke natürlich auch allen bisher nicht erwähnten Mitgliedern der Arbeitskreise Schnick, Johrendt, Lotsch, Oeckler, Bräuniger und Hoch für die großartige Arbeitsatmosphäre im zweiten Stock.

Mein allergrößter Dank geht jedoch an meine Familie. Ohne meine Eltern, Geschwister und meinen Freund Dominik, wäre ich zweifellos nicht da, wo ich jetzt bin.

Contents

1. Introduction

The alkali metal lithium was discovered 1817 by Arfvedson, a student of Berzelius, in bound form in the mineral *Petalit* ($LiAl[Si_2O_5]_2$) (Figure 1) and shortly afterwards also in *Spodumen* ($LiAl[SiO_3]_2$) and *Lepidolith* ($(K,Li)\{Al_2(OH,F)_2[AlSi_3O_{10}]\}$). In the following years, lithium was found in low concentration in numerous silicates. As the name lithium (from Greek: lithos = stone) suggests, lithium was thought to be only found in minerals in contrast to sodium and potassium, which are components of plants as well.[1] In 1818, Gmelin prepared different lithium-salts and discovered the red flame coloration in different salts.[2] In the same year, Davy succeeded in synthesizing small amounts of elemental lithium by electrolysis of Li_2CO_3. 37 years later, Bunsen and Matthiessen were able to obtain larger amounts of elemental lithium by electrolysis of LiCl-melts.[1] In 1923/24 a commercial manufacturing of lithium in Langelsheim (Harz, Germany) started.[3] Until now, lithium (Figure 1) is synthesized in high purity by electrolysis of LiCl.[1,2]

Figure 1. Picture of *Petalit* ($LiAl[Si_2O_5]_2$) (left) and lithium metal in seald silica ampoule (right).

Physical properties of lithium resemble those of other alkali metals. It shows silver, metallic luster, has the lowest density of all metals (M = 0.53 g cm^{-3}) and is soft enough to be cut with a knife. The most prominent features are the strongly negative electrochemical potential (−3.04 V versus standard hydrogen electrode) and the high reactivity. Lithium reacts, for example, with molecular nitrogen to Li_3N at room temperature.[4] Due to the high reactivity it is never found in its native element form, although it is relatively common in Earth's crust with about 18.5 ppm. The alkali metal is concentrated especially in pegmatites, formed in granite-producing magmatic processes. In arid areas weathering of such lithium rich rocks can result in brines with higher concentration located in evaporate deposits.[1,5] In more humid areas this can concentrate lithium

in clays. Both types of resources, which are estimated at more than 33 million tons, are used for lithium extraction. These reserves exceed the expected demand for the next generations. More than 60 % of the lithium resources are located in South America.[3,5] The annual production in 2016 was 40 000 metric tons of pure lithium metal. It is predicted that the global demand for lithium will increase to 500 000 metric tons in 2025.[6] The most important lithium derivates are Li_2CO_3 (46 % of annual production of lithium derivates) and LiOH (19 %), because all other lithium derivates can be generated from them.[3,5]

Since its discovery, lithium emerged from an energy critical element[7] to a strategic raw material, because it cannot be substituted in various areas of application.[3] Until the Second World War, lithium was used in high-temperature greases to improve the performance of aero engines. The importance of the alkali metal increased rapidly with the application as safe storage material of heavy hydrogen in nuclear weapons for the reaction to tritium. The discovery of high-temperature stable lithium compounds makes it indispensable for ceramic and glass industries and as an alloying agent to facilitate and increase the strength of a number of metals.[5] Since 1949, lithium is also used in psychotherapeutic medication.[2] But with 41 % of all lithium produced most is used for lithium ion batteries in electric car industry and for portable electrical storage applications, required by today's information-rich, mobile society (Figure 2).[4,5]

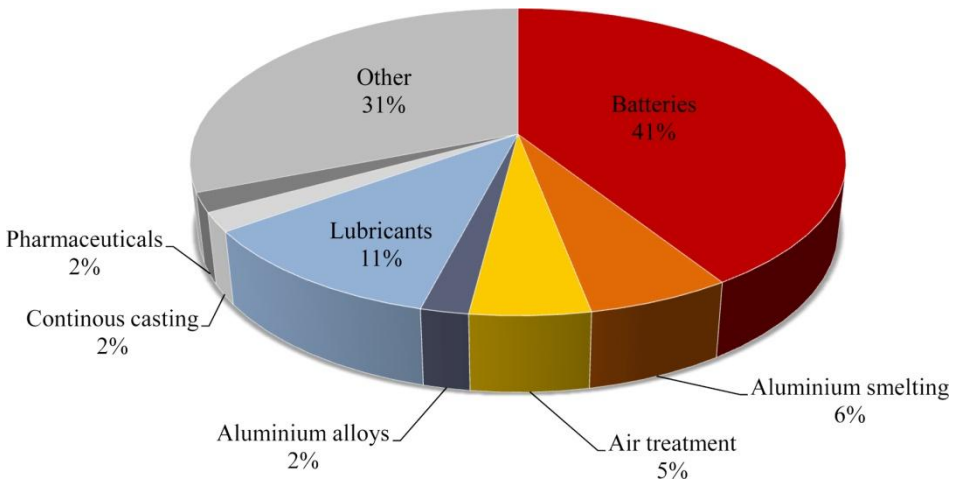

Figure 2. Utilization of lithium (2014). The concept of the figure was extracted from citation number [5].

Nowadays, as the global markets gear toward alternative and clean energies and storage systems, lithium ion batteries move into the focus of research as their efficiency makes them promising candidates for a broad application.[8,9] The first lithium ion battery dates back to the 1960s, when the first solid electrolytes were examined.[10] In the early 1970s, the interest on solid-state

electrochemistry grew enormously and led to the discovery of numerous inorganic compounds that react with alkali metals. Beside silver based batteries for low drain applications, Li‖I_2 cells have been used as all solid-state batteries (ASSBs) for heart pacemakers.[11] During the search for highly conducting electrolytes Li_3N was discussed as a solid electrolyte (SE), but it is too reactive and the electrochemical window is too small for practical applications.[11–13] Based on this high conductivity many lithium alloys have been investigated systematically.[11,14] In the 1980s, Goodenough laid the foundation of the first commercially available lithium ion battery (LIB) (Sony Corporation in 1991).[15,16] The discovery of the highly reversible, low voltage lithium intercalation-deintercalation process in carbonaceous material, led to the creation of the C/$LiCoO_2$ rocking-chair cell.[4,17] Further developments led to the first reliable and practically rechargeable lithium ion hybrid polymer electrolyte (Li-HPE) battery, which has been commercially available as thin-film battery since 1999.[4,18] Later on studies have focused mainly on ion conducting oxides like oxonitrides and oxosulfides.[19]

Almost all hitherto known commercially available lithium batteries consist of an anode, a cathode and a liquid electrolyte. For example, the C|$LiPF_6$|$LiCoO_2$ cell is composed of graphite (anode), $LiCoO_2$ (cathode), and $LiPF_6$ (liquid electrolyte), which is dissolved in ethylene carbonate.[20] Despite the verified and widely-used application of such batteries, there are repeatedly alarming headlines about laptops or mobile phones which caught fire spontaneously. For example, in the 90s incidents with overheating lithium ion batteries led to product recalls. One of the most popular recalls was that of Sony in 2006, where millions of laptops were recalled. Recently, also Samsung was confronted with overheating batteries (Samsung Galaxy Note 7).[21] These safety problems commonly result from overloading or too low discharging, leading to lithium metal depositions in dendritic form at the cathode. These dendrites lead to a chemical short-circuit perforating the liquid electrolytes.[11,19,20] To gain new trust to battery technology, different non-flammable electrolyte compounds were investigated recently. Thereby solid electrolytes (SEs) turn out to be promising candidates due to their superior electrochemical, mechanical, and thermal stability and the absence of leakage, leading to advanced safety compared to liquid electrolytes. An important advantage is also the possibility of battery downsizing.[11]

LiPON (e.g. $Li_{2.88}PO_{3.73}N_{0.14}$) is one of the most prominent SE compounds, beside LISICON (e.g. $Li_{14}ZnGe_4O_{16}$), NASICON (e.g. $Li_{1.3}Al_{0.3}Ti_{1.7}(PO_4)_3$), perovskites (e.g. $La_{0.5}Li_{0.5}TiO_3$), antiperovskites (e.g. Li_3OX with X = Cl, Br) or garnets (e.g. $Li_7La_3Zr_2O_{12}$). The ionic conductivities of these compounds amount to 10^{-6} to 10^{-3} $\Omega^{-1}cm^{-1}$ at room temperature and an activation energy E_a for lithium ion conductivity of 0.3 to 0.6 eV.[19,22] $Li_{10}GeP_2S_{12}$ (LGPS: $\sigma_{RT} = 1.2 \times 10^{-2}$ $\Omega^{-1}cm^{-1}$, $E_a = 24$ kJ mol^{-1}) and $Li_7P_3S_{11}$ (LPS: $\sigma_{RT} = 1.6 \times 10^{-4}$ $\Omega^{-1}cm^{-1}$, $E_a = 34$ kJ mol^{-1}) have one of the highest reported lithium ion conductivities to date. [11,19,23–25] In

comparison, LiPON compounds do not exhibit a very high conductivity ($LiPON_{0.14}$: $\sigma_{RT} = 2 \times 10^{-6}\ \Omega^{-1}cm^{-1}$, $E_a = 55\ kJmol^{-1}$)[26] and systematic investigations regarding long-time stability are lacking, although the latter are used in commercial available solid-state batteries (SSBs) with $LiCoO_2$ as cathode- and lithium as anode-material.[11,27,28] In general, the sample treatment prior to lithium ion conductivity measurements is decisive. For instance impedance measurements of cold pressed pellets of bulk material show much lower lithium ion conductivity than optimized multilayered films of the SE. Sample treatment by pulsed laser deposition (PLD) prior to measurement of e.g. Li_3OCl enhanced the ionic conductivity significantly (two orders of magnitude) in comparison to the bulk measurements.[22]

Even though some of the mentioned compounds are discussed as SEs for new generation batteries, almost all relevant lithium electrolytes known so far are thermodynamically unstable in contact with metallic lithium. In particular, sulfides are thermodynamically unstable against the high voltage cathodes. In contrast, binary lithium compounds like LiI, Li_3P, Li_2S or Li_3N are stable against contact with lithium metal, but naturally have a very narrow thermodynamic stability window.[11] In this window no redox-reactions occur. With the antiperovskite $Li_2(OH)_{0.9}F_{0.1}Cl$, a promising SE was recently published, which is stable against contact with metallic lithium, but the lithium ion conductivity is lower than that of e.g. garnet and LISICON.[29] By contact with metallic lithium SEs form different types of solid electrolyte interphases (SEIs).[30,31] Such SEIs must have sufficient ionic conductivity to enable access of ions to the electrode, but low enough electronic conductivity. If the electronic conductivity is too high, the interphase layer will grow to macroscopic dimensions.[11] In rechargeable LIBs the kinetics of the SEIs (Figure 3) between the electrodes and the electrolyte are essential for battery function and durability of electrochemical devices.[30]

In general, there are three different types of interphase formation (Figure 3):[30,32]

(a) Thermodynamically stable interphase: the SE does not react with lithium metal.

(b) Mixed ionic-electronic conducting interphase (MCI): the SE reacts with lithium metal (thermodynamically unstable) and the formed interphase allows for continuous flow of lithium and electrons. As a result, the SE is completely reacted with lithium.

(c) Kinetically stable interphase: the SE reacts with lithium metal (thermodynamically unstable) and forms a kinetically stable SEI.

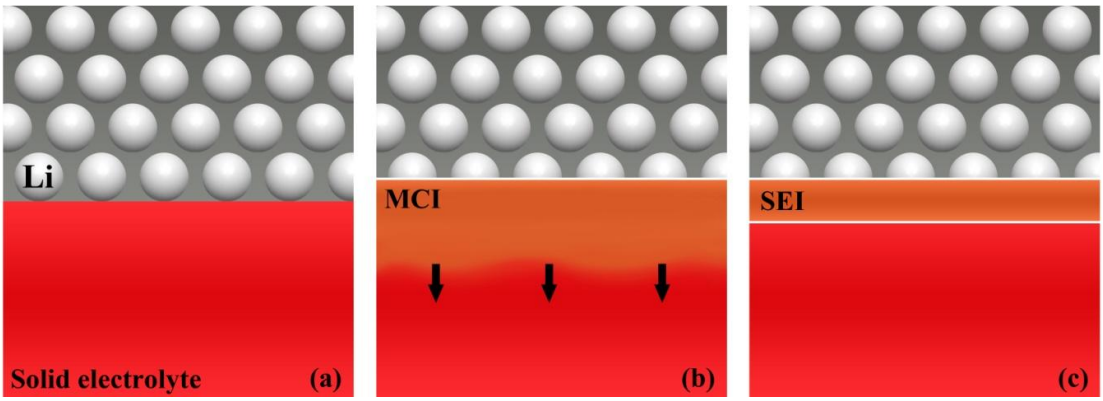

Figure 3. Different types of interphases between a solid lithium ion conductor and lithium metal. (Solid electrolyte: red; lithium metal: gray; interphase: orange) (a) Non-reactive and thermodynamically stable interphase. (b) Reactive and mixed conducting interphase (MCI). (c) Reactive and metastable solid electrolyte interphase (SEI). The concept of the figure was extracted from citation number [30].

There are very few SEs that are thermodynamically stable against lithium metal, because most of them are reduced to e.g. Li_2O or Li_2S. Electrolyte materials which form a MCI, will result in rapid degradation and finally in a short-circuit. Thus it behaves more like an electrode material than an electrolyte, which can be observed in e.g. LLTO ($Li_{0.35}La_{0.55}TiO_3$).[30,32] The third group of interfaces gets more and more into focus of many scientists, because the SEIs passivate the SE material and stop the continued decomposition into the bulk of the SE.[33]

Recently, some lithium ion conductors for ASSBs have been examined with regard to the stability against lithium metal by *in situ* X-ray photoelectron spectroscopy (XPS) in combination with time-resolved reactions. For example, the high-conducting materials LPS and LGPS are not stable against lithium and form a kinetically stable SEI.[32,34] After sputtering with lithium, LPS shows an increasing impedance with time, which could be assigned to the formation of an interphase that can be classified as a non-growing (kinetically stable) SEI. During lithiation, Li_2S and Li_3P were formed as decomposition products (Equation 1).[34]

$$Li_7P_3S_{11} + 24\ Li \rightarrow 11\ Li_2S + 3\ Li_3P \qquad (1)$$

The reaction of LGPS with elemental lithium leads to further decomposition to germanium or $Li_{15}Ge_4$ (Equation 2 and 3). The thickness of the SEI is still growing after decomposition, which indicates that the SEI is not entirely electronically insulating and that the ionic transport is fast. This may complicate the use of LGPS as a practical solid electrolyte in direct contact with lithium metal anodes in ASSBs.[32]

$$Li_{10}GeP_2S_{12} + 20\ Li \rightarrow 12\ Li_2S + 2\ Li_3P + Ge \quad (2)$$

$$Li_{10}GeP_2S_{12} + 23.7\ Li \rightarrow 12\ Li_2S + 2\ Li_3P + ¼\ Li_{15}Ge_4 \quad (3)$$

Investigations on amorphous LiPON show that it is not stable against lithium metal and a stable interphase is formed during lithiation.[26] Furthermore, it was shown that lithium reacts preferentially with the bridging oxygen which disrupts the network of the amorphous glass, yielding in formation of Li_2O, Li_3N and phosphates or phosphides (Equation 4 and 5).[28,35,36] Despite interfacial reactions in LiPON compounds the LiPON based thin-film lithium ion batteries achieve a cycle life of over 10 000 cycles.[37,38]

$$2\ Li_6P_3O_9N + 12\ Li \rightarrow Li_3PO_4 + Li_4P_2O_7 + Li_3N + 7\ Li_2O \quad (4)$$

$$Li_4P_2O_7 + 8\ Li \rightarrow Li_3PO_4 + Li_3P + 3\ Li_2O \quad (5)$$

The formed SEI layers with different chemical and physical properties significantly affect the electrochemical performance of ASSLiBs.[33] The decomposition products are mostly binary lithium compounds like LiF, Li_2O, Li_2S, Li_3N or Li_3P, which are thermodynamically stable against lithium metal and thus protect the SE against further lithiation.

In summary, the development of novel lithium stable protection materials or SEs is essential for batteries with lithium metal anodes.[38] In addition, the ionic conductivity of the decomposition products is crucial, because poor ionic conductors would result in high interfacial resistance.[33]

One serious disadvantage of e.g. LiPON and LPS is that the Li/electrolyte SEI includes Li_2O or Li_2S, which limits the ionic conductivity. Although the SEI consists also of the fast lithium ion conductors Li_3N and Li_3P,[33,39,40] the total performance of the battery is limited to that of Li_2O or Li_2S, respectively.[41] This might imply that if lithium nitridophosphates react analogously to LiPON and LPS the SEI will only include the fast ionic conductors Li_3N and Li_3P (Equation 6).

$$\text{“}LiPN_2 + 8\ Li \rightarrow 2\ Li_3N + Li_3P\text{”} \quad (6)$$

Thus, there may be a spontaneously formed SEI with high ionic conductivity in contact with the anode. Furthermore, calculations concerning the stability against lithium metal indicate that nitrides show negative reduction potential and significantly lower cathodic limits compared to other oxides, sulfides or halides.[38] Hitherto, the stability of lithium nitridophosphates against lithium metal and a possible SEI formation was not yet examined.

Due to the lack of knowledge about lithium nitridophosphate compounds and their behavior as SE, further research into these materials seems profitable. Until now, only three ternary lithium

nitridophosphate compounds were structurally elucidated (Li_7PN_4, $Li_{10}P_4N_{10}$, $LiPN_2$) and only two of them were examined concerning their lithium ion conductivity. In addition, a possible structure of $Li_{12}P_3N_9$ was postulated.[42–46] $LiPN_2$ and Li_7PN_4 were the first representatives of nitridophosphates and were described in 1960 and 1971, respectively.[47–49] In the 1980s, both lithium nitridophosphates were reinvestigated and in the beginning of the 1990s Schnick and coworkers started to investigate this new class of materials.[45] Thus, the detailed knowledge of the structures of $LiPN_2$, Li_7PN_4, and $Li_{10}P_4N_{10}$ [44] laid the foundation for a successful research of nitridophosphates with a wide range of intriguing properties.

$LiPN_2$ is the lithium nitridophosphate with the lowest content of lithium ions and is the only representative that is resistant against oxidation and hydrolysis by air so far. It is isoelectronic to SiO_2 and is made up of a three-dimensional network of corner sharing PN_4 tetrahedra in a matrix of lithium ions. The latter are tetrahedrally coordinated by N atoms.[42] In contrast, Li_7PN_4 has the highest content on lithium ions and is sensitive to oxygen and moisture. It is made of non-condensed PN_4 tetrahedra which are framed by lithium ions forming distorted LiN_4 tetrahedra.[43] The lithium ion conductivity of both compounds was also investigated: Li_7PN_4 ($\sigma_{400K} = 10^{-5}\ \Omega^{-1}cm^{-1}$, $E_a = 46.7$ kJmol^{-1}) exhibits a higher ionic conductivity than $LiPN_2$ ($\sigma_{400K} = 10^{-7}\ \Omega^{-1}cm^{-1}$, $E_a = 58.9$ kJmol^{-1}), due to different respective crystal structures and number of available charge carriers. Li_7PN_4 exhibits a large number of interstitial sites that can be occupied by Li^+ ions. In contrast, $LiPN_2$ shows a closely packed atomic arrangement with no comparable interstitial positions.[46]

With $Li_{10}P_4N_{10}$ a lithium nitridophosphate was synthesized whose degree of condensation (ratio of tetrahedra centers to tetrahedra corners per sum formula: κ = atomic ratio P/N) is between those of $LiPN_2$ and Li_7PN_4. It consists of adamantane type $[P_4N_{10}]^{10-}$ ions isoelectronic to $[P_4O_{10}]$ in a matrix of lithium ions.[44] Furthermore, $Li_{12}P_3N_9$ was postulated to have a $[Si_3O_9]^{6-}$ analogue ring-structure of vertex sharing PN_4 tetrahedra.[45,50] Thus, only four different linking patterns of PN_4 tetrahedra are known, including the postulated *dreier*-rings in $Li_{12}P_3N_9$. However, these four examples already show the great structural variety with isolated ions, rings, cages and a three-dimensional network structure. Figure 4 shows the different P/N substructures in lithium nitridophosphates, which exhibit a wide range of degrees of condensation from 0.25 to 0.5.

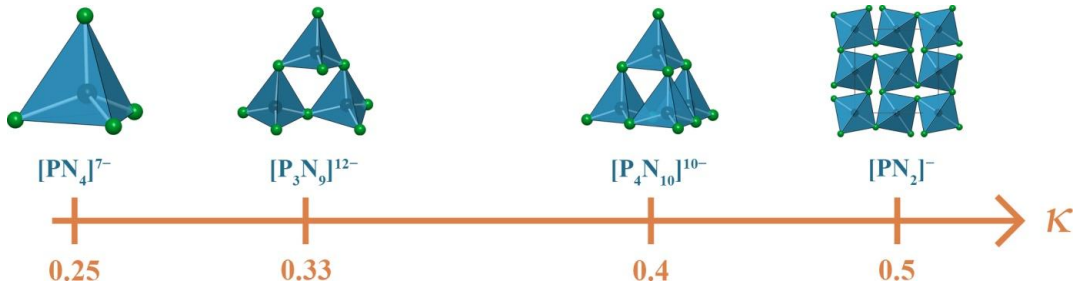

Figure 4. Degree of condensation and PN partial structures of lithium nitridophosphate compounds. From left to right: Li_7PN_4, $Li_{12}P_3N_9$, $Li_{10}P_4N_{10}$ and $LiPN_2$.[45]

All of the above mentioned lithium nitridophosphates can be synthesized by solid-state reaction of Li_3N and P_3N_5 below 850 °C at ambient pressure under strict exclusion of air.[42–45] Synthesis temperatures above this temperature lead to decomposition of the starting material P_3N_5. Due to its limited thermal stability P_3N_5 decomposes into its elements already at temperatures above 850 °C (Equation 7).[45,51]

$$P_3N_5 \rightleftarrows 3\ PN + N_2 \rightleftarrows 3/4\ P_4 + 5/2\ N_2 \qquad (7)$$

However, typical synthesis temperatures of most nitridophosphates lie in the range of about 1100 °C. Therefore, standard synthetic approaches under ambient pressure in silica ampoules or in a high-frequency furnance often do not lead to the desired results.[45] Following Le Chatelier's principle, the decomposition of P_3N_5 can be suppressed by pressure. Consequently, high-pressure and high-temperature synthesis employing the multianvil technique emerged as a powerful technique for synthesis of novel nitridophosphates with unusual network structures.[52] Prominent examples of these are the nitride clathrate $P_4N_4(NH)_4(NH)_3$, the (oxo)nitride zeolites NPO and NPT, $Ba_3P_5N_{10}Br:Eu^{2+}$, or δ-PON and β-PN(NH).[52–58] The nitride zeolites could potentially be used in industrial applications such as gas separation or catalysis.[53–55] $Ba_3P_5N_{10}X:Eu^{2+}$ (X = Cl, Br, I) or $MP_2N_4:Eu^{2+}$ (M = Ca, Sr, Ba) are efficient luminescent materials,[59–61] and vitreous Li–Ca–P–N compounds exhibit remarkable refractive indices and hardness.[62,63]

By this high-pressure and high-temperature method also a number of high-pressure polymorphs with unprecedented structures were reported. For example, different polymorphs of silica analogous PON were characterized, in addition to HP_4N_7 or P_3N_5.[57,58,64–70] The ambient pressure polymorph α-P_3N_5 consists of corner and edge-sharing PN_4 tetrahedra and exhibits a very high degree of condensation ($\kappa = 0.6$).[68,69,71] By high-pressure and high-temperature synthesis of the α-polymorph, also fivefold coordination number of phosphorus (square-pyramidal PN_5 polyhedra) was observed in γ-P_3N_5. The high-pressure polymorph γ-HP_4N_7 contains PN_5

polyhedra with distorted square-pyramidal and trigonal-bipyramidal geometry.[58,70,72] For the high-pressure phases δ- and δ'-P_3N_5, and spinel type BeP_2N_4 even octahedral PN_6 units were predicted.[73,74]

So far, high-pressure/high-temperature synthesis of nitridophosphates implies some difficulties with the characterization of the products. The reaction products typically only contain single crystals too small for conventional single-crystal X-ray structure determination. Therefore, synthesis of novel nitridophosphates requires phase-pure products for structure solution by combination of different analytical methods, like powder X-ray diffraction, solid-state MAS NMR spectroscopy, and electron microscopy.[51,57]

Consequently, it is important to develop new synthetic strategies to increase the crystal size of nitridophosphates allowing for structure determination of not only main phase compounds but also minority phases. Recently, three different approaches have been established to overcome this challenge. The addition of a mineralizer to the starting mixture leads to an increase the growth of single crystals. NH_4Cl turned out to be quite beneficial, due to HCl, formed intermediately, by thermal decomposition of the mineralizer. The HCl enables reversible and reconstructive P–N bond cleavage and reformation. NH_4Cl was successfully used to crystallize a number of new compounds like β-PN(NH) or β- and γ-P_4N_6(NH).[58,75–77] But in some cases NH_4Cl induces H^+-transfer reactions, thus acting not only as mineralizer. Therefore, this approach cannot be used for the synthesis of hydrogen free compounds, if they are sensitive to the incorporation of hydrogen.[58,76,77] A second approach to grow single crystals with a diameter of up to a few hundred microns is high-pressure metathesis, in which a metal halide (e.g. NdF_3) and an alkali-metal nitridophosphate (e.g. $LiPN_2$) react at high-pressure/high-temperature conditions. The *in situ* formed alkali halide (e.g. LiF) serves as mineralizer, which can be removed by washing. With this method structures of novel nitridophosphates like $LiNdP_4N_8$, two polymorphs of $Ln_2P_3N_7$ (Ln = Pr, Nd, Sm, Eu, Ho, Yb, La, Ce, Pr), $Ho_3[PN_4]O$ or $Ce_4Li_3P_{18}N_{35}$ were elucidated.[78–81] With high-pressure metathesis only thermodynamically stable phases have been characterized so far.[78–81] Another approach that increases the crystal size of nitride compounds is the addition of alkali metal fluxes such as a Na or Li flux, which can be separated by sublimation in vacuum after the reaction. This technique was already used for the synthesis of nitridogallates.[82,83] But for multianvil syntheses this approach may be problematic due to the increasing volume during melting of the alkali metal, which will lead to pressure fluctuations. In addition, alkali metals might react with most starting compounds leading to a multitude of side phases.[84] An extension of this concept circumvents these two problems by replacement of the alkali metal by alkali nitrides. Li_3N, for instance, was used as a flux to grow single crystals of GaN or *c*-BN.[85,86]

The aim of this thesis was the explorative search for new lithium nitridophosphates and their classification as lithium ion conductors. The focus was on the synthesis and characterization of novel structural motifs in nitridophosphates. A relation between the different structural motifs and the respective lithium ion conductivity should be established, via the incorporation of lithium into nitridophosphates. To expand the structural variety of this compound class, the common synthetic route for lithium nitridophosphates (solid-state reaction in silica ampoules) was expanded to high-pressure/high-temperature syntheses using the multianvil technique. Since the single-crystals obtained by this approach are usually too small for conventional single-crystal X-ray diffraction, different methods to increase the crystal size of lithium nitridophosphates were investigated. Several methods were combined to identify and structurally characterize the novel compounds. X-ray diffraction on single-crystals and powders was performed as the main means of structure determination. ^{31}P, ^{7}Li, ^{6}Li, and ^{11}B solid-state MAS NMR measurements as well as FTIR and EDX spectroscopy supplemented the diffraction techniques in order to offset the inherent limitations of the X-ray methods. In addition, temperature dependent powder X-ray diffraction was used to evaluate the stability regions of the compounds. Theoretical studies including DFT calculations and topological analyses corroborated analytical data for several structures. For example, the phase transition of different polymorphs was confirmed by volume pressure calculations. Topological analysis based on Voronoi-Dirichlet polyhedra revealed possible movement of the lithium ions in three dimensions, indicating lithium ion conductivity with respect to the structures. The quantification of the lithium ion conductivity was performed via temperature dependent impedance measurements. Finally, XPS measurements were carried out to investigate the stability of lithium nitridophosphates being in contact with the anode material lithium, which is essential for lithium ion battery function and the durability of electrochemical devices.

1.1. References

[1] A. F. Holleman, E. Wiberg, N. Wiberg, *Lehrbuch der Anorganischen Chemie*, Walter De Gruyter Verlag, Berlin, **2007**.

[2] J. Deberitz, G. Boche, *Chem. Unserer Zeit* **2003**, *37*, 258–266.

[3] M. Bertau, W. Voigt, A. Schneider, G. Martin, *Chem. Ing. Tech.* **2017**, *89*, 1107–1107.

[4] J.-M. Tarascon, M. Armand, *Nature* **2001**, *414*, 359–367.

[5] V. Zepf, A. Reller, C. Rennie, M. Ashfield, S. J., *Materials Critical to the Energy Industry. An Introduction. 2nd Edition.*, BP, **2014**.

[6] C. Siedenbiedel, *Umstellung auf Elektroautos – Wird Lithium das neue Öl?*, in: *Frankfurter Allgemeine – Finanzen*, **09.09.2017**.

[7] R. Jaffe, J. Price, G. Ceder, R. Eggert, T. Graedel, K. Gschneidner, M. Hitzman, F. Houle, A. Hurd, R. Kelley, et al., *Energy Critical Elements: Securing Materials for Emerging Technologies*, Washington, DC, **2011**.

[9] J. F. M. Oudenhoven, L. Baggetto, P. H. L. Notten, *Adv. Energy Mater.* **2011**, *1*, 10–33.

[9] V. Aravindan, J. Gnanaraj, S. Madhavi, H.-K. Liu, *Chem. Eur. J.* **2011**, *17*, 14326–14346.

[10] B. B. Owens, J. E. Oxley, A. F. Sammells, *Solid State Electrochemistry*, Springer-Verlag Berlin, **1977**.

[11] B. V. Lotsch, J. Maier, *J. Electroceramics* **2017**, 1–14.

[12] U. v. Alpen, A. Rabenau, G. H. Talat, *Appl. Phys. Lett.* **1977**, *30*, 621–623.

[13] A. Rabenau, *Solid State Ionics* **1982**, *6*, 277–293.

[14] R. A. Huggins, *J. Power Sources* **1999**, *81–82*, 13–19.

[15] K. Mizushima, P. C. Jones, P. J. Wiseman, J. B. Goodenough, *Mater. Res. Bull.* **1980**, *15*, 783–789.

[16] M. M. Thackeray, W. I. F. David, P. G. Bruce, J. B. Goodenough, *Mater. Res. Bull.* **1983**, *18*, 461–472.

[17] M. Mohri, N. Yanagisawa, Y. Tajima, H. Tanaka, T. Mitate, S. Nakajima, M. Yoshida, Y. Yoshimoto, T. Suzuki, H. Wada, *J. Power Sources* **1989**, *26*, 545–551.

[18] J.-M. Tarascon, A. S. Gozdz, C. Schmutz, F. Shokoohi, P. C. Warren, *Solid State Ionics* **1996**, *86–88*, 49–54.

[19] Y. Wang, W. D. Richards, S. P. Ong, L. J. Miara, J. C. Kim, Y. Mo, G. Ceder, *Nat. Mater.* **2015**, *14*, 1026–1031.

[20] A. Vezzini, *Phys. Unserer Zeit* **2010**, *41*, 36–42.

[21] Telekommunikation: dpa, *Immer wieder Hitzeprobleme mit Lithium-Ionen-Akkus*, in: *Süddeutsche Zeitung*, **11.10.2016**.

[22] X. Lü, J. W. Howard, A. Chen, J. Zhu, S. Li, G. Wu, P. Dowden, H. Xu, Y. Zhao, Q. Jia, *Adv. Sci.* **2016**, *3*, 1500359.

[23] N. Kamaya, K. Homma, Y. Yamakawa, M. Hirayama, R. Kanno, M. Yonemura, T. Kamiyama, Y. Kato, S. Hama, K. Kawamoto, A. Mitsui, *Nat. Mater.* **2011**, *10*, 682–686.

[24] Y. Seino, T. Ota, K. Takada, A. Hayashi, M. Tatsumisago, *Energy Environ. Sci.* **2014**, *7*, 627–631.

[25] Z. Liu, W. Fu, E. A. Payzant, X. Yu, Z. Wu, N. J. Dudney, J. Kiggans, K. Hong, A. J. Rondinone, C. Liang, *J. Am. Chem. Soc.* **2013**, *135*, 975–978.

[26] X. Yu, *J. Electrochem. Soc.* **1997**, *144*, 524–532.

[27] J. Janek, W. G. Zeier, *Nat. Energy* **2016**, *1*, 16141.

[28] A. Schwöbel, R. Hausbrand, W. Jaegermann, *Solid State Ionics* **2015**, *273*, 51–54.

[29] Y. Li, W. Zhou, S. Xin, S. Li, J. Zhu, X. Lü, Z. Cui, Q. Jia, J. Zhou, Y. Zhao, J. B. Goodenough, *Angew. Chem. Int. Ed.* **2016**, *55*, 9965–9968; *Angew. Chem.* **2016**, *128*, 10119–10122.

[30] S. Wenzel, T. Leichtweiss, D. Krüger, J. Sann, J. Janek, *Solid State Ionics* **2015**, *278*, 98–105.

[31] M. Park, X. Zhang, M. Chung, G. B. Less, A. M. Sastry, *J. Power Sources* **2010**, *195*, 7904–7929.

[32] S. Wenzel, S. Randau, T. Leichtweiß, D. A. Weber, J. Sann, W. G. Zeier, J. Janek, *Chem. Mater.* **2016**, *28*, 2400–2407.

[33] Y. Zhu, X. He, Y. Mo, *J. Mater. Chem. A* **2016**, *4*, 3253–3266.

[34] S. Wenzel, D. A. Weber, T. Leichtweiss, M. R. Busche, J. Sann, J. Janek, *Solid State Ionics* **2016**, *286*, 24–33.

[35] W. D. Richards, L. J. Miara, Y. Wang, J. C. Kim, G. Ceder, *Chem. Mater.* **2016**, *28*, 266–273.

[36] S. Sicolo, M. Fingerle, R. Hausbrand, K. Albe, *J. Power Sources* **2017**, *354*, 124–133.

[37] J. Li, C. Ma, M. Chi, C. Liang, N. J. Dudney, *Adv. Energy Mater.* **2015**, *5*, 1–6.

[38] Y. Zhu, X. He, Y. Mo, *Adv. Sci.* **2017**, 1600517.

[39] U. V. Alpen, A. Rabenau, G. H. Talat, *Appl. Phys. Lett.* **1977**, *30*, 621–623.

[40] G. Nazri, *Solid State Ionics* **1989**, *34*, 97–102.

[41] P. Heitjans, S. Indris, *J. Phys. Condens. Matter* **2003**, *15*, R1257–R1289.

[42] W. Schnick, J. Lücke, *Z. Anorg. Allg. Chem.* **1990**, *588*, 19–25.

[43] W. Schnick, J. Luecke, *J. Solid State Chem.* **1990**, *87*, 101–106.

[44] W. Schnick, U. Berger, *Angew. Chem. Int. Ed. Engl.* **1991**, *30*, 830–831; *Angew. Chem.* **1991**, *103*, 857–858.

[45] W. Schnick, *Angew. Chem. Int. Ed. Engl.* **1993**, *32*, 806–818; *Angew. Chem.* **1993**, *105*, 846–858.

[46] W. Schnick, J. Luecke, *Solid State Ionics* **1990**, *38*, 271–273.

[47] P. Eckerlin, C. Langereis, I. Maak, A. Rabenau, *Angew. Chem.* **1960**, *72*, 268–268.

[48] R. Marchand, P. L'Haridon, Y. Laurent, *J. Solid State Chem.* **1982**, *43*, 126–130.

[49] J. F. Brice, J. P. Motte, A. El Maslout, J. Aubry, *C. R. Seances Acad. Sci., Ser. C* **1971**, *273*, 744–746.

[50] W. Schnick, *Phosphorus. Sulfur. Silicon Relat. Elem.* **1993**, *76*, 183–186.

[51] F. W. Karau, L. Seyfarth, O. Oeckler, J. Senker, K. Landskron, W. Schnick, *Chem. Eur. J.* **2007**, *13*, 6841–6852.

[52] F. Karau, W. Schnick, *Angew. Chem. Int. Ed.* **2006**, *45*, 4505–4508; *Angew. Chem.* **2006**, *118*, 4617–4620.

[53] S. Correll, O. Oeckler, N. Stock, W. Schnick, *Angew. Chem. Int. Ed.* **2003**, *42*, 3549–3552; *Angew. Chem.* **2003**, *115*, 3674–3677.

[54] S. Correll, N. Stock, O. Oeckler, J. Senker, T. Nilges, W. Schnick, *Z. Anorg. Allg. Chem.* **2004**, *630*, 2205–2217.

[55] S. J. Sedlmaier, M. Döblinger, O. Oeckler, J. Weber, J. Schmedt Auf Der Günne, W. Schnick, M. Döblinger, O. Oeckler, J. Weber, J. Schmedt auf der Günne, et al., *J. Am. Chem. Soc.* **2011**, *133*, 12069–12078.

[56] A. Marchuk, W. Schnick, *Angew. Chem. Int. Ed.* **2015**, *54*, 2383–2387; *Angew. Chem.* **2015**, *127*, 2413–2417.

[57] D. Baumann, S. J. Sedlmaier, W. Schnick, *Angew. Chem. Int. Ed.* **2012**, *51*, 4707–4709; *Angew. Chem.* **2012**, *124*, 4785–4787.

[58] D. Baumann, W. Schnick, *Angew. Chem. Int. Ed.* **2014**, *53*, 14490–14493; *Angew. Chem.* **2014**, *126*, 14718–14721.

[59] D. Baumann, R. Niklaus, W. Schnick, *Angew. Chem. Int. Ed.* **2015**, *54*, 4388–4391; *Angew. Chem.* **2015**, *127*, 4463–4466.

[60] A. Marchuk, S. Wendl, N. Imamovic, F. Tambornino, D. Wiechert, P. J. Schmidt, W. Schnick, *Chem. Mater.* **2015**, *27*, 6432–6441.

[61] F. J. Pucher, A. Marchuk, P. J. Schmidt, D. Wiechert, W. Schnick, *Chem. Eur. J.* **2015**, *21*, 6443–6448.

[62] J.-M. Léger, J. Haines, L. S. de Oliveira, C. Chateau, A. Le Sauze, R. Marchand, S. Hull, *J. Phys. Chem. Solids* **1999**, *60*, 145–152.

[63] T. Grande, S. Jacob, J. R. Holloway, P. F. McMillan, C. A. Angell, *J. Non. Cryst. Solids* **1995**, *184*, 151–154.

[64] L. Boukbir, R. Marchand, Y. Laurent, P. Bacher, G. Roult, *Ann. Chem.* **1989**, *14*, 475.

[65] M. Bykov, E. Bykova, V. Dyadkin, D. Baumann, W. Schnick, L. Dubrovinsky, N. Dubrovinskaia, *Acta Crystallogr. Sect. E Crystallogr. Commun.* **2015**, *71*, 1325–1327.

[66] S. Horstmann, E. Irran, W. Schnick, *Angew. Chem. Int. Ed. Engl.* **1997**, *36*, 1992–1994; *Angew. Chem.* **1997**, *109*, 2085–2087.

[67] S. Horstmann, E. Irran, W. Schnick, *Z. Anorg. Allg. Chem.* **1998**, *624*, 221–227.

[68] S. Horstmann, E. Irran, W. Schnick, *Angew. Chem. Int. Ed. Engl.* **1997**, *36*, 1873–1875; *Angew. Chem.* **1997**, *109*, 2085–2087.

[69] S. Horstmann, E. Irran, W. Schnick, *Z. Anorg. Allg. Chem.* **1998**, *624*, 620–628.

[70] K. Landskron, H. Huppertz, J. Senker, W. Schnick, *Angew. Chem. Int. Ed.* **2001**, *40*, 2643–2645; *Angew. Chem.* **2001**, *113*, 2713–2716.

[71] W. Schnick, J. Lücke, F. Krumeich, W. Schnick, *Chem. Mater.* **1996**, *8*, 281–286.

[72] K. Landskron, H. Huppertz, J. Senker, W. Schnick, *Z. Anorg. Allg. Chem.* **2002**, *628*, 1465.

[73] P. Kroll, W. Schnick, *Chem. Eur. J.* **2002**, *8*, 3530–3537.

[74] F. J. Pucher, S. R. Römer, F. W. Karau, W. Schnick, *Chem. Eur. J.* **2010**, *16*, 7208–7214.

[75] S. J. Sedlmaier, E. Mugnaioli, O. Oeckler, U. Kolb, W. Schnick, *Chem. Eur. J.* **2011**, *17*, 11258–11265.

[76] A. Marchuk, F. J. Pucher, F. W. Karau, W. Schnick, *Angew. Chem. Int. Ed.* **2014**, *53*, 2469–2472; *Angew. Chem.* **2014**, *126*, 2501–2504.

[77] D. Baumann, W. Schnick, *Inorg. Chem.* **2014**, *53*, 7977–7982.

[78] S. D. Kloß, W. Schnick, *Angew. Chem. Int. Ed.* **2015**, *54*, 11250–11253; *Angew. Chem.* **2015**, *127*, 11402–11405.

[79] S. D. Kloß, N. Weidmann, R. Niklaus, W. Schnick, *Inorg. Chem.* **2016**, *55*, 9400–9409.

[80] S. D. Kloß, N. Weidmann, W. Schnick, *Eur. J. Inorg. Chem.* **2017**, 1930–1937.

[81] S. D. Kloß, L. Neudert, M. Döblinger, M. Nentwig, O. Oeckler, W. Schnick, *J. Am. Chem. Soc.* **2017**, *139*, 12724–12735.

[82] F. Hintze, F. Hummel, P. J. Schmidt, D. Wiechert, W. Schnick, *Chem. Mater.* **2012**, *24*, 402–407.

[83] F. Hintze, N. W. Johnson, M. Seibald, D. Muir, A. Moewes, W. Schnick, *Chem. Mater.* **2013**, *25*, 4044–4052.

[84] P. Bridgman, *Phys. Rev.* **1926**, *27*, 68–86.

[85] H. Li, H. Q. Bao, G. Wang, B. Song, W. J. Wang, X. L. Chen, *Cryst. Growth Des.* **2008**, *8*, 2775–2779.

[86] G. Bocquillon, C. Loriers-Susse, J. Loriers, *J. Mater. Sci.* **1993**, *28*, 3547–3556.

2. $Li_{12}P_3N_9$ with Non-Condensed $[P_3N_9]^{12-}$ Rings and its High-Pressure Polymorph Li_4PN_3 with Infinite Chains of PN_4-Tetrahedra

Eva-Maria Bertschler, Robin Niklaus, Wolfgang Schnick

published in: *Chem. Eur. J.* **2017**, *23*, 9592-9599. DOI: 10.1002/chem.201700979

Abstract

$Li_{12}P_3N_9$ was synthesized by solid-state reaction of Li_3N and P_3N_5 at 790 °C. It is made up of non-condensed $[P_3N_9]^{12-}$ *dreier*-rings of PN_4-tetrahedra. The corresponding high-pressure polymorph, Li_4PN_3, was synthesized under high-pressure/high-temperature conditions from $Li_{12}P_3N_9$ or $LiPN_2$ and Li_7PN_4 at 6 or 7 GPa, respectively, using the multianvil technique. Li_4PN_3 is the first lithium *catena*-nitridophosphate and contains PN_3 *zweier*-chains of corner sharing PN_4-tetrahedra. To confirm the structure elucidated from single-crystal X-ray data, Rietveld refinement, ^{6}Li, ^{7}Li, and ^{31}P solid-state NMR spectroscopy, FTIR spectroscopy and EDX measurements were carried out. To examine the phase transition of $Li_{12}P_3N_9$ to Li_4PN_3 at 6 GPa and to corroborate the latter as the corresponding high-pressure polymorph, DFT calculations were conducted. Electronic band gap and electron localization function (ELF) calculations were carried out to elucidate the electronic properties and bonding behavior of both polymorphs.

2.1. Introduction

PN_4-tetrahedra are the characteristic structural motif of nitridophosphates.[1, 2] Due to the ability to form framework structures, from networks of corner- and/or edge-sharing tetrahedra, these compounds are of high interest concerning their structural variety and their technical applicability.[2-6] Prominent examples of such materials include optical materials for example, $Ba_3P_5N_{10}Br:Eu^{2+}$,[7] a promising white-light-emitting luminescent material, (oxo)nitridophosphate zeolites,[8-10] or lithium ion conductors (e.g., in materials like "*LiPON*").[11-14] High hardness was observed in γ-P_3N_5, where besides PN_4-tetrahedra, square PN_5-pyramids occur as well.[15, 16] Accordingly, exploration of new structures with new topologies or new compositions leads to interesting new materials.[5]

In lithium nitridophosphates different linking patterns of corner-sharing PN_4-tetrahedra occur, surrounded by a matrix of Li^+ ions.[1] Yet, only five ternary lithium nitridophosphates were described in literature. Li_7PN_4 has the lowest atomic ratio P/N and contains non-condensed $[PN_4]^{7-}$ ions.[17] Preliminary investigations assumed that the PN_4-tetrahedra in $Li_{12}P_3N_9$ form non-condensed *dreier*-rings[18, 19] isoelectronic to $[Si_3O_9]^{6-}$, but until now no complete structural analysis has been published.[1, 20] In $Li_{18}P_6N_{16}$ the $[P_6N_{16}]^{18-}$ tricyclic ring structure is composed of one *vierer*-ring with two annulated *dreier*-rings.[14] A cage like structure occurs in $Li_{10}P_4N_{10}$ with adamantane like $[P_4N_{10}]^{10-}$ ions, isoelectronic to $[P_4O_{10}]$.[21] $LiPN_2$ has the lowest Li content and is made up of a three-dimensional network-structure with corner sharing PN_4-tetrahedra that is isoelectronic to SiO_2.[22] All of these lithium nitridophosphates, except $Li_{18}P_6N_{16}$, can be synthesized from Li_3N and P_3N_5 below 850 °C in Ta or W crucibles. Higher reaction temperatures lead to decomposition of P_3N_5, due to its limited thermal stability.[1] To prevent decomposition, high-pressure/high-temperature synthesis emerged as a powerful tool to obtain new lithium nitridophosphates with the Li_3N self-flux method. $Li_{18}P_6N_{16}$ is the first lithium nitridophosphate synthesized by high-pressure/high-temperature technique.[14]

Recently, a number of intriguing P/N-networks, with high degrees of condensation, were synthesized by this high-pressure/high-temperature approach, for example, β-cristobalite-type PN(NH),[23, 24] and β-PN(NH);[25] α-P_4N_6(NH),[6, 26] β-P_4N_6(NH),[5] and γ-P_4N_6(NH).[27]

In this contribution we report on synthesis and structural investigation of $Li_{12}P_3N_9$ (="3 Li_4PN_3") and its high-pressure polymorph Li_4PN_3. We were able to grow single crystals of both polymorphs, enabling structure determination on the basis of single-crystal X-ray diffraction data. DFT calculations corroborate the observed high-pressure phase transition.

2.2. Results and Discussion

2.2.1. Synthesis

$Li_{12}P_3N_9$ and Li_4PN_3 were synthesized by different approaches after empirical optimization [Equations (1) to (5)]. $Li_{12}P_3N_9$ was obtained at high-temperatures and normal pressure, while Li_4PN_3 is accessible at high-temperature and high-pressure conditions. To avoid hydrolysis, all compounds were handled under inert conditions.

$$4\ Li_3N + P_3N_5 \xrightarrow{\Delta T} Li_{12}P_3N_9 \quad (1)$$

$$3\ LiPN_2 + 3\ Li_3N \xrightarrow{\Delta T} Li_{12}P_3N_9 \quad (2)$$

$$2\ LiPN_2 + Li_7PN_4 + Li_3N \xrightarrow{\Delta T} Li_{12}P_3N_9 \quad (3)$$

$$Li_{12}P_3N_9 \xrightarrow{\Delta T,\ \Delta p} 3\ Li_4PN_3 \quad (4)$$

$$LiPN_2 + Li_7PN_4 \xrightarrow{\Delta T,\ \Delta p} 2\ Li_4PN_3 \quad (5)$$

According to Equations (1), (2), and (3), different amounts of $Li_{12}P_3N_9$ were obtained together with Li_3P, Li_7PN_4, $Li_{10}P_4N_{10}$, or $LiPN_2$ as side phases depending on initial weight ratio and reaction temperature. For all routes we used a Li_3N flux method, in open Ta-crucibles sealed in silica ampoules under nitrogen atmosphere, with different amounts of Li_3N excess. The high-pressure polymorph Li_4PN_3 was synthesized according to two different routes. According to Equation (4) Li_4PN_3 was made from $Li_{12}P_3N_9$ at 6 GPa and 820 °C using a Walker-type multianvil assembly.[28-32] Products with smaller amounts of side products were obtained by reaction from non-equimolar amounts of $LiPN_2$ and Li_7PN_4 (molar ratio 1:2.25). The significant excess of Li_7PN_4 leads to an in situ formation of Li_3N (self-flux), as described in previous work.[14] According to this route, 9 GPa and 1200 °C seemed to be favorable. Due to the better crystal quality after synthesis according to Equation (1) and (5), single-crystals of these approaches were used for structure analysis. Detailed information on the synthesis of the two polymorphs is given in the Experimental section.

2.2.2. Crystal Structure

The crystal structures of both polymorphs were solved and refined from single-crystal X-ray diffraction data. $Li_{12}P_3N_9$ crystallizes in monoclinic space group *Cc* (no. 9) with four formula units per unit cell (Table 1).

The reflection conditions *hkl* for $h+k=2n$ and $h0l$ for $l=2n$ are in accordance with space groups *Cc* or *C*2/*c*. The E-value statistics suggest a non-centrosymmetric space group. Furthermore, the orthorhombic space group $Cmc2_1$ exhibits significant higher *R* values, especially for wR_2 (R_{int} is twice as high). Thus, $Li_{12}P_3N_9$ was refined in *Cc* as a pseudo-orthorhombic twin with a two-fold axis (100 0−10 00−1). All P and N positions were determined during structure solution and were refined anisotropically. The Li atom positions were localized during structure refinement from difference Fourier maps. The P/N substructure of $Li_{12}P_3N_9$ is made up of three corner sharing PN_4-tetrahedra forming *dreier*-rings in chair conformation, analogously to the cyclo-trisilicate $[Si_3O_9]^{6-}$ (Figure 1).[33]

Table 1. Crystallographic data of $Li_{12}P_3N_9$ and Li_4PN_3.

Formula	**$Li_{12}P_3N_9$**	**Li_4PN_3**
crystal size [mm^3]	0.01 x 0.01 x 0.01	0.01 x 0.01 x 0.01
formula mass [g mol^{-1}]	302.28	100.76
crystal system	monoclinic	orthorhombic
space group	Cc (no. 9)	Pccn (no. 56)
twin	$100\ 0\bar{1}0\ 00\bar{1}$	
BASF	0.203(7)	
cell parameters/ Å,°	a = 12.094(5)	a = 9.6597(4)
	b = 7.649(3)	b = 11.8392(6)
	c = 9.711(4)	c = 4.8674(2)
	β = 90.53(2)	
cell volume/ $Å^3$	898.3(6)	556.65(4)
formula units/ cell	4	8
calculated density/ g · cm^{-3}	2.235	2.405
F(000)	576	384
diffractometer	Bruker D8 Venture	
temperature/ °C	−173	25
radiation, monochromator	Mo-K_α (λ = 0.71073 Å), Goebel mirror	
absorption correction	multi scan	
θ range/ °	2.10-30.53	2.72-28.30
number of collected data	5897	6353
number of unique data	2625	698
number of unique data with $I \geq 2\sigma(I)$	2298	597
refined parameters	158	61
GooF	1.093	1.116
R indices [$F_0^2 \geq 2\sigma(F_0^2)$]	R_1 = 0.0442, wR_2 = 0.0942[a]	R_1 = 0.0388, wR_2 = 0.0844[b]
R indices (all data)	R_1 = 0.0554, wR_2 = 0.0994[a]	R_1 = 0.0497, wR_2 = 0.0982[b]
max/min res. electron density/ e$Å^{-3}$	0.50/ −0.42	0.79/−0.62
R_{int}/ R_σ	0.0595/0.0869	0.0560/0.0317

[a] $w = 1/[\sigma^2(F_o^2)+(0.0318P)^2]$, $P=(F_o^2+2F_c^2)/3$.

[b] $w = 1/[\sigma^2(F_o^2)+(0.0064P)^2+3.6207P]$, $P=(F_o^2+2F_c^2)/3$:

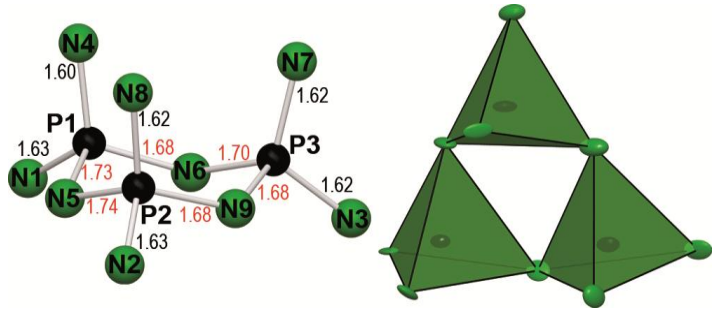

Figure 1. Left: $[P_3N_9]^{12-}$ anion in chair conformation with P−N distances. Right: $[P_3N_9]^{12-}$ anion with PN_4 tetrahedra of the P/N-framework in green. The thermal ellipsoids are depicted at 90 % probability level. (P: black, N: green).

These *dreier*-rings are not further condensed and form two types of layers (Figure 2: orange and green). Within one layer all $[P_3N_9]^{12-}$ units are orientated equally. In every other layer the *dreier*-rings are orientated differently, but also equally within the layer.

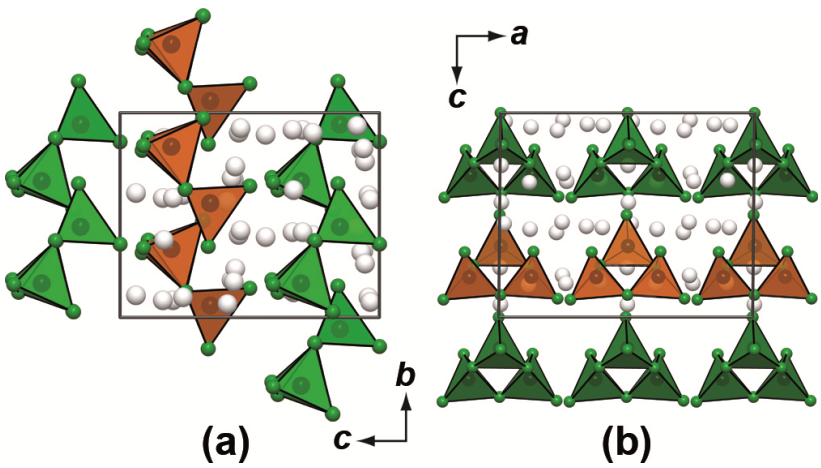

Figure 2. Packing of $Li_{12}P_3N_9$: viewed along *a* (a) and viewed along *b* (b). (P: black, N: green; Li: gray; PN_4 tetrahedra: green or orange depending on the orientation).

The high-pressure polymorph Li_4PN_3 crystallizes in the centrosymmetric orthorhombic space group *Pccn* (no. 56). Analogously to $Li_{12}P_3N_9$, all P and N positions were determined during structure solution and were refined anisotropically. The Li atom positions were localized from difference Fourier maps. Li_4PN_3 is made of infinite *zweier*-chains of corner sharing PN_4-tetrahedra ${}^3_\infty[PN_2N_{2/2}]^{4-}$, running along *c* (shortest lattice parameter).

The *catena*-nitridophosphate chains have a stretching factor of f_s=0.923 and a chain periodicity of P=2 ($f_s=I_{chain}/(I_T\times P)$=4.855/(2.627×2). For definitions of I_{chain} and I_T see Figure 3a. Liebau introduced f_s for the classification of chain and layer silicates and this formalism can also be

adapted to nitridophosphates. This value is a measure of infinitely extended chains.[18] Maximal stretched chains (f_s=1) occur in for example, Ca_2PN_3.[34, 35] Less stretched chains of corner sharing PN_4-tetrahedra have been reported for Mg_2PN_3[34] and Zn_2PN_3 (f_s=0.88).[36] Li_4PN_3 contains four infinite chains per unit cell with two different orientations (Figure 3, orange and green).

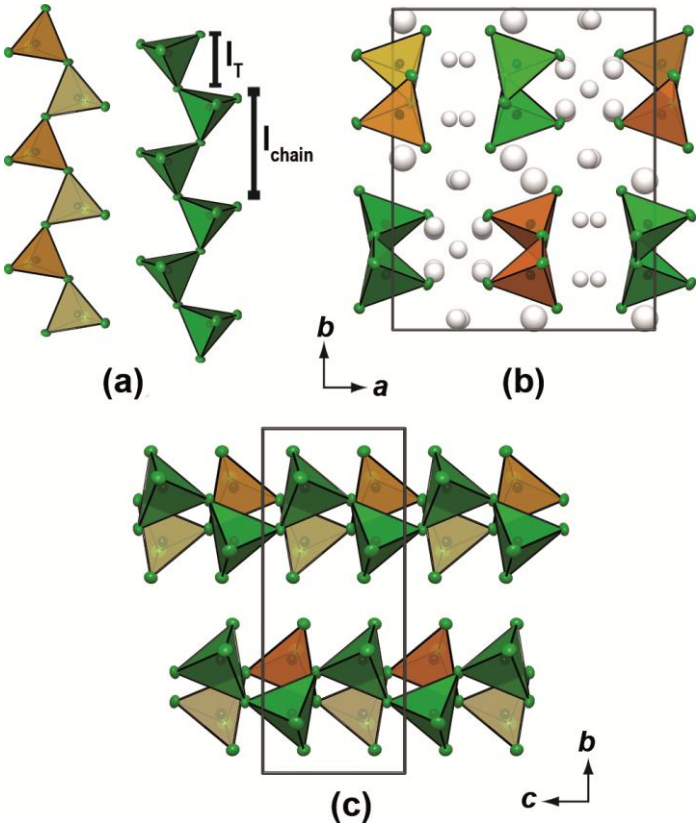

Figure 3. (a) *Zweier*-chains in Li_4PN_3. (b) Li_4PN_3 viewed along *c*. (c) Li_4PN_3 viewed along *a*. The thermal ellipsoids are depicted at 90 % probability level in (a), (b), and (c). (P: black, N: green; Li: gray; PN_4 tetrahedra: green or orange depending on the orientation).

The P−N distances for $Li_{12}P_3N_9$ vary from 1.60 to 1.73 Å and for Li_4PN_3 from 1.61 to 1.73 Å. Analogously to other nitridophosphates the values for P−N bond lengths to terminal nitrogen atoms of PN_4-tetrahedra are shorter than those to bridging ones.[14, 37] These values are in accordance with other nitridophosphates.[14, 21]

The $[P_3N_9]^{12-}$ and $[PN_3]^{4-}$ anions are surrounded by Li^+ ions. The latter were not refined anisotropically, due to their low scattering intensity. In $Li_{12}P_3N_9$ the Li^+ ions are coordinated by N with coordination numbers 3, 4, and 5 sharing edges or corners of resulting polyhedra. The shortest Li−Li distance is 2.31 Å, which is comparable to Li−Li distances in other multinary lithium compounds (e.g., $LiCa_3Si_2N_5$).[38] In the high-pressure polymorph Li_4PN_3 there are only

$[LiN_4]$ and $[LiN_5]$ polyhedra. A free refinement of the occupation factors of the Li atoms showed partial occupation for three Li sites (Li4 (8*e*): 50 %, Li5 (8*e*): 30 %, Li6 (4*c*): 40 %). Involving the partially occupation, the shortest Li−Li distance is between Li2 and Li5 with 2.14 Å, which also corresponds with other Li containing compounds.[38]

2.2.3. Structural analysis of possible lithium migration pathways

Calculating Voronoi–Dirichlet polyhedra with TOPOS yields the possible voids and migration pathways for Li^+.[39-42]

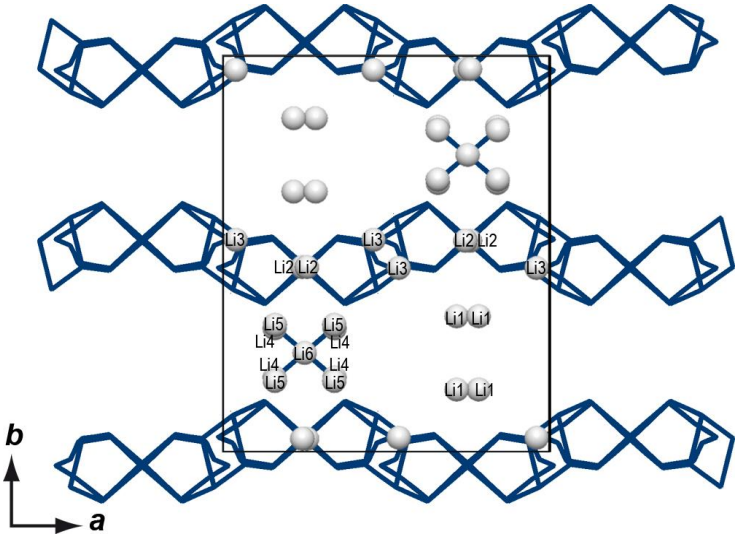

Figure 4. Calculated possible Li^+ pathways (blue) according to the voids in the structure and unit cell of Li_4PN_3 viewed along *c*. (Li: gray).

$Li_{12}P_3N_9$ shows a possible movement of the Li^+ ions in three different directions in space (Supporting Information Figure S15). In Li_4PN_3 Li4, Li5, and Li6 indicate possible movement between each other in contrast to Li1, which shows no movement. The possible migration pathways of Li2 and Li3 build chains along *a* (Figure 4). According to these calculations both polymorphs seem to be promising candidates for lithium ion conductivity. Measurements of other lithium nitridophosphates show lithium ion conductivity in the range of $10^{-5}\ \Omega^{-1}\ cm^{-1}$ at 127 °C, which we also expect for $Li_{12}P_3N_9$ and Li_4PN_3.[12, 14]

2.2.4. Solid State NMR-Spectroscopy

^{31}P, ^{6}Li, and ^{7}Li solid-state MAS NMR spectroscopy was performed to corroborate the crystal structure models of $Li_{12}P_3N_9$ and Li_4PN_3 (Supporting Information, Figures S5–S10). The ^{31}P NMR spectrum of $Li_{12}P_3N_9$ shows two strong resonances at 22.76 and 15.08 ppm together with the resonances for Li_7PN_4 (50.23 ppm) and Li_3P (−274.5 ppm). Integration of the two strong signals of $Li_{12}P_3N_9$ results in a ratio of 2:1, which is in accordance with three crystallographically independent P sites, two of which exhibit the same chemical shift (22.76 ppm). This corresponds to P1 and P2, which exhibit nearly the same bonding lengths to N. P3 has one shorter distance to N6 and corresponds to the signal at 15.08 ppm (Figure 1). The ^{6}Li solid-state MAS NMR spectrum shows four strong resonances in the range of 5.2 to 1.9 ppm; they all exhibit shoulders. The ^{7}Li solid-state MAS spectrum shows one broad signal at 4.87 ppm (with Li_7PN_4 and Li_3P as side phase). Due to the small chemical shift differences of the Li signals of $Li_{12}P_3N_9$ and the side phases, no differentiation of the phases and the crystallographically independent sites can be observed in the Li spectra.

The ^{31}P solid-state MAS NMR spectrum of Li_4PN_3 shows one strong resonance at 21.58 ppm, corresponding to one crystallographically independent P site. The ^{31}P MAS NMR signals of both polymorphs are similar with other nitridophosphates (Zn_2PN_3: 42.8 ppm; $Li_{18}P_6N_{16}$: 22.24 to 5.51 ppm).[14, 36] The ^{6}Li and ^{7}Li solid-state MAS NMR spectra show one strong signal each (2.41 and 2.59 ppm, respectively). The values found for both compounds are similar to those of other ternary nitridophosphates or lithium nitridophosphates/silicates for ^{7}Li (0.3 for $LiLa_5Si_4N_{10}O$ to 2.8 ppm for $LiCa_3Si_2N_5$; $Li_{18}P_6N_{16}$: 1.6 ppm; Li_7PN_4 (with Li_3P as side phase): 3.33 ppm).[14, 38, 43]

2.2.5. Chemical analysis (EDX, IR, Powder Diffraction)

To determine the elemental composition, EDX measurements were carried out. Besides phosphorus and nitrogen, only traces of oxygen were found, which can be explained by the hydrolysis of the compounds during contact with air (Supporting Information, Table S10 and S11). The determined atomic ratio P/N is in agreement with the results from the crystal structure analysis ($Li_{12}P_3N_9$: P/N=0.32; Li_4PN_3: P/ N=0.33).

FTIR spectroscopy of both compounds was performed to prove the absence of hydrogen (Supporting Information, Figure S13 and S14). Both spectra show significant vibrations between 600 and 1500 cm^{-1} and no marked signals in the region around 3000 cm^{-1} (N−H). A weak signal can be explained by surface hydrolysis of the sample.

To determine phase purity of the samples a powder diffraction pattern was collected (Supporting Information, Figure S3 and S4). Rietveld refinement confirms the structure determined by single-crystal structure analysis.

2.2.6. Thermal stability

In order to corroborate that Li_4PN_3 is a high-pressure polymorph of $Li_{12}P_3N_9$, a temperature-dependent powder X-ray diffraction pattern was recorded between room temperature and 1000 °C. The results (Figure 5) show that at ambient pressure, Li_4PN_3 transforms back into the ambient pressure polymorph $Li_{12}P_3N_9$ at 650 °C. At 880 °C the first indications of further decomposition can be observed.

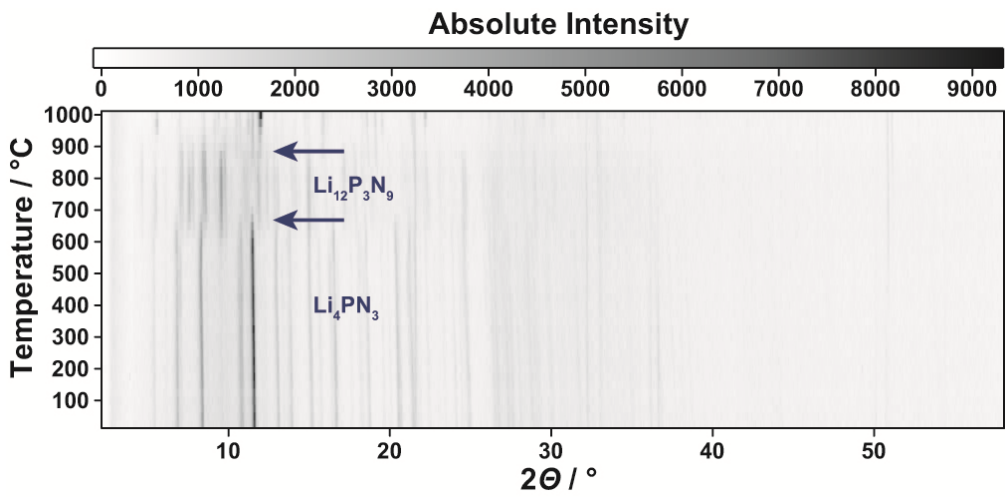

Figure 5. Temperature-dependent powder X-ray diffraction data for Li_4PN_3 under ambient pressure. The transformation to $Li_{12}P_3N_9$ starts at 650 °C.

2.2.7. Comparison of density

The density of Li_4PN_3 (ρ=2.405 g cm^{-3}) is 7 % higher than that of $Li_{12}P_3N_9$ (ρ=2.235 g cm^{-3}), which is in accordance with the principle of Le Chatelier and suggests that Li_4PN_3 is a high-pressure polymorph of $Li_{12}P_3N_9$. A density difference in this range is also observed in P_4N_6(NH) with 5 and 16 % (α-P_4N_6(NH): 2.88,[26] β-P_4N_6(NH): 3.037,[5] γ-P_4N_6(NH): 3.613 g cm^{-3}).[27] A smaller difference is observed in PN(NH) with 2 % (β-cristobalite-type PN(NH): 2.66,[23] β-PN(NH): 2.71 g cm^{-3})[25] and a higher in P_3N_5 with 32 % (α-P_3N_5: 2.77, γ-P_3N_5: 3.65 g cm^{-3}).[15]

2.2.8. Density functional theory calculations

2.2.8.1. Volume pressure calculations

Due to different observed partial occupancies of three Li sites in Li_4PN_3 we constructed a charge neutral model for Li_4PN_3 with full Li occupancies. This was done by removing the Li6-Wyckoff site (40 % occupation) and subsequently converting half of the partially occupied Li4 (50 %) and Li5 (30 %) sites into new fully ordered Li sites for our calculations (Figure 6).

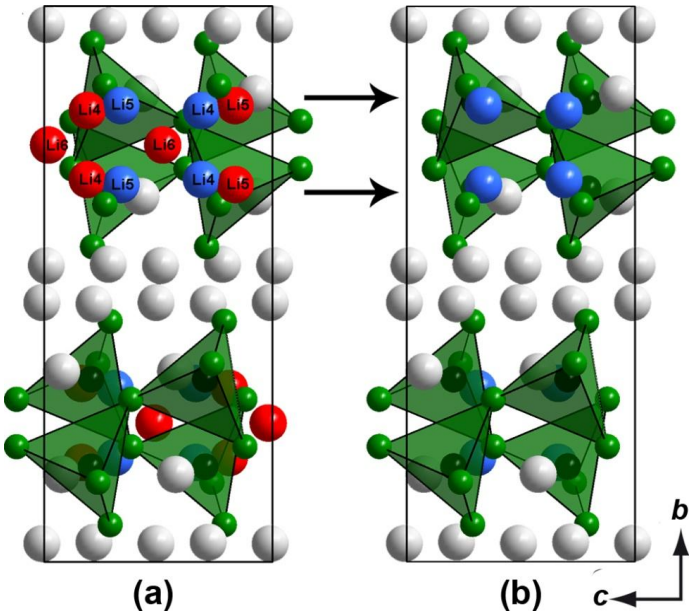

Figure 6. (a) Unit cell of Li_4PN_3 with partially occupied Li positions (Li4: 50 %, Li5: 30 %, Li6: 40 %). (b) Ordering model of Li_4PN_3 with fully occupied Li atoms. Red: Li positions which were removed; blue: Li positions which were retained and adjusted to 100 % occupancy. (P: black, N: green; Li: gray; PN_4 tetrahedra: green).

Experimental synthesis pressures were covered by structural relaxations for a variety of constant volume compressions and expansions (91 % to 105 % with 19 steps for both compounds) of the respective unit cells, maintaining the space group. The resulting energy-volume (EV) curves are shown in Figure 7a. $Li_{12}P_3N_9$ is energetically favored by 0.217 eV (20.94 kJ mol^{-1}) at ambient pressure. By fitting the EV curves according to the Murnaghan equation of state[44] we obtained the bulk modulus (B=83.8 for $Li_{12}P_3N_9$ and B=87.4 GPa for Li_4PN_3) and calculated the enthalpy difference ΔH from the equation $H=E+pV$, while pressure p is obtained by a numerical differentiation of $p=\partial E/\partial V$. Figure 7b depicts the relative enthalpy with respect to the presumed low pressure polymorph $Li_{12}P_3N_9$. Without accounting for temperature, the transition pressure

from $Li_{12}P_3N_9$ to Li_4PN_3 can be estimated to 6.55 GPa, evidently corroborating Li_4PN_3 as high-pressure polymorph of $Li_{12}P_3N_9$, being in line with the observed synthesis pressure of 6 GPa.

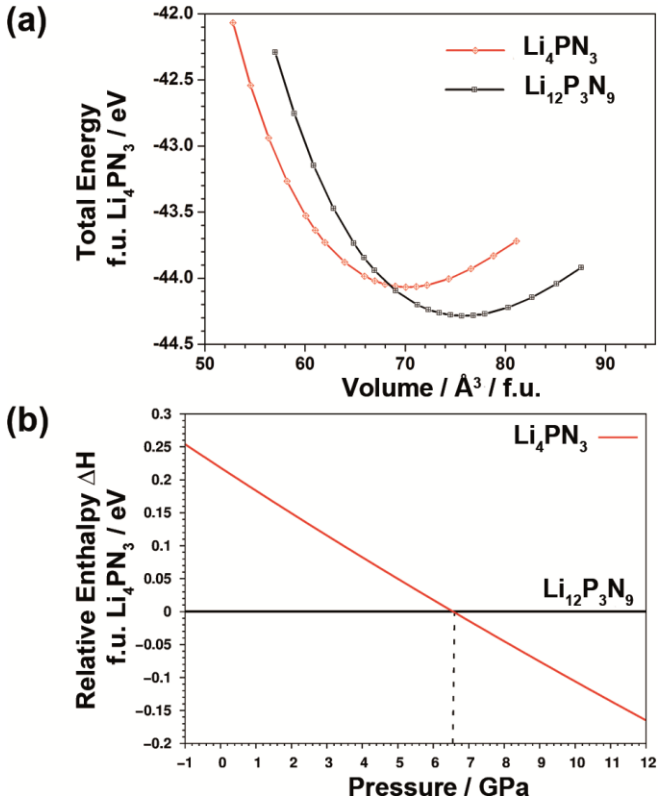

Figure 7. (a) Energy–volume diagram for $Li_{12}P_3N_9$ and Li_4PN_3. Each point constitutes one structural optimization at constant volume. Energy and Volume are given per formula unit (f.u.) of Li_4PN_3. (b) Enthalpy–pressure diagram for the high-pressure phase transition of $Li_{12}P_3N_9$ to Li_4PN_3, obtained from a fit of the Murnaghan equation of state to the energy-volume diagram. The enthalpy is given per formula unit of Li_4PN_3 relative to $Li_{12}P_3N_9$.

2.2.8.2. Electronic band structure

In Figure 8 it can be seen that both Li/P/N polymorphs are electronically insulating materials with a wide electronic indirect band-gap of 5 eV for $Li_{12}P_3N_9$ (Y to Γ) and an increased direct band gap of 6.1 eV for the high-pressure polymorph Li_4PN_3 (Γ to Γ).

The value found for $Li_{12}P_3N_9$ is in approximately the same range as in the case of α-P_3N_5 (indirect band gap of 5.21 eV).[45] In comparison, the Si_3N_4 and Ge_3N_4 spinels have direct band gaps and the values are decreasing with increasing pressure (α-Si_3N_4: 5.3, β-Si_3N_4: 5.18, γ-Si_3N_4: 3.45 eV; α-Ge_3N_4: 3.18, β-Ge_3N_4: 3.10, γ-Ge_3N_4: 2.22 eV).[46] Horvath-Bordon et al. report that band gaps in high-pressure phases of some nitrides are reduced while the elastic moduli are increased compared to the values found for ambient pressure polymorphs.[46] In contrast Li_3N and BN

behave inversely, not moving the system towards a metallic system (α-Li_3N: 1.25, α'-Li_3N: 1.3, β-Li_3N: 1.5, γ-Li_3N: 6 eV; *h*-BN: 3.81–4.10, *c*-BN: 4.20–5.18, *w*-BN: 4.90–5.81 eV).[47, 48]

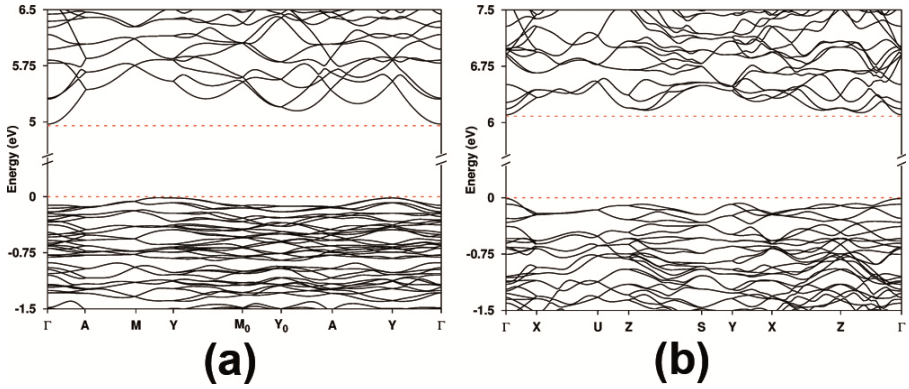

Figure 8. Electronic band structure along high-symmetry directions in the first Brillouin zone for (a) $Li_{12}P_3N_9$ and (b) Li_4PN_3.

2.2.8.3. Electronic localization function

In order to analyze the chemical bonding in both polymorphs we calculated the electron localization function (ELF), constituting the probability of finding an electron of opposed spin within the proximity of another, effectively revealing positions of chemical bonds or electron lone pairs.[49] No indication of covalent bonds between Li and N can be found, corroborating chemical intuition of a strong ionic character. The P−N bonding situation for an ELF isovalue η=0.83 reveals strong covalency within the $[P_3N_9]^{12-}$ and $^{3}_{\infty}[PN_2N_{2/2}]^{4-}$units (Supporting Information, Figures S16 to S18). The P−N bonds show strong N-polarization and free electron pairs of N^{3-} are found at terminal and bridging N atoms, as expected from VSEPR considerations.

Recently, highly polarized (almost ionic) P−N bonds have been discussed in $(PNCl_2)_3$. Analysis of the density distribution showed that the rings can be separated into Cl_2PN units that indicate perfect transferability between the different rings, which excludes the presence of aromatic delocalization in the planar P_3N_3 ring of $(PNCl_2)_3$.[50]

2.3. Conclusion

Herein we report on synthesis and full characterization of two lithium nitridophosphate polymorphs, namely $Li_{12}P_3N_9$ and Li_4PN_3. The ambient pressure polymorph $Li_{12}P_3N_9$ was prepared in ampoules and the high-pressure polymorph Li_4PN_3 by solid-state high-pressure synthesis. We showed that Li_4PN_3 is a reconstructive high-pressure polymorph of $Li_{12}P_3N_9$. This

phase relation was deduced from experimental data as well as temperature-dependent powder X-ray diffraction and DFT calculations. $Li_{12}P_3N_9$ is made of *dreier*-rings, which are not further condensed, surrounded by a matrix of Li^+ ions. The new lithium *catena*-nitridophosphate with infinite chains of corner sharing PN_4-tetrahedra has a stretching factor of f_s=0.923 and a chain periodicity P=2.

Li_4PN_3 reveals that high-pressure synthesis gives an important boost to nitridophosphate chemistry by realizing compounds that were not accessible before. Furthermore, it shows that this approach is a powerful technique to obtain novel lithium nitridophosphates with unprecedented structures and interesting properties. In addition, this finding could indicate that even ternary lithium nitridophosphates with layered structures could be accessible using multianvil techniques.

2.4. Experimental Section

2.4.1. Synthesis of starting materials

P_3N_5[51] was synthesized by reaction of P_4S_{10} (8 g, Sigma–Aldrich, 99 %) in a constant flow of ammonia (Air-Liquide, 99.999). After saturation for 4 h with NH_3, the silica tube was heated to 1123 K with 5 K min^{-1} and kept at this temperature for an additional 4 h. It was subsequently cooled down to room temperature with 5 K min^{-1}. To eliminate side products, the orange product was washed with water, ethanol, and acetone. Powder X-ray diffraction and FTIR spectroscopy confirmed phase purity of P_3N_5. All further steps were performed with strict exclusion of oxygen and moisture in an argon filled glove box (Unilab, MBraun, Garching, O_2 <1 ppm, H_2O <0.1 ppm).

$LiPN_2$[22] and Li_7PN_4[17] were synthesized by reaction of Li_3N (Rockwood Lithium, 95 %) and P_3N_5 ($LiPN_2$: molar ratio 1.2:1; Li_7PN_4: 7.2:1) in sealed silica ampoules under N_2 atmosphere. After grinding the starting materials they were transferred into a Ta-crucible, which was placed in a dried silica tube. The sealed silica ampoule was heated for 90 h in a tube furnace at 1073 or 893 K, respectively. To eliminate side products, $LiPN_2$ was washed with diluted hydrochloric acid, water, and ethanol. Li_7PN_4 was not washed. Powder X-ray diffraction and FTIR spectroscopy confirmed phase purity of the starting materials.

2.4.2. Synthesis of $Li_{12}P_3N_9$

$Li_{12}P_3N_9$ can be synthesized according to three different routes in sealed silica ampoules under Ar atmosphere. For synthesis according to Equation (1) Li_3N (Rockwood Lithium, 95 %) and P_3N_5 were mixed with a molar ratio of 4.2:1 (Equation (2): $LiPN_2$ and Li_3N with a molar ratio of 1:1.2; Equation (3): $LiPN_2$, Li_7PN_4 and Li_3N with a molar ratio of 2:1 : 1.1). After grinding the starting materials in an agate mortar, the mixture was transferred into a tantalum crucible, which was placed in a dried silica tube. The ampoules were heated for 120 h in a tube furnace at 790 °C (Equation (2): 680 °C; Equation (3): 650 °C). All syntheses yielded a colorless powder containing dark traces (Li_3P) and single crystals of $Li_{12}P_3N_9$. The product was sensitive to traces of air and moisture.

2.4.3. High-pressure synthesis of Li_4PN_3

Li_4PN_3 can be synthesized according to two different routes at high-pressure/high-temperature conditions with a modified Walker-type multianvil module in combination with a 1000 t press (Voggenreiter, Mainleus, Germany).[28-32] After mixing the starting materials, they were ground under argon atmosphere and compactly packed in a *h*-BN crucible (Henze BNP GmbH, Kempten, Germany). The *h*-BN crucible was transferred into the specially prepared pressure medium (Cr_2O_3 doped (5 %) MgO-octahedra (Ceramic Substrates & Components, Isle of Wight, UK); edge length 18 mm [Eq. (4)] or 14 mm [Eq. (5)]. Then the octahedron was placed centrically in eight truncated WC cubes (Hawedia, Marklkofen, Germany, truncation length 11 mm [Eq. (4)] or 8 mm [Eq. (5)]) separated by pyrophyllite gaskets. Detailed information describing the complete setup can be found in the literature.[29, 30, 32] According to Equation (4) (Equation (5)) the assembly was compressed to 6 GPa (9 GPa) at room temperature within 2.6 h (4 h) and then heated to about 820 °C (1200 °C) within 1 h (1 h). Under these conditions, the sample was treated for 1.6 h (1 h) and cooled down to room temperature within 1.6 h (1 h). Subsequently, the sample was decompressed in 8 h (12.5 h). Both syntheses yielded a colorless powder containing single crystals. The product is sensitive to traces of air and moisture.

2.4.4. Single-crystal X-ray analysis

Single-crystal X-ray diffraction was performed with a D8 Venture diffractometer (Bruker, Billerica MA, USA) using $Mo_{K\alpha}$ radiation from a rotating anode source. The collected data were averaged with Xprep[52] and the program package WinGX (SHELXS-97, SHELXL-97, PLATON)[40, 53-55] was used for structure solution by direct methods and refinement (see

Table 1).[56] All P and N atoms were refined anisotropically. The crystal structure was visualized using DIAMOND.[57]

2.4.5. Powder X-ray diffraction

To check phase purity of the products, X-ray powder diffraction was carried out with a STOE StadiP diffractometer (Stoe & Cie, Darmstadt, Germany) in parafocusing Debye–Scherrer geometry. With a Ge(111) single-crystal monochromator the $Cu_{K\alpha 1}$ radiation was selected. A Mythen 1 K Si-strip detector (Dectris, Baden, Switzerland) was used for detection of the diffracted radiation. For measurement the samples were enclosed in glass capillaries with 0.5 mm diameter (Hilgenberg, Malsfeld, Germany) under inert gas. Rietveld refinement was carried out using the program package TOPAS-Academic v4.1.[58] The background was handled with a shifted Chebychev function and the peak shapes were described using the fundamental parameters approach.[59, 60]

Temperature-dependent powder X-ray diffraction data were recorded on a STOE StadiP diffractometer equipped with a graphite furnace with $Mo_{K\alpha 1}$ radiation (λ=0.70930 Å) in Debye–Scherrer geometry, an image plate position sensitive detector and a Ge(111) monochromator. Data were collected every 25 °C, starting from room temperature up to 1000 °C, with a heating rate of 5 °C min^{-1}.

2.4.6. Solid-state NMR MAS (magic angle spinning) NMR methods

^{6}Li, ^{7}Li, and ^{31}P solid-state MAS NMR spectra of both polymorphs were recorded on a DSX Avance spectrometer (Bruker) with a magnetic field of 11.7 T. The sample was transferred into a ZrO_2 rotor, with an outer diameter of 2.5 mm, which was mounted in a commercial MAS probe (Bruker) under inert conditions. The rotor was spun at rotation frequency of 20 kHz. The experimental data were analyzed by device-specific software.

2.4.7. EDX measurements

The atomic ratio P/N of the samples was analyzed by energy-dispersive X-ray spectroscopy. A carbon-coated sample was examined with a scanning electron microscope (SEM) JSM-6500F (Joel, Tokyo, Japan, maximum acceleration voltage 30 kV). Qualitative and semiquantitative elemental analyses were executed by an energy dispersive spectrometer (Model 7418, Oxford Instruments, Abington, United Kingdom) and analyzed by INCA.[61]

2.4.8. Fourier-transformed infrared (FTIR) spectroscopy

Infrared spectroscopy measurements were carried out on a Bruker FTIR-IFS 66v/S spectrometer. Before measurement in the range of 400–4000 cm^{-1} the sample was mixed with KBr in a glove box and cold-pressed into a pellet (Ø=12 mm). The data were evaluated by OPUS.[62]

2.4.9. Computational details

The structural relaxation of both of $Li_{12}P_3N_9$ and Li_4PN_3 were carried out with the Vienna ab initio simulation package (Vasp).[63-65] Total energies of the unit cell were converged to 10^{-7} eV $atom^{-1}$ with residual atomic forces below 5×10^{-3} eV $Å^{-1}$. The exchange correlation was treated within the generalized gradient approximation (GGA) of Perdew, Burke, and Ernzerhof (PBE)[66, 67] and the projector-augmented-wave (PAW) method.[68, 69] A plane-wave cut-off of 535 eV was chosen for the calculations with a Brillouin zone sampling on a Γ-centered *k*-mesh, produced from the method of Monkhorst and Pack,[70] of 5×7×6 ($Li_{12}P_3N_9$) and 6×5×11 (Li_4PN_3) respectively. Additional calculations were performed with the modified Becke–Johnson formalism (GGA-mbj)[71, 72] to treat the electronic band gaps.

2.5. Acknowledgements

We would like to thank Dr. Peter Mayer for single-crystal X-ray measurements, Thomas Miller for high-temperature powder diffraction measurements, Christian Minke for EDX, SEM, and solid-state MAS NMR measurements, Marion Sokoll for IR measurements, and Dr. Constantin Hoch for helpful discussions concerning the structural analysis (all at Department of Chemistry of LMU Munich). We gratefully acknowledge financial support and granted by the Fonds der Chemischen Industrie (FCI), the Deutsche Forschungsgemeinschaft (DFG).

2.6. References

[1] W. Schnick, *Angew. Chem. Int. Ed. Engl.* **1993**, *32*, 806–818; *Angew. Chem.* **1993**, *105*, 846–858.

[2] W. Schnick, J. Luecke, F. Krumeich, *Chem. Mater.* **1996**, *8*, 281–286.

[3] S. Horstmann, E. Irran, W. Schnick, *Angew. Chem. Int. Ed. Engl.* **1997**, *36*, 1873–1875; *Angew. Chem.* **1997**, *109*, 1938–1940.

[4] W. Schnick, J. Lücke *Angew. Chem. Int. Ed. Engl.* **1992**, *31*, 213–215; *Angew. Chem.* **1992**, *104*, 208–209.

[5] D. Baumann, W. Schnick, *Inorg. Chem.* **2014**, *53*, 7977–7982.

[6] S. Horstmann, E. Irran, W. Schnick, *Angew. Chem. Int. Ed. Engl.* **1997**, *36*, 1992–1994; *Angew. Chem.* **1997**, *109*, 2085–2087.

[7] A. Marchuk, W. Schnick, *Angew. Chem. Int. Ed.* **2015**, *54*, 2383–2387; *Angwe. Chem.* **2015**, *127*, 2413–2417.

[8] S. J. Sedlmaier, M. Döblinger, O. Oeckler, J. Weber, J. Schmedt auf der Günne, W. Schnick, *J. Am. Chem. Soc.* **2011**, *133*, 12069–12078.

[9] S. Correll, O. Oeckler, N. Stock, W. Schnick, *Angew. Chem. Int. Ed.* **2003**, *42*, 3549–3552; *Angew. Chem.* **2003**, *115*, 3674–3677.

[10] S. Correll, N. Stock, O. Oeckler, J. Senker, T. Nilges, W. Schnick, *Z. Anorg. Allg. Chem.* **2004**, *630*, 2205–2217.

[11] S. Zhao, Z. Fu, Q. Qin, *Thin Solid Films* **2002**, *415*, 108–113.

[12] W. Schnick, J. Luecke, *Solid State Ionics* **1990**, *38*, 271–273.

[13] S. Correll, N. Stock, W. Schnick, *Solid State Sci.* **2004**, *6*, 953–965.

[14] E.-M. Bertschler, C. Dietrich, J. Janek, W. Schnick, *Chem. Eur. J.* **2017**, *23*, 2185–2191.

[15] K. Landskron, H. Huppertz, J. Senker, W. Schnick, *Angew. Chem. Int. Ed.* **2001**, *40*, 2643–2645, *Angew. Chem.* **2001**, *113*, 2713–2716.

[16] K. Landskron, H. Huppertz, J. Senker, W. Schnick, *Z. Anorg. Allg. Chem.* **2002**, *628*, 1465–1471.

[17] W. Schnick, J. Luecke, *J. Solid State Chem.* **1990**, *87*, 101–106.

[18] F. Liebau, *Structural Chemistry of Silicates*, Springer-Verlag Berlin, **1985**.

[19] The term dreier (vierer) ring was coined by Liebau and is derived from the German word “drei” (“vier”). A dreier (vierer) ring comprised three (four) tetrahera centers.

[20] W. Schnick, Habilitationsschrift, Universit y of Bonn, **1991**.

[21] U. Berger, W. Schnick, *Angew. Chem. Int. Ed. Engl.* **1991**, *30*, 830–831; *Angew. Chem.* **1991**, *103*, 857–858.

[22] W. Schnick, J. Lücke, *Z. Anorg. Allg. Chem.* **1990**, *588*, 19–25.

[23] W. Schnick, J. Lücke, *Z. Anorg. Allg. Chem.* **1992**, *610*, 121–126.

[24] R. Nymwegen, S. Doyle, T. Wroblewski, W. Kockelmann, H. Jacobs, *Z. Anorg. Allg. Chem.* **1997**, *623*, 1467–1474.

[25] A. Marchuk, F. J. Pucher, F. W. Karau, W. Schnick, *Angew. Chem.* **2014**, *126*, 2501–2504, *Angew. Chem.* **2014**, *126*, 2501–2504.

[26] S. Horstmann, E. Irran, W. Schnick, *Z. Anorg. Allg. Chem.* **1998**, *624*, 221–227.

[27] D. Baumann, W. Schnick, *Angew. Chem. Int. Ed.* **2014**, *53*, 14490–14493; *Angew. Chem.* **2014**, *126*, 14718–14721.

[28] N. Kawai, S. Endo, *Rev. Sci. Instrum.* **1970**, *41*, 1178–1181.

[29] D. Walker, M. A. Carpenter, C. M. Hitch, *Am. Mater.* **1990**, *75*, 1020–1028.

[30] D. Walker, *Am. Mater.* **1991**, *76*, 1092–1100.

[31] D. C. Rubie, *Phase Transitions* **1999**, *68*, 431–451.

[32] H. Huppertz, *Z. Kristollogr.* **2004**, *219*, 330–338.

[33] W. Schnick, *Phosphorus. Sulfur. Silicon Relat. Elem.* **1993**, *76*, 183–186.

[34] V. Schultz-Coulon, W. Schnick, *Z. Anorg. Allg. Chem.* **1997**, *623*, 69–74.

[35] V. Schulz-Coulon, W. Schnick, *Angew. Chem.* **1993**, *105*, 308–309; *Angew. Chem.* **1993**, *108*, 308–309.

[36] S. J. Sedlmaier, M. Eberspächer, W. Schnick, *Z. Anorg. Allg. Chem.* **2011**, *637*, 362–367.

[37] A. Durif, *Crystal Chemistry of Condensed Phosphates*, Springer, Berlin, **1995**.

[38] S. Lupart, W. Schnick, *Z. Anorg. Allg. Chem.* **2012**, *638*, 2015–2019.

[39] V. A. Blatov, *Cryst. Rev.* **2004**, *10*, 249–318.

[40] G. M. Sheldrick, *SHELXS*, University of Göttingen, **1997**.

[41] N. A. Anurova, V. A. Blatov, G. D. Ilyushin, O. A. Blatova, A. K. Ivanov-Schitz, L. N. Dem'yanets, *Solid State Ionics* **2008**, *179*, 2248–2254.

[42] A. P. Shevchenko, V. N. Serezhkin, V. A. Blatov, *J. Appl. Cryst.* **1999**, *32*, 377–377.

[43] S. Lupart, W. Schnick, *Z. Anorg. Allg. Chem.* **2012**, *638*, 94–97.

[44] F. D. Murnaghan, *Proc. Natl. Acad. Sci. USA* **1944**, *30*, 244-247.

[45] T. M. Tolhurst, C. Braun, T. D. Boyko, W. Schnick, A. Moewes, *Chem. Eur. J.* **2016**, *22*, 10475–10483.

[46] E. Horvath-Bordon, R. Riedel, A. Zerr, P. F. McMillan, G. Auffermann, Y. Prots, W. Bronger, R. Kniep, P. Kroll, *Chem. Soc. Rev.* **2006**, *35*, 987.

[47] Y. Yan, J. Y. Zhang, T. Cui, Y. Li, Y. M. Ma, J. Gong, Z. G. Zong, G. T. Zou, *Eur. Phys. J. B* **2008**, *61*, 397–403.

[48] C. E. Dreyer, J. L. Lyons, A. Janotti, C. G. Van De Walle, *Appl. Phys. Express* **2014**, *7*, 31001..

[49] A. D. Becke, K. E. Edgecombe, *J. Chem. Phys.* **1990**, *92*, 5397–5403.

[50] V. Jancik, F. Cortés-Guzmán, R. Herbst-Irmer, D. Martínez-Otero, *Chem. Eur. J.* **2017**, *23*, 6964–6968.

[51] A. Stock, H. Grüneberg, *Ber. Dtsch. Chem. Ges.* **1907**, *40*, 2573–2578.

[52] XPREP Reciprocal Space Exploration, *Vers. 6.12*, Bruker-AXS, Karlsruhe, **2001**.

[53] G. M. Sheldrick, *Acta Crystallogr., Sect. A* **2008**, *64*, 112–122.

[54] L. J. Farrugia, *J. Appl. Crystallogr.* **1999**, *32*, 837–838.

[55] L. J. Farrugia, *PLATON, Vers. 1.16*, University of Glasgow, **1995**.

[56] Further details of the crystal structure investiation can be obatined from the Fachinformations-Zentrum Karlsruhe, 76344 Eggenstein- Leopoldshafen, Germany (Fax: (+49)7247-808-666; E-Mail: Crysdata@fiz-Karlsruhe.de) on Quoting the Depository Number CSD- 432590 ($Li_{12}P_3N_9$) and CSD- 432591 (Li_4PN_3).

[57] K. Brandenburg, Crystal Impact GbR: Bonn **2005**.

[58] A. Coelho, *TOPAS-Academic* **2007**.

[59] R. W. Cheary, A. A. Coelho, *J. Appl. Crystallogr.* **1992**, *25*, 109–121.

[60] R. W. Cheary, A. A. Coelho, *J. Res. Natl. Inst. Stand. Technol.* **2007**, *109*, 1–25.

[61] *INCA, Version 4.02*, OXFORD Instruments**.**

[62] *OPUS/IR*, Bruker Analytik GmbH, **2000**.

[63] G. Kresse, J. Hafner, *Phys. Rev. B* **1993**, *47*, 558–561.

[64] G. Kresse, J. Hafner, *Phys. Rev. B* **1994**, *49*, 14251–14269.

[65] G. Kresse, J. Furthmüller, *Comput. Mater. Sci.* **1996**, *6*, 15–50.

[66] J. P. Perdew, K. Burke, M. Ernzerhof, *Phys. Rev. Lett.* **1996**, *77*, 3865–3868.

[67] J. P. Perdew, K. Burke, M. Ernzerhof, *Phys. Rev. Lett.* **1997**, *78*, 1396–1396.

[68] P. E. Blöchl, *Phys. Rev. B* **1994**, *50*, 1758–1775.

[69] G. Kresse, D. Joubert, *Phys. Rev. B* **1999**, *59*, 1758–1775.

[70] H. J. Monkhorst, J. D. Pack, *Phys. Rev. B* **1976**, *13*, 5188–5192.

[71] F. Tran, P. Blaha, *Phys. Rev. Lett.* **2009**, *102*, 226401.

[72] J. A. Camargo-Martínez, R. Baquero, *Phys. Rev. B* **2012**, *86*, 195106.

3. $Li_{18}P_6N_{16}$ – A Lithium Nitridophosphate with Unprecedented Tricyclic $[P_6N_{16}]^{18-}$ Ions

Eva-Maria Bertschler, Christian Dietrich, Jürgen Janek, Wolfgang Schnick

published in: *Chem. Eur. J.* **2017**, *23*, 2185-2191. DOI: 10.1002/chem.201605316

Abstract

$Li_{18}P_6N_{16}$ was synthesized by reaction of $LiPN_2$ and Li_7PN_4 at 5.5 GPa and 1273 K employing the multi-anvil technique. It is the first lithium nitridophosphate obtained by high-pressure synthesis. Moreover, it is the first example received by reaction of two ternary lithium nitrides. The combination of high-pressure conditions with a Li_3N flux enabled a complete structure determination using single-crystal X-ray diffraction. The hitherto unknown tricyclic $[P_6N_{16}]^{18-}$ anion is composed of six vertex-sharing PN_4 tetrahedra forming one *vierer*- and two additional *dreier*-rings. To confirm the structure, Rietveld refinement, ^{7}Li and ^{31}P solid-state NMR spectroscopy, FTIR spectroscopy and EDX measurements were carried out. To validate the ionic properties, the migration pathways of the Li^+ ions were evaluated, and the conductivity and its temperature dependence were determined by impedance spectroscopy measurements. In order to obtain a clearer picture of the formation mechanism of this compound class, different synthetic approaches were compared, enabling targeted syntheses of unprecedented P/N-anion topologies with intriguing properties.

3.1. Introduction

Nitridophosphates have gained remarkable importance due to their wide range of structural diversity and their great potential as functional materials.[1-7] For example, the nitridic clathrate $P_4N_4(NH)_4NH_3$ contains encapsulated molecules of ammonia and was discussed as a possible gas-storage material.[8, 9] Phosphorus nitride imide PN(NH)[10, 11] is of special interest due to the fact that it is isoelectronic to silica and PON (phosphorus oxonitride).[12-18] $Ba_3P_5N_{10}Br:Eu^{2+}$,[19] a promising white-light-emitting luminescent material was synthesized by high-pressure synthesis. Additionally, lithium ion conductivity has been reported for a number of (oxo)nitridophosphates, for example, $LiPN_2$,[20] Li_7PN_4,[20] $Li_xH_{12-x-y+z}[P_{12}O_yN_{24-y}]X_z$ (X=Cl, Br)[13] and Li_2PO_2N.[21, 22] All of these compounds have been discussed as candidates for Li battery applications. As thin films of amorphous "*LiPON*"[22, 23] can readily be prepared by sputtering, it finds applications as a solid electrolyte in thin-film batteries.[24] Materials optimization by doping with bivalent cations and sintering (e.g. $Li_{0.925}Ca_{0.075}Si_2N_3$) may lead to an enhancement of the conductivity and lowering of the activation energy.[22, 25]

One binary basis of ternary and higher nitridophosphates, with electropositive elements, is the parent compound P_3N_5, which has a limited thermal stability (P_3N_5 decomposes into the elements at $T > 1100$ K).[5] Therefore, synthesis of crystalline P_3N_5 requires reactions in closed systems or under pressure.[26] Consequently the multianvil technique emerged as a powerful technique for the synthesis of novel nitridophosphates with great structural variety.[8] So far, however, only a few nitridophosphates have been synthesized below 1100 K in ampoules; for example, Li_7PN_4,[27] the only lithium nitridophosphate with non-condensed PN_4 tetrahedra, $Li_{12}P_3N_9$,[5] with vertex-sharing PN_4 tetrahedra forming cyclic $[P_3N_9]^{12-}$ ions isoelectronic to $[Si_3O_9]^{6-}$, $Li_{10}P_4N_{10}$,[28] with adamantane-type $[P_4N_{10}]^{10-}$ ions isoelectronic to $[P_4O_{10}]$, or $LiPN_2$,[29] the lithium nitridophosphate with the lowest content of Li^+ ions. In $LiPN_2$ the PN_4 tetrahedra are arranged in a three-dimensional network that is isoelectronic to SiO_2 and crystallizes in the β-cristobalite structure type.[20, 29] The reaction temperature of most nitridophosphates is, however, above 1273 K and thus they are only accessible by high-pressure/high-temperature synthesis. This synthetic approach implies some difficulties, in particular in characterization of the obtained products. Besides products with poor quality of single crystals, they are often only obtained as microcrystalline powders. The latter requires phase-pure synthesis for powder X-ray diffraction, solid-state NMR spectroscopy, or electron microscopy for structure analysis.[17, 30] Recently, three different approaches to circumvent these difficulties have been established. The addition of NH_4Cl as a mineralizer leads to an increase of crystallinity and isolation of macroscopic single crystals, which can be analyzed by conventional single-crystal structure determination. Thereby, a number of new compounds, for example, β-PN(NH)[11] or β- and γ-$P_4N_6(NH)$,[7, 31] have been

structurally elucidated. Recently, a second approach to grow single-crystals by application of high-pressure metathesis was described.[32] A third approach to grow single crystals of nitrides in high-pressure/high-temperature synthesis is the addition of nitrides, like Li_3N, which has been used to obtain single crystals of GaN[33] or *c*-BN.[34]

In this work we report on the synthesis and structural investigation of the first lithium nitridophosphate obtained by high-pressure synthesis, namely $Li_{18}P_6N_{16}$. We succeeded in growing single crystals by reaction of Li_3N and P_3N_5 and obtained phase-pure products by reaction of $LiPN_2$ and Li_7PN_4, enabling ion conductivity measurements.

3.2. Results and Discussion

3.2.1. Synthesis

After empirical optimization, $Li_{18}P_6N_{16}$ was synthesized by two different approaches according to Equations (1), (2). For both routes we used a Li_3N self-flux method under high-pressure/high-temperature conditions. The compounds were handled in an argon atmosphere to avoid hydrolysis.

$$6\ Li_3N + 2\ P_3N_5 \rightarrow Li_{18}P_6N_{16} \quad (1)$$

$$4\ LiPN_2 + 2\ Li_7PN_4 \rightarrow Li_{18}P_6N_{16} \quad (2)$$

After synthesis according to Equation (1), only small amounts of $Li_{18}P_6N_{16}$ were obtained together with $LiPN_2$ and in some cases $Li_{10}P_4N_{10}$ as by-products, depending on the initial weight ratio (different amounts of Li_3N excess) and heating time. Phase-pure samples were only obtained when starting from equimolar amounts of $LiPN_2$ and Li_7PN_4. Thus, despite Equation (2), a significant excess of Li_7PN_4 seems to be favorable. Li_7PN_4 contains some fraction of amorphous by-products that could not be removed by washing, and a small fraction of Li_3P. The crystal quality after synthesis according to Equation (1) was, however, better than after reaction according to Equation (2). As described in the literature, Li_3N is used as a flux in the synthesis of GaN[33] or *c*-BN[34] to obtain single crystals. *c*-BN crystallizes from Li_3N flux when the pressure and temperature conditions reach the thermodynamic stability conditions. The flux consists of Li_3N and *h*-BN as well as boron and Li_3BN_2. The boron, formed in situ, could serve as a nucleus

for the *c*-BN crystals.[34] Similarly, it may be possible that by high-pressure/high-temperature reaction of P_3N_5 with Li_3N various nitridophosphate anions containing *dreier*- and *vierer*-rings (as defined by Liebau),[35, 36] or other ring and cage sizes of PN_4 tetrahedra exist in the self-flux of Li_3N, which can serve as building units or their precursors for crystal growth of $Li_{18}P_6N_{16}$. The different ring sizes can either be excised from P_3N_5 by reaction with Li_3N or could be formed under equilibrium conditions in Li_3N melts. *Dreier*- and *vierer*-rings are common building units in nitridophosphates. For example, *dreier*-rings occur in $Li_{12}P_3N_9$,[5] or NPO-zeolite (**n**itrido**p**hosphate **o**ne).[12, 13, 37] In NPT-zeolite (**n**itrido**p**hosphate **t**wo), *vierer*- and *achter*-rings occur together with *dreier*-rings.[37] Moreover, vierer-rings are frequently a building unit of high-pressure phases, for example, δ-PON,[17] or $M_3P_6O_6N_8$ (M=Sr, Ba).[38, 39]

Due to the better crystal quality after the synthesis route given in Equation (1), a single-crystal of this approach was used for structure analysis. With respect to the phase-pure synthesis according to Equation (2) (reaction of $LiPN_2$ and Li_7PN_4), it seems rather unlikely that the *vierer*-rings of $Li_{18}P_6N_{16}$ have been excised from P_3N_5 (built up of different P_nN_n ring sizes other than n=3).[4] Most likely, under high-pressure conditions, $LiPN_2$ is fragmented into different building blocks similar to P_3N_5 in the approach according to Equation (1). Presumably, an excess of Li_7PN_4 leads to the in situ formation of Li_3N ($3\ LiPN_2 + 3\ Li_7PN_4 \rightarrow Li_{18}P_6N_{16} + 2\ Li_3N$), which could serve as a flux. Later on it evaporates or may react with the *h*-BN crucible. In essence, $Li_{18}P_6N_{16}$ is the first lithium nitridophosphate obtained by the reaction of two ternary lithium nitridophosphates and was only obtained at high-pressure/high-temperature reactions employing the multianvil technique.

3.2.2. Crystal structure

The crystal structure of $Li_{18}P_6N_{16}$ was solved and refined from single-crystal X-ray diffraction data in the triclinic space group $P\overline{1}$ (no. 2) with one formula unit per unit cell (Table 2, Experimental Section). During structure solution all N and P atom positions were determined. The positions of the Li atoms were localized from difference Fourier maps during structure refinement. All P and N atom positions were refined anisotropically.

The nitridophosphate substructure (Figure 1) represents an unprecedented anion topology consisting of six vertex-sharing PN_4 tetrahedra. Four tetrahedra each share two corners building a *vierer*-ring. Additionally, two PN_4 tetrahedra of this *vierer*-ring are linked to further PN_4 tetrahedra forming two *dreier*-rings. The center of the *vierer*-ring represents the center of symmetry of $[P_6N_{16}]^{18-}$.

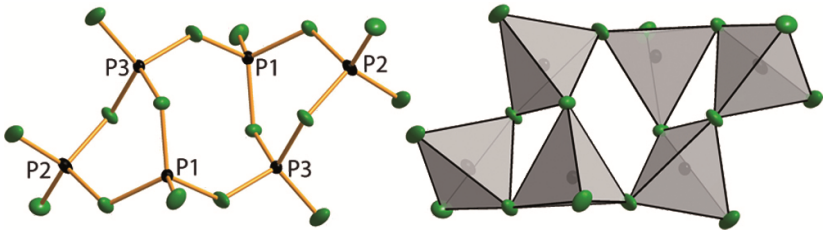

Figure 1. Left: $[P_6N_{16}]^{18-}$ anion. Right: $[P_6N_{16}]^{18-}$ anion with PN_4 tetrahedra of the P/N-framework in gray. The thermal ellipsoids are depicted at 90 % probability. (P: black, N: green).

The framework anion topology was determined by the TOPOS software,[40, 41] and is represented by the point symbol $(3.4.5)^2(3)$. The tricyclic anions in $Li_{18}P_6N_{16}$ are stacked forming columns along [1 0 0] (Figure 2). This tricyclic anion of condensed tetrahedra represents a novel molecular topology with no analogue in main group chemistry.

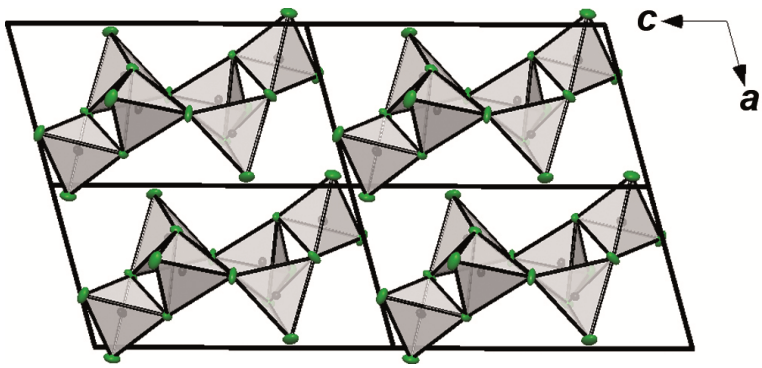

Figure 2. Packing of the $[P_6N_{16}]^{18-}$ anions viewing along [0 1 0]. Li^+ sites are omitted for clarity and displacement parameters are depicted at 90 % probability. (P: black, N: green, PN tetrahedra: gray).

The P−N distances in the $[P_6N_{16}]^{18-}$ anion vary from 1.588(2) to 1.6955(19) Å. The distances for terminal N atoms are on an average about 4.6 % shorter than those of the bridging N atoms. These distances are in agreement with the values of other lithium nitridophosphates ($Li_{10}P_4N_{10}$: P−N 1.58–1.68 Å, $LiPN_2$: P−N 1.65 Å, Li_7PN_4: P−N 1.69–1.73 Å).[27-29] The tetrahedrally coordinated P atoms, with bond angles P-N-P of 105–115° deviate slightly from the regular tetrahedral angle, but are consistent with corresponding values in other lithium nitridophosphates ($Li_{10}P_4N_{10}$: P-N-P 106–116°, $LiPN_2$: P-N-P 107–115°, Li_7PN_4: P-N-P 108–112°).[27-29]

The $[P_6N_{16}]^{18-}$ anions are coordinated by Li^+ ions. A free refinement of the occupation factors of the Li atoms showed partial occupation of four Li sites (Li8 to Li11); all remaining sites (Li1 to Li7) are fully occupied. These four partially occupied Li sites show a distribution of two Li atoms

to Li8, Li9, Li10 and Li11. Li8 has an occupation factor of about 60 %, Li9 of about 50 %, Li10 of about 40 % and Li11 of about 50 %. Due to the low atomic weight of Li and the large displacement parameters, the Li^+ ions were not refined anisotropically. As shown in Figure 3, the four partially occupied Li sites (Li8 to Li11) have rather short Li−Li distances. For this reason only Li8 and Li10, Li8 and Li11, or Li9 and Li11, respectively, can be occupied at the same time. As a consequence, inclusion of the partially occupied sites (Li8 to Li11) yields interatomic Li−Li distances in the range 1.52–2.65 Å (R_{sd} (radius of spherical domain) of Li^+=1.450 Å).[40-43] By comparison, in Li_2SiN_2 various Li−Li distances have been reported below 2.5 Å (shortest distance: 2.335(7) Å).[44] The Li−Li distances of the other crystallographic sites, which are 100 % occupied, are between 2.05 (Li6 to Li11) and 2.85 Å (Li1 to Li3). These distances are comparable with Li−Li distances in other nitride compounds containing Li^+ (e.g. $LiCa_3Si_2N_5$).[45] The Li^+ ions are coordinated by distorted nitrogen polyhedra $[LiN_4]$ and $[LiN_5]$, which share edges or corners (see the Supporting Information, Figure S1). Presumably, the distortion and the uncommon coordination polyhedra are indicative of the mobility of the Li^+ ions.

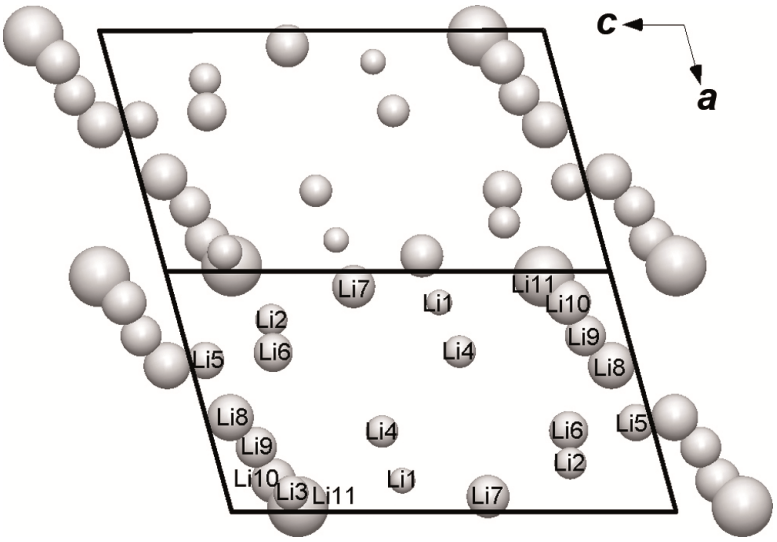

Figure 3. Packing of the Li^+ ions in $Li_{18}P_6N_{16}$ viewed along [0 1 0].

3.2.3. Solid-state NMR spectroscopy

To corroborate the crystal structure model of $Li_{18}P_6N_{16}$, ^{31}P and ^{7}Li solid-state MAS NMR spectroscopy was performed (see the Supporting Information, Figure S4). The ^{31}P spectrum shows three strong resonances at 5.51, 18.57, and 22.24 ppm, which are in accordance with three crystallographically independent P sites. The signals of P1 and P3 overlap due to similar surroundings. P1 and P3 are part of the *dreier*- and *vierer*-ring. The signal at 5.51 ppm can be assigned to P2, which is part of the *dreier*-ring. The ^{7}Li MAS NMR spectrum shows one isotropic

signal at 1.6 ppm. Due to the small chemical shift differences of the ^{7}Li solid-state MAS NMR signals, no differentiation of the crystallographically independent sites can be observed in the spectrum. The chemical shifts for lithium in lithium nitridophosphates/silicates occur most frequently in the range 1.3 to 2.7 ppm, which is in good agreement with chemical shifts observed in $Li_{18}P_6N_{16}$.[44-47]

3.2.4. Chemical analysis

EDX measurements were used to determine the elemental composition of the product. Besides phosphorus and nitrogen, only traces of oxygen were found (see the Supporting Information, Table S6). The observation of oxygen can be explained by partial hydrolysis of the compound during contact of the sample with air. The determined atomic ratio of P/N is in agreement with the results from the crystal structure analysis. Li could not be detected by EDX measurements. No elements other than P, N and O were found.

To examine the lithium amount with regard to the P/N ratio, an elemental analysis was performed (Pascher, Remagen, Germany). The molecular formula, $Li_{17.5}P_{5.7}N_{16.8}$, obtained by elemental analysis is in good agreement with that determined by crystal structure analysis ($Li_{18}P_6N_{16}$).

In order to prove the absence of hydrogen (N−H) in the title compound, FTIR spectroscopy was performed (see the Supporting Information, Figure S7). The spectrum shows no significant valence vibration in the region of 3000 cm^{-1}, where N−H vibrations are expected. A weak signal in that region can be explained by surface hydrolysis of the sample. Thus, the incorporation of stoichiometric amounts of hydrogen seems unlikely. In the case of stoichiometric amounts of hydrogen in the structure, the characteristic N−H absorption bands are usually much more intense, like in $MH_4P_6N_{12}$ (M=Mg, Ca) or HP_4N_7.[31, 48] Much more significant are the characteristic P/N-framework vibrations between 600 and 1500 cm^{-1}.[28]

To determine the bulk composition of the samples and exclude possible side phases, a powder diffraction pattern was collected (see the Supporting Information, Figure S2). Rietveld refinement of this diffraction pattern shows phase purity and confirms the structure determined by single-crystal structure analysis.

For investigations of the thermal stability of $Li_{18}P_6N_{16}$, high-temperature powder X-ray diffraction was performed. No phase transition or decomposition was observed up to 1073 K (Supporting Information, Figure S6).

3.2.5. Structural analysis of possible lithium migration pathways

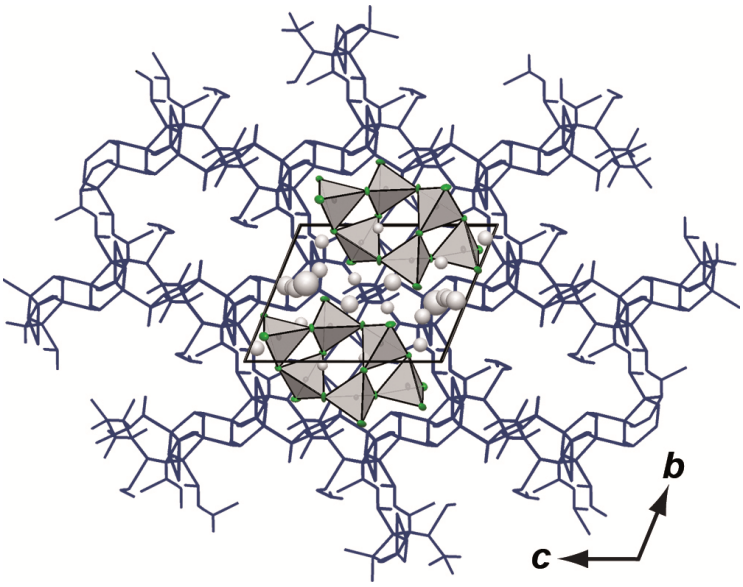

Figure 4. Calculated possible Li^+ pathways (blue) according to the voids in the structure and unit cell of $Li_{18}P_6N_{16}$ viewing along [1 0 0].

Possible voids and migration pathways in $Li_{18}P_6N_{16}$ were analyzed with TOPOS (Figure 4, additional viewing directions in the Supporting Information, Figure S8 and S9).[42, 49-51] The voids in the crystal structure were calculated by employing Voronoi–Dirichlet polyhedra. Each void smaller than 1.45 Å (the Slater radius of Li^+)[43] was omitted. The analysis of the space between the voids leads to the possible migration pathways illustrated in Figure 4.

We assume that the channels become accessible for lithium ion jumps if the sum of the radii of lithium and the nitrogen framework atom exceed the channel radius no more than by 10–15 %, and so the dimensions of the resulting pathways were examined. The analysis of the different viewing directions shows a possible movement of the Li^+ ions in three different directions in space. In direction [1 0 0] the Li^+ ions can move around the nitridophosphate anions (Figure 4). Along [0 0 1] the possible migration direction of the partially occupied Li^+ ions can be observed (see the Supporting Information, Figure S9). According to these calculations $Li_{18}P_6N_{16}$ seems to be a promising candidate for lithium ion conductivity with respect to the structural properties.

3.2.6. Conductivity measurements

To confirm the ionic character of $Li_{18}P_6N_{16}$, conductivity measurements were performed.

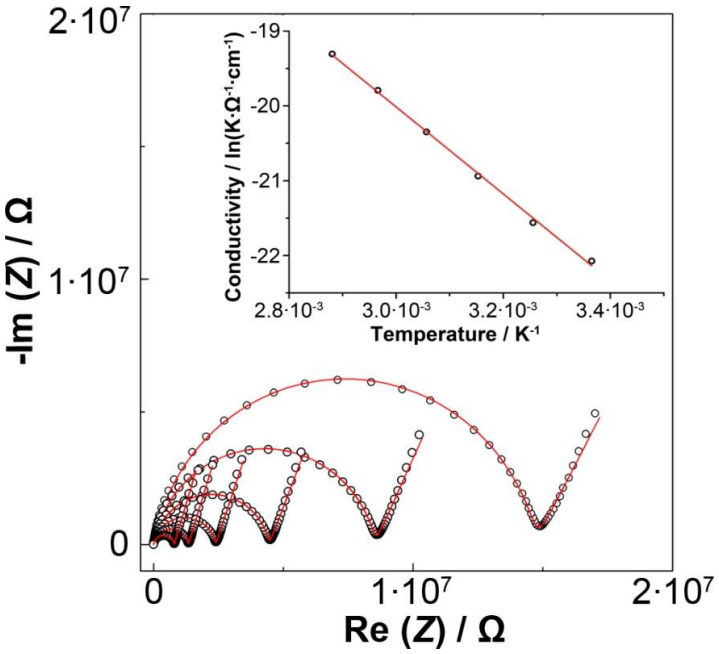

Figure 5. Main: Nyquist plots of the measurements at different temperatures from 298 to 348 K (right to left), comprising a semi-circle (bulk and grain boundary transport) and a tail (ionic adsorption and charge transfer between $Li_{18}P_6N_{16}$ and blocking electrodes). (The equivalent circuit used as fit model is shown in the Supporting Information, Figure S10). Inset: Arrhenius plot obtained from the impedance spectroscopy measurements at different temperatures of an Au/$Li_{18}P_6N_{16}$/Au cell. Experimental data: black dots and fit: red line.

The impedance spectrum acquired from the Au/$Li_{18}P_6N_{16}$/Au cell at room temperature is shown in Figure 5. The conductivity at room temperature is about $\sigma = 7.70\times10^{-8}\ \Omega^{-1}\,cm^{-1}$ and $\sigma = 1.43\times10^{-6}\ \Omega^{-1}\,cm^{-1}$ was determined at 348 K. The Nyquist plot shows a typical semicircle in the higher frequency region that represents the bulk and grain boundary resistance of the electrolyte, and a tail at low frequencies that represents the diffusion of Li in the Au electrodes. The Arrhenius-type plot obtained after fitting all measurements at different temperatures is shown in the insert in Figure 5.

The calculation of the activation energy results in $E_a = 48.3\ kJ\,mol^{-1}$, which corresponds to 0.50 eV. These values are in good agreement with the conductivity of other lithium nitridophosphates/silicates (Table 1). The higher conductivity of Li_7PN_4 and $Li_{18}P_6N_{16}$ is due to the large number of Li^+ ions occupying interstitial sites and the high carrier concentration. Due to their relatively high formal charge, the $[P_6N_{16}]^{18-}$ anions are expected to exhibit strong attraction

to the Li^+ ions, which may reduce the mobility of the ions. The closely packed atomic arrangement of $LiPN_2$ has no comparable interstitial positions and thus leads to a lower conductivity.[20] Accordingly, the difference of the conductivity is caused by the differing crystal structure, the coordination of the lithium atoms, and the number of charge carriers available.[20]

Table 1. Conductivity and activation energy of some lithium nitridophosphates/silicates.

	$\sigma_{400\,K}$ [$\Omega^{-1}cm^{-1}$]	E_a [$kJmol^{-1}$]	Ref.
Li_7PN_4	$1.7 \cdot 10^{-5}$	47	[20]
$Li_{18}P_6N_{16}$	$1.5 \cdot 10^{-5}$	48	this work
Li_2SiN_2	$1.1 \cdot 10^{-5}$	53	[52]
$LiPN_2$	$6.9 \cdot 10^{-7}$	59	[20]
$LiSi_2N_3$	$1.9 \cdot 10^{-7}$	64	[52]

The conductivity of these lithium nitridophosphates is comparable to other ternary *p*-block lithium nitride compounds, for example, Li_2SiN_2,[52] $LiSi_2N_3$,[52] or $Li_{14}Ln_5[Si_{11}N_{19}O_5]O_2F_2$ (Ln = Ce, Nd),[53] but they are significantly lower than the value found for Li_3N ($\sigma = 8\times10^{-3}\ \Omega^{-1}\,cm^{-1}$ at 400 K and $E_a = 24.1$ kJ mol^{-1}).[54, 55]

It is important to point out that the samples of the lithium nitridophosphates were cold pressed and not sintered. Thus, the grain boundaries are not relaxed, and annealing may improve the conduction significantly. Optimizations of the ion transport properties may lead to an enhancement of the conductivity and decrease of the activation energy, as demonstrated by doping of $LiSi_2N_3$ with Ca^{2+}.[25] The substitution of Li^+ by Ca^{2+} is expected to create Li^+ vacancies for charge compensation, and the increased number of vacancies in the structure may enhance Li^+ migration. In addition, doping may expand the lattice and lead to easier Li movement. The latter effect is, however, expected to be less effective than the former. By doping, the ionic conductivity increased from $\sigma = 3.1\times10^{-11}\ \Omega^{-1}\,cm^{-1}$ ($LiSi_2N_3$) to $\sigma = 1.6\times10^{-7}\ \Omega^{-1}\,cm^{-1}$ ($Li_{0.925}Ca_{0.075}Si_2N_3$) at 298 K.[25]

The relatively low costs in production of the starting materials and the high thermal stability of the lithium nitridophosphates, combined with the Li ion conductivity, makes this compound class interesting for future research and optimization by for example, doping with bivalent cations. A particular advantage for practical applications might be the formation of stable and well-

conducting SEI (solid electrolyte interphases) composed only of Li_3N and Li_3P in contact with lithium metal electrodes.[56, 57]

3.3. Conclusion

In this work we report on the synthesis, structural investigation, and ion conductivity of the first lithium nitridophosphate, $Li_{18}P_6N_{16}$, obtained by high pressure synthesis. The unprecedented structure with tricyclic $[P_6N_{16}]^{18-}$ units consists of six corner sharing PN_4 tetrahedra, embedded in a matrix of Li^+ ions. The migration pathways for Li^+ ions calculated with TOPOS[40, 42, 50, 51] indicate an ion conductivity, which was confirmed by impedance measurements. The better understanding of the building mechanism of nitridophosphates at high-pressure/high-temperature conditions enables a targeted research for unprecedented anion topologies with interesting properties, and their optimizations in future experiments, for example, cation doping to optimize the defect chemistry and kinetics of this compound class. Consequently, further high-pressure/high-temperature experiments will probably lead to novel lithium nitridophosphates with interesting structures and properties.

3.4. Experimental Section

3.4.1. Synthesis of starting materials

The parent compound, P_3N_5,[1] was synthesized by reaction of P_4S_{10} (8 g, Sigma–Aldrich, 99 %) in a constant ammonia flow (Air-Liquide, 99.999 %). After saturation with NH_3 at room temperature for 4 h, the silica tube was heated to 1123 K at a rate of 278 K min^{-1} and kept at this temperature for additional 4 h, and subsequently cooled down to room temperature at 278 K min^{-1}. The orange product was washed with water, ethanol, and acetone in order to eliminate side products. All further work steps were performed with strict exclusion of oxygen and moisture in an argon filled glove box (Unilab, MBraun, Garching, O_2<1 ppm, H_2O<0.1 ppm).

$LiPN_2$[29] and Li_7PN_4[27] were both prepared by reaction of Li_3N (Rockwood Lithium, 95 %) and P_3N_5 ($LiPN_2$: molar ratio 1.2:1; Li_7PN_4: 7.2:1) in sealed silica ampoules under N_2 atmosphere. After grinding the starting materials in an agate mortar the mixture was transferred into a tantalum crucible, which was placed in a dried silica tube. The sealed silica ampoule was heated in a tube furnace at 1073 or 893 K for 90 h, respectively. $LiPN_2$ was washed with diluted hydrochloric acid,

water, and ethanol. Li_7PN_4 was not washed. Phase purity of the starting materials was verified by powder X-ray diffraction and FTIR spectroscopy.

3.4.2. High-pressure synthesis of $Li_{18}P_6N_{16}$

$Li_{18}P_6N_{16}$ was prepared under high-pressure/high-temperature conditions in a modified Walker-type multi-anvil module, in combination with a 1000 t press (Voggenreiter, Mainleus, Germany).[58-62] The starting materials were mixed and ground under an argon atmosphere before packing compactly in an *h*-BN crucible (Henze BNP GmbH, Kempten, Germany). Subsequently, the crucible was transferred into the specially prepared pressure medium (5 % Cr_2O_3 doped)-MgO-octahedra (Ceramic Substrates & Components, Isle of Wight, UK; edge length 18 mm). The octahedron was placed centrically in eight truncated WC cubes (Hawedia, Marklkofen, Germany; truncation length 11 mm) separated by pyrophyllite gaskets. Detailed information describing the complete setup can be found in the literature.[59, 60, 62] For synthesis according to Equation (1) (Equation (2)) the assembly was compressed to 3 GPa (5.5 GPa) at room temperature within 1.5 h (2.3 h) and then heated to about 1073 K (1273 K) within 4 h (2 h). Under these conditions, the sample was treated for 7.5 h (4 h) and cooled down to room temperature within 4 h (5 h). Subsequently, the sample was decompressed in 6.5 h. Both syntheses yielded a colorless powder containing single crystals. The product was sensitive to traces of air and moisture.

3.4.3. Single-crystal X-ray analysis

As a standardized method, single-crystal X-ray diffraction was performed with a D8 Venture diffractometer (Bruker, Billerica MA, USA) using Mo-K_α radiation from a rotating anode source. The collected data were averaged with Xprep[63] and the program package WinGX (SHELXS-97, SHELXL-97, PLATON)[49, 64-66] was used for structure solution by direct methods, and refinement (see Table 2).[67] All P and N atoms were refined anisotropically. The crystal structure was visualized using DIAMOND.[68]

Table 2. Crystallographic data of $Li_{18}P_6N_{16}$.

Formula	$Li_{18}P_6N_{16}$
crystal size/ mm^3	0.02 x 0.03 x 0.05
formula mass/ $g \cdot mol^{-1}$	534.9
crystal system	triclinic
space group	$P\overline{1}$ (no. 2)
cell parameters/ Å,°	a = 5.4263(4)
	b = 7.5354(5)
	c = 9.8584(7)
	α = 108.481(2)
	β = 99.288(2)
	γ = 104.996(4)
cell volume/ $Å^3$	356.02(4)
formula units/ cell	1
calculated density/ $g \cdot cm^{-3}$	2.49471
F(000)	256
diffractometer	Bruker D8 Venture
temperature/ K	173
radiation, monochromator	Mo-K_α (λ = 0.71073 Å), Goebel mirror
absorption correction	multi scan
θ range/ °	3.02-30.56
measured reflections	14048
independent reflections	2180
observed reflections	1904
refined parameters	148
GooF	1.093
R indices $[F_0^2 \geq 2\sigma(F_0^2)]$	R_1 = 0.0360, wR_2 = 0.0912
R indices (all data)	R_1 = 0.0449, wR_2 = 0.0956
max/min res. Electron density/ $eÅ^{-3}$	0.963/ −0.570
R_{int}/ R_σ	0.0326/ 0.0247

$w = 1/[\sigma^2(F_0^2) + (0.0372P)^2 + 1.0853P]$ with $P = (F_0^2 + 2F_c^2)/3$.

3.4.4. Powder X-ray diffraction

Phase purity of the products was proven by powder X-ray diffraction data, collected with a STOE Stadi P diffractometer (Stoe & Cie, Darmstadt, Germany) in parafocusing Debye–Scherrer geometry. With a Ge(111) single-crystal monochromator, Cu-$K_{\alpha 1}$ radiation was selected. For detection of the diffracted radiation a Mythen 1 K Si-strip detector (Dectris, Baden, Switzerland)

was used. For measurement the samples were enclosed in glass capillaries with 0.5 mm diameter (Hilgenberg, Malsfeld, Germany) under inert gas. Rietveld refinement was carried out using the program package TOPAS-Academic v4.1.[69] The background was handled using a shiftedChebychev function, and the peak shapes were described using the fundamental parameters approach.[70, 71] Temperature-dependent powder X-ray diffraction data were recorded on a STOE Stadi P diffractometer, equipped with a graphite furnace, with Mo-$K_{\alpha 1}$ radiation (λ=0.70930 Å) in Debye–Scherrer geometry, and a Ge(111) monochromator. Data were collected every 25 K starting from room temperature up to 1273 K with a heating rate of 278 K min^{-1}.

3.4.5. Solid-state MAS (magic angle spinning) NMR methods

^{7}Li and ^{31}P solid-state MAS NMR spectra of $Li_{18}P_6N_{16}$ were recorded on a DSX Avance spectrometer (Bruker) with a magnetic field of 11.7 T. Under inert conditions the sample was transferred into a ZrO_2 rotor with an outer diameter of 2.5 mm, which was mounted in a commercial MAS probe (Bruker). The rotor was spun at rotation frequency of 20 kHz. The experimental data were analyzed by device-specific software.

3.4.6. EDX measurements

To investigate the atomic ratio P/N, the sample was analyzed by energy-dispersive X-ray spectroscopy. A carbon-coated sample was examined with a scanning electron microscope (SEM) JSM-6500F (Jeol, Tokyo, Japan; maximum acceleration voltage 30 kV). Qualitative and semiquantitative elemental analyses were executed by an energy dispersive spectrometer (Model 7418, Oxford Instruments, Abingdon, United Kingdom) and analyzed by INCA.[72]

3.4.7. Fourier transform infrared (FTIR) spectroscopy

Infrared spectroscopy measurements were performed on a Bruker FTIR-IFS 66v/S spectrometer. The sample was mixed with KBr in a glove box and cold-pressed into a pellet (Ø=12 mm), before measurement in the range of 400–4000 cm^{-1}. The data were evaluated by OPUS.[73]

3.4.8. Conductivity measurements

The single-phase sample was cold-pressed into a dense pellet (Ø=5 mm, d=1.3 mm) in a glove box, for determination of the total conductivity. The pellets were coated with gold thin films blocking electrodes (150 nm) by thermal evaporation (Ø=4.5 mm). Impedance measurements

were carried out in the frequency range of 7 MHz to 100 mHz with an amplitude of 100 mV using a frequency response analyzer (BioLogic SP-300). The obtained conductivity values follow the Arrhenius equation in the measured temperature range between 253 and 358 K ($\sigma \cdot T = A \cdot \exp(-E_a/RT)$). To compare the measured conductivity of $Li_{18}P_6N_{16}$ to that of $LiPN_2$ and Li_7PN_4 the conductivity was extrapolated to 400 K, assuming no change of activation energy.

3.5. Acknowledgements

We would like to thank Dr. Peter Mayer for single-crystal X-ray measurements, Thomas Miller for high-temperature powder diffraction measurements, Christian Minke for EDX, SEM and solid-state MAS NMR measurements, Marion Sokoll for IR measurements, and Dr. Constantin Hoch for helpful discussions concerning the structural analysis (all at Department of Chemistry, LMU Munich). We gratefully acknowledge financial support that was granted by the Fonds der Chemischen Industrie (FCI), the Deutsche Forschungsgemeinschaft (DFG) and by STORE-E (LOEWE program funded by State of Hessen).

3.6. References

[1] A. Stock, H. Grüneberg, *Ber. Dtsch. Chem. Ges.* **1907**, *40*, 2573–2578.

[2] S. Horstmann, E. Irran, W. Schnick, *Angew. Chem. Int. Ed. Engl.* **1997**, *36*, 1992–1994; *Angew. Chem.* **1997**, *109*, 2085-2087.

[3] S. Horstmann, E. Irran, W. Schnick, *Z. Anorg. Allg. Chem.* **1998**, *624*, 620–628.

[4] S. Horstmann, E. Irran, W. Schnick, *Angew. Chem. Int. Ed. Engl.* **1997**, *36*, 1873–1875; *Angew. Chem.* **1997**, *109*, 1938-1940.

[5] W. Schnick, *Angew. Chem. Int. Ed. Engl.* **1993**, *32*, 806–818; *Angew. Chem.* **1993**, *105*, 846-858.

[6] H. Huppertz, W. Schnick, *Angew. Chem. Int. Ed. Engl.* **1996**, *35*, 1983–1984; *Angew. Chem.* **1996**, *108*, 2115-2116.

[7] D. Baumann, W. Schnick, *Angew. Chem. Int. Ed.* **2014**, *53*, 14490–14493; *Angew. Chem.* **2014**, *126*, 14718-14721.

[8] F. Karau, W. Schnick, *Angew. Chem. Int. Ed.* **2006**, *45*, 4505–4508; *Angew. Chem.* **2006**, *118*, 4617-4620.

[9] M. Pouchard, *Nature* **2006**, *442*, 878–879.

[10] K. J. Kingma, R. E. G. Pacalo, P. F. McMillan, *Eur. J. Solid State Inorg. Chem.* **1997**, *34*, 679–692.

[11] A. Marchuk, F. J. Pucher, F. W. Karau, W. Schnick, *Angew. Chem. Int. Ed.* **2014**, *53*, 2469-2472; *Angew. Chem.* **2014**, *126*, 2501–2504.

[12] S. Correll, N. Stock, O. Oeckler, W. Schnick, *Angew. Chem. Int. Ed.* **2003**, *42*, 3549-3552; *Angew. Chem.* **2003**, *115*, 3674–3677.

[13] S. Correll, N. Stock, O. Oeckler, J. Senker, T. Nilges, W. Schnick, *Z. Anorg. Allg. Chem.* **2004**, *630*, 2205–2217.

[14] J. M. Léger, J. Haines, C. Chateau, G. Bocquillon, M. W. Schmidt, S. Hull, F. Gorelli, A. Lesauze, R. Marchand, *Phys. Chem. Miner.* **2001**, *28*, 388–398.

[15] J.-M. Léger, J. Haines, L. S. de Oliveira, C. Chateau, A. Le Sauze, R. Marchand, S. Hull, *J. Phys. Chem. Solids* **1999**, *60*, 145–152.

[16] J. Haines, C. Chateau, J. M. Léger, A. Le Sauze, N. Diot, R. Marchand, S. Hull, *Acta Crystallogr. Sect. B* **1999**, *55*, 677–682.

[17] D. Baumann, S. J. Sedlmaier, W. Schnick, *Angew. Chem. Int. Ed.* **2012**, *51*, 4707–4709; *Angew. Chem.* **2012**, *124*, 4785-4787.

[18] D. Baumann, R. Niklaus, W. Schnick, *Angew. Chem. Int. Ed.* **2015**, *54*, 4388–4391, *Angew. Chem.* **2015**, *127*, 4463-4466.

[19] A. Marchuk, W. Schnick, *Angew. Chem. Int. Ed.* **2015**, *54*, 2383–2387; *Angew. Chem.* **2015**, *127*, 2413-2417.

[20] W. Schnick, J. Luecke, *Solid State Ionics* **1990**, *38*, 271–273.

[21] K. Senevirathne, C. S. Day, M. D. Gross, A. Lachgar, N. A. W. Holzwarth, *Solid State Ionics* **2013**, *233*, 95–101.

[22] $LiPN_2$ (σ = 6.9 x 10^{-7} $\Omega^{-1}cm^{-1}$ at 400 K; E_a = 0.48 eV); Li_7PN_4 (σ = 1.7 x 10^{-5} $\Omega^{-1}cm^{-1}$ at 400 K; E_a = 0.61 eV); $Li_xH_{12-x-y+z}[P_{12}O_yN_{24-y}]X_z$ (X = Cl, Br) (σ = 3.3 x 10^{-6} $\Omega^{-1}cm^{-1}$ at 372 K; E_a = 0.85 eV); Li_2PO_2N (σ = 8.8 x 10^{-7} $\Omega^{-1}cm^{-1}$ at 353 K; E_a = 0.57).

[23] S. Zhao, Z. Fu, Q. Qin, *Thin Solid Films* **2002**, *415*, 108–113.

[24] J. Bartes, N. Dudney, G. Gruzalski, R. Zuhr, A. Choudhury, C. Luck, J. Robertson, *Power Sources* **1993**, *43*, 103–110.

[25] E. Narimatsu, Y. Yamamoto, T. Takeda, T. Nishimura, N. Hirosaki, *J. Mater. Res.* **2011**, *26*, 1133–1142.

[26] F. W. Karau, W. Schnick, *J. Solid State Chem.* **2005**, *178*, 135–141.

[27] W. Schnick, J. Luecke, *J. Solid State Chem.* **1990**, *87*, 101–106.

[28] U. Berger, W. Schnick, *Angew. Chem. Int. Ed. Engl.* **1991**, *30*, 830–831; *Angew. Chem.* **1991**, *103*, 857-858.

[29] W. Schnick, J. Lücke, *Z. Anorg. Allg. Chem.* **1990**, *588*, 19–25.

[30] F. W. Karau, L. Seyfarth, O. Oeckler, J. Senker, K. Landskron, W. Schnick, *Chem. Eur. J.* **2007**, *13*, 6841–6852.

[31] D. Baumann, W. Schnick, *Inorg. Chem.* **2014**, *53*, 7977–7982.

[32] S. D. Kloß, W. Schnick, *Angew. Chem. Int. Ed.* **2015**, *54*, 11250–11253; *Angew. Chem.* **2015**, *127*, 11402-11405.

[33] H. Li, H. Q. Bao, G. Wang, B. Song, W. J. Wang, X. L. Chen, *Cryst. Growth Des.* **2008**, *8*, 2775–2779.

[34] G. Bocquillon, C. Loriers-Susse, J. Loriers, *J. Mater. Sci.* **1993**, *28*, 3547–3556.

[35] F. Liebau, *Structural Chemistry of Silicates*, Springer-Verlag Berlin, **1985**.

[36] The term dreier (vierer) ring was coined by Liebau and is derived from the german word “drei” (“vier”). A dreier (vierer) ring comprised three (four) tetrahera centers.

[37] S. J. Sedlmaier, M. Döblinger, O. Oeckler, J. Weber, J. Schmedt Auf Der Günne, W. Schnick, *J. Am. Chem. Soc.* **2011**, *133*, 12069–12078.

[38] S. J. Sedlmaier, J. Schmedt Auf Der Günne, W. Schnick, *Dalt. Trans.* **2009**, 4081–4084.

[39] S. J. Sedlmaier, D. Weber, W. Schnick, *Z. Kristallogr. - New Cryst. Struct.* **2012**, *227*, 1–2.

[40] V. A. Blatov, *IUCr Comp Comm Newsl.* **2006**, *7*, 4–38.

[41] V. A. Blatov, M. O'Keeffe, D. M. Proserpio, *CrystEngComm* **2010**, *12*, 44–48.

[42] V. A. Blatov, *Cryst. Rev.* **2004**, *10*, 249–318.

[43] J. C. Slater, *J. Chem. Phys.* **1964**, *41*, 3199–3204.

[44] S. Pagano, M. Zeuner, S. Hug, W. Schnick, *Eur. J. Inorg. Chem.* **2009**, 1579–1584.

[45] S. Lupart, W. Schnick, *Z. Anorg. Allg. Chem.* **2012**, *638*, 2015–2019.

[46] S. Pagano, S. Lupart, S. Schmiechen, W. Schnick, *Z. Anorg. Allg. Chem.* **2010**, *636*, 1907–1909.

[47] M. Orth, W. Schnick, *Z. Anorg. Allg. Chem.* **1999**, *625*, 1426–1428.

[48] A. Marchuk, V. R. Celinski, J. Schmedt Auf Der Günne, W. Schnick, *Chem. Eur. J.* **2015**, *21*, 5836–5842.

[49] G. M. Sheldrick, *SHELXS*, University of Göttingen, **1997**.

[50] N. A. Anurova, V. A. Blatov, G. D. Ilyushin, O. A. Blatova, A. K. Ivanov-Schitz, L. N. Dem'yanets, *Solid State Ionics* **2008**, *179*, 2248–2254.

[51] A. P. Shevchenko, V. N. Serezhkin, V. A. Blatov, *J. Appl. Cryst.* **1999**, *32*, 377–377.

[52] H. Yamane, S. Kikkawa, M. Koizumi, *Solid State Ionics* **1987**, *25*, 183–191.

[53] S. Lupart, G. Gregori, J. Maier, W. Schnick, *J. Am. Chem. Soc.* **2012**, *134*, 10132–10137.

[54] A. Rabenau, *Solid State Ionics* **1982**, *6*, 277–293.

[55] N. Tapia-Ruiz, M. Segalés, D. H. Gregory, *Coord. Chem. Rev.* **2013**, *257*, 1978–2014.

[56] S. Wenzel, D. A. Weber, T. Leichtweiss, M. R. Busche, J. Sann, J. Janek, *Solid State Ionics* **2016**, *286*, 24–33.

[57] S. Wenzel, T. Leichtweiss, D. Krüger, J. Sann, J. Janek, *Solid State Ionics* **2015**, *278*, 98–105.

[58] N. Kawai, S. Endo, *Rev. Sci. Instrum.* **1970**, *41*, 1178–1181.

[59] D. Walker, M. A. Carpenter, C. M. Hitch, *Am. Mater.* **1990**, *75*, 1020–1028.

[60] D. Walker, *Am. Mater.* **1991**, *76*, 1092–1100.

[61] D. C. Rubie, *Phase Transitions* **1999**, *68*, 431–451.

[62] H. Huppertz, *Z. Kristallogr.* **2004**, *219*, 330–338.

[63] *XPREP Reciprocal Space Exploration, Vers. 6.12*, Bruker-AXS, Karlsruhe, **2001**.

[64] G. M. Sheldrick, *Acta Crystallogr., Sect. A Found. Crystallogr.* **2008**, *64*, 112–122.

[65] L. J. Farrugia, *J. Appl. Crystallogr.* **1999**, *32*, 837–838.

[66] L. J. Farrugia, *PLATON, Vers. 1.16*, University of Glasgow, **1995**.

[67] Further details of the crystal structure investiation can be obatined from the Fachinformations-Zentrum Karlsruhe, 76344 Eggenstein- Leopoldshafen, Germany (Fax: (+49)7247-808-666; E-Mail: crysdata@fiz-Karlsruhe.de) on quoting the depository number CSD- 431316.

[68] K. Brandenburg, Crystal Impact GbR: Bonn **2005**.

[69] A. Coelho, *TOPAS-Academic* **2007**.

[70] R. W. Cheary, A. A. Coelho, *J. Appl. Crystallogr.* **1992**, *25*, 109–121.

[71] R. W. Cheary, A. A. Coelho, *J. Res. Natl. Inst. Stand. Technol.* **2007**, *109*, 1–25.

[72] *INCA, Version 4.02*, OXFORD Instruments.

[73] *OPUS/IR*, Bruker Analytik GmbH, **2000**.

4. Li^+ Ion Conductors with Adamantane-type Nitridophosphate Anions – β-$Li_{10}P_4N_{10}$ and $Li_{13}P_4N_{10}X_3$ with X = Cl, Br

Eva-Maria Bertschler, Christian Dietrich, Thomas Leichtweiß, Jürgen Janek, Wolfgang Schnick

published in: *Chem. Eur. J.* **2018**, *24*, 196–205. DOI: 10.1002/chem.201704305

Abstract

β-$Li_{10}P_4N_{10}$ and $Li_{13}P_4N_{10}X_3$ with X=Cl, Br have been synthesized from mixtures of P_3N_5, Li_3N, LiX, $LiPN_2$, and Li_7PN_4 at temperatures below 850 °C. β-$Li_{10}P_4N_{10}$ is the low-temperature polymorph of α-$Li_{10}P_4N_{10}$ and crystallizes in the trigonal space group $R3$. It is made up of non-condensed $[P_4N_{10}]^{10-}$ T2 supertetrahedra, which are arranged in sphalerite-analogous packing. $Li_{13}P_4N_{10}X_3$ (X=Cl, Br) crystallizes in the cubic space group $Fm\bar{3}m$. Both isomorphic compounds comprise adamantane-type $[P_4N_{10}]^{10-}$, Li^+ ions, and halides, which form octahedra. These octahedra build up a face-centered cubic packing, whose tetrahedral voids are occupied by the $[P_4N_{10}]^{10-}$ ions. The crystal structures have been elucidated from X-ray powder diffraction data and corroborated by EDX measurements, solid-state NMR, and FTIR spectroscopy. Furthermore, we have examined the phase transition between α- and β-$Li_{10}P_4N_{10}$. To confirm the ionic character, the migration pathways of the Li^+ ions have been evaluated and the ion conductivity and its temperature dependence have been determined by impedance spectroscopy. XPS measurements have been carried out to analyze the stability with respect to Li metal.

4.1. Introduction

Over the past few decades, nitrides have attracted increasing attention due to their broad technical applicability, for example, as hard materials, high-temperature ceramics, electronic semiconductors, luminescent materials, and ion conductors.[1–6] Nitridophosphates are of particular interest due to their structural variability. The ability to form different linking patterns of corner- and/or edge-sharing PN_4 tetrahedra as primary building units leads to a variety of complex structures and allows materials to be optimized for many purposes.[7–11]

Synthetic approaches to nitridophosphates are somewhat challenging due to the limited thermal stability of the starting materials (e.g., P_3N_5 decomposes above 850 °C).[12] To prevent thermal dissociation at higher temperatures, the multi-anvil technique has emerged as a powerful tool, and has led to nitridophosphates with unprecedented topologies and properties.[9, 12–14] To date, a number of lithium nitridophosphates have been obtained at reaction temperatures below 850 °C.[6, 15–19] Reaction of the binary nitrides P_3N_5 and Li_3N between 620 and 800 °C led to four lithium nitridophosphates with different complex P/N anions in a matrix of Li^+ ions.[20–23] Recently, we succeeded in expanding this substance class with two new complex P/N anions by using the multianvil technique in combination with the Li_3N self-flux method.[22, 24] Li_7PN_4 (620 °C, ambient pressure) is the lithium nitridophosphate with the lowest P/N atomic ratio and consists of non-condensed $[PN_4]^{7-}$ tetrahedra.[23] Non-condensed $[P_3N_9]^{12-}$ *dreier*-rings,[25, 26] which are isoelectronic with $[Si_3O_9]^{6-}$, are observed in $Li_{12}P_3N_9$ (790 °C, ambient pressure).[22] At 820 °C and 6 GPa, these non-condensed $[P_3N_9]^{12-}$ *dreier*-rings polymerize to infinite *zweier*-chains of corner-sharing PN_4 tetrahedra (Li_4PN_3).[22] A tricyclic ring structure of one *vierer*-ring with two annelated *dreier*-rings is the characteristic structural motif $[P_6N_{16}]^{18-}$ in $Li_{18}P_6N_{16}$, which has hitherto only been accessible under conditions of high temperature and high pressure (1000 °C, 5.5 GPa).[24] α-$Li_{10}P_4N_{10}$ (720 °C, ambient pressure) consists of adamantane-like $[P_4N_{10}]^{10-}$ ions, isoelectronic with $[P_4O_{10}]$.[21] A higher reaction temperature (800 °C) at ambient pressure is necessary for the synthesis of $LiPN_2$. It consists of corner-sharing PN_4 tetrahedra forming a three-dimensional network structure isoelectronic to that of SiO_2.[20]

Recently, some nitrides have been discussed as buffer materials to protect fast ionic conductors in Li batteries against Li metal, due to their negative reduction potential and their unique thermodynamic stability. The Li reduction potential (cathodic limit with respect to Li/Li^+) of, for example, Li_7PN_4, is 0.01 V, and the reaction energy E_D for lithiation is −0.01 eV per Li. Hence, such nitrides seem to exhibit significantly higher stability with respect to Li metal compared to oxides (Li_3PO_4: cathodic limit with respect to Li/Li^+ 0.69 V), sulfides (Li_3PS_4: 1.72 V), and

halides ($LiPF_6$: 2.74 V).[27] To avoid continuous decomposition by Li metal, the use of only non-metal elements (P, Cl, Br, I) has been discussed, because they form passivating interphases (solid electrolyte interphases, SEI), which again enable stability with respect to Li metal, such as in LiPON, argyrodites,[28] or Li_3OCl/Li_3OBr.[27] Three ternary lithium nitridophosphates have hitherto been investigated with regard to their ion conductivity: Li_7PN_4 ($1.7\times10^{-5}\,\Omega^{-1}cm^{-1}$ at 125 °C, 0.49 eV),[29] $Li_{18}P_6N_{16}$ ($1.5\times10^{-5}\,\Omega^{-1}cm^{-1}$ at 125 °C, 0.50 eV),[24] and $LiPN_2$ ($6.8\times10^{-7}\,\Omega^{-1}cm^{-1}$ at 125 °C, 0.61 eV).[29] The conductivities of these lithium nitridophosphates are comparable to those of other lithium nitride compounds of p-block elements. LiPON ($1.6\times10^{-6}\,\Omega^{-1}cm^{-1}$ at 25 °C, 0.58 eV), for example, has already found application as a solid electrolyte in thin-film batteries.[4] Differences in the conductivities of these compounds depend on their crystal structures, the coordination of the lithium atoms, and the number of available charge carriers.[24] Trends in known Li^+ ion conductors show that a *bcc* anion framework allows the lowest activation barrier and highest ionic conductivity, because it allows direct Li hops between tetrahedral sites.[30] However, it has recently been shown in the case of the lithium argyrodites Li_6PS_5X (X=Cl, Br, I) that the prefactor and the activation energy of ionic conduction are closely linked, and that a low activation energy alone may not be sufficient to achieve high ion conductivity.[31]

In this contribution, we report a re-investigation of cubic α-$Li_{10}P_4N_{10}$. By lowering the synthesis temperature, we have succeeded in synthesizing the new polymorph β-$Li_{10}P_4N_{10}$, and have elucidated the phase transition between the α- and β-polymorphs. Furthermore, we have synthesized the first quaternary lithium nitridophosphate halides $Li_{13}P_4N_{10}X_3$ with X = Cl, Br. Phase-pure products of all of the title compounds have enabled ion conductivity measurements and investigations concerning their stability with respect to Li metal.

4.2. Results and Discussion

4.2.1. Synthesis

In 1991, Berger et al. described three different approaches to synthesize α-$Li_{10}P_4N_{10}$ in tungsten crucibles. α-$Li_{10}P_4N_{10}$ was prepared by reaction of the binary nitrides P_3N_5 and Li_3N at 720 °C, and was obtained together with $LiPN_2$, Li_3P, and small amounts of amorphous material. Reaction of Li_3N with $LiPN_2$ at 700 °C led to smaller amounts of these side products. Only Li_3P as a side phase was formed by the reaction of Li_7PN_4 and P_3N_5 at 630 °C.[21, 32] Recent re-investigations of $Li_{10}P_4N_{10}$ to obtain phase-pure products for Li^+ ion conductivity measurements indicated that less Li_3P was obtained as a side phase at lower synthesis temperatures. At these decreased synthesis

temperatures, the low-temperature phase β-$Li_{10}P_4N_{10}$ became accessible. After optimization, it could be synthesized according to Equations (1), (2), (3), or (4). For all of these routes, we used a Li_3N flux or self-flux, in open Ta crucibles sealed in silica ampoules under argon or nitrogen atmosphere, with different excesses of Li_3N or Li_7PN_4 as appropriate. We have already described these synthetic approaches in previous work.[22, 24, 33]

$$10\ Li_3N + 4\ P_3N_5 \xrightarrow{680\ °C} 3\ \beta\text{-}Li_{10}P_4N_{10} \quad (1)$$

$$4\ LiPN_2 + 2\ Li_3N \xrightarrow{680\ °C} \beta\text{-}Li_{10}P_4N_{10} \quad (2)$$

$$10\ Li_7PN_4 + 6\ P_3N_5 \xrightarrow{630\ °C} 7\ \beta\text{-}Li_{10}P_4N_{10} \quad (3)$$

$$3\ LiPN_2 + Li_7PN_4 \xrightarrow{630\ °C} \beta\text{-}Li_{10}P_4N_{10} \quad (4)$$

According to these equations, different amounts of β-$Li_{10}P_4N_{10}$ were obtained together with Li_3P, depending on the initial weight ratio and reaction temperature. Synthesis according to Equation (4) gave the product with the lowest amount of Li_3P. This side phase could be removed by washing with dry ethanol under inert conditions.

By adding LiCl or LiBr to the reaction mixtures, we were able to synthesize the first quaternary lithium nitridophosphate halides $Li_{13}P_4N_{10}X_3$ (X = Cl, Br) according to the following equations:

$$10\ Li_3N + 4\ P_3N_5 + 9\ LiCl \xrightarrow{720\ °C} 3\ Li_{13}P_4N_{10}Cl_3 \quad (5)$$

$$18\ Li_3N + 4\ (PNCl_2)_3 \xrightarrow{700\ °C} 3\ Li_{13}P_4N_{10}Cl_3 + 15\ LiCl \quad (6)$$

$$10\ Li_3N + 4\ P_3N_5 + 9\ LiBr \xrightarrow{580\ °C} 3\ Li_{13}P_4N_{10}Br_3 \quad (7)$$

For successful reactions, excesses of LiCl/LiBr and Li_3N were used for Equations (5 and (7). The side phases Li_3P and LiCl/LiBr were removed by washing with dry ethanol. All products proved to be sensitive to moisture and air, with $Li_{13}P_4N_{10}Cl_3$ and $Li_{13}P_4N_{10}Br_3$ being much more sensitive

than β-$Li_{10}P_4N_{10}$. To avoid hydrolysis, all compounds were handled under inert conditions. Detailed information on the synthesis of the three compounds is given in the Experimental Section. Similar experiments were also performed with LiF and LiI, but no analogous structures have hitherto been identified.

4.2.2. Crystal structure determination

The crystal structures of β-$Li_{10}P_4N_{10}$, $Li_{13}P_4N_{10}Cl_3$, and $Li_{13}P_4N_{10}Br_3$ [34] (Table 1) were elucidated from powder X-ray diffraction data. Rietveld refinement did not indicate any side phases.

β-$Li_{10}P_4N_{10}$ crystallizes in the trigonal space group $R3$ with lattice parameters a = 8.71929(8) and c = 21.4656(2) Å. Further crystallographic data (atomic positions, isotropic displacement parameters) are given in the Supporting Information. During the structure determination of β-$Li_{10}P_4N_{10}$, different space groups were tested and compared.

The P–N distances with free refinement of all atom positions in $R3$ (β-$Li_{10}P_4N_{10}$) vary from 1.54 to 1.72 Å. The P–N distances to terminal N atoms are shorter (1.54 to 1.63 Å) than those to bridging N atoms (1.63 to 1.72 Å). This is in accordance with the P–N distances in α-$Li_{10}P_4N_{10}$ (1.58 Å to terminal and 1.68 Å to bridging N atoms).[21] In comparison, the refinement in $R\bar{3}m$ results in P–N distances ranging from 1.54 to 1.75 Å and the following residuals: R_{wp} = 0.0578, R_{exp} = 0.0255, R_p = 0.0424, R_{Bragg} = 0.0209, GoF = 2.267 with 47 parameters (Supporting Information, Figures S5 and S6). Similarly, in the refinement in $R\bar{3}$ (P–N distances: 1.54 to 1.75 Å; R_{wp} = 0.0579, R_{exp} = 0.0255, R_p = 0.0425, R_{Bragg} = 0.0208, GoF = 2.270 with 46 parameters, Supporting Information, Figures S7 and S8), the reflection at, for example, 2θ = 66°, is not explained. In $R3$, the peaks are fitted correctly by the structural model (Figure 1).

Even lower symmetry in $P3$ leads to an unusual distribution of P–N distances ranging from 1.2 to 1.8 Å with significantly larger errors, which is caused by correlation problems during refinement due to the number of parameters. Moreover, the use of constraints or restraints yields no appropriate structure refinement. Typically, P–N distances in lithium nitridophosphates vary from 1.59 to 1.74 Å.[20, 22--24] Distances in the range 1.48 to 1.79 Å were found in $Li_{47}B_3P_{14}N_{42}$.[33] Consequently, it can be surmised that the extinction observed in the powder pattern clearly indicates an R-centering. Furthermore, only in $R3$ the reflection at is $2\theta \approx 66°$ explained.

Table 1. Crystal data for β-$Li_{10}P_4N_{10}$, $Li_{13}P_4N_{10}Cl_3$, and $Li_{13}P_4N_{10}Br_3$.

Formula	β-$Li_{10}P_4N_{10}$	$Li_{13}P_4N_{10}Cl_3$	$Li_{13}P_4N_{10}Br_3$
Formula mass [g mol^{-1}]	333.4	460.6	593.9
Crystal system/space group	trigonal $R\bar{3}$ (no. 146)	cubic $Fm\bar{3}m$ (no. 225)	cubic $Fm\bar{3}m$ (no. 225)
Lattice parameters [Å]	a=8.71929(8)	a=13.9321(2)	a=14.1096(6)
	c=21.4656(2)		
Cell volume [Å^3]	1413.30(3)	2704.27(12)	2809.0(4)
Formula units per cell [Z]	6	8	8
X-ray density [g cm^{-3}]	2.35015(5)	2.26242(12)	2.8088(4)
Absorption coefficient [cm^{-1}]	73.77	107.00	150.07
Radiation	$Cu_{K\alpha1}$ (λ = 1.540596 Å)		
Monochromator	Ge(111)		
Diffractometer	Stoe StadiP		
Detector	linear PSD		
2θ range [°]	5–110	5–96	5–114
T [K]	298(2)		
Data points	7003	6042	7285
Number of observed reflections	1216	95	131
Number of parameters	79	43	42
Program used	TOPAS Academic V4.1		
Structure refinement	Rietveld method		
Profile function	fundamental parameters		
Background function	shifted Chebychev		
Terms (backgr. function)	12	18	18
R_{wp}	0.0493	0.0670	0.1169
R_{exp}	0.0255	0.0425	0.0499
R_p	0.0369	0.0501	0.0873
R_{Bragg}	0.0146	0.0187	0.0224
χ^2	1.938	1.576	2.234

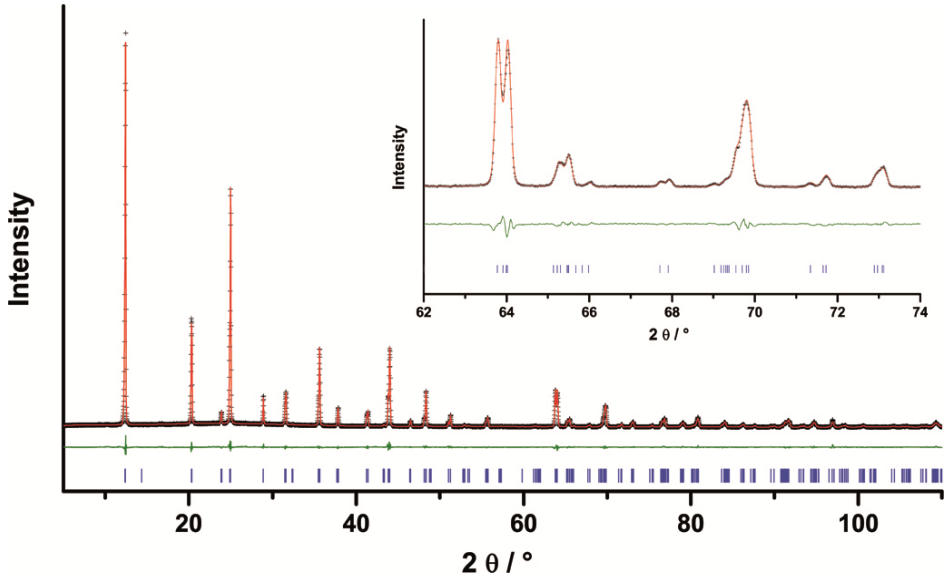

Figure 1. Observed (crosses) and calculated (red line) powder diffraction pattern of β-$Li_{10}P_4N_{10}$ ($R3$) as well as position of Bragg reflections (blue bars) and difference profile (green line). Enlarged images are given in the Supporting Information (Figures S9 and S10).

$Li_{13}P_4N_{10}Cl_3$ and $Li_{13}P_4N_{10}Br_3$ crystallize in the cubic space group $Fm\bar{3}m$ with lattice parameters a = 13.9321(2) and 14.1096(6) Å, respectively. Further crystallographic data are summarized in the Supporting Information. Comparison of the X-ray powder data of $Li_{13}P_4N_{10}Cl_3$ (Figure 2, enlarged in Figure S17) and $Li_{13}P_4N_{10}Br_3$ (Figure 3, enlarged in Figure S18) shows that the reflections of $Li_{13}P_4N_{10}Br_3$ are slightly broadened towards smaller angles, which may derive from lattice imperfections.

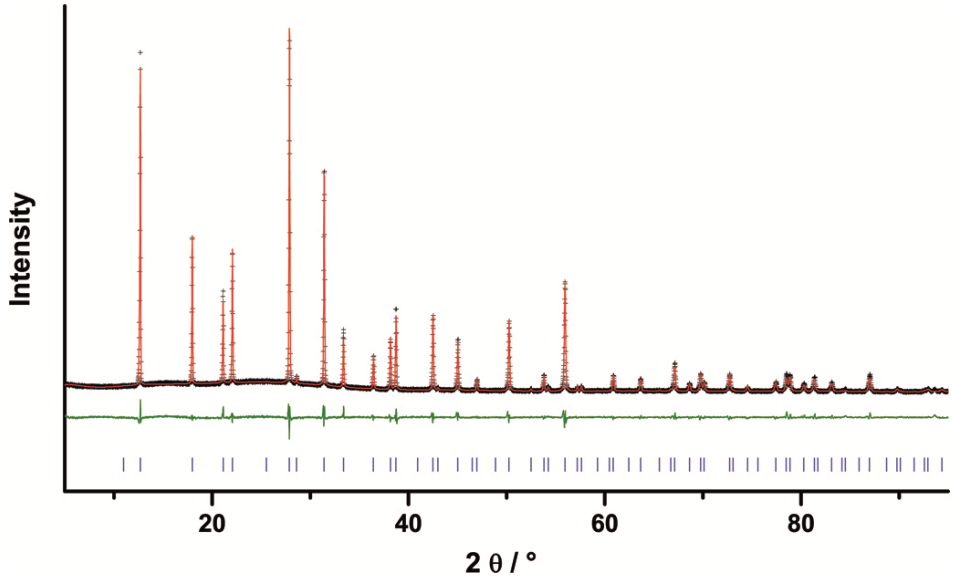

Figure 2. Observed (crosses) and calculated (red line) powder diffraction pattern of $Li_{13}P_4N_{10}Cl_3$ as well as position of Bragg reflections (blue bars) and difference profile (green line). An enlarged image is given in the Supporting Information (Figure S17).

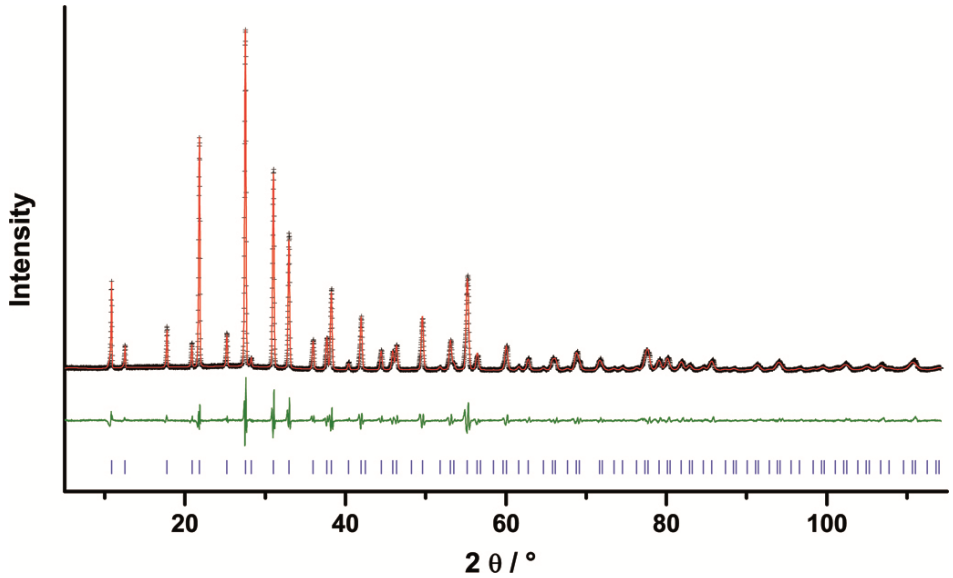

Figure 3. Observed (crosses) and calculated (red line) powder diffraction pattern of $Li_{13}P_4N_{10}Br_3$ as well as position of Bragg reflections (blue bars) and difference profile (green line). An enlarged image is given in the Supporting Information (Figure S18).

4.2.3. Crystal structure description

Both polymorphs α- and β-$Li_{10}P_4N_{10}$ contain adamantane-like T2 supertetrahedra, which are made up of four PN_4 units (Figure 4). The PN_4 tetrahedra in trigonal β-$Li_{10}P_4N_{10}$ are slightly distorted compared to those in cubic α-$Li_{10}P_4N_{10}$.

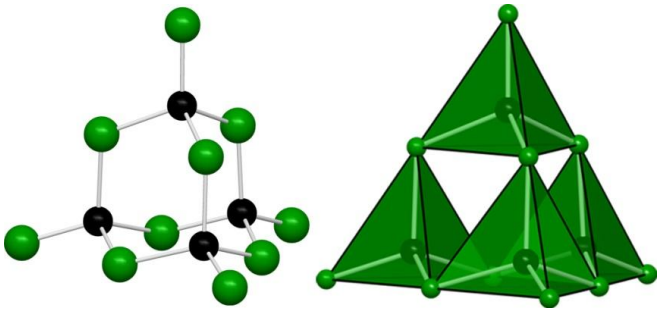

Figure 4. Left: Adamantane-like $[P_4N_{10}]^{10-}$ anion. Right: $[P_4N_{10}]^{10-}$ anion with PN_4 tetrahedra of the P/N framework in green. (P: black, N: green).

In β-$Li_{10}P_4N_{10}$, the T2 supertetrahedra have two different orientations (A and B), in analogy to the situation in α-$Li_{10}P_4N_{10}$ (Figure 5). Each supertetrahedra of type A is surrounded by four of type B. A and B face each other in a parallel arrangement with their triangular surfaces, and are additionally rotated by 60°. Thus, five $[P_4N_{10}]^{10-}$ supertetrahedra consistently form AB_4 tetrahedra (A–B: 5.34 and 5.35 Å). These AB_4 tetrahedra are corner-sharing at all vertices, forming a sphalerite-analogous packing. In other words, the centers of gravity of the equally orientated $[P_4N_{10}]^{10-}$ units form an *fcc* partial structure. The latter are mutually shifted by about −1/3, 1/3, 0.09. In comparison, in α-$Li_{10}P_4N_{10}$, the two *fcc* partial lattices are mutually shifted by ¼, ¼, ¼. Thus, in α-$Li_{10}P_4N_{10}$, the AB_4 tetrahedra (A–B: 5.36 Å) are also in a sphalerite-type arrangement.[21] Consequently, the AB_4 tetrahedra, and thus also the PN_4 tetrahedra, in β-$Li_{10}P_4N_{10}$ are more distorted than those in α-$Li_{10}P_4N_{10}$.

The $[P_4N_{10}]^{10-}$ supertetrahedra in β-$Li_{10}P_4N_{10}$ are surrounded by a matrix of Li^+ ions, which are coordinated by N atoms forming distorted polyhedra with coordination numbers of 3, 4, and 6, analogous to those in α-$Li_{10}P_4N_{10}$ (Supporting Information, Figure S2). The LiN_x polyhedra share edges or corners. The Li–N distances in β-$Li_{10}P_4N_{10}$ vary from 1.87 to 2.43 Å (α-$Li_{10}P_4N_{10}$: Li–N 1.93 to 2.20 Å).[21] Accordingly, the LiN_x polyhedra are more distorted in the β-phase.

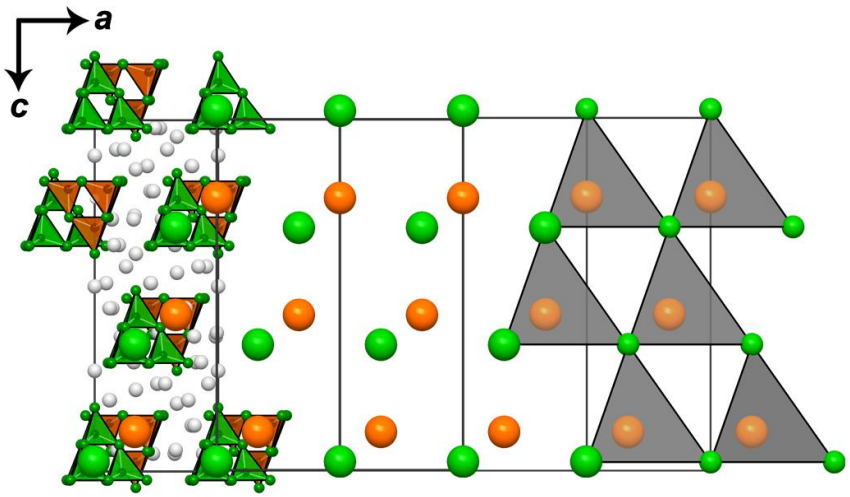

Figure 5. Packing of β-$Li_{10}P_4N_{10}$ in $R3$. From left to right: Unit cell with two different orientations of the T2 supertetrahedra (P: black, N: green, Li: gray, supertetrahedra A: orange, supertetrahedra B: green); orange (A) and green (B) spheres mark the centers of gravity of the supertetrahedra; corner-sharing AB_4 tetrahedra (gray) forming a sphalerite-analogous packing. A slightly rotated view of the right part is given in the Supporting Information (Figure S1).

The nitridophosphate anions $[P_4N_{10}]^{10-}$ in $Li_{13}P_4N_{10}X_3$ (X = Cl, Br) are analogous to those in α- and β-$Li_{10}P_4N_{10}$. The adamantane-like T2 supertetrahedra also have two different orientations per unit cell and they are located at the tetrahedral voids of an *fcc* lattice (Figure 6, left). The Cl or Br atoms form octahedra (Cl–Cl: 3.61 Å, Br–Br: 3.70 Å). The centers of gravity of these halide octahedra build up the *fcc* lattice (Figure 6, middle). Each Cl or Br atom is square-pyramidally surrounded by five Li^+ ions. These Li positions correspond to Li1 (Wyckoff 24*e*) and Li2 (Wyckoff 32*f*). A similar arrangement of atoms has been found in clusters such as $[Mo_6X_{14}]^{2-}$ (X=Br, I).[35] In $Li_{13}P_4N_{10}X_3$ (X = Cl, Br), the X atoms occupy the Mo positions and the Li atoms occupy the Cl positions, forming X_6Li_{14} (X = Cl, Br) building blocks. The Li^+ ions are further connected to N atoms of the P/N supertetrahedra. In total, there are three different Li^+ positions. The third one (Wyckoff 48*i*) is coordinated by four N atoms in a planar manner. Two of these planar LiN_4 units share one edge and are located in the voids between two $[P_4N_{10}]^{10-}$ supertetrahedra (Figure 6, right).

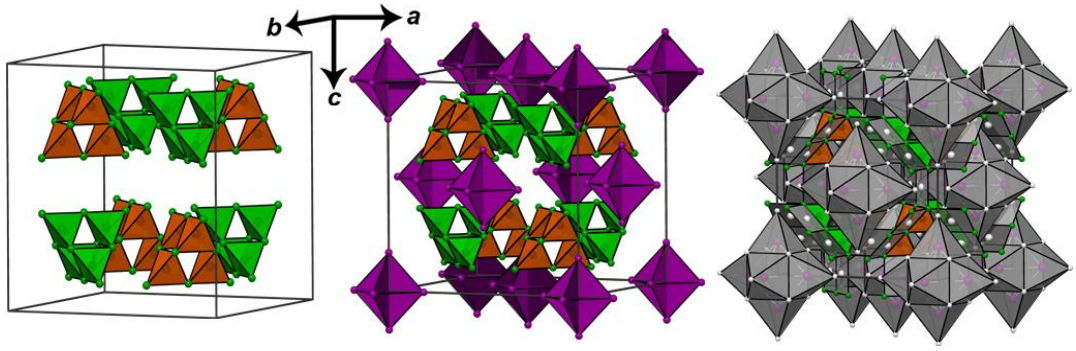

Figure 6. Packing of $Li_{13}P_4N_{10}X_3$ (X = Cl, Br). Left: packing of the $[P_4N_{10}]^{10-}$ ions with two different orientations (orange and green); middle: added octahedra of Cl/Br atoms; left: added Li atoms with their coordination polyhedra. (P: black, N: green, Cl/Br: violet, Li: gray).

In $Li_{13}P_4N_{10}Cl_3$ and $Li_{13}P_4N_{10}Br_3$, the P–N distances are 1.57/1.68 Å and 1.55/1.68 Å, respectively. As in other nitridophosphates, the P–N distances for the terminal N atoms of PN_4 tetrahedra are shorter than those to bridging N atoms.[21, 22, 24, 36] The Li^+ ions are coordinated by N and Cl or Br, with coordination numbers of 4, 5, and 6 (Supporting Information, Figures S3 and S4).

4.2.4. Phase transition between α- and β-$Li_{10}P_4N_{10}$

At about 90 °C, a reversible phase transition from β- to α-$Li_{10}P_4N_{10}$ according to Equation (8) was observed (Figure 7). This reversible phase transition starts at about 30 °C and is completed at about 90 °C.

$$\beta\text{-}Li_{10}P_4N_{10} \rightleftarrows \alpha\text{-}Li_{10}P_4N_{10} \quad (8)$$

$$\beta\text{-}Li_{10}P_4N_{10} \rightarrow \beta\text{-}Li_{10}P_4N_{10}\ \text{(sintered)} \quad (9)$$

$$\beta\text{-}Li_{10}P_4N_{10}\ \text{(sintered)} \rightarrow \alpha\text{-}Li_{10}P_4N_{10} \quad (10)$$

$$\beta\text{-}Li_{10}P_4N_{10} \rightarrow \alpha\text{-}Li_{10}P_4N_{10} \quad (11)$$

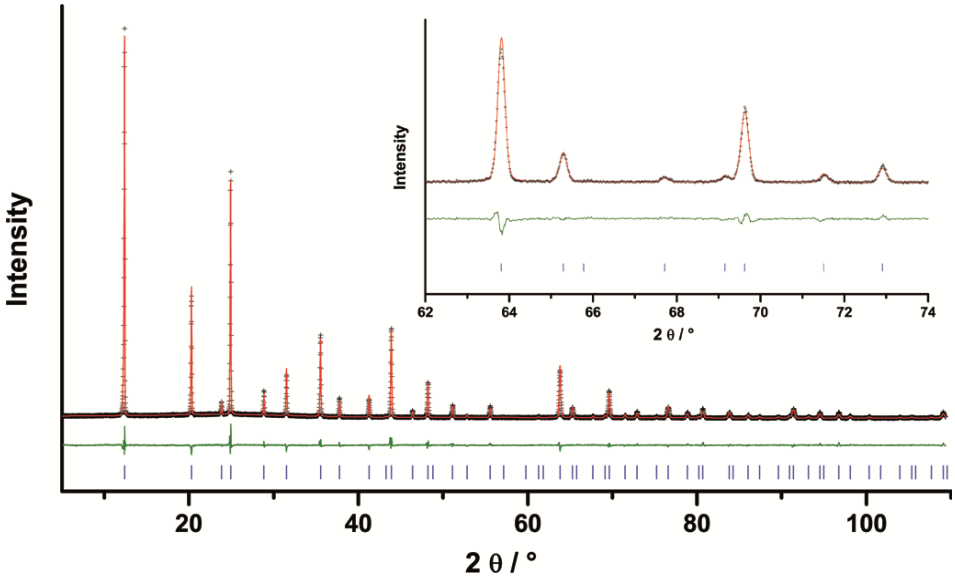

Figure 7. Observed (crosses) and calculated (red line) powder diffraction pattern of α-$Li_{10}P_4N_{10}$[21] at about 90 °C [Eq. (8)] as well as position of Bragg reflections (blue bars) and difference profile (green line). Enlarged images are given in the Supporting Information (Figures S11 and S12).

After heating β-$Li_{10}P_4N_{10}$ between 120 and 200 °C [Eq. (9)], an asymmetric broadening of the peak profile was observed. Each reflection in the powder pattern showed the same broadening, while remaining relatively sharp (Figure 8). This effect may derive from inhomogeneities, possibly originating from lattice imperfections (Rietveld refinement of the sintered sample yielded a marginally larger unit cell, a = 8.723(3), c = 21.4676(9) Å; Supporting Information, Figures S13 and S14), microstructural effects, grain boundaries, and stacking or twin defects.[37–42]

Upon further heating these samples to about 600 °C, an irreversible phase transition to α-$Li_{10}P_4N_{10}$ was observed. Heating of β-$Li_{10}P_4N_{10}$ at this temperature also led to α-$Li_{10}P_4N_{10}$. According to Equations (10) and (11), α-$Li_{10}P_4N_{10}$ was obtained together with an unknown side phase (black body color), which could not be removed by washing with dry ethanol (Supporting Information, Figure S16). Thus, the phase transition from β-$Li_{10}P_4N_{10}$ to α-$Li_{10}P_4N_{10}$ is reversible below 600 °C and irreversible above this temperature.

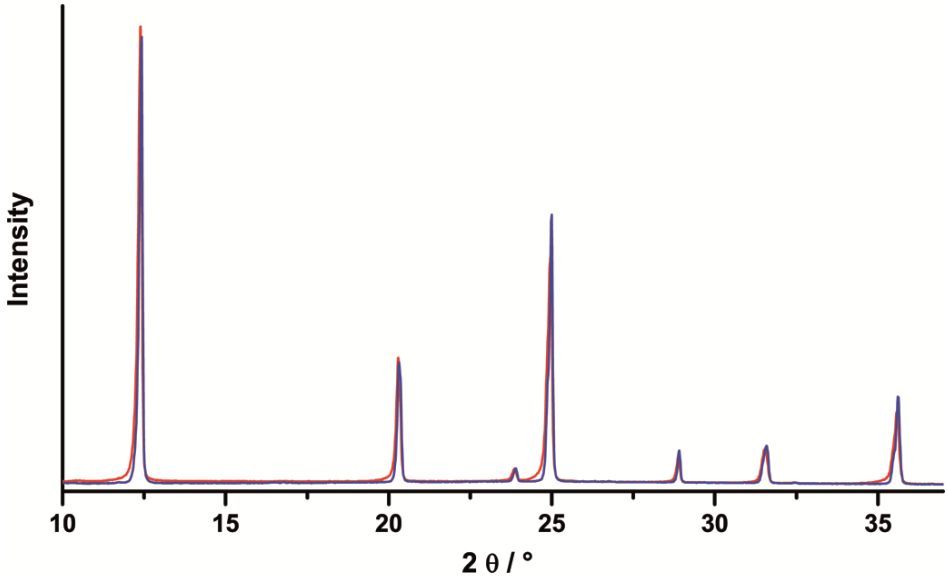

Figure 8. Comparison of the X-ray powder diffraction data of β-$Li_{10}P_4N_{10}$. Both spectra were acquired at room temperature. Blue: after synthesis according to Equation (1) and washing with EtOH; red: after sintering this sample at 190 °C. The complete diagram is given in the Supporting Information (Figure S15).

4.2.5. Thermal stability

To assess the thermal stabilities of all three title compounds, high-temperature X-ray diffraction analyses were performed. $Li_{10}P_4N_{10}$ was seen to decompose at above 700 °C. At this temperature, Li_3P was identified as a side product. At 900 °C, $LiPN_2$ could also be identified, along with Li_7PN_4 at 950 °C, besides other unknown decomposition products. At 950 °C, $Li_{10}P_4N_{10}$ could no longer be observed (Supporting Information, Figure S35). Decompositions of $Li_{13}P_4N_{10}Cl_3$ and $Li_{13}P_4N_{10}Br_3$ were seen to commence at about 750 °C (Supporting Information, Figures S36 and S37).

4.2.6. Solid-state NMR spectroscopy

^{31}P, ^{6}Li, and ^{7}Li solid-state MAS NMR spectroscopy was performed to confirm the structural model of the title compounds (Supporting Information, Figures S19–S31). The ^{31}P NMR spectrum of β-$Li_{10}P_4N_{10}$ shows four strong overlapping resonances at δ = 15.4, 14.0, 12.4, and 9.0 ppm. Integration of these signals results in a ratio of about 1:2:3:1, which is not in accordance with the multiplicity of the Wyckoff sites (2×3*a* and 2×9*b*). Lorentz functions were used for fitting with the program IGOR PRO 7 (WaveMetrics). However, it should be mentioned that the phase transition from β- to α-$Li_{10}P_4N_{10}$ starts at about 30 °C. Such a temperature may have been inadvertently reached within the NMR probe by rotation. Furthermore, deconvolution of the

spectra is challenging due to severe overlap. The ^{31}P NMR spectrum of α-$Li_{10}P_4N_{10}$ [after reaction according to Equation (10)] shows one broad signal at δ = 12.8 ppm and a significantly weaker signal at δ = 30.14 ppm, which we assign to the side phase. The signal of α-$Li_{10}P_4N_{10}$ is therefore slightly shifted to higher ppm value with respect to the most intense signal of β-$Li_{10}P_4N_{10}$ at δ = 12.4 ppm. Hence, we fitted both polymorphs to the ^{31}P NMR spectrum of β-$Li_{10}P_4N_{10}$, and integration then resulted in a ratio of about 1:2:2:1 (Supporting Information, Figure S20). Analysis of the signal width (FWHM) showed that the signals were narrower for β-$Li_{10}P_4N_{10}$ (1.0–1.3 ppm) than the fitted signal of α-$Li_{10}P_4N_{10}$ (3.3 ppm). Consequently, our structural model was confirmed insofar as the spectrum showed four different crystallographically independent P sites, each with two identical Wyckoff sites. The deviation from the expected ratio (1:3:3:1) may be rationalized in terms of the high forces of radial acceleration (of the order of millions of g) that affect the sample during measurement and lead to reversible phase transitions. The ^{6}Li (δ = 2.3, 1.6, and −0.7 ppm) and ^{7}Li (δ = 2.4, 1.7, and −0.5 ppm) NMR spectra of β-$Li_{10}P_4N_{10}$ show three signals, which correspond to the three different coordination spheres of the Li^+ ions. The corresponding spectra of α-$Li_{10}P_4N_{10}$ also show three signals with related chemical shifts (^{6}Li: δ = 2.3, 1.6, and −0.6 ppm; ^{7}Li: δ = 2.3, 1.8, and −0.5 ppm). Typical NMR shifts for lithium nitridophosphates are about δ = 5.5 and 50.2 ppm (^{31}P) and δ = 4.9 to 1.6 ppm (^{7}Li).[22, 24]

The ^{31}P NMR spectra of $Li_{13}P_4N_{10}X_3$ (X=Cl, Br) feature one signal at δ = 4.71 (X=Cl) and δ = 4.74 ppm (X=Br), in accordance with one crystallographically independent P site. The ^{6}Li NMR spectra feature three different signals, which also correspond to the three different Li sites and coordination spheres. The ^{7}Li NMR spectra do not show this arrangement (X = Cl: δ = −1.11 and 0.18 ppm; X = Br: δ = −1.32 ppm).

4.2.7. Chemical analysis (EDX, IR)

For determination of the elemental composition, EDX measurements were carried out. In β-$Li_{10}P_4N_{10}$, only P and N were found, beside traces of oxygen. In $Li_{13}P_4N_{10}Cl_3$ and $Li_{13}P_4N_{10}Br_3$, Cl and Br, respectively, were additionally identified. The traces of oxygen might be explained by hydrolysis during contact with air. Li could not be detected by EDX measurements (Supporting Information, Tables S10–S12).

To prove the absence of hydrogen, FTIR spectroscopy was performed. The spectra showed no significant vibrations in the region around 3000 cm^{-1}. A weak signal could be attributed to slight surface hydrolysis (Supporting Information, Figures S38–S40). The incorporation of stoichiometric amounts of hydrogen would have led to N–H absorption bands, as seen for $MH_4P_6N_{12}$ (M = Mg, Ca) or HP_4N_7.[9, 43]

4.2.8. Structural analysis of possible lithium migration pathways

The possible voids and migration pathways for Li^+ can be calculated by considering Voronoi–Dirichlet polyhedra with the TOPOS program package.[24, 44–47] β-$Li_{10}P_4N_{10}$, $Li_{13}P_4N_{10}Cl_3$, and $Li_{13}P_4N_{10}Br_3$ show possible pathways in three different directions in space and seem to be promising candidates for lithium ion conductivity in terms of their structural properties (Supporting Information, Figures S41–S43). Through these calculations, we additionally confirmed the positions of the Li^+ ions found during structure determination.

4.2.9. Ionic conductivity measurements

Conductivity measurements were performed to confirm the ionic character of the title compounds and to examine the influence of different halides on the conductivity. The conductivity of β-$Li_{10}P_4N_{10}$ at room temperature is about $\sigma = 8.6 \times 10^{-7}\ \Omega^{-1}cm^{-1}$. The conductivity increases on heating to about 90 °C, then decreases until it reaches a broad minimum at about 120 °C, and then increases once more with a different activation energy. The transition region from β- to α-$Li_{10}P_4N_{10}$ is kinetically dominated and is furthermore dependent on the heating rate, which accounts for the small jump in conductivity when the temperature is decreased once more. After sintering, the conductivity decreases to about $\sigma = 4.3 \times 10^{-10}\ \Omega^{-1}cm^{-1}$ at room temperature (Figure 9).

Besides the asymmetric broadening of the peaks in the X-ray diffractogram, this effect shows that sintering of β-$Li_{10}P_4N_{10}$ leads to modifications of the sample, which in turn lower conductivity. This decrease may be caused, for example, by the relaxation of grain boundaries. In contrast, sintering and annealing significantly improves the conduction in most compounds, for example, Li_3N.[48] In comparison, $Li_{13}P_4N_{10}X_3$ (X = Cl, Br) show conductivities of about $\sigma = 8.8 \times 10^{-10}\ \Omega^{-1}cm^{-1}$ and $\sigma = 1.1 \times 10^{-8}\ \Omega^{-1}cm^{-1}$, respectively, at room temperature.

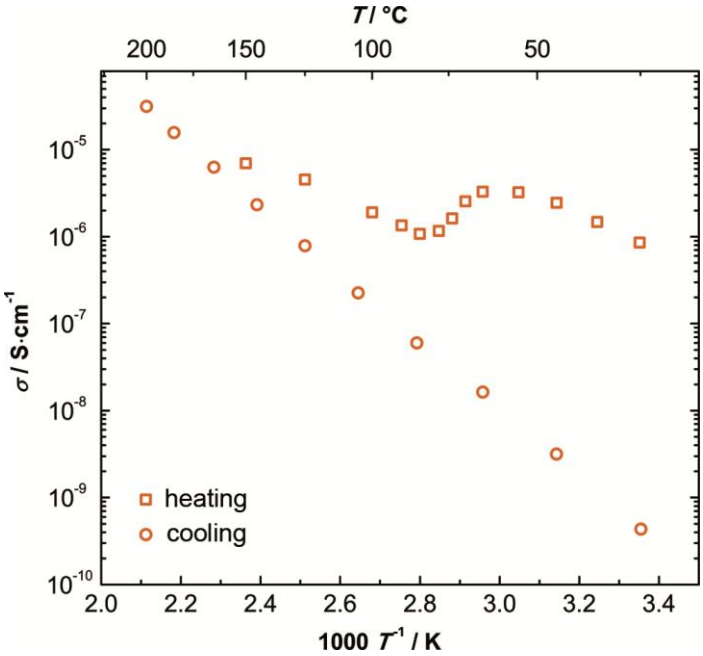

Figure 9. Ion conductivity plot of $Li_{10}P_4N_{10}$ obtained from impedance spectroscopy measurements. Untreated $Li_{10}P_4N_{10}$ was heated to 200 °C (squares) and then cooled to room temperature (circles). The resistance of the sintered $Li_{10}P_4N_{10}$ increased by over three orders of magnitude at room temperature.

Figure 10 shows Arrhenius plots for β-$Li_{10}P_4N_{10}$, sintered β-$Li_{10}P_4N_{10}$, and $Li_{13}P_4N_{10}X_3$ (X = Cl, Br). The samples are stable in the plotted area and the activation energies are constant in this range. β-$Li_{10}P_4N_{10}$ has the lowest activation energy at 0.41 eV. By sintering, this value is increased to 0.80 eV. By incorporation of halides, the activation energy changes to 0.72 eV for Cl and 0.61 eV for Br. Thus, incorporation of Br leads to higher ion conductivity than incorporation of Cl. Generally, it is assumed that the relatively high activation barriers are caused by the high ionic character or the polarizability of the anions.

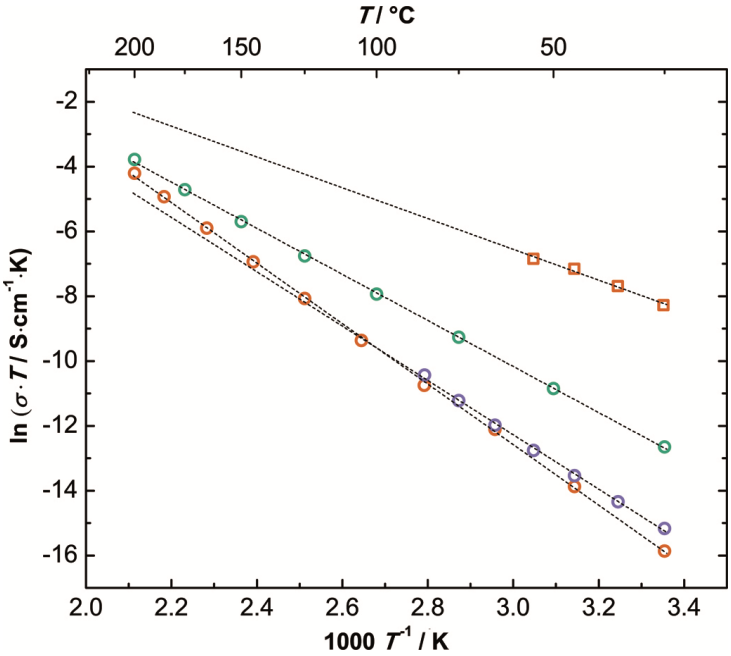

Figure 10. Arrhenius plots of all title compounds obtained from impedance spectroscopy measurements at different temperatures (orange: $Li_{10}P_4N_{10}$ (squares: untreated, circles: sintered), violet: $Li_{13}P_4N_{10}Cl_3$, green: $Li_{13}P_4N_{10}Br_3$).

The conductivities of the title compounds are comparable to those of other lithium nitridophosphates (Table 2). The samples of the lithium nitridophosphates were cold-pressed and not sintered. All of the compounds except β-$Li_{10}P_4N_{10}$ proved to be stable up to 600 °C. Therefore, sintering and annealing may improve the conductivity of these samples.

Table 2. Conductivities and activation energies of some lithium nitridophosphates.

	σ_{RT} [$\Omega^{-1}cm^{-1}$]	σ_{400K} [$\Omega^{-1}cm^{-1}$]	E_a [eV]	Ref.
$Li_{10}P_4N_{10}$	8.6×10^{-7}	–	0.41	
Li_7PN_4	–	1.7×10^{-5}	0.49	[29]
$Li_{18}P_6N_{16}$	7.7×10^{-8}	1.5×10^{-5}	0.50	[24]
$Li_{13}P_4N_{10}Br_3$	1.1×10^{-8}	3.3×10^{-6}	0.61	
$LiPN_2$	–	6.8×10^{-7}	0.61	[29]
$Li_{13}P_4N_{10}Cl_3$	8.8×10^{-10}	7.7×10^{-7}	0.72	
$Li_{10}P_4N_{10}$ (sintered)	4.3×10^{-10}	9.1×10^{-7}	0.80	

In the Li/P/S compound class, halide-substituted derivatives also show changes with regard to ion mobility. For example, annealed samples of cubic Li_6PS_5X (X = Cl, Br) show an ionic

conductivity of about $7 \times 10^{-4}\ \Omega^{-1}cm^{-1}$ at ambient temperature. Through ^7Li NMR and impedance experiments, intrinsic local lithium mobilities of the order of $10^{-3}\ \Omega^{-1}cm^{-1}$ were determined at room temperature. The authors assumed that the packing was determined by the P/S anions and that the smaller halide ions enhanced the ion mobility. Conversely, incorporation of I leads to a decrease in the ion mobility due to ion size (it impedes the interconnection of local pathway cages).[49] In comparison, Li_7PS_6 has a bulk Li^+ ion conductivity of $1.6 \times 10^{-6}\ \Omega^{-1}cm^{-1}$ at 40 °C and an activation energy of 0.16 eV below 210 °C. Above this temperature, the conductivity changes due to an order–disorder phase transition[50] and the activation energy increases to 0.35 eV ($3\times10^{-5}\ \Omega^{-1}cm^{-1}$ at 300 °C).[51, 52] The lower conductivity of P–N compounds compared to P–S compounds may be attributed to the higher ionic character of nitridophosphates.

4.2.10. XPS measurements

For investigations concerning stability with respect to Li metal, XPS measurements were carried out. Detailed spectra of the N 1s region during stepwise lithiation are shown in Figure 11.

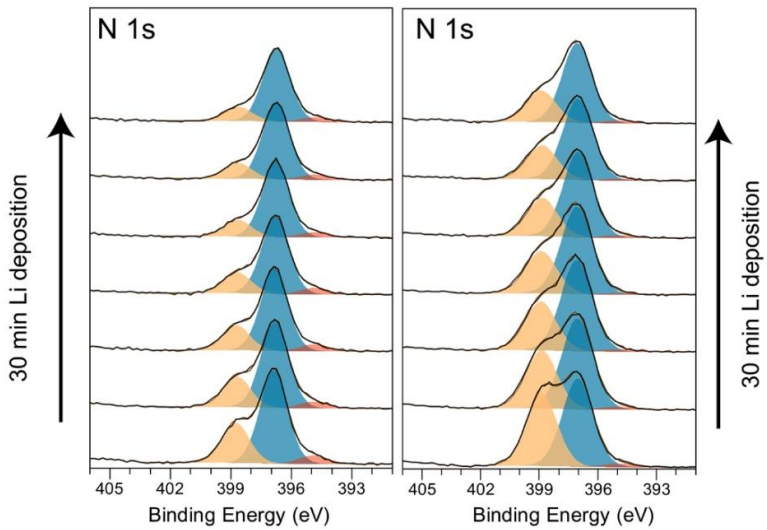

Figure 11. Evolution of the N 1s X-ray photoemission signals of β-$Li_{10}P_4N_{10}$ (left) and $Li_{13}P_4N_{10}Cl_3$ (right) during stepwise exposure to lithium vapor.

The N 1s signals of both pristine samples (bottom) can be attributed to two different N species in both compounds, arising from different chemical environments. According to the structure of the $[P_4N_{10}]^{10-}$ anion, the ratio of terminal and bridging N species should be 4:6. Therefore, we assume that the weaker signal at higher binding energy is related to terminal nitrogen atoms, and the signal at lower binding energy is attributed to bridging nitrogen atoms. Deviations from the expected ratio can be explained by the presence of oxygen in the topmost surface layer of the

sample (Supporting Information, Figure S45), which most likely stems from surface hydrolysis during sample transfer or traces of oxygen and water in the UHV chamber. During stepwise lithiation, the signal at higher binding energy diminishes. Formation of Li_3N, as in $Li_6P_3O_9N$ ($2\ Li_6P_3O_9N + 12\ Li \rightarrow Li_3PO_4 + Li_4P_2O_7 + Li_3N + 7\ Li_2O$), during the process cannot be unambiguously verified, as the expected Li_3N signal (in the range 395–396 eV) would be located directly under the signal of β-$Li_{10}P_4N_{10}$ or $Li_{13}P_4N_{10}Cl_3$.[53] However, in view of the relative decrease in the N signal at higher binding energy, the formation of Li_3N seems likely. The P 2p signal (Supporting Information, Figure S45) remains almost unchanged, as does the Cl 2p signal in $Li_{13}P_4N_{10}Cl_3$. Formation of Li_3P would lead to a signal in the range 126–127 eV, at which no signal is observed.[54] The presence of a small amount of oxygen leads to the formation of Li_2O upon exposure of the lithium. This effect has previously been observed during XPS measurements of $Li_7P_3S_{11}$.[54] Considering the decrease in the N signal related to terminal N species and the likely formation of Li_3N, it may be assumed that during lithiation a solid electrolyte interphase (SEI) is formed according to the following equation:

$$\beta\text{-}Li_{10}P_4N_{10} + 8\ Li \quad \rightarrow \quad \text{“}Li_6P_4N_6\text{”} + 4\ Li_3N \qquad (12)$$

According to this proposed mechanism, the terminal N atoms react with Li to form Li_3N, whereas the bridging nitrogen species remain intact.

4.3. Conclusions

In this work, we have reported the synthesis, structural investigation, ion conductivity, and investigations concerning the stability with respect to Li metal of the low-temperature polymorph β-$Li_{10}P_4N_{10}$ and the first quaternary lithium nitridophosphate halides $Li_{13}P_4N_{10}X_3$ (X=Cl, Br). β-$Li_{10}P_4N_{10}$ is composed of distorted adamantane-like $[P_4N_{10}]^{10-}$ T2 supertetrahedra, and transforms into α-$Li_{10}P_4N_{10}$ at about 90 °C. In contrast, in α-$Li_{10}P_4N_{10}$, the T2 supertetrahedra show no distortion. In both polymorphs, the P/N units are arranged analogously as in sphalerite in a matrix of Li^+ ions. $Li_{13}P_4N_{10}X_3$ (X = Cl, Br) are also made up of adamantane-like supertetrahedra, which occupy the tetrahedral voids of an *fcc* arrangement. The *fcc* lattice is made up of halide anions, which form octahedra. The calculated migration pathways of Li^+ ions indicate ion conductivity, which has been confirmed by impedance measurements. Furthermore, the influence of halides on the ion conductivity has been investigated. In addition, we have examined the stability of lithium nitridophosphates with respect to Li metal by XPS for the first time. These results should contribute to a better understanding of the mobility characteristics of lithium nitridophosphates and enable more targeted research towards obtaining optimized Li^+ ion conductors.

4.4. Experimental Section

4.4.1. Synthesis of starting materials

P_3N_5[55] was synthesized by the reaction of P_4S_{10} (8 g, Sigma–Aldrich, 99 %) with a constant flow of ammonia (Air Liquide, 99.999 %). The silica tube was saturated with NH_3 for 4 h. It was then heated to 850 °C at 5 °C min^{-1} and kept at this temperature for a further 4 h. Subsequently, it was cooled to room temperature at a rate of 5 °C min^{-1}. To eliminate side products, the orange product was washed with water, ethanol, and acetone. Powder X-ray diffraction and FTIR spectroscopic analyses confirmed the phase purity of the P_3N_5. All further steps were performed with strict exclusion of oxygen and moisture in an argon-filled glove box (Unilab, MBraun, Garching, O_2 < 1 ppm, H_2O < 0.1 ppm).

$LiPN_2$[20] and Li_7PN_4[23] were synthesized in sealed silica ampoules under N_2 atmosphere by reaction of Li_3N (Rockwood Lithium, 94 %) and P_3N_5 ($LiPN_2$: molar ratio 1.2:1; Li_7PN_4: 7.2:1). After grinding the starting materials, they were transferred to a Ta crucible, which was placed in a dried silica tube. The sealed silica ampoule was heated for 90 h in a tube furnace at 1073 or 893 K, respectively. To eliminate side products, $LiPN_2$ was washed with dilute hydrochloric acid, water, and ethanol. Li_7PN_4 was not washed. Powder X-ray diffraction and FTIR spectroscopic analyses confirmed the purities of the starting materials.

4.4.2. Synthesis of β-$Li_{10}P_4N_{10}$

β-$Li_{10}P_4N_{10}$ could be synthesized in sealed silica ampoules under Ar or N_2 atmosphere according to four different routes. For synthesis according to Equation (1), Li_3N (Rockwood Lithium, 95 %) and P_3N_5 were mixed in a molar ratio of 2.8:1. According to Equation (2), $LiPN_2$ and Li_3N were mixed in a molar ratio of 2.2:1. According to Equation (3), Li_7PN_4 and P_3N_5 were mixed in a molar ratio of 1.9:1. According to Equation (4), $LiPN_2$ and Li_7PN_4 were mixed in a molar ratio of 3:1. After grinding the starting materials in an agate mortar, the mixture was transferred to a Ta crucible, which was placed in a dried silica tube. The ampoules were heated for 120 h [Eqs. (1), (2), and (4)] or 240 h [Eq. (3)] in a tube furnace at 680 °C [Eqs. (1) and (2)] or 630 °C [Eqs. (3) and (4)]. All syntheses yielded a colorless powder containing dark traces of Li_3P. To obtain phase-pure products, the traces of Li_3P were removed by washing with dry ethanol. The product was sensitive to traces of air and moisture.

4.4.3. Synthesis of $Li_{13}P_4N_{10}Cl_3$

$Li_{13}P_4N_{10}Cl_3$ could be synthesized in sealed silica ampoules under Ar or N_2 atmosphere according to two different routes. For synthesis according to Equation (5), Li_3N (Rockwood Lithium, 95 %), P_3N_5, and LiCl (Alfa Aesar, 99.995 %) were mixed in a molar ratio of 2.8:1:6.2. According to Equation (6), Li_3N and $(PNCl_2)_3$ (Sigma-Aldrich, 98.5 %) were mixed in a molar ratio of 4.5:1. After grinding the starting materials in an agate mortar, the mixture was transferred to a Ta crucible, which was placed in a dried silica tube. The ampoules were heated for 55 h in a tube furnace at 720 °C [Eq. (5)] or 24 h at 700 °C [Eq. (6)]. Both syntheses yielded a colorless powder containing few dark traces (Li_3P). Li_3P and excess LiCl were removed by washing the product with dry ethanol under inert conditions. The product was sensitive to traces of air and moisture.

4.4.4. Synthesis of $Li_{13}P_4N_{10}Br_3$

$Li_{13}P_4N_{10}Br_3$ was synthesized in sealed silica ampoules under Ar or N_2 atmosphere. Li_3N (Rockwood Lithium, 95 %), P_3N_5, and LiBr (Alfa Aesar, 99.998 %) were mixed in a molar ratio of 2.8:1:6.2. After grinding the starting materials in an agate mortar, the mixture was transferred to a Ta crucible, which was placed in a dried silica tube. Each ampoule was heated for 60 h in a tube furnace at 580 °C. The synthesis yielded a colorless powder containing a few dark traces (Li_3P). Li_3P and the excess LiBr were removed by washing the product with dry ethanol under inert conditions. The product was sensitive to traces of air and moisture.

4.4.5. Powder X-ray diffraction

X-ray powder diffraction analysis was carried out with a STOE StadiP diffractometer (Stoe & Cie, Darmstadt, Germany) in parafocusing Debye–Scherrer geometry. $Cu_{K\alpha 1}$ radiation was selected with a Ge(111) single-crystal monochromator. A Mythen 1 K Si strip detector (Dectris, Baden, Switzerland) was used for detection of the diffracted radiation. For measurement, the samples were enclosed in glass capillaries of diameter 0.5 mm (Hilgenberg, Malsfeld, Germany) under inert gas. Rietveld refinement was carried out using the program package TOPAS-Academic v4.1.[56] Reflections were indexed using the SVD algorithm[57] and their intensities were extracted by the Pawley method. The full structural model was obtained using the charge-flipping algorithm.[58] Final refinement was carried out using the Rietveld method, employing the fundamental parameters approach (direct convolution of source emission profiles, axial instrument contributions, and crystallite size and microstrain effects).[58–60] The background was handled with a shifted Chebychev function and the peak shapes were described using the fundamental parameters approach.[61, 62] Capillary absorption correction (inner diameter 0.48 mm)

was carried out using the calculated absorption. To acquire X-ray diffraction data at about 90 °C, we used a thermionic soldering station (Hakko, Fr-810 B) for heating. The temperature was measured with a digital thermal sensor (Geisinger Electronics, GMH 3210) before and after measurement.

Temperature-dependent powder X-ray diffraction data were acquired on a STOE StadiP diffractometer equipped with a graphite furnace with $Mo_{K\alpha 1}$ radiation (λ = 0.70930 Å) in Debye–Scherrer geometry, an image plate position-sensitive detector, and a Ge(111) monochromator. Starting from room temperature, data were collected at intervals of 25 °C up to 1000 °C at a heating rate of 5 °C min^{-1}. The data collection was performed at constant temperature.

4.4.6. Solid-state MAS (magic-angle spinning) NMR methods

^6Li, ^7Li, and ^{31}P solid-state MAS NMR spectra of both polymorphs were recorded on a DSX Advance spectrometer (Bruker) with a magnetic field of 11.7 T. The sample was placed in a ZrO_2 rotor with an outer diameter of 4, 2.5, or 1.3 mm, which was mounted in a commercial MAS probe (Bruker) under inert conditions. The rotor was spun at a rotation frequency of 10, 20, or 50 kHz. The experimental data were analyzed with the aid of device-specific software.

4.4.7. EDX measurements

The P/N atomic ratios of the samples were analyzed by energy-dispersive X-ray spectroscopy. A carbon-coated sample (BAL-TEC MED 020, Bal Tec AG) was examined with a JSM-6500 F scanning electron microscope (SEM) with a maximum acceleration voltage of 30 kV (JEOL, Tokyo, Japan) for β-$Li_{10}P_4N_{10}$ and $Li_{13}P_4N_{10}Cl_3$, and an FEI Helios G3 UC SEM (field-emission gun, acceleration voltage 30 kV) for $Li_{13}P_4N_{10}Br_3$. Qualitative and semiquantitative elemental analyses were performed by means of an energy-dispersive spectrometer (Model 7418, Oxford Instruments, Abingdon, United Kingdom) and analyzed with INCA software.[63]

4.4.8. Fourier-transform infrared (FTIR) spectroscopy

Infrared spectroscopic measurements were carried out on a Bruker FTIR-IFS 66v/S spectrometer. The sample was mixed with KBr in a glove box and cold-pressed into a pellet (Ø = 12 mm) prior to measurement in the range 400–4000 cm^{-1}. The data were evaluated with OPUS software.[64]

4.4.9. Conductivity measurements

Electrical conductivities were measured by AC impedance spectroscopy. $Li_{13}P_4N_{10}Cl_3$ was cold-pressed into a dense pellet (Ø = 10 mm, d = 1.0 mm) and coated with thin-film Au electrodes (150 nm thickness) by thermal evaporation (Ø = 8 mm, cell constant = 0.20 cm^{-1}). Electrical impedance analysis (EIS) was conducted in the temperature range 25–85 °C using a frequency response analyzer (BioLogic SP-300) with a frequency range of 7 MHz to 10 mHz and an amplitude of 50 mV. $Li_{10}P_4N_{10}$ and $Li_{13}P_4N_{10}Br_3$ were examined in a custom-built hot-press set-up.[65] Powders of $Li_{10}P_4N_{10}$ and $Li_{13}P_4N_{10}Br_3$ were pressed at 1.5 t into dense pellets (Ø = 12 mm) with a thickness of 1.0 mm (cell constant 0.062 cm^{-1}) or 0.81 mm (cell constant 0.073 cm^{-1}), respectively. EIS was conducted in the temperature range 25–200 °C using a frequency response analyzer (BioLogic SP-150) with a frequency range of 1 MHz to 10 Hz and amplitude of 20 mV. As the resistance of $Li_{10}P_4N_{10}$ increases with time at above 45 °C, prior to data collection it was heated at 200 °C until no further changes in resistance could be observed.

4.4.10. XPS measurements

X-ray photoelectron spectroscopy (XPS) measurements were performed using a PHI Versaprobe II scanning ESCA microprobe (Physical Electronics) with a monochromated $Al_{K\alpha}$ X-ray source (beam diameter 200 µm, X-ray power 50 W). Stepwise *in situ* lithium deposition was carried out using the built-in argon ion gun with a deposition step time of 3 min, as described previously.[66] Sample handling and transfer to the XPS chamber were performed under inert gas atmosphere (Ar). The pass energy of the analyzer was set to 49.5 eV and the internal charge neutralization system was used. During the measurements, the chamber pressure was around 10^{-7} Pa. Spectral data were evaluated using the CasaXPS software package. Charge correction of the binding energy scale was carried out relative to the adventitious carbon signal (284.8 eV).

4.5. Acknowledgements

We would like to thank Thomas Miller for high-temperature powder diffraction measurements, Christian Minke for EDX, SEM, and solid-state MAS NMR measurements, Marion Sokoll for IR measurements, and Dr. Thomas Bräuniger and Otto Zeman (all at Department of Chemistry of LMU Munich) for helpful discussions concerning the solid-state MAS NMR spectroscopy. We gratefully acknowledge financial support granted by the Fonds der Chemischen Industrie (FCI), the Deutsche Forschungsgemeinschaft (DFG) (project no. SCHN377/18-1), and STORE-E (LOEWE program funded by the State of Hessen).

4.6. References

[1] J. E. Lowther, in *Handbook of Ceramic Hard Materials*, Wiley-VCH Verlag GmbH, Weinheim, Germany, **2008**, pp. 253–270.

[2] E. Horvath-Bordon, R. Riedel, A. Zerr, P. F. McMillan, G. Auffermann, Y. Prots, W. Bronger, R. Kniep, P. Kroll, *Chem. Soc. Rev.* **2006**, *35*, 987–1014.

[3] A. Rabenau, *Solid State Ionics* **1982**, *6*, 277–293.

[4] S. Zhao, Z. Fu, Q. Qin, *Thin Solid Films* **2002**, *415*, 108–113.

[5] P. Pust, P. J. Schmidt, W. Schnick, *Nat. Mater.* **2015**, *14*, 454–458.

[6] W. Schnick, *Angew. Chem. Int. Ed. Engl.* **1993**, *32*, 806–818; *Angew. Chem.* **1993**, *105*, 846–858.

[7] S. Horstmann, E. Irran, W. Schnick, *Angew. Chem. Int. Ed. Engl.* **1997**, *36*, 1873–1875; *Angew. Chem.* **1997**, *109*, 1938–1940.

[8] W. Schnick, J. Lücke, F. Krumeich, W. Schnick, *Chem. Mater.* **1996**, *8*, 281–286.

[9] D. Baumann, W. Schnick, *Inorg. Chem.* **2014**, *53*, 7977–7982.

[10] S. Horstmann, E. Irran, W. Schnick, *Angew. Chem. Int. Ed. Engl.* **1997**, *36*, 1992–1994; *Angew. Chem.* **1997**, *109*, 2085–2087.

[11] A. Marchuk, W. Schnick, *Angew. Chem. Int. Ed.* **2015**, *54*, 2383–2387; *Angew. Chem.* **2015**, *127*, 2413–2417.

[12] F. Karau, W. Schnick, *Angew. Chem. Int. Ed.* **2006**, *45*, 4505–4508; *Angew. Chem.* **2006**, *118*, 4617–4620.

[13] D. Baumann, S. J. Sedlmaier, W. Schnick, *Angew. Chem. Int. Ed.* **2012**, *51*, 4707–4709; *Angew. Chem.* **2012**, *124*, 4785–4787.

[14] S. D. Kloß, W. Schnick, *Angew. Chem. Int. Ed.* **2015**, *54*, 11250–11253: *Angew. Chem.* **2015**, *127*, 11402–11405.

[15] W. Schnick, J. Lücke, *Z. Anorg. Allg. Chem.* **1992**, *610*, 121–126.

[16] W. Schnick, J. Lücke, *Angew. Chem. Int. Ed. Engl.* **1992**, *31*, 213–215; *Angew. Chem.* **1992**, *104*, 208–209.

[17] V. Schulz-Coulon, W. Schnick, *Angew. Chem. Int. Ed. Engl.* **1993**, *32*, 280–281; *Angew. Chem.* **1993**, *105*, 308–309.

[18] V. Schulz-Coulon, W. Schnick, *Z. Anorg. Allg. Chem.* **1997**, *623*, 69–74.

[19] S. J. Sedlmaier, M. Döblinger, O. Oeckler, J. Weber, J. Schmedt auf der Günne, W. Schnick, *J. Am. Chem. Soc.* **2011**, *133*, 12069–12078.

[20] W. Schnick, J. Lücke, *Z. Anorg. Allg. Chem.* **1990**, *588*, 19–25.

[21] W. Schnick, U. Berger, *Angew. Chem. Int. Ed. Engl.* **1991**, *30*, 830–831; *Angew. Chem.* **1991**, *103*, 857–858.

[22] E.-M. Bertschler, R. Niklaus, W. Schnick, *Chem. Eur. J.* **2017**, *23*, 9592–9599.

[23] W. Schnick, J. Luecke, *J. Solid State Chem.* **1990**, *87*, 101–106.

[24] E.-M. Bertschler, C. Dietrich, J. Janek, W. Schnick, *Chem. Eur. J.* **2017**, *23*, 2185–2191.

[25] F. Liebau, *Structural Chemistry of Silicates*, Springer-Verlag Berlin, **1985**.

[26] The term dreier (vierer) ring was coined by Liebau and is derived from the German word "drei" ("vier"). A *dreier* (*vierer*)-ring comprised three (four) tetrahedra centers.

[27] Y. Zhu, X. He, Y. Mo, *Adv. Sci.* **2017**, 1600517.

[28] S. Wenzel, S. J. Sedlmaier, C. Dietrich, W. G. Zeier, J. Janek, *Solid State Ionics* **2017**, http://dx.doi.org/10.1016/j.ssi.2017.07.005.

[29] W. Schnick, J. Luecke, *Solid State Ionics* **1990**, *38*, 271–273.

[30] Y. Wang, W. D. Richards, S. P. Ong, L. J. Miara, J. C. Kim, Y. Mo, G. Ceder, *Nat. Mater.* **2015**, *14*, 1026–1031.

[31] M. A. Kraft, S. P. Culver, M. Calderon, F. Böcher, T. Krauskopf, A. Senyshyn, C. Dietrich, A. Zevalkink, J. Janek, W. G. Zeier, *J. Am. Chem. Soc.* **2017**, *139*, 10909–10918.

[32] U. Berger, *Diploma Thesis*, $Li_{10}P_4N_{10}$: Reindarstellung und Kristallstruktur eines neuen Lithium-Phosphor(V)–nitrids, University of Bonn, **1991**.

[33] E.-M. Bertschler, T. Bräuniger, C. Dietrich, J. Janek, W. Schnick, *Angew. Chem. Int. Ed.* **2017**, *56*, 4806–4809; *Angew. Chem.* **2017**, *129*, 4884–4887.

[34] Further details of the crystal structure investigation can be obtained from the Fachinformations-Zentrum Karlsruhe, 76344 Eggenstein- Leopoldshafen, Germany (fax: (+49)7247--808-666; e-Mail: crysdata@fiz-Karlsruhe.de) on quoting the deposition number CSD-433514 (β-$Li_{10}P_4N_{10}$), CSD-433515 ($Li_{13}P_4N_{10}Cl_3$) and CSD-433516 ($Li_{13}P_4N_{10}Br_3$).

[35] K. Kirakci, S. Cordier, C. Perrin, *Z. Anorg. Allg. Chem.* **2005**, *631*, 411–416.

[36] S. J. Sedlmaier, M. Eberspächer, W. Schnick, *Z. Anorg. Allg. Chem.* **2011**, *637*, 362–367.

[37] D. Balzar, *Int. Union Crystallogr. Monogr. Crystallogr.* **1999**, *10*, 94–126.

[38] A. Leineweber, E. J. Mittemeijer, *Z. Kristallogr. Suppl.* **2006**, *23*, 117–122.

[39] L. Velterop, R. Delhez, T. H. de Keijser, E. J. Mittemeijer, D. Reefman, *J. Appl. Crystallogr.* **2000**, *33*, 296–306.

[40] E. J. Mittemeijer, R. Delhez, *J. Appl. Phys.* **1978**, *49*, 3875–3878.

[41] R. Delhez, T. H. Keijser, E. J. Mittemeijer, *Fresenius Z. Anal. Chem.* **1982**, *312*, 1–16.

[42] A. Leineweber, *Z. Kristallogr.* **2011**, *226*, 905–923.

[43] A. Marchuk, V. R. Celinski, J. Schmedt auf der Günne, W. Schnick, *Chem. Eur. J.* **2015**, *21*, 5836–5842.

[44] V. A. Blatov, *Cryst. Rev.* **2004**, *10*, 249–318.

[45] N. Anurova, V. Blatov, G. Ilyushin, O. Blatova, A. Ivanovschitz, L. Demyanets, *Solid State Ionics* **2008**, *179*, 2248–2254.

[46] G. M. Sheldrick, *SHELXS*, University of Göttingen, **1997**.

[47] V. A. Blatov, A. P. Shevchenko, V. N. Serezhkin, *J. Appl. Crystallogr.* **1999**, *32*, 377–377.

[48] T. Lapp, *Solid State Ionics* **1983**, *11*, 97–103.

[49] P. R. Rayavarapu, N. Sharma, V. K. Peterson, S. Adams, *J. Solid State Electrochem.* **2012**, *16*, 1807–1813.

[50] S.-T. Kong, H.-J. Deiseroth, C. Reiner, Ö. Gün, E. Neumann, C. Ritter, D. Zahn, *Chem. Eur. J.* **2010**, *16*, 2198–2206.

[51] H.-J. Deiseroth, J. Maier, K. Weichert, V. Nickel, S.-T. Kong, C. Reiner, *Z. Anorg. Allg. Chem.* **2011**, *637*, 1287–1294.

[52] H.-J. Deiseroth, S.-T. Kong, H. Eckert, J. Vannahme, C. Reiner, T. Zaiß, M. Schlosser, *Angew. Chem. Int. Ed.* **2008**, *47*, 755–758; *Angew. Chem.* **2008**, *120*, 767–770.

[53] A. Schwöbel, R. Hausbrand, W. Jaegermann, *Solid State Ionics* **2015**, *273*, 51–54.

[54] S. Wenzel, D. A. Weber, T. Leichtweiss, M. R. Busche, J. Sann, J. Janek, *Solid State Ionics* **2016**, *286*, 24–33.

[55] A. Stock, H. Grüneberg, *Ber. Dtsch. Chem. Ges.* **1907**, *40*, 2573–2578.

[56] A. Coelho, *TOPAS-Academic* **2007**.

[57] A. A. Coelho, *J. Appl. Crystallogr.* **2003**, *36*, 86.

[58] G. Oszlányi, A. Sütö, *Acta Crystallogr., Sect. A Found. Crystallogr.* **2004**, *60*, 134–141.

[59] G. Oszlányi, A. Sütö, *Acta Crystallogr., Sect. A Found. Crystallogr.* **2008**, *64*, 123–134.

[60] A. A. Coelho, *Acta Crystallogr., Sect. A Found. Crystallogr.* **2007**, *63*, 400.

[61] R. W. Cheary, A. A. Coelho, *J. Appl. Crystallogr.* **1992**, *25*, 109–121.

[62] R. W. Cheary, A. A. Coelho, *J. Res. Natl. Inst. Stand. Technol.* **2007**, *109*, 1–25.

[63] *INCA, Version 4.02*, OXFORD Instruments.

[64] *OPUS/IR*, Bruker Analytik GmbH, **2000**.

[65] M. R. Busche, D. A. Weber, Y. Schneider, C. Dietrich, S. Wenzel, T. Leichtweiss, D. Schröder, W. Zhang, H. Weigand, D. Walter, et al., *Chem. Mater.* **2016**, *28*, 6152–6165.

[66] S. Wenzel, T. Leichtweiss, D. Krüger, J. Sann, J. Janek, *Solid State Ionics* **2015**, *278*, 98–105.

5. Reversible Polymerization of Adamantane-type $[P_4N_{10}]^{10-}$ Anions to Honeycomb-type $[P_2N_5]^{5-}$ Layers under High-Pressure

Eva-Maria Bertschler, Robin Niklaus, Wolfgang Schnick

published in: *Chem. Eur. J.* **2018**, *24*, 736–742. DOI: 10.1002/chem.201704975

Abstract

The high-pressure polymorph $Li_5P_2N_5$ of $Li_{10}P_4N_{10}$ (= "2 $Li_5P_2N_5$") was synthesized by high-pressure/high-temperature reaction of $LiPN_2$ and Li_7PN_4 or β-$Li_{10}P_4N_{10}$ at 9 GPa, using the Li_3N self-flux method in a Walker-type multianvil assembly. $Li_5P_2N_5$ is the first lithium nitridophosphate with a layered structure and is made up of corner sharing PN_4 tetrahedra forming a corrugated honeycomb-type layer of linked *sechser*-rings in chair conformation. The arrangement of the P atoms is analogous to that of black phosphorus. The structure was elucidated from single-crystal X-ray data. To confirm the structure Rietveld refinement, ^{6}Li, ^{7}Li and ^{31}P solid-state NMR spectroscopy were conducted. To corroborate $Li_5P_2N_5$ as the corresponding high-pressure polymorph of β-$Li_{10}P_4N_{10}$ DFT calculations and temperature dependent X-ray powder diffraction were carried out. DFT calculations estimated the transition pressure to 6.5 GPa (without accounting for temperature), which is in line with the synthesis pressure.

5.1. Introduction

Nitridophosphates are closely related to silicates, but they offer a broader structural diversity, due to the possibility of triply bridging N atoms.[1-4] The tetrahedral PN_4 group, the primary building unit of nitridophosphates, allows various linking patterns and leads to an intriguing structural variability and interesting properties.[5] Representatives in this compound class include nitridic zeolites (NPO, NPT),[6-8] clathrates ($P_4N_4(HN)_4(NH_3)$),[9] glassy compounds (Li–Ca–P–N),[10, 11] luminescent materials ($Ba_3P_5N_{10}X$:Eu^{2+} (X=Cl, Br, I) or MP_2N_4:Eu^{2+} (M=Ca, Sr, Ba)),[12-14] or lithium ion conductors ("*LiPON*").[15]

The discovery of new nitridophosphates was in particular facilitated by the use of high-pressure techniques.[16] For example the high-pressure polymorph γ-P_3N_5, where remarkable hardness was observed, is made up of square PN_5 pyramids beside PN_4 tetrahedra.[17, 18] Furthermore different polymorphs of silica analogous PON and isoelectronic PN(HN) were characterized.[19-25] Recently, we established different approaches to obtain sufficiently large crystals for structure determination. By addition of the mineralizer NH_4Cl, the crystallinity of nitridophosphates increases and compounds like β- and γ-$P_4N_6(NH)$[16, 26] have been structurally elucidated.[25] To gain access to rare-earth-metal nitridophosphates high-pressure metathesis was established.[27] A third approach to grow single crystals by application of high-pressure is the Li_3N flux/self-flux method.[28] By this method we were able to structurally characterize lithium nitridophosphates with unprecedented topologies. Recently, we described different linking patterns of corner sharing PN_4 tetrahedra which form various P/N anions (Figure1) in a matrix of Li^+ ions. Yet, lithium nitridophosphates with non-condensed PN_4 tetrahedra (a), rings (b), annelated ring-systems (c), cages (d), chains (e), or even three-dimensional network structures have been found (f).

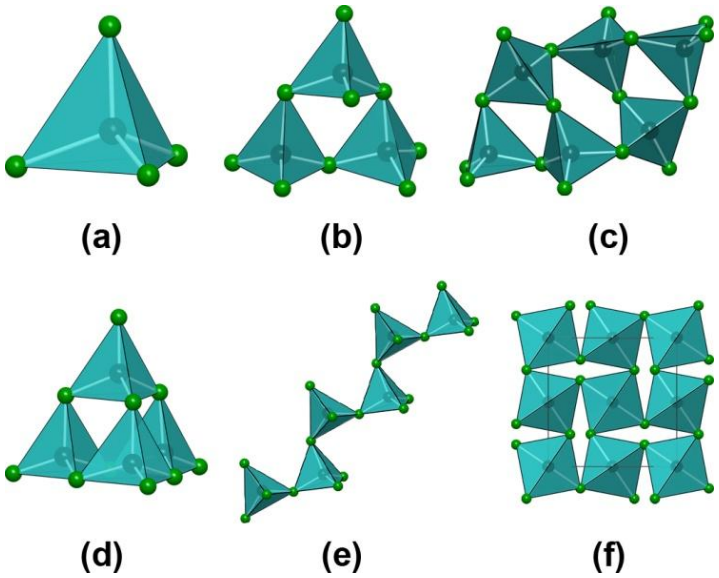

Figure 1. Known linking patterns of PN_4 tetrahedra in lithium nitridophosphates. (a) Isolated PN_4 tetrahedra in Li_7PN_4. (b) *Dreier*-rings in $Li_{12}P_3N_9$. (c) An annulated ring-system in $Li_{18}P_6N_{16}$. (d) A cage like structure in α- and β-$Li_{10}P_4N_{10}$. (e) *Zweier*-chains in Li_4PN_3. (f) A three-dimensional network structure in $LiPN_2$.[5, 28-33] (P: black, N: green).

Li_7PN_4 has the lowest atomic ratio P/N (Figure 1 a).[29] In $Li_{12}P_3N_9$ $[P_3N_9]^{12-}$ units form *dreier*-rings of PN_4 tetrahedra (Figure 1 b).[30, 34, 35] $Li_{18}P_6N_{16}$ is composed of one *vierer*-ring with two annelated *dreier*-rings (Figure 1 c).[28] In α- and β-$Li_{10}P_4N_{10}$ a cage like structure occurs with adamantane like $[P_4N_{10}]^{10-}$ T2 supertetrahedra, which are isoelectronic to $[P_4O_{10}]$ (Figure1 d). β-$Li_{10}P_4N_{10}$ transforms reversibly to the α-polymorph at about 80 °C and irreversibly at about 600 °C. Both polymorphs differ in distortion of the polyhedra.[31, 32] Li_4PN_3 is the high-pressure polymorph of $Li_{12}P_3N_9$ (6 GPa and 820 °C) and represents the first chain like structure in lithium nitridophosphates. It transforms back to $Li_{12}P_3N_9$ at 650 °C (Figure 1 e).[30] $LiPN_2$ is made up of a three-dimensional network structure with corner sharing PN_4 tetrahedra isoelectronic to SiO_2 (Figure 1 f).[33]

In this work we report on synthesis and structural investigation of the high-pressure polymorph $Li_5P_2N_5$, which represents the first layered structure in lithium nitridophosphates. With the Li_3N self-flux method we were able to grow crystals that were sufficiently large for single-crystal structure determination. Furthermore DFT calculations were performed to corroborate the observed high-pressure phase transition.

5.2. Results and Discussion

5.2.2. Synthesis

According to Equation (1) and Equation (2) $Li_5P_2N_5$ was synthesized by the Li_3N self-flux method[28] under high-pressure/high-temperature conditions. All compounds were handled under argon atmosphere to avoid hydrolysis.

$$\beta\text{-}Li_{10}P_4N_{10} \rightarrow 2\ Li_5P_2N_5 \quad (1)$$

$$3\ LiPN_2 + Li_7PN_4 \rightarrow 2\ Li_5P_2N_5 \quad (2)$$

According to Equation (1) $Li_5P_2N_5$ was made from the low temperature polymorph β-$Li_{10}P_4N_{10}$ at 9 GPa and 1000 °C using a Walker-type multianvil assembly.[36-40] $Li_5P_2N_5$ was obtained together with $LiPN_2$ and unknown side-phases. Synthesis at 7 or 8 GPa and 800 °C leads to higher amount of unknown side phases. Reaction of equimolar amounts of $LiPN_2$ and Li_7PN_4 (excess of Li_7PN_4) at 9 GPa and 1000 °C leads to in situ formation of Li_3N (self-flux), which is beneficial for the growth of single crystals. Due to the better crystal quality resulting from this treatment, a single-crystal of this approach was used for structure analysis. $Li_5P_2N_5$ was obtained together with Li_4PN_3 and unknown side phases. As we described in previous work, the in situ formed Li_3N may evaporate later on, or may react with the *h*-BN crucible.[28] Detailed information on the synthesis is given in the Experimental section.

5.2.3. Crystal Structure

The crystal structure of $Li_5P_2N_5$ was solved and refined from single-crystal X-ray diffraction data. $Li_5P_2N_5$ crystallizes as colorless platelets in monoclinic space group *C*2/*c* (no. 15) with 12 formula units per unit cell (Table 1).[41]

It was refined as a two component twin with a translation matrix of [1 $\bar{1}$ 0.33 / 0 $\bar{1}$ 0 / 0 0 $\bar{1}$]. The relatively high residual electron density of 1.53 e $Å^{-3}$ is due to the mobility and disorder of the Li^+ ions. The Fourier map shows clearly that the Li^+ ions appear as smeared and are not localized on discrete sites (Supporting Information, Figure S2). An anisotropic refinement of the Li positions leads to rather large ellipsoids, which also indicates a lack of localization.

Table 1. Crystallographic Data of $Li_5P_2N_5$.

	$Li_5P_2N_5$
crystal size [mm^3]	0.01× 0.03× 0.03
formula mass [g mol^{-1}]	166.69
crystal system, space group	monoclinic, *C* 2/*c* (no. 15)
twin	two component twin [1 $\bar{1}$ 0.33 / 0 $\bar{1}$ 0 / 0 0 $\bar{1}$]
BASF	0.479(4)
a [Å]	14.770(3)
b [Å]	17.850(4)
c [Å]	4.8600(10)
β [°]	93.11(3)
cell volume [$Å^3$]	1279.4(5)
formula units/ cell	12
calculated density [g cm^{-3}]	2.596
F(000)	960
diffractometer	Bruker D8 Venture
temperature [°C]	293(2)
radiation, monochromator	$Mo_{K\alpha}$ (λ=0.71073 Å), Goebel mirror
absorption correction	multi scan
θ range [°]	2.28–27.46
number of collected data	7667
number of unique data	2864
number of unique data with $I \geq 2\sigma(I)$	2320
refined parameters	127
GooF	1.057
R indices [$F_0^2 \geq 2\sigma(F_0^2)$]	R_1= 0.0547, wR_2= 0.1280
R indices (all data)	R_1= 0.0705, wR_2= 0.1369
max/min res. electron density [e $Å^{-3}$]	1.53/−0.81
R_{int}/ R_σ for component 1	0.0252/0.0318
R_σ (both components)	0.0423

$w=1/[\sigma^2(F_o^2)+(0.0513P)^2+10.9661P]$ where $P=(F_o^2+2F_c^2)/3$.

The P/N substructure is made up of corner sharing PN_4 tetrahedra forming a corrugated layer of linked *sechser*-rings in chair conformation (Figure 2). The arrangement of the P atoms is analogous to that of black phosphorus.[42] The unit cell is made up of two layers (layer 1 (green) and 2 (orange)) perpendicular to *a*. Both layers can be transformed into each other by rotation around 180°.

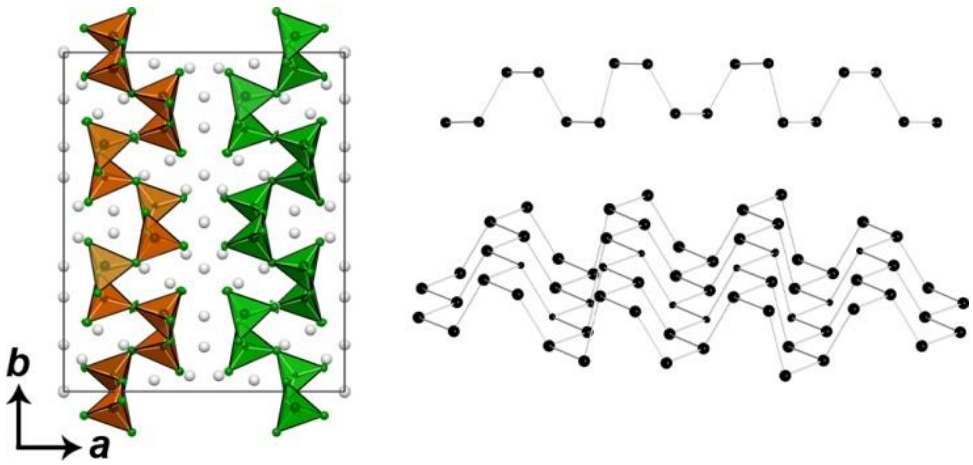

Figure 2. Left: Unit cell of $Li_5P_2N_5$, view along *c*. The anisotropic displacement ellipsoids are depicted at 90 % probability. Right top: P atoms of layer 1 (green) viewing along *c*. Right bottom: P atoms of layer 1 viewing along *hkl* = (5 0 9). (P: black, N: green, Li: gray).

The framework anion topology was determined by the TOPOS software. It is represented by the point symbol 6^3. Thus, the network can be described as an uninodal three-connected net with the *hcb* (honeycomb) topology (Shubnikov hexagonal plane), which is shown in Figure 3.[43-45]

A related polymerization from an adamantane-type structure (P_4O_{10})[46] to layers (o'-P_2O_5)[47] was observed in phosphorous(V) oxide at 360 °C (2–3 weeks). The layers in o'-P_2O_5 are made up of corner sharing PO_4 tetrahedra forming a corrugated layer of linked *sechser*-rings in boat conformation with *hcb* topology as well.[47] Hence, the polymerization products $Li_5P_2N_5$ and o'-P_2O_5 only differ by the conformation (chair/boat) of the *sechser*-rings.

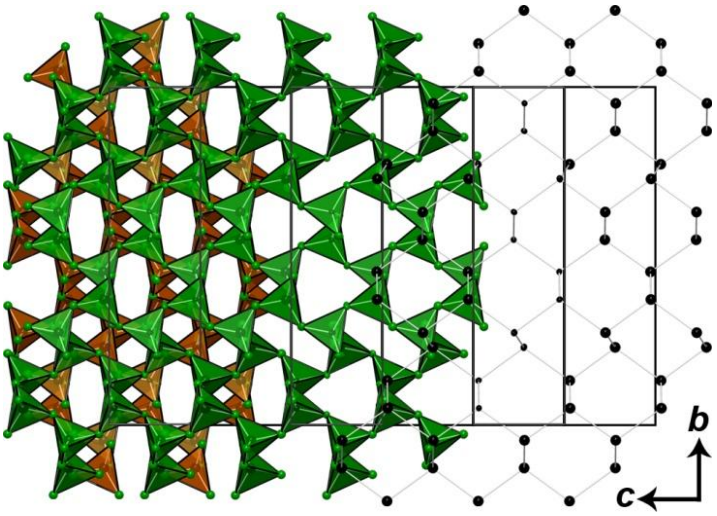

Figure 3. Unit cell of $Li_5P_2N_5$ viewing along *a*. Li is omitted for clarity. The anisotropic displacement ellipsoids are depicted at 90 % probability. From left to right: Layer 1 (green) and 2 (orange); Layer 1 (green); P atoms of layer 1. (P: black, N: green).

The P−N distances vary from 1.59 to 1.70 Å. Similar with other nitridophosphates, the bond lengths to terminal nitrogen atoms of PN_4 tetrahedra are shorter than those to bridging ones.[28, 30, 48] These P−N distances are in accordance with values found in other lithium nitridophosphates.[5, 28-33] The P/N layers are surrounded by Li^+ ions, which are coordinated by N with coordination numbers 4, 5, and 6. The different polyhedra are sharing edges or corners. The shortest Li−Li distance is 1.94 Å (Li8-Li9). This value corresponds with those of other Li containing compounds.[49] The distortion of the Li-N polyhedra in combination with the smeared electron density suggest a mobility of the Li^+ ions.

5.2.4. Structural analysis of possible lithium migration pathways

To confirm the possible movement of the Li^+ ions, possible voids and migration pathways were analyzed with TOPOS.[50-52] Calculating the Voronoi–Dirichlet polyhedra leads to possible migration pathways. The migration pathways of the Li positions build two different layers along *c* (Figure 4: red and blue). Both layers can be transformed into each other by a shift along *b*. According to these calculations $Li_5P_2N_5$ seems to be a promising candidate for Li^+ ion conductivity, due to the defined layers in which the Li^+ ions can migrate.

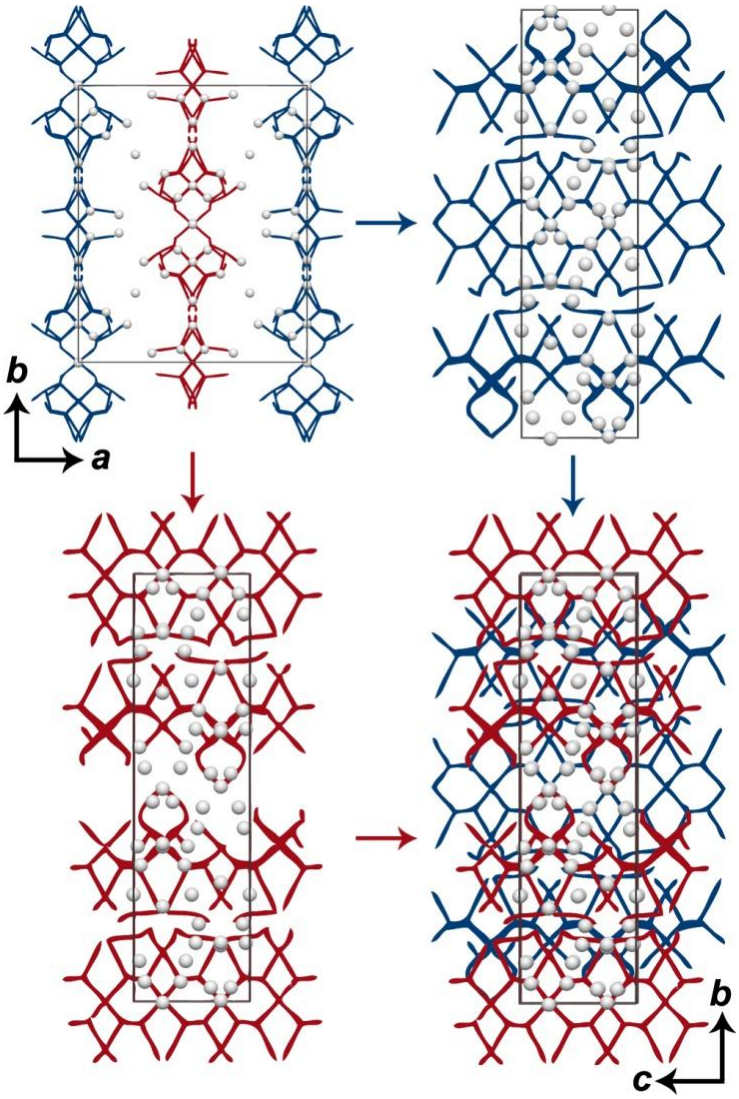

Figure 4. Calculated possible Li^+ pathways of different layers (red and blue) according to the voids in the structure and unit cell of $Li_5P_2N_5$. (Li: gray).

Figure 4 (left, top) shows that there is one Li position (Li10) which indicates no movement. Li10 is placed in the middle of a *sechser*-ring and is coordinated by 6 N atoms building an octahedron (Figure 5).

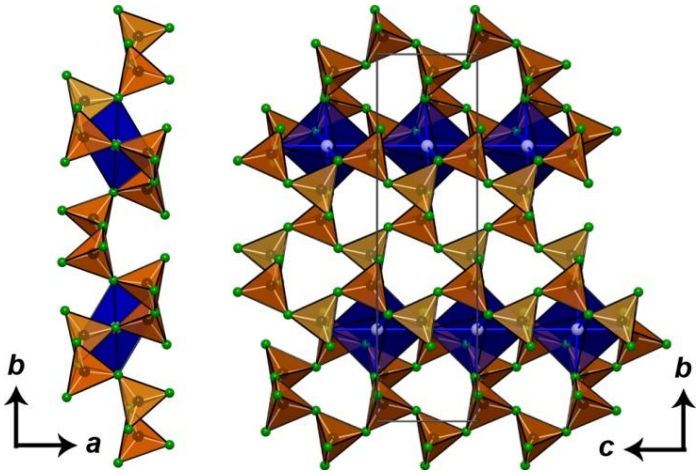

Figure 5. Layer 2 of $Li_5P_2N_5$ together with the Li position Li10, which forms an octahedron (blue) in the middle *sechser*-rings. (P: black, N: green, Li: gray).

5.2.5. Solid-state NMR spectroscopy

^{31}P, ^{7}Li, and ^{6}Li NMR spectroscopy of $Li_5P_2N_5$ were performed to corroborate the crystal structure model (Supporting Information, Figure S4–S6). The ^{31}P spectrum shows one strong narrow resonance at 5.22 ppm and four smaller and broader ones at 19.42, 8.98, −7.55, and −14.36 ppm, which we assign to side phases. $Li_5P_2N_5$ has three crystallographically independent P sites, which all exhibit very similar bonding lengths to N (Supporting Information, Table S3) and therefore the same chemical shift at 5.22 ppm. This effect was already observed in $Li_{12}P_3N_9$.[30] The side phase $LiPN_2$ exhibits one strong resonance at 5.68 ppm, which corresponds to one crystallographically independent P site. The ^{6}Li NMR spectrum shows two strong resonances at 5.43 and 1.87 ppm. The resonance at 1.87 ppm exhibits a shoulder. Due to the small shift differences of the signals, no differentiation of the 9 crystallographically independent sites can be achieved. But the three signals (including the shoulder) can be assigned to the three different coordination numbers of Li that occur in $Li_5P_2N_5$. The side phase $LiPN_2$ shows one resonance at 1.64 ppm. The ^{7}Li NMR spectrum shows two overlapping signals at 4.9 and 1.7 ppm. Due to the small chemical differences of the Li signals and the side phases (among others $LiPN_2$: 1.66 ppm), no differentiation of the phases and the crystallographically independent sites can be achieved.

5.2.6. Chemical analysis (EDX) FTIR-spectroscopy, powder diffraction

EDX measurements were carried out to determine the elemental composition of the product. Besides P and N only traces of O were found, which can be explained by surface hydrolysis of the sample during contact with air (Supporting Information, Table S6). The determined atomic ratio P/N is in agreement with the results from the crystal structure analysis ($Li_5P_2N_5$: P/N=0.4).

To prove the absence of hydrogen FTIR spectroscopy (cold-pressed KBr pellet) was performed (Supporting Information, Figure S8). The spectrum shows the characteristic PN framework vibrations between 400 and 1500 cm^{-1}. A weak signal in the region around 3000 cm^{-1} (N−H) can be explained by slight hydrolysis of the sample during preparation.

Phase purity of the product was determined by powder diffraction (Supporting Information, Figure S3). Beside the main phase $Li_5P_2N_5$, $LiPN_2$, and *h*-BN (crucible) were detected, together with further unknown side phases. Rietveld refinement confirms the determined crystal structure (Supporting Information, Table S5).

5.2.7. Thermal stability

Temperature dependent powder X-ray diffraction patterns were recorded between room temperature and 900 °C to corroborate that $Li_5P_2N_5$ is a high-pressure polymorph of β-$Li_{10}P_4N_{10}$. Figure 6 shows that, at ambient pressure, $Li_5P_2N_5$ transforms back to the ambient pressure polymorph at 700 °C.

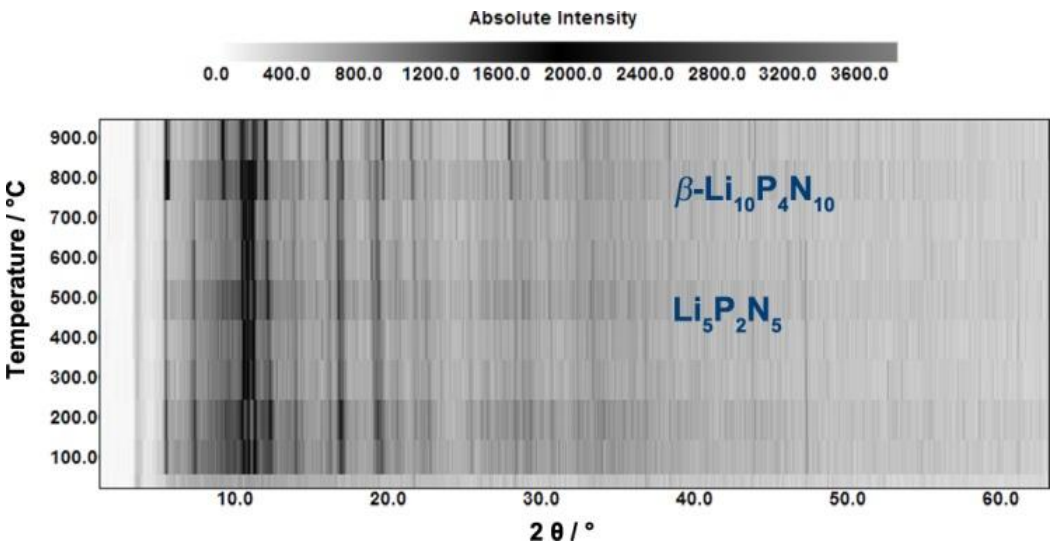

Figure 6. Temperature-dependent powder X-ray diffraction data for $Li_5P_2N_5$ under ambient pressure.

5.2.8. Comparison of the density

According to Le Chatelier, the density for high-pressure polymorphs is higher than that of the corresponding low-pressure polymorphs. This principle is also adaptable to lithium nitridophosphates. The calculated density of $Li_5P_2N_5$ (2.596 g cm^{-3}) is about 9.5 % higher than that of β-$Li_{10}P_4N_{10}$ (2.350 g cm^{-3}). In $Li_{12}P_3N_9$ the polymerization of *dreier*-rings to chains leads

to a decrease of density of about 7 %. For this reaction a lower synthesis pressure (6 GPa) was necessary.[30] Both differences in density are similar to other high-pressure transformations of nitridophosphates, for example, $P_4N_6(NH)$ with 5 (α to β) and 16 % (β to γ).[16, 26, 53] In comparison the calculated density of o'-P_2O_5 (2.928 g cm^{-3}) is about 22 % higher than that of h-P_2O_5 (2.276 g cm^{-3}).[46, 47]

5.2.9. Density functional theory calculations

5.2.9.1. Volume pressure calculations

Due to the observed partial occupancy of one Li site (occupancy of 2/3) in β-$Li_{10}P_4N_{10}$ we constructed a charge neutral model with full Li occupancies (Supporting Information, Figure S10).

By means of structural relaxations for a variety of constant volume compressions and expansions (92 % to 105 % with 1 % steps (0.5 % steps around equilibrium); β-$Li_{10}P_4N_{10}$: 17 steps, $Li_5P_2N_5$: 18 steps) of the respective unit cells (maintaining the space group), experimental synthesis pressures were covered.

Figure 7 (top) shows the resulting energy–volume (EV) curves. β-$Li_{10}P_4N_{10}$ is energetically favored by 0.87 eV (84 kJ mol^{-1}) at ambient pressure. By fitting the EV curves according to the Murnaghan equation of state,[54] we obtained a bulk modulus of B=84.0 for β-$Li_{10}P_4N_{10}$ and B=96.4 GPa for $Li_5P_2N_5$. We calculated the enthalpy difference ΔH from the equation $H=E+pV$, while pressure p is obtained by a numerical differentiation of $p=\partial E/\partial V$.

Figure 7 (bottom) shows the relative enthalpy with respect to the presumed low pressure polymorph β-$Li_{10}P_4N_{10}$. The transition pressure from β-$Li_{10}P_4N_{10}$ to $Li_5P_2N_5$ can be estimated as 6.5 GPa without accounting for temperature (0 K). Consequently $Li_5P_2N_5$ is corroborated as high-pressure polymorph of β-$Li_{10}P_4N_{10}$. The observed synthesis pressure of 8 GPa is slightly increased with respect to the calculated reaction pressure, but $Li_5P_2N_5$ was also obtained as a side phase (small percentages) at reaction pressure of about 7 GPa.

The densities of β-$Li_{10}P_4N_{10}$ and $Li_5P_2N_5$ were calculated from the volume at the equilibrium (Figure 7 top) with respect to one formula unit of $Li_{10}P_4N_{10}$ (="2 $Li_5P_2N_5$"). The calculated densities (DFT) show a difference of about 10 % (β-$Li_{10}P_4N_{10}$: ρ=2.32 g cm^{-3}; $Li_5P_2N_5$: ρ=2.58 g cm^{-3}), which is in line with the densities calculated from X-ray measurements. These results corroborate $Li_5P_2N_5$ as the high-pressure polymorph.

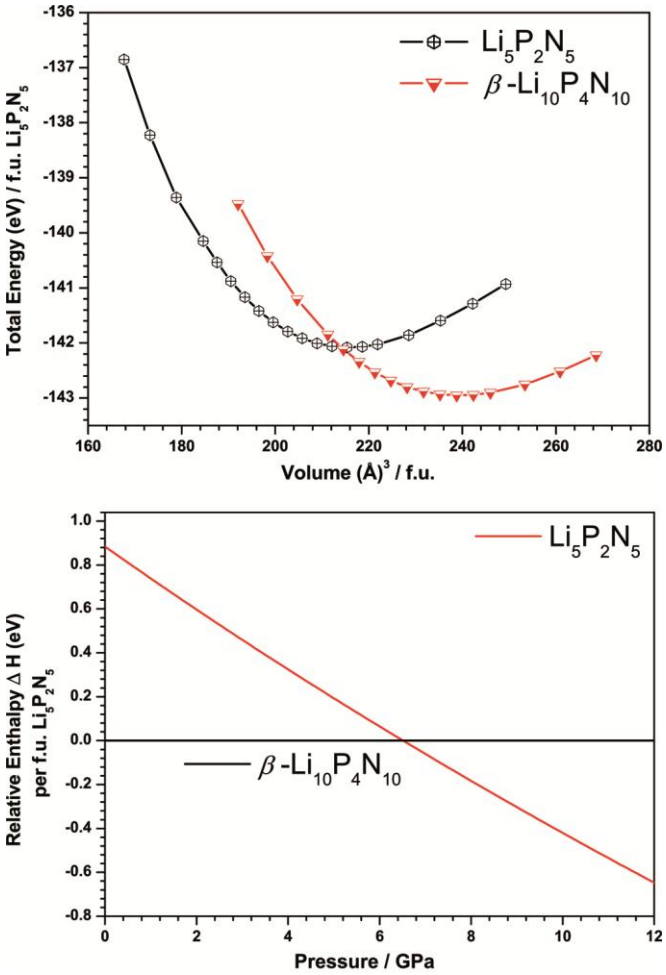

Figure 7. Top: Energy–volume diagram of β-$Li_{10}P_4N_{10}$ and $Li_5P_2N_5$. Each point constitutes one structural optimization at constant volume. Energy and volume are given per formula unit (f.u.) of $Li_5P_2N_5$. Bottom: Enthalpy–pressure diagram for the high-pressure phase transition of β-$Li_{10}P_4N_{10}$ to $Li_5P_2N_5$, obtained from a fit of the Murnaghan equation of state to the energy-volume diagram. The enthalpy is given per formula unit of $Li_5P_2N_5$ relative to β-$Li_{10}P_4N_{10}$.

5.2.9.2. Electronic band structure

$Li_5P_2N_5$ is an electronically insulating material with a wide electronic direct band-gap of 5.6 eV (at Γ) (Supporting Information, Figure S10). The band-gap for the low pressure polymorph β-$Li_{10}P_4N_{10}$ was estimated to 3.5 eV (Supporting Information, Figure S11). This trend was also found for $Li_{12}P_3N_9$ (indirect band-gap of 5 eV from Y to Γ) and its high-pressure polymorph Li_4PN_3 (direct band-gap of 6.1 eV at Γ).[30]

5.3. Conclusions

Herein we report on synthesis and thorough characterization of the first layered lithium nitridophosphate, namely $Li_5P_2N_5$. The high-pressure polymorph $Li_5P_2N_5$ can be prepared by solid-state reaction of $LiPN_2$ and Li_7PN_4 with the Li_3N self-flux method, or directly starting from the low pressure polymorph β-$Li_{10}P_4N_{10}$. By temperature dependent X-ray powder diffraction we showed that $Li_5P_2N_5$ is a high-pressure polymorph of β-$Li_{10}P_4N_{10}$, because it transforms back at about 700 °C. This result was also confirmed by DFT calculations. The adamantane like T2 supertetrahedra in β-$Li_{10}P_4N_{10}$ polymerizes to corrugated layers of corner sharing PN_4 tetrahedra, forming *sechser*-rings in chair conformation under high-pressure/high-temperature conditions. The framework topology can be described as a honeycomb-type (*hcb*) net.

Together with the recently published polymerization from *dreier*-rings in $Li_{12}P_3N_9$ to chains in Li_4PN_3, this shows that high-pressure/high-temperature synthesis is a powerful technique to obtain lithium nitridophosphates with unprecedented structures, which range from isolated ions (rings, ring-systems, cages) to chains, layers, and nets of corner-sharing PN_4 tetrahedra. With our work we are aiming for a better understanding of the synthesis conditions of these compounds, which will help to optimize materials with regard to their properties. Higher pressures could also make structures accessible with additional edge-sharing tetrahedra, PN_5 square-pyramids, or even PN_6 octahedra, which will lead to a plethora of yet unexplored structures and unexpected properties as well.

5.4. Experimental Section

5.4.2. Synthesis of Starting Materials

P_3N_5[1] was synthesized by reaction of P_4S_{10} (8 g, Sigma–Aldrich, 99 %) in a constant flow of ammonia (Air-Liquide, 99.999) at 850 °C (4 h). Before heating, the silica tube was saturated for 4 h with NH_3. By washing with water, ethanol, and acetone, any side products were eliminated. Powder X-ray diffraction and FTIR spectroscopy confirmed the phase purity of P_3N_5. All further steps were performed with strict exclusion of oxygen and moisture in an argon filled glove box (Unilab, MBraun, Garching, O_2<1 ppm, H_2O<0.1 ppm).

$LiPN_2$,[22] Li_7PN_4,[52] and β-$Li_{10}P_4N_{10}$[32] were synthesized by reaction of Li_3N (Rockwood Lithium, 94 %) and P_3N_5 ($LiPN_2$: molar ratio 1.2:1; Li_7PN_4: 7.2:1; β-$Li_{10}P_4N_{10}$: 2.8:1) in sealed silica ampoules under Ar atmosphere. The starting materials were ground and transferred into a Ta-crucible, which was placed in a dried silica tube. The sealed silica ampoule was heated for

90 h or 120 h in a tube furnace at 800, 600, or 680 °C. To eliminate side products, $LiPN_2$ was washed with diluted hydrochloric acid, water, and ethanol. Li_7PN_4 was not washed and was used with Li_3P as side phase. β-$Li_{10}P_4N_{10}$ was washed with dry ethanol to eliminate Li_3P as side phase. Powder X-ray diffraction and FTIR spectroscopy confirmed phase purity of the starting materials.

5.4.3. High-Pressure Synthesis of $Li_5P_2N_5$

$Li_5P_2N_5$ can be synthesized according to two different routes at high-pressure/high-temperature conditions, with a modified Walker-type multianvil module in combination with a 1000 t press (Voggenreiter, Mainleus, Germany).[36-40] The starting materials were ground under argon atmosphere and compactly packed in an *h*-BN crucible (Henze BNP GmbH, Kempten, Germany). The *h*-BN crucible was transferred into the specially prepared pressure medium (Cr_2O_3 doped (5 %) MgO-octahedra (Ceramic Substrates & Components, Isle of Wight, UK); edge length 18 mm (Eq. 4) or 14 mm (Eq. 5)). Then the octahedron was placed centrically in eight truncated WC cubes (Hawedia, Marklkofen, Germany, truncation length 11 mm (Eq. 1) or 8 mm (Eq. 2)) separated by pyrophyllite gaskets. Detailed information describing the complete setup is given in literature.[37, 38, 40] The assembly was compressed to 9 GPa at room temperature and then heated to about 1000 °C within 60 min (30 min for Eq. 2). Under these conditions, the sample was treated for 60 min and cooled down to room temperature within 60 min (200 min) and then decompressed. Both syntheses yielded a powder containing colorless single crystals. The product is sensitive to traces of air and moisture.

5.4.4. Single-Crystal X-ray Analysis

With a D8 Venture diffractometer, single-crystal X-ray diffraction was performed (Bruker, Billerica MA, USA) using $Mo_{K\alpha}$ radiation from a rotating anode source. During collection of the data two twin components were identified and indexed with CELL_NOW.[55] After integration with the Bruker SAINT Software package[56, 57] the final cell constants were calculated and the intensity data were corrected for absorption with TWINABS.[57, 58] Both twin components can be transformed into each other by [1 $\bar{1}$ 0.33 / 0 $\bar{1}$ 0 / 0 0 $\bar{1}$]. The data of component 1 (HKLF4) were averaged with Xprep[59] and the program package WinGX (SHELXS-97, SHELXL-97, PLATON)[59-63] was used for structure solution by direct methods, and refinement (see Table 1). For final structure refinement the refined structure of component 1 was handled taking to account both twin components (HKLF5). All P and N atoms were refined anisotropically. The Li atom positions were determined during structure refinement from difference Fourier maps. The crystal structure was visualized using DIAMOND.[64]

5.4.5. Powder X-ray Diffraction

X-ray powder diffraction was carried out with a STOE StadiP diffractometer (Stoe & Cie, Darmstadt, Germany) in parafocusing Debye–Scherrer geometry, to prove phase purity of the products. A Ge(111) single-crystal monochromator was used to select $Cu_{K\alpha 1}$ radiation. A Mythen 1 K Si-strip detector (Dectris, Baden, Switzerland) was used for detection of the diffracted radiation. For measurement the samples were enclosed in glass capillaries with 0.5 mm diameter (Hilgenberg, Malsfeld, Germany) under inert gas. Rietveld refinement was carried out using the program package TOPAS-Academic v4.1.[65] The background was handled with a shifted Chebychev function and the peak shapes were described using the fundamental parameters approach.[66, 67]

Temperature dependent powder X-ray diffraction data were recorded on a STOE StadiP diffractometer equipped with a graphite furnace using $Mo_{K\alpha 1}$ radiation (λ=0.70930 Å) in Debye–Scherrer geometry, an image plate position sensitive detector, and a Ge(111) monochromator. Data were collected every 25 °C starting from room temperature, up to 900 °C, with a heating rate of 5 °C min^{-1}.

5.4.6. Solid-State MAS (Magic Angle Spinning) NMR (Nuclear Magnetic Resonance) Methods

^{6}Li, ^{7}Li, and ^{31}P solid-state MAS NMR spectra of both polymorphs were recorded on a DSX Avance spectrometer (Bruker) with a magnetic field of 11.7 T. The sample was transferred into a ZrO_2 rotor with outer diameter of 2.5 mm ($LiPN_2$) and 1.3 mm ($Li_5P_2N_5$), which was mounted in a commercial MAS probe (Bruker) under inert conditions. The rotor was spun at a rotation frequency of 20 or 50 kHz, respectively. The experimental data were analyzed by device-specific software.

5.4.7. EDX Measurements

The atomic ratio P/N of the samples was analyzed by energy-dispersive X-ray spectroscopy. A carbon coated sample (BAL-TEC MED 020, Bal Tec AG) was examined with a FEI Helios G3 UC scanning electron microscope (SEM, field emission gun, acceleration voltage 30 kV). Qualitative and semiquantitative elemental analyses were executed by an energy dispersive spectrometer and analyzed by INCA.[68]

5.4.8. Fourier Transform Infrared (FTIR) Spectroscopy

Infrared spectroscopy measurements were carried out on a Bruker FTIR-IFS 66v/S spectrometer. Before measurement in the range of 400–4000 cm^{-1} the sample was mixed with KBr in a glove box and cold-pressed into a pellet (Ø=12 mm). The data were evaluated with OPUS.[69]

5.4.9. Computational Details

The structural relaxation of both of polymorphs were carried out with the Vienna ab initio simulation package (VASP).[70-72] Total energies of the unit cell were converged to 10^{-7} eV $atom^{-1}$ with residual atomic forces below 5×10^{-3} eV $Å^{-1}$. The exchange correlation was treated within the generalized gradient approximation (GGA) of Perdew, Burke, and Ernzerhof (PBE)[73, 74] and the projector-augmented-wave (PAW) method.[75, 76] A plane-wave cut-off of 535 eV was chosen for the calculations with a Brillouin zone sampling on a Γ-centered *k*-mesh of 6×6×3 (β-$Li_{10}P_4N_{10}$) and 4×4×11 ($Li_5P_2N_5$) respectively, produced from the method of Monkhorst and Pack.[77] Additional calculations were performed with the modified Becke–Johnson formalism (GGA-mbj)[78, 79] to treat the electronic band gaps.

5.5. Acknowledgements

We would like to thank Dr. Peter Mayer for single-crystal X-ray measurements, Thomas Miller for high-temperature powder diffraction measurements, Christian Minke for EDX, SEM, and solid-state MAS NMR measurements, Marion Sokoll for IR measurements, and Dr. Constantin Hoch for helpful discussion concerning the twinning of the single-crystal (all Department of Chemistry of LMU Munich). We gratefully acknowledge financial support granted by the Fonds der Chemischen Industrie (FCI), and the Deutsche Forschungsgemeinschaft (DFG), project SCHN377/18.

5.6. References

[1] A. Stock, H. Grüneberg, *Ber. Dtsch. Chem. Ges.* **1907**, *40*, 2573–2578.

[2] S. Horstmann, E. Irran, W. Schnick, *Angew. Chem. Int. Ed. Engl.* **1997**, *36*, 1873–1875; *Angew. Chem.* **1997**, *109*, 1938–1940.

[3] S. Horstmann, E. Irran, W. Schnick, *Z. Anorg. Allg. Chem.* **1998**, *624*, 620–628.

[4] S. Horstmann, E. Irran, W. Schnick, *Angew. Chem. Int. Ed. Engl.* **1997**, *36*, 1992–1994; *Angew. Chem.* **1997**, *109*, 2085–2087.

[5] W. Schnick, *Angew. Chem. Int. Ed. Engl.* **1993**, *32*, 806–818; *Angew. Chem.* **1993**, *105*, 846–858.

[6] S. Correll, O. Oeckler, N. Stock, W. Schnick, *Angew. Chem. Int. Ed.* **2003**, *42*, 3549–3552; *Angew. Chem.* **2003**, *115*, 3674–3677.

[7] S. Correll, N. Stock, O. Oeckler, J. Senker, T. Nilges, W. Schnick, *Z. Anorg. Allg. Chem.* **2004**, *630*, 2205–2217.

[8] S. J. Sedlmaier, M. Döblinger, O. Oeckler, J. Weber, J. Schmedt auf der Günne, W. Schnick, *J. Am. Chem. Soc.* **2011**, *133*, 12069–12078.

[9] F. Karau, W. Schnick, *Angew. Chem. Int. Ed.* **2006**, *45*, 4505–4508; *Angew. Chem.* **2006**, *118*, 4617–4620.

[10] T. Grande, S. Jacob, J. R. Holloway, P. F. McMillan, C. A. Angell, *J. Non-Cryst. Solids* **1995**, *184*, 151–154.

[11] E. Horvath-Bordon, R. Riedel, A. Zerr, P. F. McMillan, G. Auffermann, Y. Prots, W. Bronger, R. Kniep, P. Kroll, *Chem. Soc. Rev.* **2006**, *35*, 987–1014.

[12] A. Marchuk, W. Schnick, *Angew. Chem. Int. Ed.* **2015**, *54*, 2383–2387; *Angew. Chem.* **2015**, *127*, 2413–2417.

[13] A. Marchuk, S. Wendl, N. Imamovic, F. Tambornino, D. Wiechert, P. J. Schmidt, W. Schnick, *Chem. Mater.* **2015**, *27*, 6432–6441.

[14] F. J. Pucher, A. Marchuk, P. J. Schmidt, D. Wiechert, W. Schnick, *Chem. Eur. J.* **2015**, *21*, 6443–6448.

[15] S. Zhao, Z. Fu, Q. Qin, *Thin Solid Films* **2002**, *415*, 108–113.

[16] D. Baumann, W. Schnick, *Inorg. Chem.* **2014**, *53*, 7977–7982.

[17] K. Landskron, H. Huppertz, J. Senker, W. Schnick, *Angew. Chem. Int. Ed.* **2001**, *40*, 2643–2645; *Angew. Chem.* **2001**, *113*, 2713–2716.

[18] K. Landskron, H. Huppertz, J. Senker, W. Schnick, *Z. Anorg. Allg. Chem.* **2002**, *628*, 1465.

[19] J. M. Léger, J. Haines, C. Chateau, G. Bocquillon, M. W. Schmidt, S. Hull, F. Gorelli, A. Lesauze, R. Marchand, *Phys. Chem. Minerals* **2001**, *28*, 388–398.

[20] J.-M. Léger, J. Haines, L. S. de Oliveira, C. Chateau, A. Le Sauze, R. Marchand, S. Hull, *J. Phys. Chem. Solids* **1999**, *60*, 145–152.

[21] J. Haines, C. Chateau, J. M. Léger, A. Le Sauze, N. Diot, R. Marchand, S. Hull, *Acta Crystallogr., Sect. B* **1999**, *55*, 677–682.

[22] D. Baumann, R. Niklaus, W. Schnick, *Angew. Chem. Int. Ed.* **2015**, *54*, 4388–4391; *Angew. Chem.* **2015**, *127*, 4463–4466.

[23] W. Schnick, J. Lücke, *Z. Anorg. Allg. Chem.* **1992**, *610*, 121–126.

[24] H. Jacobs, R. Nymwegen, S. Doyle, T. Wroblewski, K. W, W. Kockelmann, H. Jacobs, *Z. Anorg. Allg. Chem.* **1997**, *623*, 1467–1474.

[25] A. Marchuk, F. J. Pucher, F. W. Karau, W. Schnick, *Angew. Chem. Int. Ed.* **2014**, *53*, 2469–2472; *Angew. Chem.* **2014**, *126*, 2501–2504.

[26] D. Baumann, W. Schnick, *Angew. Chem. Int. Ed.* **2014**, *53*, 14490–14493; *Angew. Chem.* **2014**, *126*, 14718–14721.

[27] S. D. Kloß, W. Schnick, *Angew. Chem. Int. Ed.* **2015**, *54*, 11250–11253: *Angew. Chem.* **2015**, *127*, 11402–11405.

[28] E.-M. Bertschler, C. Dietrich, J. Janek, W. Schnick, *Chem. Eur. J.* **2017**, *23*, 2185–2191.

[29] W. Schnick, J. Luecke, *J. Solid State Chem.* **1990**, *87*, 101–106.

[30] E.-M. Bertschler, R. Niklaus, W. Schnick, *Chem. Eur. J.* **2017**, *23*, 9592–9599.

[31] W. Schnick, U. Berger, *Angew. Chem. Int. Ed. Engl.* **1991**, *30*, 830–831; *Angew. Chem.* **1991**, *103*, 857–858.

[32] E.-M. Bertschler, C. Dietrich, T. Leichtweiss, J. Janek, W. Schnick, *Chem. Eur. J.* **2017**, DOI: 10.1002/chem.201704305.

[33] W. Schnick, J. Lücke, *Z. Anorg. Allg. Chem.* **1990**, *588*, 19–25.

[34] F. Liebau, *Structural Chemistry of Silicates*, Springer-Verlag Berlin, **1985**.

[35] The term *dreier (vierer, sechser)* ring was coined by Liebau and is derived from the German word “drei” (“vier”, “sechs”). A *dreier (vierer, sechser)* ring is comprised of three (four, six) tetrahedra centers.

[36] N. Kawai, S. Endo, *Rev. Sci. Instrum.* **1970**, *41*, 1178–1181.

[37] D. Walker, M. A. Carpenter, C. M. Hitch, *Am. Mineral.* **1990**, *75*, 1020–1028.

[38] D. Walker, *Am. Mineral.* **1991**, *76*, 1092–1100.

[39] D. C. Rubie, *Phase Transitions* **1999**, *68*, 431–451.

[40] H. Huppertz, *Z. Kristallogr.* **2004**, *219*, 330–338.

[41] Further details of the crystal structure investigation can be obtained from the Fachinformations-Zentrum Karlsruhe, 76344 Eggenstein- Leopoldshafen, Germany (fax: (+49)7247-808-666; e-Mail: crysdata@fiz-Karlsruhe.de) on quoting the deposition number CSD-433592.

[42] L. Cartz, S. R. Srinivasa, R. J. Riedner, J. D. Jorgensen, T. G. Worlton, *J. Chem. Phys.* **1979**, *71*, 1718–1721.

[43] V. A. Blatov, *IUCr CompComm Newsl.* **2006**, *7*, 4–38.

[44] V. a. Blatov, M. O'Keeffe, D. M. Proserpio, *CrystEngComm* **2010**, *12*, 44–48.

[45] T. G. Mitina, V. A. Blatov, *Cryst. Growth Des.* **2013**, *13*, 1655–1664.

[46] M. Jansen, Luer Burkhard, *Z. Kristallogr.* **1986**, *177*, 149–151.

[47] D. Stachel, I. Svoboda, H. Fuess, *Acta Crystallogr., Sect. C* **1995**, *51*, 1049–1050.

[48] A. Durif, *Crystal Chemistry of Condensed Phosphates*, Springer, Berlin, **1995**.

[49] S. Lupart, W. Schnick, *Z. Anorg. Allg. Chem.* **2012**, *638*, 2015–2019.

[50] V. A. Blatov, *Crystallogr. Rev.* **2004**, *10*, 249–318.

[51] N. Anurova, V. Blatov, G. Ilyushin, O. Blatova, A. Ivanovschitz, L. Demyanets, *Solid State Ionics* **2008**, *179*, 2248–2254.

[52] V. A. Blatov, A. P. Shevchenko, V. N. Serezhkin, *J. Appl. Crystallogr.* **1999**, *32*, 377–377.

[53] S. Horstmann, E. Irran, W. Schnick, *Z. Anorg. Allg. Chem.* **1998**, *624*, 221–227.

[54] F. D. Murnaghan, *Proc. Natl. Acad.Sci. USA*, **1944**, *30*, 244-247.

[55] G. M. Sheldrick, *Cell_NOW, Version 2008/4*, Georg-August-Universtiät Göttingen, Göttingen, Germany, **2008**.

[56] *SAINT, Data Integration Software*, Madison, Wisconsin, USA, **1997**.

[57] *APEX 3 v 2016.5-0*, Bruker-AXS, **2016**.

[58] G. M. Sheldrick, *TWINABS*, Universtiy Of Göttingen, Göttingen, Germany.

[59] *XPREP Reciprocal Space Exploration, Vers. 6.12*, Bruker-AXS, Karlsruhe, **2001**.

[60] G. M. Sheldrick, *SHELXS*, University of Göttingen, **1997**.

[61] G. M. Sheldrick, *Acta Crystallogr., Sect. A Found. Crystallogr.* **2008**, *64*, 112–122.

[62] L. J. Farrugia, *J. Appl. Crystallogr.* **1999**, *32*, 837–838.

[63] L. J. Farrugia, *PLATON, Vers. 1.16*, University of Glasgow, **1995**.

[64] K. Brandenburg, H. Putz, *Diamond - Crystal and Molecular Structure Visualization*, Crystal Impact, Bonn, Germany.

[65] A. Coelho, *TOPAS-Academic* **2007**.

[66] R. W. Cheary, A. A. Coelho, *J. Appl. Crystallogr.* **1992**, *25*, 109–121.

[67] R. W. Cheary, A. A. Coelho, *J. Res. Natl. Inst. Stand. Technol.* **2007**, *109*, 1–25.

[68] *INCA, Version 4.02*, OXFORD Instruments.

[69] *OPUS/IR*, Bruker Analytik GmbH, **2000**.

[70] G. Kresse, J. Hafner, *Phys. Rev. B* **1993**, *47*, 558–561.

[71] G. Kresse, J. Hafner, *Phys. Rev. B* **1994**, *49*, 14251–14269.

[72] G. Kresse, J. Furthmüller, *Comput. Mater. Sci.* **1996**, *6*, 15–50.

[73] J. P. Perdew, K. Burke, M. Ernzerhof, *Phys. Rev. Lett.* **1996**, *77*, 3865–3868.

[74] J. P. Perdew, K. Burke, M. Ernzerhof, *Phys. Rev. Lett.* **1997**, *78*, 1396–1396.

[75] P. E. Blöchl, *Phys. Rev. B* **1994**, *50*, 17953–17979.

[76] G. Kresse, D. Joubert, *Phys. Rev. B* **1999**, *59*, 1758–1775.

[77] H. J. Monkhorst, J. D. Pack, *Phys. Rev. B* **1976**, *13*, 5188–5192.

[78] F. Tran, P. Blaha, *Phys. Rev. Lett.* **2009**, *102*, 226401.

[79] J. A. Camargo-Martínez, R. Baquero, *Phys. Rev. B* **2012**, *86*, 195106.

6. $Li_{47}B_3P_{14}N_{42}$ – A Lithium Nitridoborophosphate with $[P_3N_9]^{12-}$, $[P_4N_{10}]^{10-}$ and the Unprecedented $[B_3P_3N_{13}]^{15-}$ Ion

Eva-Maria Bertschler, Thomas Bräuniger, Christian Dietrich, Jürgen Janek, Wolfgang Schnick

published in: *Angew. Chem. Int. Ed.* **2017**, *56*, 4806-4809. DOI: 10.1002/anie.201701084

published in: *Angew. Chem.* **2017**, *129*, 4884-4887. DOI: 10.1002/ange.201701084

Abstract

$Li_{47}B_3P_{14}N_{42}$, the first lithium nitridoborophosphate, is synthesized by two different routes using a Li_3N flux enabling a complete structure determination by single-crystal X-ray diffraction data. $Li_{47}B_3P_{14}N_{42}$ comprises three different complex anions: a cyclic $[P_3N_9]^{12-}$, an adamantane-like $[P_4N_{10}]^{10-}$, and the novel anion $[P_3B_3N_{13}]^{15-}$. $[P_3B_3N_{13}]^{15-}$ is the first species with condensed B/N and P/N substructures. Rietveld refinement, ^{6}Li, ^{7}Li, ^{11}B, and ^{31}P solid-state NMR spectroscopy, FTIR spectroscopy, EDX measurements, and elemental analyses correspond well with the structure model from single-crystal XRD. To confirm the mobility of Li^+ ions, their possible migration pathways were evaluated and the temperature-dependent conductivity was determined by impedance spectroscopy. With the Li_3N flux route we gained access to a new class of lithium nitridoborophosphates, which could have a great potential for unprecedented anion topologies with interesting properties.

6.1. Introduction with Results and Discussion

Phosphorus chemistry offers a great diversity of complex ring and cage structures, especially in P/S, P/O, or P/N chemistry.[1] Various neutral binary compounds with cage-like structures (e.g. P_4S_{10},[2] P_4O_{10},[3] P_3N_5)[4, 5] were described, alongside with cyclic anions (e.g. $[P_3S_8]^{3-}$,[6] $[P_4S_8]^{4-}$,[7] $[P_4O_{12}]^{4-}$,[8] $[P_3N_9]^{12-}$).[9] The well-established variety of different ring sizes and cages in phosphorus chemistry occurs in lithium nitridophosphate chemistry as well. As we described in a previous contribution on $Li_{18}P_6N_{16}$, the starting materials for the synthesis of lithium nitridophosphates are being fragmented in an in situ formed Li_3N self-flux, forming different building blocks of corner-sharing PN_4 tetrahedra. They crystallize under different reaction conditions forming a variety of nitridophosphate ions in a matrix of Li^+ ions.[10] Yet only four non-polymeric nitridophosphate ions have been described to date: isolated $[PN_4]^{7-}$ in Li_7PN_4,[11] cyclic $[P_3N_9]^{12-}$ in $Li_{12}P_3N_9$,[9] adamantane-like $[P_4N_{10}]^{10-}$ in $Li_{10}P_4N_{10}$,[12] and the tricyclic $[P_6N_{16}]^{18-}$ ion made up of one *vierer*-ring and two annelated *dreier*-rings in $Li_{18}P_6N_{16}$.[10, 13, 14] The Li_3N flux method has already been employed for preparation of other nitrides, for example, *c*-BN. Analysis of the reaction melt during synthesis of *c*-BN indicates presence of Li_3N, *h*-BN, in situ formed B and Li_3BN_2.[15] Li_3BN_2 can also be synthesized from Li_3N and *h*-BN and contains isolated $[BN_2]^{3-}$ units.[16] Further B/N anions such as $[BN_3]^{6-}$, $[B_3N_6]^{9-}$, or $[B_2N_4]^{8-}$ have been described.[17] Both $[BN_3]^{6-}$ and $[B_3N_6]^{9-}$ units can be considered as cutouts of *h*-BN, which also serves as starting material for nitridoborates in combination with Li_3N—the self-flux medium to deliver single crystals of lithium nitridophosphates.[10, 17-19] However, ternary B/P/N compounds and the condensation of B/N with P/N substructures have not been observed so far. Examples of other mixed ternary nitrides of p-block elements are BC_2N[20] and $Si_3B_3N_7$.[21]

Herein we report on synthesis and structural investigation of the novel triple salt $Li_{47}[P_3N_9][P_4N_{10}]_2[B_3P_3N_{13}]$, the first lithium nitridoborophosphate with a condensed B/P/N substructure and further two P/N anions in a matrix of Li^+. $Li_{47}B_3P_{14}N_{42}$ was synthesized by two different routes.

Following Equation (1) the target compound was synthesized by solid-state reaction with a slight excess of Li_3N (2 %) at 1098 K in a Ta-crucible placed in a dried silica tube under N_2 atmosphere. By this synthesis route $Li_{47}B_3P_{14}N_{42}$ was obtained together with Li_3P.

$$47\ Li_3N + 14\ P_3N_5 + 9\ BN \xrightarrow{\Delta T} 3\ Li_{47}B_3P_{14}N_{42} \qquad (1)$$

Phase-pure products were obtained according to Equation (2) by high-pressure/high-temperature synthesis at 3.5 GPa and 1298 K using a 1000 t hydraulic press combined with a modified Walker-type multi-anvil module.[22-26]

$$17\ LiPN_2 + 11\ Li_7PN_4 + 6\ BN \xrightarrow{\Delta p,\ \Delta T} 2\ Li_{47}B_3P_{14}N_{42} \qquad (2)$$

An excess of Li_7PN_4 (molar ratio $LiPN_2$:Li_7PN_4=1:2) was used for in situ formation of a Li_3N self-flux similar to the synthesis of $Li_{18}P_6N_{16}$.[10] A colorless air-sensitive product containing single crystals was obtained. The crystal structure of $Li_{47}B_3P_{14}N_{42}$ was solved and refined from single-crystal X-ray diffraction data using direct methods (Tables S1–S4, in the Supporting Information).[27] It crystallizes in the non-centrosymmetric (polar) space group *P*3*c*1 as a plane and inversion twin. The non-centrosymmetric space group is in accordance with the arrangement of the different stacking sequences and the tetrahedral building units, explained in Figure 2. Owing to a high number of crystallographically independent sites in combination with a moderate crystal quality all atoms were refined isotropically.

The lithium nitridoborophosphate $Li_{47}B_3P_{14}N_{42}$ comprises an unprecedented anion-topology consisting of three different species: cyclic $[P_3N_9]^{12-}$,[9] adamantane-like $[P_4N_{10}]^{10-}$,[12] and the novel nitridoborophosphate ion $[P_3B_3N_{13}]^{15-}$ (Figure 1). The $[P_3B_3N_{13}]^{15-}$ ion can be envisioned to be formed by condensation of three BN_3- and three PN_4-units. The central B_3N_7-moiety represents a cutout of *h*-BN but has not been observed as an "isolated" ion as yet.

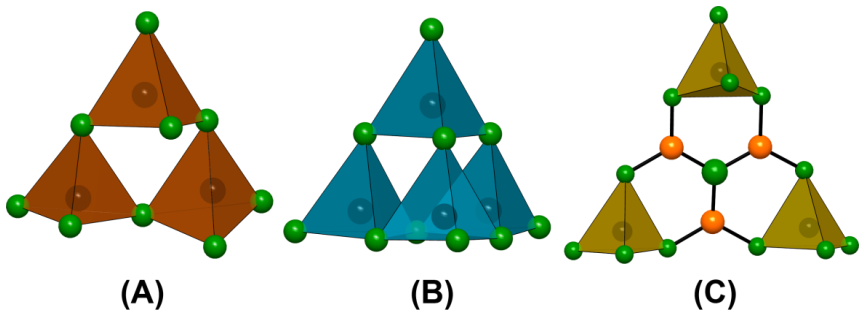

Figure 1. Three different anions in $Li_{47}B_3P_{14}N_{42}$. (A) $[P_3N_9]^{12-}$, (B) $[P_4N_{10}]^{10-}$, (C) $[B_3P_3N_{13}]^{15-}$. P black, N green, B orange.

These three isolated ions build up two different columns (Figure 2 (A),(B)), each composed of two different stacking sequences ((1) to (4) in Figure 2) along *c*. Column (A) consists of $[P_4N_{10}]^{10-}$ ions, which are inversely orientated to each other. The stacking sequences (1) and (2) can be transformed into each other by a 180° rotation around *a* (continuous and dashed line; Figure 2, left side). Column (B) contains alternating $[P_3N_9]^{12-}$ and $[P_3B_3N_{13}]^{15-}$ ions. Thereby, the vertices and the faces of the PN_4 tetrahedra of both building blocks are facing each other. By 180° rotation around *a*, the stacking sequences (3) and (4) can be transformed into each other (continuous and dashed line; Figure 2, right side).

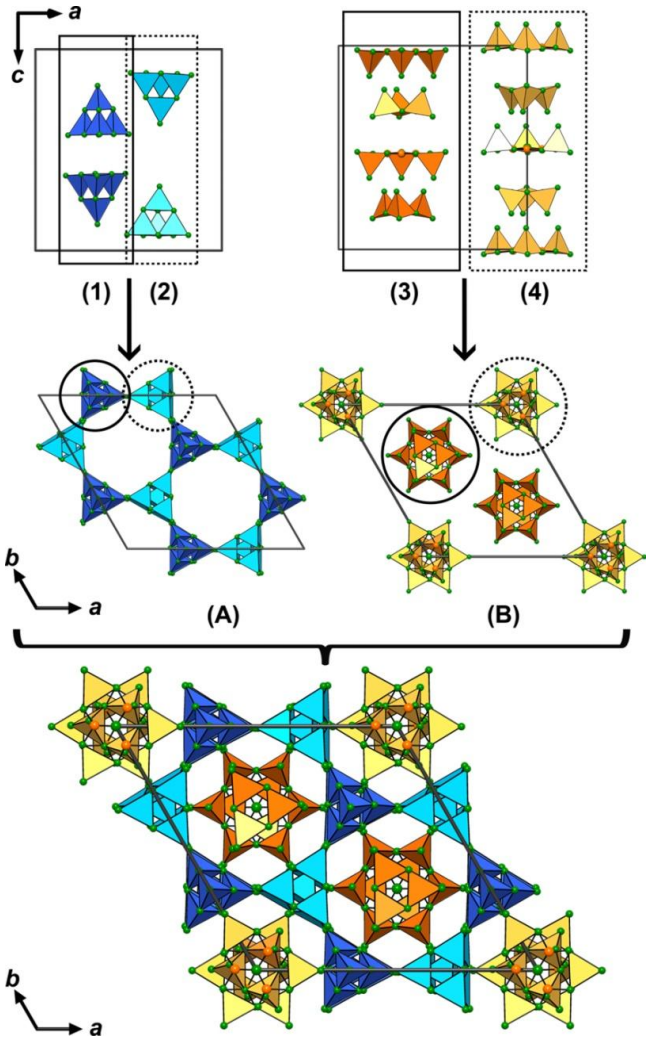

Figure 2. Left side: Column (A) with two different stacking sequences (1) and (2). Right side: Column (B) with two different stacking sequences (3) and (4). Below: Packing of $Li_{47}B_3P_{14}N_{42}$. P black, N green, B orange. Li^+ atom positions are omitted for clarity. For a more detailed visualization see Supporting Information, Figure S1.

The range of P–N distances (148–179 pm) and N-P-N angles (90–117°) in $Li_{47}B_3P_{14}N_{42}$ are consistent with corresponding values for PN_4 tetrahedra in other lithium nitridophosphates.[10-12, 28] B−N bond lengths (135–156 pm) in $Li_{47}B_3P_{14}N_{42}$ are in a typical range (*h*-BN: B-N 145 pm, N-B-N 120°). The trigonal BN_3 units are slightly distorted (N-B-N 114–126°) in contrast to the trigonal planar angles in *h*-BN. Li^+ ions are coordinated by distorted N polyhedra, which are sharing corners, edges or faces. Most of the Li^+ ions are coordinated by four N, 15 by five N and one by six N atoms.

Energy dispersive X-ray (EDX) spectroscopy was carried out and the obtained atomic ratio B/P/N is in good agreement with the crystallographically refined composition (see Table S6). The Li amount with regard to the B/P/N ratio was checked by elemental analysis (Pascher, Remagen,

Germany). The absence of N−H and O−H bonds was confirmed by FTIR spectroscopy (added information in Figure S8). High-temperature powder diffraction experiments (Figure S7) show phase stability up to 1200 K in Ar atmosphere.

The structural model and phase purity of $Li_{47}B_3P_{14}N_{42}$ have been checked by Rietveld refinement of X-ray powder diffraction data (Table S5, Figure S2). The structural model obtained from Rietveld refinement differs slightly from the single-crystal data concerning some Li^+ sites, which may be attributed to different data collection temperatures (Figure 3). This disorder indicates possible mobility of the Li^+ ions in $Li_{47}B_3P_{14}N_{42}$. To confirm this assumption possible voids and migration pathways of Li^+ were analyzed with TOPOS.[29-31] The migration pathways show a possible movement of the Li^+ ions in three different directions in space.

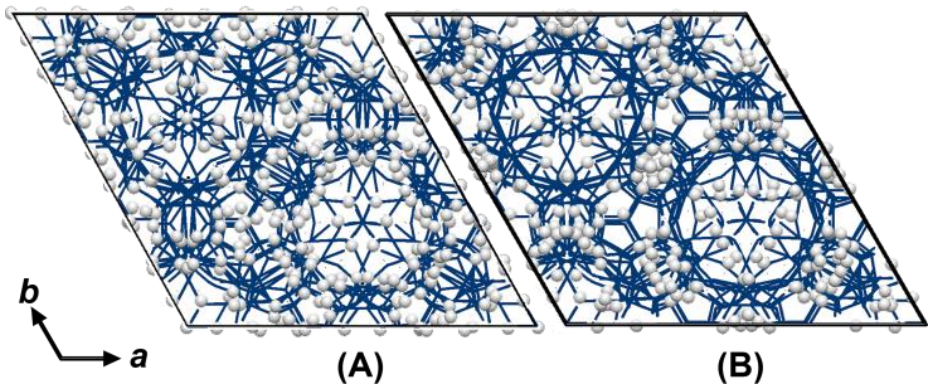

Figure 3. Calculated possible migration pathways (blue) according to the voids in the structure and unit cell of $Li_{47}B_3P_{14}N_{42}$ (view along *c*). (A) Positions of the Li^+ ions (white spheres) at 100 K (SCXRD). (B) Positions of the Li^+ ions at 298 K (PXRD).

The mobility of the Li^+ ions is also supported by the Fourier map in Figure 4 (B). The $[P_3B_3N_{13}]^{15-}$ and $[P_4N_{10}]^{10-}$ units (Figure 4 (A)) are also shown in the F_{obs} (Figure 4 (B)). Thereby, only a section of the $[P_4N_{10}]^{10-}$ units is depicted. The Fourier map was calculated with data of the single-crystal refinement. It is evident that the Li^+ ions appeared as smeared and are not localized on discrete sites. Owing to the lack of localization, the numerous Li^+ positions and the multitude of possible Li^+ migration pathways, the residual electron density from refinement of isotropic thermal displacement parameters is quite high. This effect is known from other lithium ion conductors (e.g. Li_3N)[32] and leads to relatively high *R*-values.

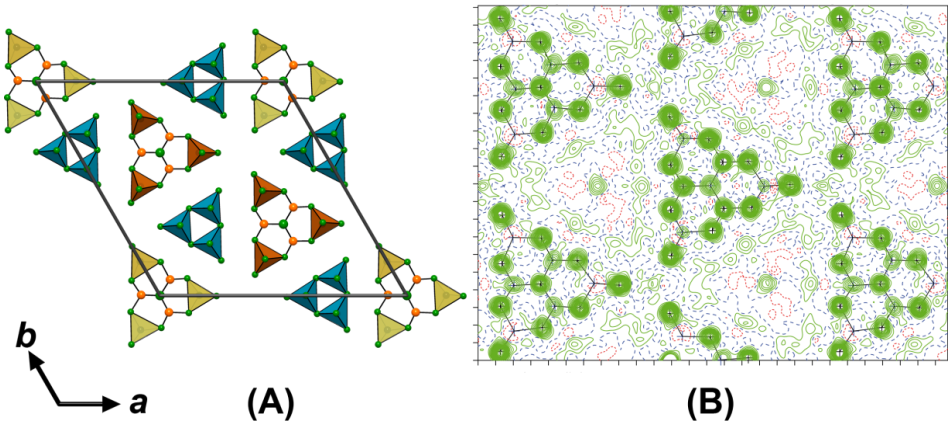

Figure 4. (A) Section of the structure of $Li_{47}B_3P_{14}N_{42}$ viewing along *c* from $z = -0.1$ to 0.2. (B) Fourier map (F_{obs}) of $Li_{47}B_3P_{14}N_{42}$ at $x = 0$, $y = 0$, and $z \approx 0$; contour level -2.00 $e^- Å^{-3}$ (dashed line = positive electron density, continuous line = negative electron density).

With respect to the suggested mobility of the Li^+ ions, conductivity measurements were acquired from a Au/$Li_{47}B_3P_{14}N_{42}$/Au cell at temperatures from 298 to 388 K. The conductivity is 1.0×10^{-7} Ω^{-1} cm^{-1} at room temperature and 1.3×10^{-5} Ω^{-1} cm^{-1} at 400 K. The Nyquist plots show typical semicircles in the higher frequency region and a tail at low frequencies (Figure S12). The Arrhenius-type plot is shown in the Supporting Information (Figure S11); an activation energy of 49.4 kJ mol^{-1} is evaluated from the linear fit.

Table 1 gives these results and those of other lithium nitridophosphates. Due to the high formal charge of the anions in $Li_{18}P_6N_{16}$ and $Li_{47}B_3P_{14}N_{42}$ there is a strong attraction to the Li^+ ions. This may reduce the mobility of the ions in comparison to Li_7PN_4. $LiPN_2$ is closely packed and contains the lowest Li content, leading to a lower conductivity.[10, 33]

Table 1. Conductivity and activation energy of some ternary lithium nitridophosphates.

	σ_{RT} [$\Omega^{-1}cm^{-1}$]	σ_{400K} [$\Omega^{-1}cm^{-1}$]	E_a [kJ mol^{-1}]	Refs.
Li_7PN_4	-	$1.7\cdot10^{-5}$	46.7	[33]
$Li_{18}P_6N_{16}$	$7.70\cdot10^{-8}$	$1.5\cdot10^{-5}$	48.3	[10]
$Li_{47}B_3P_{14}N_{42}$	$1.03\cdot10^{-7}$	$1.3\cdot10^{-5}$	49.4	this work
$LiPN_2$	-	$6.9\cdot10^{-7}$	58.9	[33]

To corroborate the results of the structure solution ^{31}P, ^{11}B, ^{6}Li, and ^{7}Li solid-state MAS NMR spectra were recorded (^{31}P, ^{7}Li, and ^{6}Li solid-state MAS NMR spectroscopy, Figure S3–S5). Figure 5 shows the quadrupolar broadened central-transition resonance of ^{11}B (I=3/2) for both $Li_{47}B_3P_{14}N_{42}$ and *h*-BN. The electronic environment of the three crystallographically independent B sites in $Li_{47}B_3P_{14}N_{42}$ is so similar that they are not distinguishable in the ^{11}B NMR spectrum. In comparison to the spectrum of the single boron site of *h*-BN, there are small but significant differences. To quantify these differences, the spectra were fitted with the DMFIT software,[34] with the resulting parameters listed in the caption of Figure 5. For both compounds, the isotropic shifts are very similar and occur in the range expected for B in trigonal coordination,[35] and those for *h*-BN are in good agreement with previously reported data.[36] The resonance lines for the two compounds do however not fully match, owing to the subtle differences in both chemical shift and quadrupolar coupling. The ^{11}B NMR thus shows that while the chemical surroundings of B in $Li_{47}B_3P_{14}N_{42}$ and *h*-BN are very similar, they are not fully identical, in agreement with the structure model proposed herein.

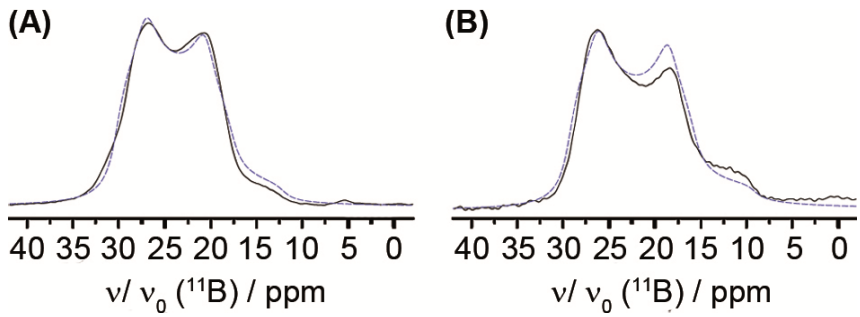

Figure 5. ^{11}B NMR spectra, acquired at 20 kHz MAS and a Larmor frequency of 160.5 MHz (black, solid lines), and the simulated spectra fitted by DMFIT[34] (blue, dashed lines): (A) $Li_{47}B_3P_{14}N_{42}$, with δ_{iso}=31.7 ppm and quadrupolar parameters χ=2.82 MHz, η=0.3; (B) *h*-BN, with δ_{iso}=31.0 ppm and quadrupolar parameters χ=2.98 MHz, η=0.25.

We obtained a lithium nitridoborophosphate namely $Li_{47}B_3P_{14}N_{42}$, which is the first representative of the B/P/N substance class. Thorough characterization was carried out by means of single-crystal and powder X-ray diffraction as well as solid-state NMR, EDX, FTIR spectroscopy and elemental analyses. Furthermore, the mobility of the Li^+ ions was confirmed by TOPOS analysis of possible Li^+ migration pathways and ion conductivity measurements. The unprecedented topology of this triple salt with $[P_4N_{10}]^{10-}$, $[P_3N_9]^{12-}$, and $[B_3P_3N_{13}]^{15-}$ ions demonstrates that the Li_3N self-flux method may accelerate investigation of novel P/N and B/P/N ions in lithium nitrido(boro)phosphates or may even facilitate synthesis of the first ternary boron phosphorus nitride. Further experiments will probably lead to a significant variety of different ring- and cage-

systems. And subsequent research will reveal a deeper insight in the relation between structural features and Li^+-ion conductivity.

6.2. Acknowledgements

We gratefully acknowledge Dr. Peter Mayer for single-crystal X-ray diffraction, Thomas Miller for high-temperature powder diffraction measurements, Christian Minke for EDX, REM, and solid-state MAS NMR, Marion Sokoll for IR spectroscopy and Dr. Constantin Hoch for helpful support concerning the structural analysis (all at Department of Chemistry, LMU Munich). We gratefully acknowledge financial support by the Fonds der Chemischen Industrie (FCI), the Deutsche Forschungsgemeinschaft (DFG), and by STORE-E (LOEWE program funded by State of Hessen).

6.3. References

[1] D. E. C. Corbridge, *Studies in Inorganic Chemistry 10. Phosphorus - An Outline of Its Chemistry, Biochemistry and Technology, Elsevier Science Publishers B.V.*, Amsterdam, **1990**.

[2] A. Stock, K. Thiel, *Ber. Dtsch. Chem. Ges.* **1905**, *38*, 2719–2730.

[3] G. C. Hampson, *A. J. Srosick, J. Am. Chem. Soc.* **1938**, *60*, 1814–1822.

[4] W. Schnick, J. Luecke, F. Krumeich, *Chem. Mater.* **1996**, *8*, 281–286.

[5] S. Horstmann, E. Irran, W. Schnick, *Angew. Chem. Int. Ed. Engl.* **1997**, *36*, 1873–1875; *Angew. Chem.* **1997**, *109*, 1938-1940.

[6] A. Schliephake, H. Falius, *Z. Anorg. Allg. Chem.* **1992**, *611*, 141–148.

[7] P. C. Minshall, G. M. Sheldrick, *Acta Crystallogr. Sect. B* **1978**, *B34*, 1378–1380.

[8] H. Ettis, H. Naili, T. Mhiri, *Cryst. Growth Des.* **2003**, *3*, 599–602.

[9] W. Schnick, *Angew. Chem. Int. Ed. Engl.* **1993**, *32*, 806–818; *Angew. Chem.* **1993**, *105*, 846.

[10] E.-M. Bertschler, C. Dietrich, J. Janek, W. Schnick, *Chem. Eur. J.* **2017**, *23*, 2185–2191.

[11] W. Schnick, J. Luecke, *J. Solid State Chem.* **1990**, *87*, 101–106.

[12] U. Berger, W. Schnick, *Angew. Chem. Int. Ed. Engl.* **1991**, *30*, 830–831; *Angew. Chem.* **1991**, *103*, 857–858.

[13] F. Liebau, *Structural Chemistry of Silicates*, Springer-Verlag Berlin, **1985**.

[14] The term dreier (vierer) ring was coined by Liebau and is derived from the German word “drei” (“vier”). A *dreier* (*vierer*) ring comprised three (four) tetrahera centers.

[15] G. Bocquillon, C. Loriers-Susse, J. Loriers, *J. Mater. Sci.* **1993**, *28*, 3547–3556.

[16] H. Yamane, S. Kikkawa, H. Horiuchi, M. Koizumi, *J. Solid State Chem.* **1986**, *65*, 6–12.

[17] H. Jing, H.-J. Meyer, *Z. Anorg. Allg. Chem.* **2002**, *628*, 1548–1551.

[18] H. Jing, J. Pickardt, H.-J. Meyer, *Z. Anorg. Allg. Chem.* **2001**, *627*, 2070–2074.

[19] O. Reckeweg, H.-J. Meyer, *Z. Anorg. Allg. Chem.* **1999**, *625*, 866.

[20] S. Hong, J. Seung-Hoon, D. Roundy, M. L. Cohen, S. G. Louie, *Phys. Rev. B* **1994**, *50*, 4976–4979.

[21] M. Jansen, J. C. Schön, L. van Wüllen, *Angew. Chem. Int. Ed.* **2006**, *45*, 4244–4263; *Angew. Chem.* **2006**, *118*, 4350–4370.

[22] N. Kawai, S. Endo, *Rev. Sci. Instrum.* **1970**, *41*, 1178–1181.

[23] D. Walker, M. A. Carpenter, C. M. Hitch, *Am. Mater.* **1990**, *75*, 1020–1028.

[24] D. Walker, *Am. Mater*. **1991**, *76*, 1092–1100.

[25] D. C. Rubie, *Phase Transitions* **1999**, *68*, 431–451.

[26] H. Huppertz, *Z. Kristallogr.* **2004**, *219*, 330–338.

[27] Further Crystal data for $Li_{47}B_3P_{14}N_{42}$: space group *P*3*c*1 (no. 158), a = 19.3036(7), c = 18.0200(7) Å, V = 5815.2(5) $Å^3$, Z = 2, ρ_{diffrn} = 2.365 g cm^{-3}, Bruker D8 Venture, Mo-K_α-radiation, multi-scan absorption correction, 69567 reflections, 29949 independent reflections, BASF 0.36852/0.22583/0.13121, least-squares refinement on F^2, *R*-values (all data/$F_0^2 \geq 2\sigma(F_0^2)$): R_1 = 0.1767/0.0733, wR_2 = 0.2228/0.1768, *GooF* = 0.917 for 69567 observed reflections ($F_0^2 \geq 2\sigma(F_0^2)$) and 335 parameters. Further details of the crystal structure investiation can be obtained from the Fachinformations-Zentrum Karlsruhe, 76344 Eggenstein- Leopoldshafen, Germany (Fax: (+49)7247-808-666; E-Mail: Crysdata@fiz-Karlsruhe.de) on Quoting the Depository Number CSD- 432318.

[28] W. Schnick, J. Lücke, *Z. Anorg. Allg. Chem.* **1990**, *588*, 19–25.

[29] V. A. Blatov, L. Carlucci, G. Ciani, D. M. Proserpio, *CrystEngComm* **2004**, *6*, 377–395.

[30] N. A. Anurova, V. A. Blatov, G. D. Ilyushin, O. A. Blatova, A. K. Ivanov-Schitz, L. N. Dem'yanets, *Solid State Ionics* **2008**, *179*, 2248–2254.

[31] A. P. Shevchenko, V. N. Serezhkin, V. A. Blatov, *J. Appl. Crystallogr.* **1999**, *32*, 377–377.

[32] H. Schulz, K. H. Thiemann, *Acta Crystallogr. Sect. A* **1979**, *35*, 309–314.

[33] W. Schnick, J. Luecke, *Solid State Ionics* **1990**, *38*, 271–273.

[34] D. Massiot, F. Fayon, M. Capron, I. King, S. Le Calve, B. Alonso, J. Durand, B. Bujoli, Z. Gan, G. Hoatson, *Magn. Reson. Chem.* **2002**, *40*, 70–76.

[35] T. Bräuniger, M. Jansen, *Z. Anorg. Allg. Chem.* **2013**, *639*, 857–879.

[36] G. Jeschke, J. Hoffbauer, M. Jansen, *Solid State Nucl. Magn. Reson.* **1998**, *12*, 1–7.

7. Summary

7.1. Objectives of the thesis

The main objectives of this thesis were the explorative search for new lithium nitridophosphates and the investigation of the relation between their structural motifs and the respective lithium ion conductivity. Due to the first-time adoption of the high-pressure/high-temperature multianvil technique to lithium nitridophosphates, the structural variety of this compound class was significantly increased. To grow single crystals under these conditions the Li_3N self-flux method was developed. Furthermore, DFT calculations were performed to corroborate the phase transitions between the different polymorphs, and topological analyses showed possible migration pathways of the lithium ions. Temperature dependent impedance measurements were carried out to identify lithium nitridophosphates as lithium ion conductors. Additional XPS measurements demonstrated the thermodynamic stability of some reported compounds with respect to lithium metal. These results contributed to a better understanding of the behavior of lithium nitridophosphates as potential solid-state electrolytes in lithium ion batteries.

7.2. $Li_{12}P_3N_9$ with Non-Condensed $[P_3N_9]^{12-}$ Rings and its High-Pressure Polymorph Li_4PN_3 with Infinite Chains of PN_4-Tetrahedra

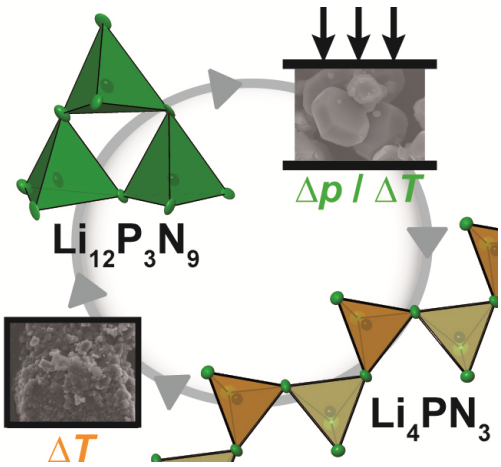

The first high-pressure polymorph of $Li_{12}P_3N_9$, namely Li_4PN_3, was synthesized in a Walker-type multianvil device. $Li_{12}P_3N_9$ represents the first lithium nitridophosphate with a ring structure and was synthesized by solid-state reaction of Li_3N and P_3N_5 at 790 °C. The non-condensed $[P_3N_9]^{12-}$ *dreier*-rings of PN_4 tetrahedra were further polymerized to the first lithium *catena*-nitridophosphate Li_4PN_3 at 6 GPa and 820 °C. To enhance the crystallinity of the high-pressure polymorph, Li_4PN_3 was also synthesized from $LiPN_2$ and Li_7PN_4 at 9 GPa and 1200 °C with the Li_3N self-flux method. The crystal structures of both polymorphs ($Li_{12}P_3N_9$: *Cc* (no. 9), a = 12.094(5), b = 7.649(3), c = 9.711(4) Å, β = 90.53(2)°, V = 898.3(6) Å^3, Z = 4; Li_4PN_3: *Pccn* (no. 56), a = 9.6597(4), b = 11.8392(6), c = 4.8674(2) Å, V = 556.65(4) Å^3, Z = 8) were solved and refined from single-crystal X-ray diffraction data and confirmed by Rietveld refinement, ^{6}Li, ^{7}Li and ^{31}P solid-state MAS NMR and FTIR spectroscopy. The high-pressure polymorph Li_4PN_3 is made up of PN_3 *zweier*-chains of corner sharing PN_4 tetrahedra $^1_\infty[(PN_2\ N_{2/2})^{4-}]$. To examine the phase transition and to corroborate Li_4PN_3 as the corresponding high-pressure polymorph to $Li_{12}P_3N_9$, DFT calculations and temperature dependent powder X-ray diffraction were carried out. Electronic band gap ($Li_{12}P_3N_9$: 5 eV; Li_4PN_3: 6 eV) and electron localization function calculations were conducted to compare the electronic properties and bonding behavior of both compounds.

This novel synthetic approach to polymerize lithium nitridophosphates under high-pressure/high-temperature conditions gives an important boost to expand the structural diversity of lithium nitridophosphates. In addition, it was demonstrated that the Li_3N self-flux method under high-pressure/high-temperature conditions is a powerful technique to allow complete structural investigations of high-pressure polymorphs from single-crystal X-ray diffraction data.

7.3. $Li_{18}P_6N_{16}$ – A Lithium Nitridophosphate with Unprecedented Tricyclic $[P_6N_{16}]^{18-}$ Ions

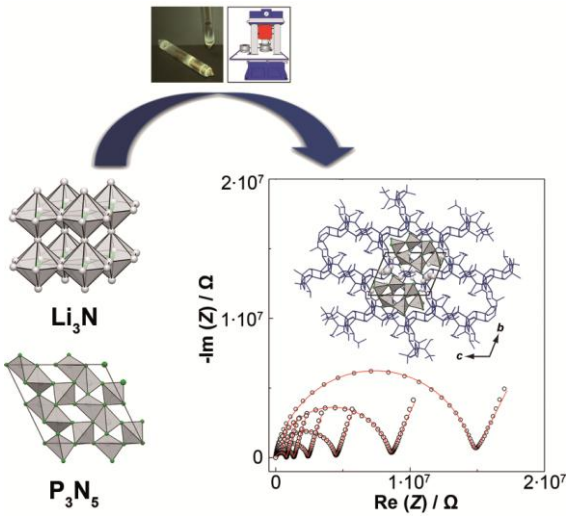

$Li_{18}P_6N_{16}$ represents the first nitridophosphate with a tricyclic ring structure. It was synthesized by two different approaches in combination with the multianvil technique: from Li_3N and P_3N_5 at 3 GPa/800 °C (Li_3N flux) and from $LiPN_2$ and Li_7PN_4 at 5.5 GPa/1000 °C (Li_3N self-flux). The crystal structure of the new lithium nitridophosphate was solved and refined from single-crystal X-ray diffraction data ($P\overline{1}$ (no. 2), a = 5.4263(4), b = 7.5354(5), c = 9.8584(7) Å, α = 108.481(2), β = 99.288(2), γ = 104.996(4)°, V = 356.02(4) Å^3, Z = 1) and confirmed by Rietveld refinement. Furthermore, the product was characterized by EDX, FTIR and ^{6}Li, ^{7}Li and ^{31}P solid-state MAS NMR spectroscopy. The hitherto unknown tricyclic $[P_6N_{16}]^{18-}$ anion is made up of six vertex sharing PN_4 tetrahedra forming one *vierer*- and two annelated *dreier*-rings. Phase-pure synthesis allowed temperature dependent impedance spectroscopy (σ_{RT} = 7.70 x 10^{-8} Ω^{-1}cm^{-1}, E_a = 0.50 eV). With respect to Li^+ ion conductivity and thermal stability, $Li_{18}P_6N_{16}$ appears to be a promising candidate for optimizations in future experiments, like pulsed laser deposition, or cation doping to optimize the defect chemistry and kinetics.

7.4. Li^+ Ion Conductors with Adamantane-type Nitridophosphate Anions – β-$Li_{10}P_4N_{10}$ and $Li_{13}P_4N_{10}X_3$ with X = Cl, Br

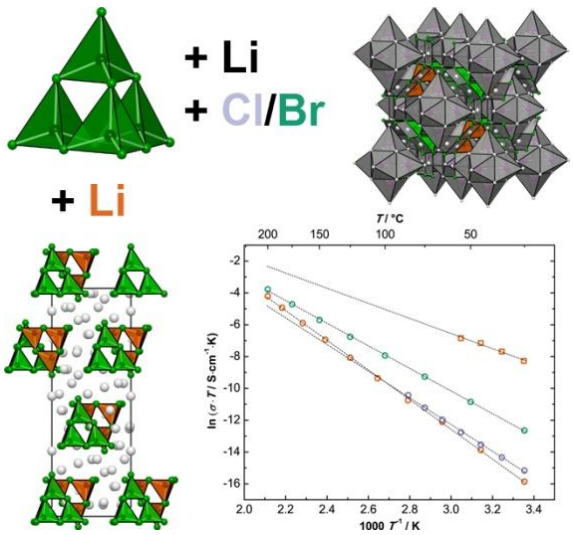

The first low-temperature polymorph β-$Li_{10}P_4N_{10}$ of the lithium nitridophosphate $Li_{10}P_4N_{10}$ was synthesized by lowering the synthesis temperature from 720 to 680 °C and starting from Li_3N and P_3N_5. In addition, quaternary lithium nitridophosphate halides were accessible for the first time via incorporation of Cl and Br. $Li_{13}P_4N_{10}X_3$ (X = Cl, Br) was synthesized by reaction of Li_3N, P_3N_5 and LiX. The crystal structures of all compounds (β-$Li_{10}P_4N_{10}$: $R3$ (no. 146), a = 8.71929(8), c = 21.4656(2) Å, V = 1413.30(3) Å^3, Z = 6; $Li_{13}P_4N_{10}Cl_3$: $Fm\bar{3}m$ (no. 225), a = 13.9321(2), V = 2704.27(12) Å^3, Z = 8; $Li_{13}P_4N_{10}Br_3$: $Fm\bar{3}m$ (no. 225), a = 14.1096(6), V = 2809.0(4) Å^3, Z = 8) were elucidated from X-ray powder diffraction data and corroborated by ^{6}Li, ^{7}Li and ^{31}P solid-state MAS NMR and FTIR spectroscopy. The elemental composition was confirmed by EDX measurements. β-$Li_{10}P_4N_{10}$ is composed of distorted adamantane-like $[P_4N_{10}]^{10-}$ T2 supertetrahedra, which are arranged in analogy to sphalerite. At 90 °C this distortion disappears and β-$Li_{10}P_4N_{10}$ transforms reversibly to the α-polymorph. By heating over 600 °C the reversible phase transition turns irreversible. $Li_{13}P_4N_{10}X_3$ (X = Cl, Br) is made up of adamantane-type T2 supertetrahedra, X_6Li_{14} building blocks and Li^+ ions (in the voids between the supertetrahedra). The X_6 octahedra build up an *fcc* lattice, whose tetrahedral voids are occupied by the T2 supertetrahedra.

To identify these novel compounds as Li^+ ion conductors, temperature dependent impedance measurements were performed (β-$Li_{10}P_4N_{10}$: σ_{RT} = 8.6 x 10^{-7}; β-$Li_{10}P_4N_{10}$ sintered: σ_{RT} = 4.3 x 10^{-10}; $Li_{13}P_4N_{10}Cl_3$: σ_{RT} = 8.8 x 10^{-10} and $Li_{13}P_4N_{10}Br_3$: σ_{RT} = 1.1 x 10^{-8} $\Omega^{-1}cm^{-1}$). Additional XPS measurements to analyze the stability of lithium nitridophosphates with respect to lithium metal were carried out to classify the behavior of these compounds as solid electrolytes (SE) in lithium ion batteries. Similar to the behavior of LiPON, a solid electrolyte interphase (SEI) is formed. This feature makes lithium nitridophosphates interesting candidates for potential application as SE in lithium ion batteries.

7.5. Reversible Polymerization of Adamantane-type $[P_4N_{10}]^{10-}$ Anions to Honeycomb-type $[P_2N_5]^{5-}$ Layers under High-Pressure

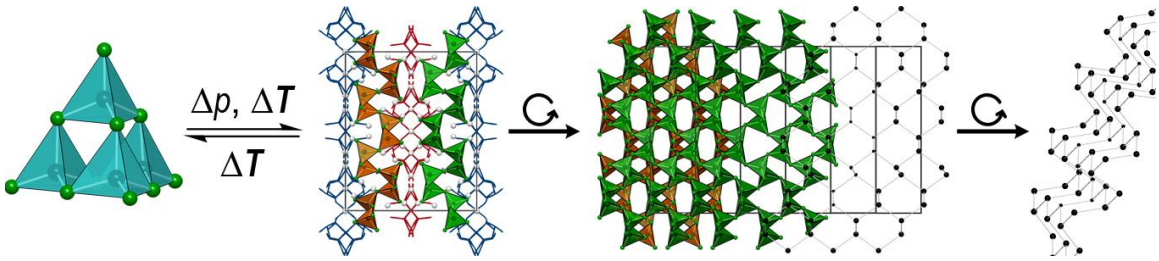

A third polymorph $Li_5P_2N_5$ of $Li_{10}P_4N_{10}$ represents the first lithium nitridophosphate with a layered structure. It was synthesized by high-pressure and high-temperature reaction starting from $LiPN_2$ and Li_7PN_4 at 9 GPa. Alternatively, $Li_5P_2N_5$ was synthesized at 9 GPa starting from β-$Li_{10}P_4N_{10}$. Synthesis starting from $LiPN_2$ and Li_7PN_4 allowed the growth of single crystals and led to successful structure determination (space group *C*2/*c* (no. 15), a = 14.770(3), b = 17.850(4), c = 4.860(1) Å, β = 93.11(3)°, V = 1279.4(5) Å^3, Z = 12) from single crystal X-ray data. The crystal structure was confirmed by Rietveld refinement, ^{6}Li, ^{7}Li and ^{31}P solid-state MAS NMR and FTIR spectroscopy. EDX measurements were carried out to confirm the elemental composition. The P/N substructure of $Li_5P_2N_5$ is made up of vertex sharing PN_4 tetrahedra forming a corrugated layer of linked *sechser*-rings. The arrangement of the P atoms is analogous to that of black phosphorus and corresponds to a uninodal three-connected net with the *hcb* (honeycomb) topology. Temperature dependent X-ray powder diffraction was carried out to corroborate $Li_5P_2N_5$ as the corresponding high-pressure polymorph of β-$Li_{10}P_4N_{10}$. This analytical result was confirmed by DFT calculations. In addition, electronic band gap (β-$Li_{10}P_4N_{10}$: 3.5 eV; $Li_5P_2N_5$: 5.6 eV) calculations were conducted, to compare the electronic properties of both compounds.

Together with the polymerization from *dreier*-rings in $Li_{12}P_3N_9$ to chains in Li_4PN_3 this result shows that high-temperature/high-pressure polymerization is a powerful technique to obtain lithium nitridophosphates with a great structural diversity. Higher pressures could also make structures with PN_5 square pyramids or even PN_6 octahedra accessible.

7.6. $Li_{47}B_3P_{14}N_{42}$ – A Lithium Nitridoborophosphate with $[P_3N_9]^{12-}$, $[P_4N_{10}]^{10-}$ and the Unprecedented $[B_3P_3N_{13}]^{15-}$ Ion

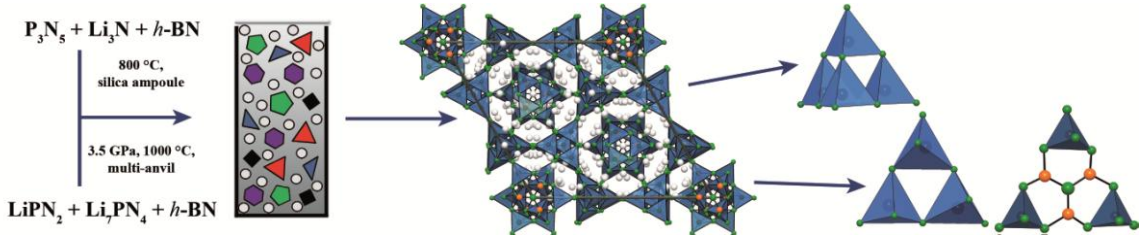

The triple salt $Li_{47}B_3P_{14}N_{42}$ is the first representative of the compound class of lithium nitridoborophosphates. It was synthesized by high-pressure/high-temperature synthesis at 3.5 GPa and 1000 °C. With the Li_3N self-flux method, single crystals of the product were obtained. Consequently, the crystal structure (*P*3*c*1 (no. 158), *a* = 19.3036(7), *c* = 18.0200(7) Å, V = 5815.2(5) $Å^3$, Z = 2) was solved and refined by single-crystal X-ray diffraction analysis. Phase purity was confirmed by Rietveld refinement. Furthermore, structure characterization includes a broad spectrum of analytical methods, such as ^6Li, ^7Li, ^{11}B and ^{31}P solid-state MAS NMR spectroscopy, elemental analysis as well as FTIR and EDX spectroscopy. $Li_{47}[P_3N_9][P_4N_{10}]_2[P_3B_3N_{13}]$ comprises three different non-condensed complex anions: cyclic $[P_3N_9]^{12-}$, adamantane-like $[P_4N_{10}]^{10-}$ and the new $[P_3B_3N_{13}]^{15-}$ anion. With the latter, a condensation of B/N and P/N substructures was observed for the first time. This novel anion could be formed by condensation of three BN_3 and three PN_4 units. The central "B_3N_7" moiety can be considered as a section of *h*-BN and has not been observed as an non-condensed ion so far. Topological analysis of the structure indicated a mobility of the lithium ions in three dimensions. With respect to the suggested mobility of the Li^+ ions, conductivity measurements were carried out (σ_{RT} = 1.03 x 10^{-7} $\Omega^{-1}cm^{-1}$, E_a = 0.51 eV).

The topology of the triple salt $Li_{47}B_3P_{14}N_{42}$ demonstrates that the high-pressure/high-temperature approach in combination with the Li_3N self-flux accelerates investigations of P/N and B/P/N ions or may even facilitate synthesis of structures with unprecedented elemental compositions and gives therefore access to new substance classes.

8. Discussion & Outlook

8.1. Li_3N self-flux method in high-pressure/high-temperature syntheses

Until this work, only four ternary lithium nitridophosphates were mentioned in literature, namely Li_7PN_4, $Li_{12}P_3N_9$, $Li_{10}P_4N_{10}$, and $LiPN_2$.[1–4] They were synthesized from Li_3N and P_3N_5 with a slight excess of Li_3N (Li_3N flux) in sealed silica ampoules with tungsten crucibles. This excess was necessary to compensate the thermal decomposition of Li_3N during syntheses. The transfer of this method to high-pressure/high-temperature syntheses led to various by-products. Phase-pure samples were only obtained starting from $LiPN_2$ and Li_7PN_4 with an excess of Li_7PN_4. Stoichiometric reaction of $LiPN_2$ and Li_7PN_4 led also to various by-products. For example, phase-pure synthesis of $Li_{18}P_6N_{16}$ required a significant excess of Li_7PN_4 (3 $LiPN_2$ + 3 Li_7PN_4 → $Li_{18}P_6N_{16}$ + 2 "Li_3N"). Presumably, this surplus leads to an *in situ* formation of Li_3N (Li_3N self-flux). Under these conditions, $LiPN_2$ and Li_7PN_4 are most likely fragmented into different P/N building blocks, which can serve as *in situ* building units or precursors for crystal growth. In addition, the *in situ* formed Li_3N serves as flux agent leading to larger single crystals. The surplus of Li_3N is supposed to react with the *h*-BN crucible during synthesis. Hitherto, studies on the reaction mixture to demonstrate clearly the *in situ* formation of Li_3N during high-pressure/high-temperature synthesis are still missing.

However, the Li_3N self-flux method in combination with the high-pressure/high-temperature synthesis cannot be transferred to nitridophosphates in general. As the Li_3N self-flux method requires $LiPN_2$ and Li_7PN_4 as starting materials, this approach increasingly leads to formation of lithium-containing nitridophosphates, even if further lithium-free reaction partners are added to the reaction mixture. The incorporation of lithium may be avoided by applying compounds like HPN_2 and HP_4N_6 or $NaPN_2$ and NaP_4N_6 as starting materials. This self-flux method would potentially lead to the *in sit*u formation of NH_3 or Na_3N, respectively, instead of Li_3N. The formally formed flux agents may open up new fields for the explorative search for crystalline compounds via high-pressure/high-temperature syntheses.

8.2. Unprecedented structural variety of lithium nitridophosphates

The main part of this thesis deals with the expansion of the structural diversity of lithium nitridophosphates. Via an explorative approach we succeeded in synthesizing and characterizing numerous novel ternary lithium nitridophosphates, namely $Li_{12}P_3N_9$, Li_4PN_3, $Li_{18}P_6N_{16}$, β-$Li_{10}P_4N_{10}$ and $Li_5P_2N_9$, with degrees of condensation κ ranging from 0.25 to 0.5 (Figure 1).

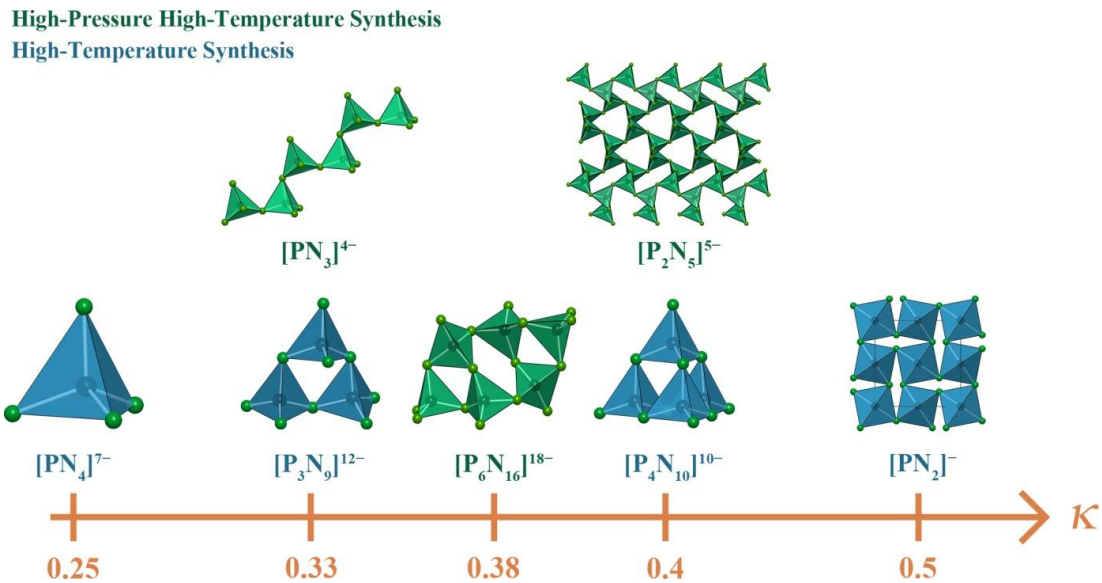

Figure 1. Hitherto known linking patterns of PN_4 tetrahedra in a matrix of lithium ions in lithium nitridophosphates: isolated PN_4 tetrahedra in Li_7PN_4 ($\kappa = 0.25$),[1] rings in $Li_{12}P_3N_9$ ($\kappa = 0.33$), chains in Li_4PN_3 ($\kappa = 0.33$), ring system in $Li_{18}P_6N_{16}$ ($\kappa = 0.38$), cages in α- and β-$Li_{10}P_4N_{10}$ ($\kappa = 0.4$),[3] layers in $Li_5P_2N_5$ ($\kappa = 0.4$), and a network in $LiPN_2$ ($\kappa = 0.5$).[4] Blue: Compounds synthesized by high-temperature synthesis. Green: Compounds synthesized by high-pressure/high-temperature synthesis.

This broad spectrum of structural motifs ranging from isolated anions to rings, ring systems, cages, chains, layers and networks of vertex-sharing PN_4 tetrahedra shows that the structural potential of this compound class is far from being exhausted. With the synthesis of further representatives we are targeting a better understanding of the synthesis conditions of these compounds, which will help to optimize materials with regard to their properties. In addition, each of these compounds is an ideal starting point for further exploration of high-pressure polymorphs, which could yield structures with additional edge-sharing tetrahedra, PN_5 square pyramids or even PN_6 octahedra.

The synthesis of the first lithium nitridoborophosphate $Li_{47}B_3P_{14}N_{42}$ shows that not only nitridophosphates with one single P/N motif are accessible, but also structures with different P/N

anions. Thus, it is merely a matter of time until the great diversity of the presented lithium nitridophosphates will get expanded even more, as simple combination of different structural motifs may lead to a plethora of new structures.

8.3. First representative of the compound class of lithium nitridoborophosphates

The discovery of the first representative, namely $Li_{47}B_3P_{14}N_{42}$, of the compound class of lithium nitridoborophosphates illustrates the feasibility of condensing B/N with P/N substructures for the first time. Experiments in the course of this work already showed that lithium nitridoborophosphates are accessible by two different approaches. $Li_{47}B_3P_{14}N_{42}$ was synthesized starting from *h*-BN, P_3N_5, and Li_3N at 825°C in silica ampoules (Li_3N flux) or phase pure by reaction of *h*-BN, $LiPN_2$, and Li_7PN_4 at 3.5 GPa and 1025 °C by high-pressure/high-temperature synthesis (Li_3N self-flux). The triple salt $Li_{47}[P_3N_9][P_4N_{10}]_2[B_3P_3N_{13}]$ is composed of three different non-condensed anions. The novel building motif $[B_3P_3N_{13}]^{15-}$ can be envisioned to be formed from three PN_4 and three BN_3 units. The latter can be considered as a section of the structure of *h*-BN. Beside the mentioned $[BN_3]^{6-}$ unit, the $[B_2N_4]^{8-}$, $[B_3N_6]^{9-}$, and $[BN_2]^{3-}$ unit can be found in nitridoborates.[5,6] The $[BN_2]^{3-}$ unit is the most common building unit in nitridoborates and occurs in $M_3[BN_2]_2$ (M = Ca, Sr, Ba, Eu)[7,8] or $LiM_4[BN_2]_3$ (M = Ca, Sr, Ba, Eu), for instance.[6] This building unit is also formed *in situ* during synthesis of *c*-BN with the Li_3N flux method. Analysis of the reaction melts indicated the presence of Li_3N, *h*-BN, boron, and Li_3BN_2.[9] Li_3BN_2 can also be synthesized from Li_3N and *h*-BN.[10]

With the presented feasibility of condensing B/N with P/N substructures, the synthesis of the first ternary boron phosphorus nitride or quaternary compounds with unprecedented elemental compositions like Si/P/B/N or B/P/C/N may appear accessible.

Mixing silicon and phosphorus in silicon phosphorous nitrides or phosphidosilicates has already been illustrated in e.g. $SiPN_3$ or Li_2SiP_2.[11,12] The latter was synthesized by heating lithium metal, silicon powder, and phosphorus under argon atmosphere.[12] With e.g. $Si_3B_3N_7$, the combination of silicon and boron in a solid-state structure was described. Amorphous ceramics like $Si_3B_3N_7$ are made up of a disordered network of silicon and boron atoms and are discussed for high-temperature applications, due to their high thermal, chemical and mechanical stabilities.[13] A combination of silicon phosphorous nitrides and silicon boron nitrides may lead to unprecedented structures with condensed Si/N, P/N and B/N building blocks. A possible synthetic approach could be the reaction of lithium metal, silicon powder, Li_7PN_4 and *h*-BN. These new compounds

may have a large potential with respect to property studies and systematic investigations via solid-state NMR spectroscopy (^{29}Si, ^{31}P and ^{7}B).

Additional combination possibilities with p-block elements are exemplified in *γ*- or *c*-BC_2N.[14] *γ*-BC_2N can be synthesized by the reaction of graphitic carbon and boron nitride and has a graphene-like structure. The high-pressure polymorph *c*-BC_2N exhibits a diamond-like structure and at higher temperatures a *c*-BN-like structure. Calculations and experimental results give estimations of the potential of *c*-BC_2N as a super hard material. In addition, it is predicted to have controllable electronic properties.[14,15] Further incorporation of phosphorus could lead to compounds with unprecedented topologies. Thus, access to Si/P/B/N or B/P/C/N compounds will open up a new field of explorative search on new materials.

8.4. Lithium oxonitridophosphates

Several amorphous LiPON compounds are discussed as lithium ion conductors, but only some of their structures are fully characterized.[16] With "$Li_{27}P_4N_9O_{10}$" ($I\bar{4}3d$; a = 12.0106(14) Å) we were able to characterize an *ortho*-oxonitridophosphate by means of single-crystal microfocus X-ray measurements (ESRF measurements in collaboration with Markus Nentwig and Prof. Dr. Oliver Oeckler – both University of Leipzig). This single crystal was extracted from a sample of *β*-$Li_{10}P_4N_{10}$ with side phases. The sample was synthesized from Li_3N and P_3N_5 at 750 °C. The data indicate that "$Li_{27}P_4N_9O_{10}$" is made up from non-condensed $P(N/O)_4$ tetrahedra and O^{2-} ions, surrounded by Li^+ ions. However, we were not able to synthesize samples with "$Li_{27}P_4N_9O_{10}$" as main phase. One potential synthetic strategy may be the addition of Li_2O to the reaction mixture of P_3N_5 and Li_3N. An alternative synthetic route could be the reaction of P_4O_{10} with P_3N_5 and Li_3N. With this reaction mixture, the crystalline LiPON electrolyte Li_2PO_2N was synthesized at 950 °C.[17] Reactions with P_3N_5 often require high reaction temperatures, leading to the formation of only thermodynamically stable compounds. This limitation can be circumvented by the use of molecular precursors with low degrees of condensation. Molecular precursors were already successfully used for the synthesis of the first *ortho*-oxonitridophosphate, namely $Li_{14}(PON_3)_2O$, synthesized from $PO(NH_2)_3$ and $LiNH_2$.[18]

Completing the characterization of "$Li_{27}P_4N_9O_{10}$" will allow a better understanding of the reaction mechanism enabling synthesis of further crystalline LiPON compounds. Lithium ion conductivity measurements will furthermore provide a deeper insight in the relation between structural features and lithium ion conductivity of the prominent LiPON compound class.

8.5. Lithium ion conductivity of lithium nitridophosphates

As topological analyses indicate potential mobility of the lithium ions in lithium nitridophosphates, they were examined concerning their ionic conductivity. Impedance measurements showed lithium ion conductivity in the range of 10^{-10} to 10^{-7} $\Omega^{-1}cm^{-1}$ at room temperature. Compared to recently discussed state-of-the-art solid electrolyte materials theses values are moderate (Table 1), but can be optimized by standard techniques.

Table 1. Lithium ion conductivities of different inorganic solid electrolytes.[19]

Type	Materials	Conductivity [$\Omega^{-1}cm^{-1}$]
Oxide	Perovskite NASICON LISICON Garnet	$10^{-5} – 10^{-3}$
Sulfide	$Li_2S–P_2S(–MS_x)$	$10^{-7} – 10^{-3}$
Thin Film	LiPON	10^{-6}
Nitride	Li–P–N	$10^{-10} – 10^{-7}$

NASICON-type compounds ($LiTi_2(PO_4)_3$), for instance, initially also showed very low ionic conductivity, but it was improved significantly by substitutions with e.g. Al or Ge. Similar substitutions may also enhance the ionic conductivity of lithium nitridophosphates.[20] However, beside the high ionic conductivity, different properties are important for practical application as solid electrolytes. For example, the perovskite $Li_{3x}La_{2/3-x}TiO_3$ exhibits a lithium ion conductivity exceeding 10^{-3} $\Omega^{-1}cm^{-1}$ at room temperature,[21] but it is not suitable for practical application due to the reduction of Ti^{4+} on contact with lithium metal.[19] XPS measurements were performed in order to investigate the chemical compatibility of lithium nitridophosphates and showed that β-$Li_{10}P_4N_{10}$ and $Li_{13}P_4N_{10}Cl_3$ are thermodynamically unstable with respect to lithium metal, and a SEI is formed. Unlike LiPON compounds, which decompose to Li_3P, Li_3N and Li_2O,[22–24] both lithium nitridophosphates decompose to a stable lithium nitridophosphate ("$Li_6P_4N_6$") and Li_3N. This indicates lithium nitridophosphates that are thermodynamically and kinetically stable in contact with lithium metal may exist. However, to decide whether the formed SEI enhances or decreases the ion conductivity of the samples, additional measurements should be performed after contact with lithium metal. Furthermore, lithium nitridophosphates require supplementary studies concerning the area-specific resistance, ionic selectivity, electrochemical stability window and the mechanical properties.

Nevertheless, the structural variety of lithium nitridophosphates in combination with the high thermal stability up to 900 °C, their simple and low cost fabrication process, as well as their environmental friendliness indicate several capabilities for further research and optimizations to increase the lithium ion conductivity by e.g. substitution and to circumvent their sensitivity towards moisture.

8.6. Final remarks

The findings of this thesis underline the great significance of high-pressure/high-temperature synthesis in lithium nitridophosphate chemistry. A combination of the latter with the conventional ampoule technique led to a broad spectrum of interesting structural motifs, opening new horizons for the explorative research.

With temperature dependent impedance measurements it could moreover be shown that lithium nitridophosphates are solid electrolytes with moderate lithium ion conductivities in the range of 10^{-10} to 10^{-7} $\Omega^{-1}cm^{-1}$ at room temperature. Still, it is obvious that the described compounds need further optimizations in order to compete with the multitude of inorganic solid electrolytes that are currently studied and optimized for application in solid-state batteries. However, the compound class of lithium nitridophosphates is just at the beginning of systematic investigations that will help in understanding structure-property relations of this interesting compound class.

8.7. References

[1] W. Schnick, J. Luecke, *J. Solid State Chem.* **1990**, *87*, 101–106.

[2] W. Schnick, *Angew. Chem. Int. Ed. Engl.* **1993**, *32*, 806–818; *Angew. Chem.* **1993**, *105*, 846–858.

[3] W. Schnick, U. Berger, *Angew. Chem. Int. Ed. Engl.* **1991**, *30*, 830–831; *Angew. Chem.* **1991**, *103*, 857–858.

[4] W. Schnick, J. Lücke, *Z. Anorg. Allg. Chem.* **1990**, *588*, 19–25.

[5] H. Jing, H.-J. Meyer, *Z. Anorg. Allg. Chem.* **2002**, *628*, 1548–1551.

[6] P. Rogl, *Int. J. Inorg. Mater.* **2001**, *3*, 201–209.

[7] R. Pöttgen, O. Reckeweg, *Z. Kristallogr.* **2017**, *232*, 653–668.

[8] W. Carnillo-Cabrera, M. Sommer, K. Peters, H. G. von Schnering, *Z. Krist. NCS* **2001**, *216*, 43–44.

[9] G. Bocquillon, C. Loriers-Susse, J. Loriers, *J. Mater. Sci.* **1993**, *28*, 3547–3556.

[10] H. Yamane, S. Kikkawa, H. Horiuchi, M. Koizumi, *J. Solid State Chem.* **1986**, *65*, 6–12.

[11] H.-P. P. Baldus, W. Schnick, J. Luecke, U. Wannagat, G. Bogedain, *Chem. Mater.* **1993**, *5*, 845–850.

[12] A. Haffner, T. Bräuniger, D. Johrendt, *Angew. Chem. Int. Ed.* **2016**, *55*, 13585–13588; *Angew. Chem.* **2016**, *128*, 13783–13786.

[13] M. Jansen, J. C. Schön, L. van Wüllen, *Angew. Chem. Int. Ed.* **2006**, *45*, 4244–4263 ; *Angew. Chem.* **2006**, *118*, 4350–4370.

[14] H. Sun, S.-H. Jhi, D. Roundy, M. L. Cohen, S. G. Louie, *Phys. Rev. B* **2001**, *64*, 94108.

[15] W. H. Lim, A. Hamzah, M. T. Ahmadi, R. Ismail, *Superlattices Microstruct.* **2017**, *112*, 328–338.

[16] J. Bartes, N. Dudney, G. Gruzalski, R. Zuhr, A. Choudhury, C. Luck, J. Robertson, *Power Sources* **1993**, *43*, 103–110.

[17] K. Senevirathne, C. S. Day, M. D. Gross, A. Lachgar, N. A. W. Holzwarth, *Solid State Ionics* **2013**, *233*, 95–101.

[18] D. Baumann, W. Schnick, *Eur. J. Inorg. Chem.* **2015**, *2015*, 617–621.

[19] A. Manthiram, X. Yu, S. Wang, *Nat. Rev. Mater.* **2017**, *2*, 16103.

[20] J. S. Thokchom, N. Gupta, B. Kumar, *J. Electrochem. Soc.* **2008**, *155*, A915–A920.

[21] Y. Inaguma, C. Liquan, M. Itoh, T. Nakamura, T. Uchida, H. Ikuta, M. Wakihara, *Solid State Commun.* **1993**, *86*, 689–693.

[22] A. Schwöbel, R. Hausbrand, W. Jaegermann, *Solid State Ionics* **2015**, *273*, 51–54.

[23] W. D. Richards, L. J. Miara, Y. Wang, J. C. Kim, G. Ceder, *Chem. Mater.* **2016**, *28*, 266–273.

[24] S. Sicolo, M. Fingerle, R. Hausbrand, K. Albe, *J. Power Sources* **2017**, *354*, 124–133.

A. Supporting Information for Chapter 2

A.1. Additional crystallographic data for $Li_{12}P_3N_9$

Table S1. Fractional atomic coordinates, isotropic thermal displacement parameters, and site occupancies for $Li_{12}P_3N_9$.

Atom	Wyckoff symbol	*x*	*y*	*z*	U_{iso} / Å^2	Occupancy
P1	4*a*	0.12676(11)	0.1655(2)	0.3023(2)	0.0033(3)	1
P2	4*a*	0.38275(12)	0.6692(2)	0.3047(2)	0.0040(3)	1
P3	4*a*	0.0060(2)	0.4422(2)	0.1523(2)	0.0038(2)	1
N1	4*a*	0.2309(4)	0.1604(7)	0.4098(6)	0.0044(10)	1
N2	4*a*	0.2818(4)	0.6837(7)	0.4147(5)	0.0051(10)	1
N3	4*a*	0.5082(6)	0.1534(5)	0.1603(5)	0.0055(8)	1
N4	4*a*	0.1347(4)	0.0265(7)	0.1793(6)	0.0043(10)	1
N5	4*a*	0.0061(5)	0.1228(5)	0.3914(4)	0.0049(8)	1
N6	4*a*	0.1157(5)	0.3748(7)	0.2494(5)	0.0044(10)	1
N7	4*a*	0.0000(5)	0.3578(5)	0.0000(4)	0.0045(8)	1
N8	4*a*	0.3638(4)	0.5300(7)	0.1821(6)	0.0056(10)	1
N9	4*a*	0.3978(5)	0.1256(7)	0.7459(5)	0.0060(11)	1
Li1	4*a*	0.2626(10)	0.416(2)	0.3351(13)	0.008(2)	1
Li2	4*a*	0.2497(9)	0.083(2)	0.7963(11)	0.008(2)	1
Li3	4*a*	0.5037(12)	0.4019(12)	0.2575(9)	0.010(2)	1
Li4	4*a*	0.1202(9)	0.1816(14)	0.5701(11)	0.006(2)	1
Li5	4*a*	0.0063(12)	0.3923(12)	0.4387(10)	0.007(2)	1
Li6	4*a*	0.6158(10)	0.131(2)	0.3412(13)	0.010(2)	1
Li7	4*a*	0.2242(9)	0.4352(13)	0.0861(11)	0.007(2)	1
Li8	4*a*	0.4048(10)	0.325(2)	0.0617(12)	0.011(2)	1
Li9	4*a*	0.2459(10)	0.075(2)	0.0354(12)	0.013(2)	1
Li10	4*a*	0.3957(9)	0.122(2)	0.3309(12)	0.009(2)	1
Li11	4*a*	0.0181(10)	0.0974(12)	0.0425(10)	0.009(2)	1
Li12	4*a*	0.3419(9)	0.2376(14)	0.5558(11)	0.011(2)	1

Table S2. Anisotropic displacement parameters occurring in $Li_{12}P_3N_9$.

Atom	U_{11} / Å^2	U_{22} / Å^2	U_{33} / Å^2	U_{12} / Å^2	U_{13} / Å^2	U_{23} / Å^2
P1	0.0049(8)	0.0021(7)	0.0031(8)	-0.0001(6)	0.0002(5)	-0.0001(5)
P2	0.0064(8)	0.0026(7)	0.0030(8)	-0.0004(6)	-0.0001(5)	-0.0006(6)
P3	0.0065(5)	0.0016(5)	0.0034(5)	-0.0004(7)	-0.0012(6)	0.0004(5)
N1	0.006(2)	0.001(2)	0.006(2)	0.000(2)	0.002 (2)	0.002(2)
N2	0.010(3)	0.004(2)	0.002(2)	-0.000(2)	0.000(2)	-0.002(2)
N3	0.009(2)	0.003(2)	0.005(2)	-0.001(3)	0.001(2)	0.000(2)
N4	0.004(2)	0.002(2)	0.007(2)	0.002(2)	-0.002(2)	-0.001 (2)
N5	0.008(2)	0.005 (2)	0.001(2)	0.001(2)	0.001(2)	0.001(2)
N6	0.007(3)	0.002(2)	0.004(2)	0.001(2)	0.001(2)	0.001(2)
N7	0.008(2)	0.003(2)	0.003(2)	-0.002(2)	-0.004(2)	0.0001(14)
N8	0.004(2)	0.006(3)	0.006(2)	0.000(2)	-0.002(2)	-0.001(2)
N9	0.011(3)	0.004(3)	0.004(3)	0.000(2)	0.001(2)	-0.000(2)

Table S3. List of interatomic distances / Å for $Li_{12}P_3N_9$.

P1—N4	1.603(5)	P2—N8	1.612(6)	P3—N7	1.616(4)
P1—N1	1.628(6)	P2—N2	1.633(5)	P3—N3^{vi}	1.617(4)
P1—N6	1.686(5)	P2—N9^{iii}	1.681(6)	P3—N9^{vii}	1.683(6)
P1—N5	1.734(6)	P2—N5^{iv}	1.742(6)	P3—N6	1.700(6)
N1—Li12	2.032(12)	N1—Li4	2.069(12)	N1—Li1	2.127(13)
N1—Li10	2.162(13)	N1—Li2^{i}	2.180(12)	N1—Li9^{viii}	2.183(13)
N2—Li7^{v}	2.026(12)	N2—Li2^{iii}	2.153(12)	N2—Li1	2.195(13)
N2—Li8^{v}	2.054(13)	N2—Li6^{vi}	2.161(14)	N2—Li9^{v}	2.230(13)
N3—Li8	2.049(13)	N3—Li3	2.123(10)	N3—Li5^{x}	2.180(11)
N3—Li4^{x}	2.054(12)	N3—Li10	2.166(13)	N3—Li6	2.183(14)
N4—Li4^{i}	1.919(12)	N4—Li9	1.984(13)	N4—Li3^{ii}	2.00(2)
N4—Li2^{i}	1.976(12)	N4—Li11	2.003(12)	N5—Li8^{xi}	2.104(12)
N5—Li5	2.113(10)	N5—Li3^{ii}	2.132(10)	N5—Li11^{viii}	2.238(10)
N5—Li4	2.253(12)	N6—Li1	1.982(13)	N6—Li7	2.119(11)
N6—Li6^{vi}	2.159(13)	N6—Li5	2.278(12)	N7—Li5^{iii}	2.003(10)
N7—Li11	2.046(10)	N7—Li6^{vii}	2.094(14)	N7—Li12^{vii}	2.121(13)
N7—Li10^{vii}	2.067(12)	N8—Li8	2.015(13)	N8—Li7	2.052(12)
N8—Li3	2.08(2)	N8—Li12^{iii}	2.175(12)	N8—Li11^{iv}	2.374(12)
N8—Li1	2.119(13)	N9—Li2	1.888(12)	N9—Li10^{viii}	2.067(13)
N9—Li12	2.139(12)	N9—Li5^{xii}	2.281(13)		

(i) x, -y, -0.5+z; (ii) -0.5+x, -0.5+y, z; (iii) x, 1-y, -0.5+z; (iv) 0.5+x, 0.5+y, z; (v) x, 1-y, 0.5+z; (vi) -0.5+x, 0.5+y, z; (vii) -0.5+x, 0.5-y, -0.5+z; (viii) x, -y, 0.5+z; (ix) 0.5+x, -0.5+y, z; (x) 0.5+x, 0.5-y, -0.5+z; (xi) -0.5+x, 0.5-y, 0.5+z; (xii) 0.5+x, 0.5-y, 0.5+z; (xiii) x, y, 1+z; (xiv) x, y, -1+z.

Table S4. List of bond angles / ° for $Li_{12}P_3N_9$.

N–P–N					
N4—P1—N1	114.2(3)	N8—P2—N2	115.2(3)	N9^{vii}—P3—N6	102.3(2)
N4—P1—N6	114.0(3)	N8—P2—N9^{iii}	112.4(3)	N7—P3—N3^{vi}	116.3(2)
N1—P1—N6	106.1(3)	N2—P2—N9^{iii}	104.0(3)	N7—P3—N9^{vii}	110.0(3)
N4—P1—N5	107.6(3)	N8—P2—N5^{iv}	109.7(3)	N3^{vi}—P3—N9^{vii}	107.1(3)
N1—P1—N5	109.0(3)	N2—P2—N5^{iv}	109.9(3)	N7—P3—N6	114.5(3)
N6—P1—N5	105.4(3)	N9^{iii}—P2—N5^{iv}	105.0(3)	N3^{vi}—P3—N6	105.3(3)
P–N–P					
P1—N5—P2^{ii}	116.2(2)	P1—N6—P3	121.1(3)		

(i) x, -y, -0.5+z; (ii) -0.5+x, -0.5+y, z; (iii) x, 1-y, -0.5+z; (iv) 0.5+x, 0.5+y, z; (v) x, 1-y, 0.5+z; (vi) -0.5+x, 0.5+y, z; (vii) -0.5+x, 0.5-y, -0.5+z; (viii) x, -y, 0.5+z; (ix) 0.5+x, -0.5+y, z; (x) 0.5+x, 0.5-y, -0.5+z; (xi) -0.5+x, 0.5-y, 0.5+z; (xii) 0.5+x, 0.5-y, 0.5+z; (xiii) x, y, 1+z; (xiv) x, y, -1+z.

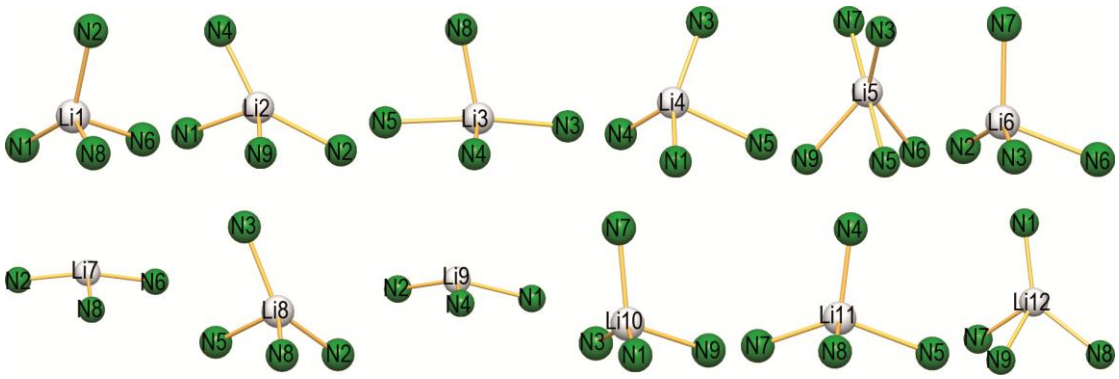

Figure S1. Coordination spheres of the Li^+ sites. Bond length up to 2.88 Å are shown by a orange line. Gray: Li, Green: N.

A.2. Additional crystallographic data for Li_4PN_3

Table S5. Fractional atomic coordinates, isotropic thermal displacement parameters, and site occupancies for Li_4PN_3.

Atom	Wyckoff symbol	*x*	*y*	*z*	U_{iso} / Å^2	Occupancy
P1	8*e*	0.52591(8)	0.17130(6)	0.2950(2)	0.0058(2)	1
N1	8*e*	0.6270(3)	0.0671(2)	0.2115(5)	0.0076(5)	1
N2	8*e*	0.5721(3)	0.2926(2)	0.1210(5)	0.0075(5)	1
N3	8*e*	0.1370(3)	0.3567(2)	0.2652(6)	0.0093(5)	1
Li1	8*e*	0.2162(6)	0.6574(5)	0.0754(12)	0.0148(12)	1
Li2	8*e*	0.2425(8)	0.0332(5)	0.0097(14)	0.0226(13)	1
Li3	8*e*	0.0387(9)	0.5356(7)	0.219(2)	0.041(2)	1
Li4	8*e*	0.1580(14)	0.1880(12)	0.189(3)	0.023(3)	0.494
Li5	8*e*	0.159(2)	0.179(2)	0.336(6)	0.023(3)	0.29
Li6	4*c*	1/4	1/4	0.019(4)	0.019(6)	0.43

Table S6. Anisotropic displacement parameters occurring in Li_4PN_3.

Atom	U_{11} / Å^2	U_{22} / Å^2	U_{33} / Å^2	U_{12} / Å^2	U_{13} / Å^2	U_{23} / Å^2
P1	0.0056(4)	0.0062(3)	0.0056(3)	-0.0006(3)	-0.0005(3)	-0.0001(3)
N1	0.0068(11)	0.0072(11)	0.0088(12)	0.0005(9)	0.000(1)	-0.0006(10)
N2	0.0092(11)	0.0085(11)	0.0048(10)	-0.0017(10)	-0.0015(10)	0.0009(10)
N3	0.0061(12)	0.0096(12)	0.0123(13)	-0.0026(9)	-0.0004(10)	-0.0009(10)

Table S7. List of interatomic distances / Å for Li_4PN_3.

P1—N3^{i}	1.614(3)	P1—N1	1.625(3)	P1—N2^{ii}	1.703(3)
P1—N2	1.725(3)	N1—Li1^{iv}	1.959(6)	N1—Li2^{viii}	2.039(7)
N1—Li1^{iii}	2.124(6)	N1—Li3^{i}	2.010(9)	N1—Li2^{ix}	2.120(7)
N1—Li3^{iv}	2.292(9)	N2—Li1^{vi}	2.115(6)	N2—Li4^{i}	2.259(14)
N2—Li1^{xi}	2.334(6)	N2—Li3^{vi}	2.203(9)	N2—Li1^{iv}	2.327(6)
N2—Li5^{i}	2.49(2)	N3—Li2^{ii}	2.038(7)	N3—Li4	2.041(14)
N3—Li6^{ii}	2.076(13)	N3—Li5^{i}	2.04(2)	N3—Li6	2.056(12)
N3—Li4^{i}	2.083(14)	N3—Li4^{ii}	2.14(2)	N3—Li5	2.14(2)
N3—Li2^{i}	2.145(7)	N3—Li3	2.332(9)		

(i) 0.5-x, 0.5-y, z; (ii) x, 0.5-y, 0.5+z; (iii) 1-x, -0.5+y, 0.5-z; (iv) 0.5+x, -0.5+y, -z; (v) 0.5-x, y, 0.5+z; (vi) 0.5+x, 1-y, 0.5-z; (vii) 0.5+x, -0.5+y, 1-z; (viii) 1-x, -y, -z;

(ix) 0.5+x, -y, 0.5-z; (x) x, 0.5-y, -0.5+z; (xi) 1-x, 1-y, -z; (xii) -0.5+x, 0.5+y, -z; (xiii) -0.5+x, 1-y, 0.5-z; (xiv) 1-x, 0.5+y, 0.5-z; (xv) 0.5-x, 1.5-y, z; (xvi) 0.5-x, y, -0.5+z; (xvii) -0.5+x, -y, 0.5-z; (xviii) -x, 1-y, -z; (xix) -x, 0.5+y, 0.5-z; (xx) -0.5+x, 0.5+y, 1-z.

Table S8. List of bond angles / ° for Li_4PN_3.

N–P–N					
$N3^{i}$—P1—N1	114.05(14)	$N3^{i}$—P1—$N2^{ii}$	112.98(14)	N1—P1—$N2^{ii}$	105.44(14)
$N3^{i}$—P1—N2	112.24(13)	N1—P1—N2	110.71(13)	$N2^{ii}$—P1—N2	100.41(9)
P–N–P					
$P1^{x}$—N2—P1	126.8(2)				

(i) 0.5-x, 0.5-y, z; (ii) x, 0.5-y, 0.5+z; (iii) 1-x, -0.5+y, 0.5-z; (iv) 0.5+x, -0.5+y, -z; (v) 0.5-x, y, 0.5+z; (vi) 0.5+x, 1-y, 0.5-z; (vii) 0.5+x, -0.5+y, 1-z; (viii) 1-x, -y, -z; (ix) 0.5+x, -y, 0.5-z; (x) x, 0.5-y, -0.5+z; (xi) 1-x, 1-y, -z; (xii) -0.5+x, 0.5+y, -z; (xiii) -0.5+x, 1-y, 0.5-z; (xiv) 1-x, 0.5+y, 0.5-z; (xv) 0.5-x, 1.5-y, z; (xvi) 0.5-x, y, -0.5+z; (xvii) -0.5+x, -y, 0.5-z; (xviii) -x, 1-y, -z; (xix) -x, 0.5+y, 0.5-z; (xx) -0.5+x, 0.5+y, 1-z.

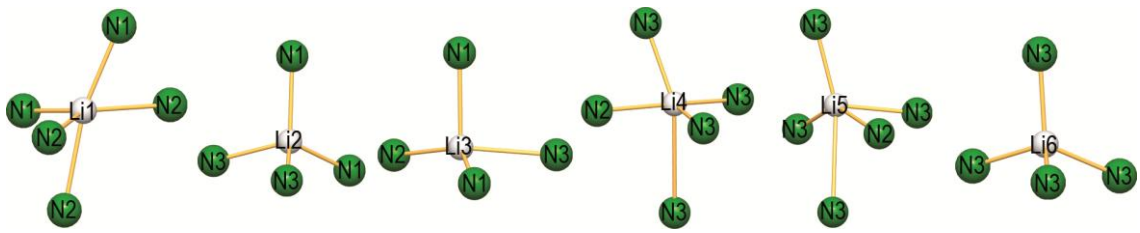

Figure S2. Coordination spheres of the Li^{+} sites. Distances up to 2.88 Å are shown by orange lines. Gray: Li, green: N.

A.3. Details of the Rietveld refinement

Table S9. Details of the Rietveld refinement of $Li_{12}P_3N_9$ and Li_4PN_3.

formula	**$Li_{12}P_3N_9$**	**Li_4PN_3**
formula mass / g · mol^{-1}	534.9	100.8
crystal system / space group	monoclinic *Cc* (no. 9)	orthorhombic *Pccn* (no. 56)
lattice parameters / Å, °	a = 12.1088(3)	a = 9.6497(2)
	b = 7.6588(2)	b = 11.8299(3)
	c = 9.7215(2)	c = 4.8677(1)
	β = 90.899(2)	
cell volume / Å^3	901.45(3)	555.67(2)
formula units per cell Z	4	8
X-ray density / g · cm^{-3}	2.22726(9)	2.40867(10)
linear absorption coefficient / cm^{-1}	73.79	
radiation	Cu-K$_{\alpha 1}$ (λ = 1.540596 Å)	
monochromator	Ge(111)	
diffractometer	Stoe StadiP	
detector	linear PSD	
2θ-range / °	5.0-92.0	5.0-113.1
temperature / K	298 (2)	
data points	5800	7208
number of observed reflections	393	373
number of parameters	86	75
program used	TOPAS Academic	
structure refinement	Rietveld method	
profile function	fundamental parameters model	
background function	shifted Chebyshev	
R_{wp}	16.122	8.631
R_{exp}	6.569	2.066
R_p	10.524	5.768
R_{Bragg}	3.836	1.882
χ^2	2.454	4.177

A.4. Detailed Rietveld plots

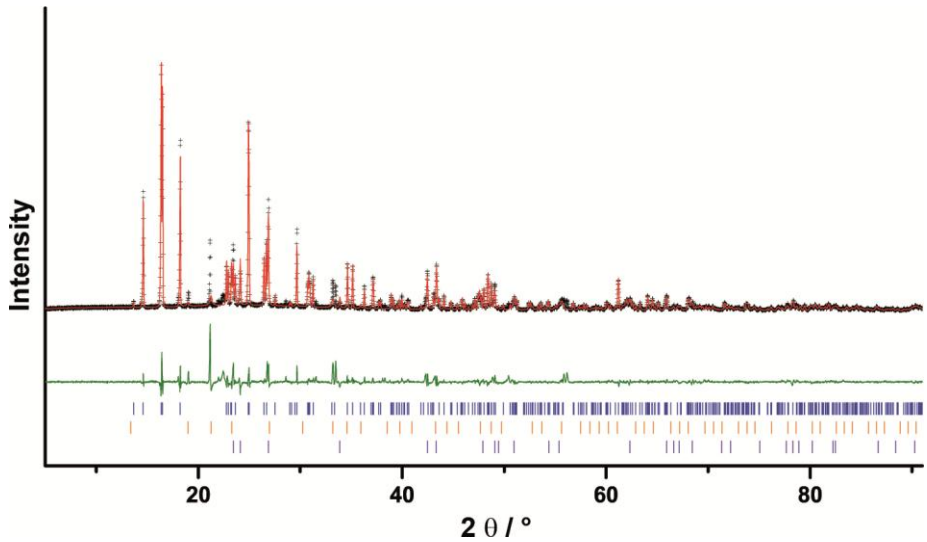

Figure S3. $Li_{12}P_3N_9$: Observed (black crosses) and calculated (red line) powder diffraction pattern as well as difference profile (green) of the Rietveld refinement. Reflex positions are marked by vertical blue bars. Peak positions of side phases are marked by vertical orange (Li_7PN_4 9.83%) and violet (Li_3P 4.69%) bars.

The difference of the peace profile of some peak positions is due to a further side phase, which could not be analyzed in detail.

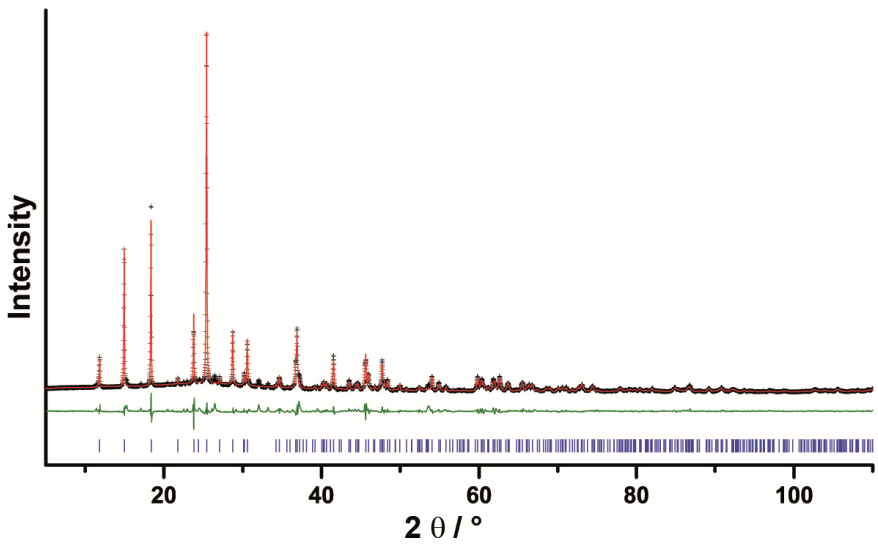

Figure S4. Li_4PN_3: Observed (black crosses) and calculated (red line) powder diffraction pattern as well as difference profile (green) of the Rietveld refinement. Reflex positions are marked by vertical blue bars.

A.5. ^{31}P, ^{6}Li and ^{7}Li solid state MAS NMR Spectroscopy

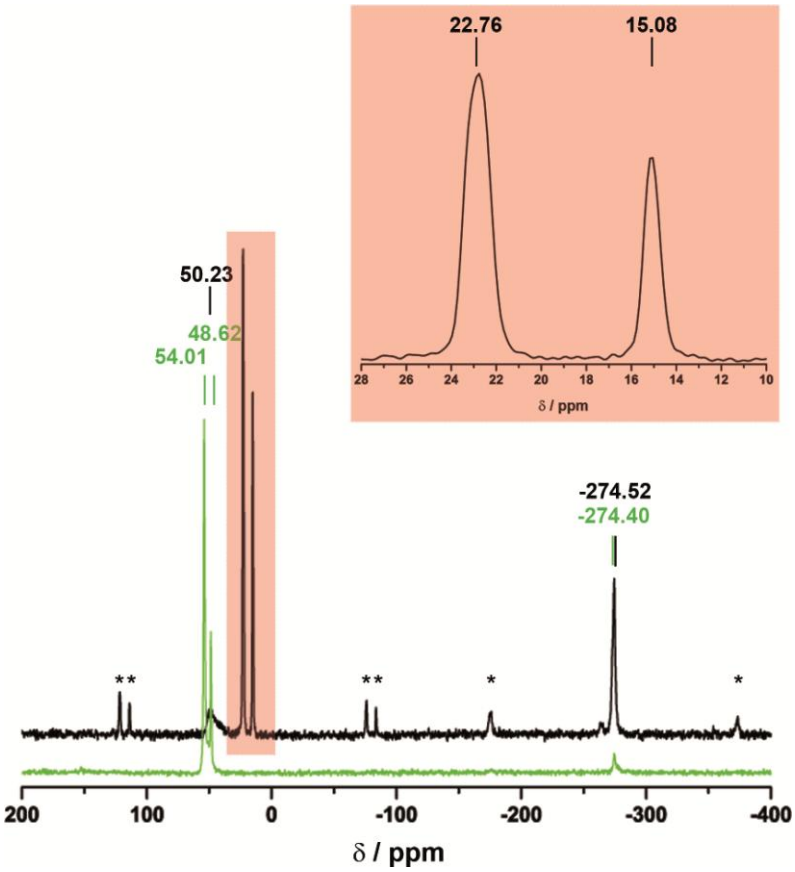

Figure S5. ^{31}P MAS NMR spectrum of $Li_{12}P_3N_9$ in black and the side phases Li_7PN_4 and Li_3P in green. Rotational sidebands are marked with asterisks.

The ^{31}P MAS NMR spectrum of $Li_{12}P_3N_9$ is shown in black and shows strong resonances at 15.08 and 22.76 ppm at a ratio of 2 to 1, which correspond to three crystallographically independent P sites (black). The ^{31}P MAS NMR-spectrum of Li_7PN_4 and Li_3P is shown in green (Li_7PN_4 with a little amount of Li_3P). The resonances at 48.62 and 54.01 ppm correspond to two crystallographically independent P sites of Li_7PN_4 (Wyck. 2*a* and 6*c* in $P\bar{4}3n$). The resonance at -274.40 ppm corresponds to Li_3P, which has one crystallographically independent site. The values for $Li_{12}P_3N_9$ correspond with those of other ternary nitridophosphates.[1]

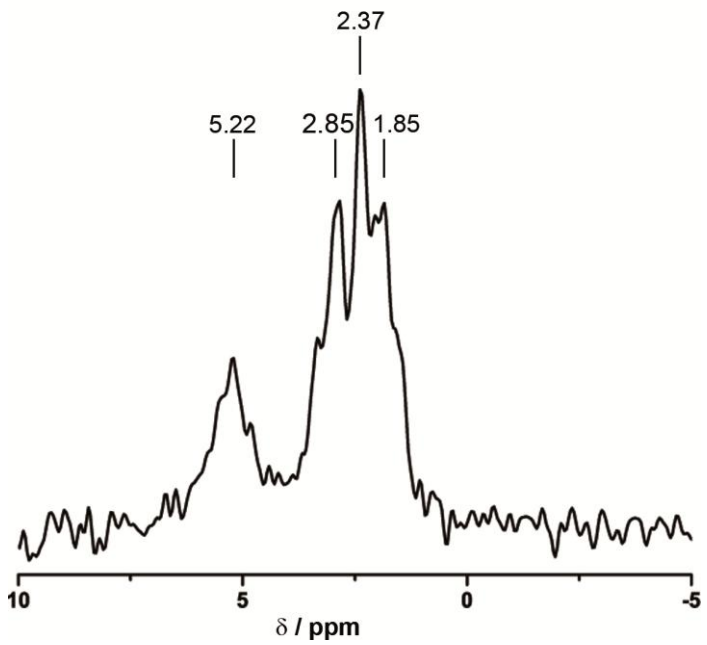

Figure S6. ^{6}Li MAS NMR spectrum of $Li_{12}P_3N_9$.

The ^{6}Li MAS NMR spectrum shows strong resonances between 5.22 and 1.85 ppm. Due to the small chemical shift differences of the signals, the differentiation of the 12 crystallographically independent sites cannot be observed in the spectrum.

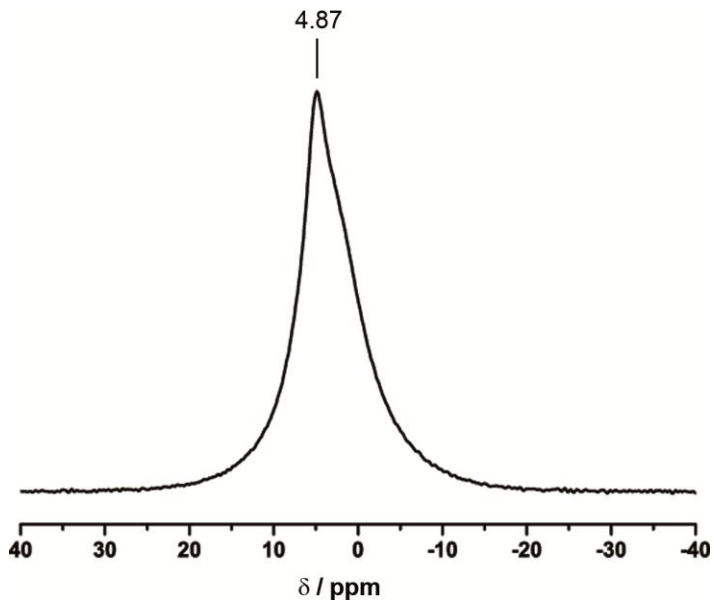

Figure S7. ^{7}Li MAS NMR spectrum of $Li_{12}P_3N_9$.

The ^{7}Li MAS NMR spectrum shows one strong resonances at 4.87 ppm. Due to the small chemical shift differences of the signals, no differentiation of the crystallographically independent sites can be observed in the spectrum. ^{7}Li MAS NMR spectra of different lithium nitridophosphates or silicates normally show one resonance in this range.[2-5]

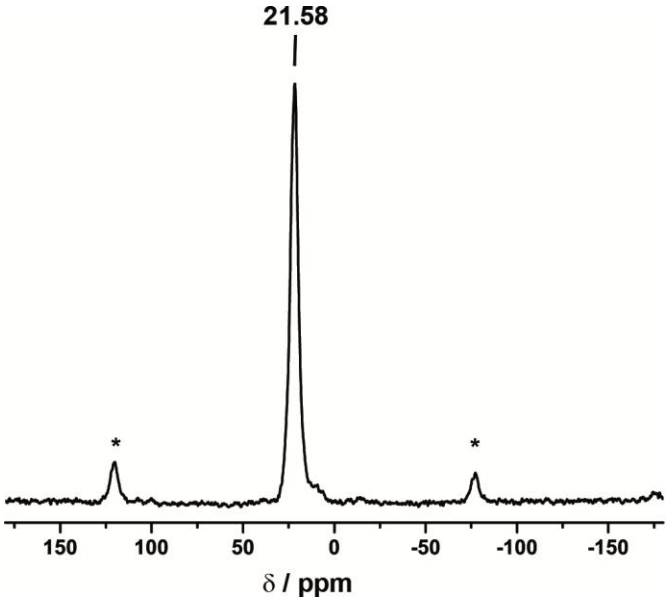

Figure S8. ^{31}P MAS NMR spectrum of Li_4PN_3. Rotational sidebands are marked with asterisks.

The ^{31}P MAS NMR spectrum shows one strong resonances at 21.58 ppm, which corresponds to one crystallographically independent P site. These values correspond with those of other ternary nitridophosphates.[1]

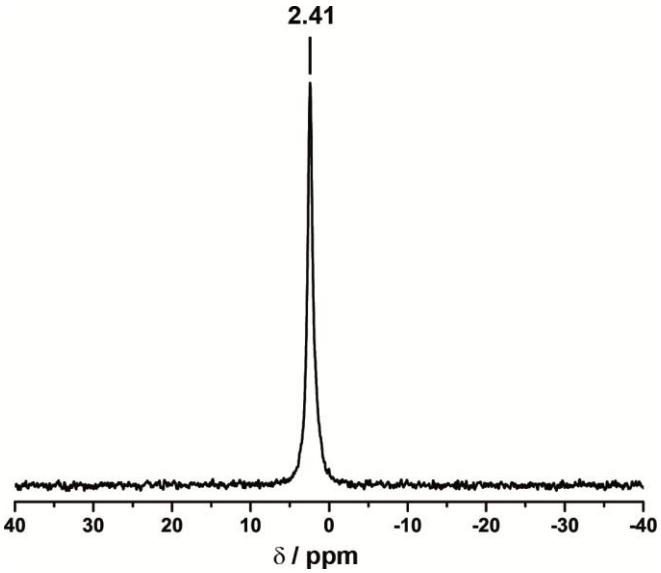

Figure S9. ^{6}Li MAS NMR spectrum of Li_4PN_3.

The ^{6}Li MAS NMR spectrum shows one strong resonances at 2.41 ppm. Due to the small chemical shift differences of the signals, no differentiation of the crystallographically independent sites can be observed in the spectrum.

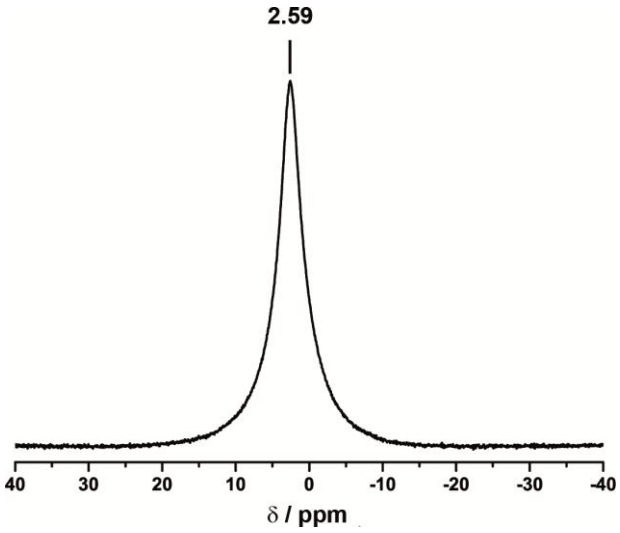

Figure S10. ^{7}Li MAS NMR spectrum of Li_4PN_3.

The ^{7}Li MAS NMR spectrum shows one strong resonances at 2.59 ppm. Due to the small chemical shift differences of the signals, no differentiation of the crystallographically independent sites can be observed in the spectrum. ^{7}Li MAS NMR spectra of different lithium nitridophosphates or silicates normally show one resonance in this range.[2-5]

A.6. Details of scanning electron microscopy

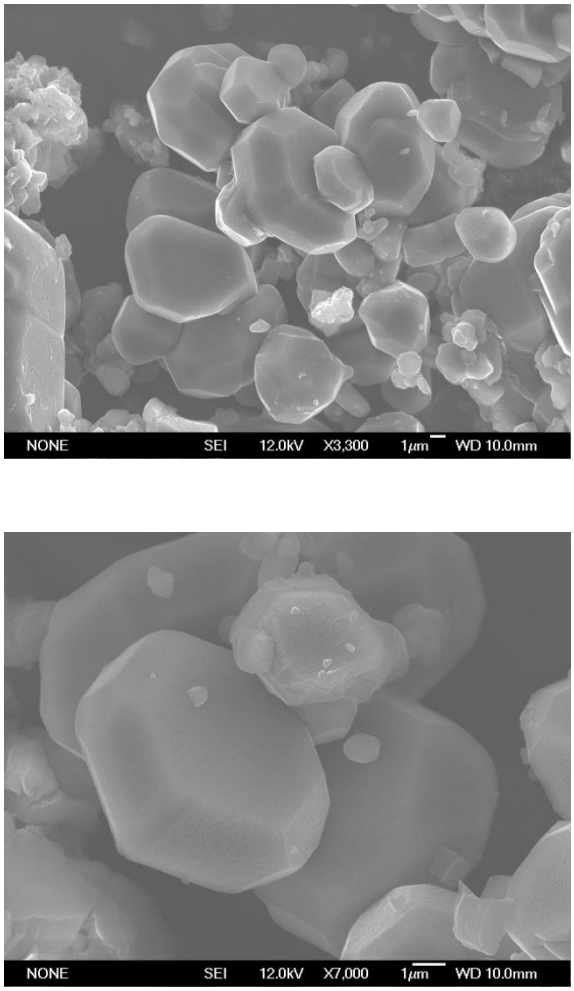

Figure S11. Scanning electron micrographs of $Li_{12}P_3N_9$.

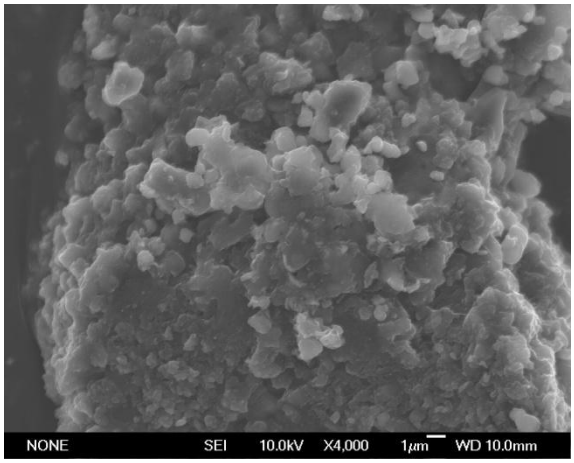

Figure S12. Scanning electron micrograph of Li_4PN_3.

Table S10. EDX analysis of $Li_{12}P_3N_9$.

	N	**O**	**P**
EDX point 1[atom %]	74.74	6.21	19.7
EDX point 2[atom %]	69.16	10.17	20.68
EDX point 3[atom %]	70.34	5.81	23.85
EDX point 4[atom %]	70.26	5.66	24.08
EDX point 5[atom %]	69.84	6.58	23.58
Average	**70.87**	**6.89**	**22.38**
Calculated atom %	**37.5**	**0**	**12.5**

Table S11. EDX analysis of Li_4PN_3.

	N	**O**	**P**
EDX point 1[atom %]	66.31	6.99	26.70
EDX point 2[atom %]	62.47	11.59	25.94
EDX point 3[atom %]	57.12	25.12	17.76
EDX point 4[atom %]	69.62	10.84	19.54
EDX point 5[atom %]	73.82	6.52	19.66
Average	**65.87**	**12.21**	**21.92**
Calculated atom %	**37.5**	**0**	**12.5**

Due to hydrolysis of the sample during mounting the sample at air, oxygen can be found in both samples.

A.7. FTIR spectrum

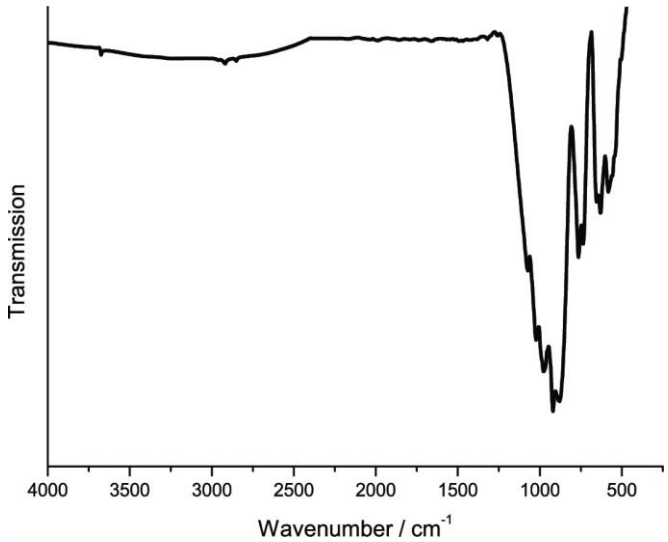

Figure S13. FTIR spectrum of $Li_{12}P_3N_9$.

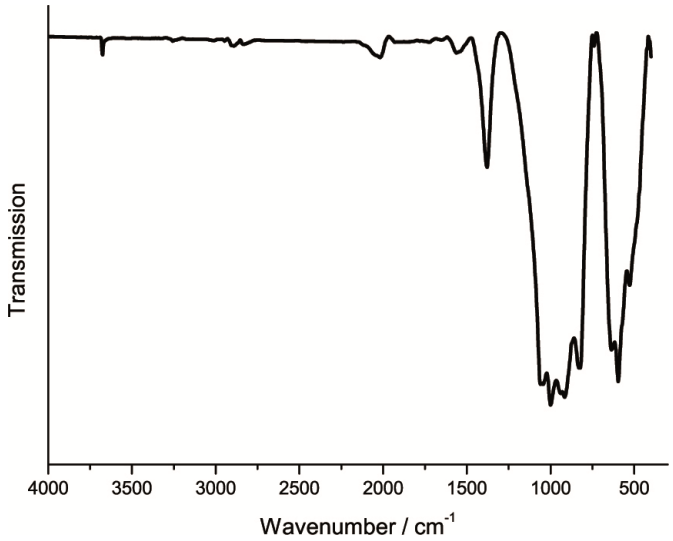

Figure S14. FTIR spectrum of Li_4PN_3.

Infrared spectroscopy measurements were performed on a Bruker FTIR-IFS 66v/S spectrometer. Before measurement in the range of 400-4000 cm^{-1} the sample was mixed with KBr in a glove box and cold-pressed into a pellet (Ø = 12 mm).The spectrum shows no significant valence vibrations in the region of 3000 cm^{-1}, where N–H vibrations are expected. A weak signal in that region can be explained by surface hydrolysis of the sample. Thus, the incorporation of

stoichiometric amounts of hydrogen seems unlikely. Much more significant are the characteristic PN framework vibrations between 600 and 1500 cm^{-1}.

A.8. Structural Analysis of Possible Lithium Migration Pathways

Possible voids and migration pathways in $Li_{12}P_3N_9$ and Li_4PN_3 were analyzed with TOPOS.[6-9]

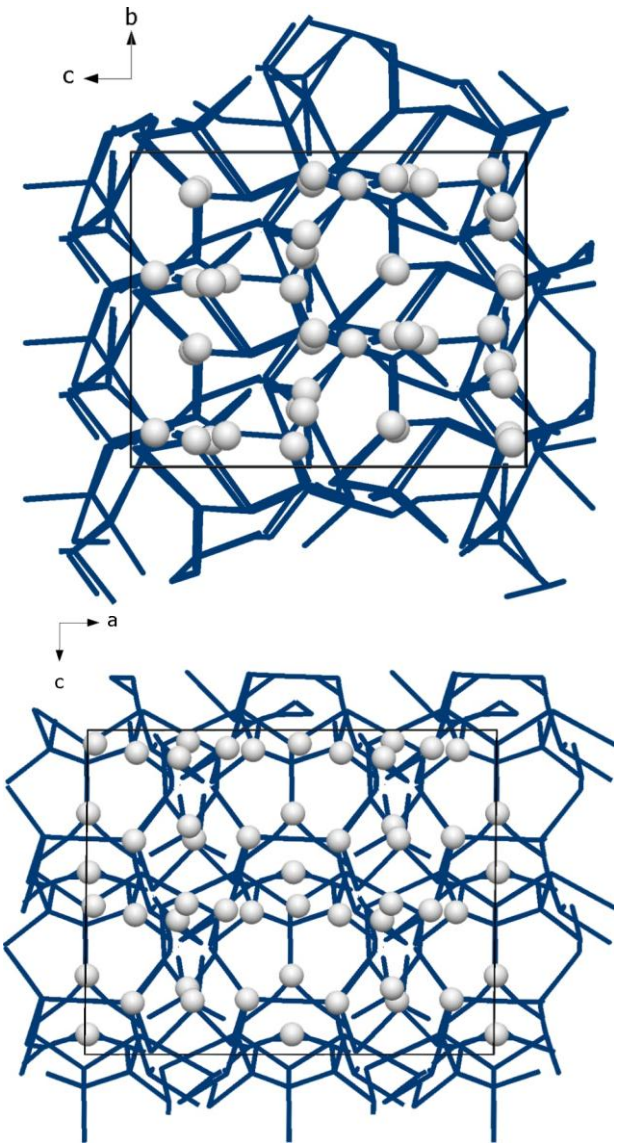

Figure S15. Calculated possible Li^+ pathways (blue) according to the voids in the structure and unit cell of $Li_{12}P_3N_9$.

A.9. Electron localization function

In order to analyze the chemical bonding with both compounds we calculated the electron localization function (ELF), constituting the probability of finding an electron of opposed spin within the proximity of another, effectively revealing positions of chemical bonds or electron lone pairs.[10] ELF is defined between 0 and 1, where 0 constitutes no localization, and a value of 0.5 being equivalent to a homogenous electron distribution as typically found in metals. Values close to 1 correspond to strong localization as found in covalent bonds.

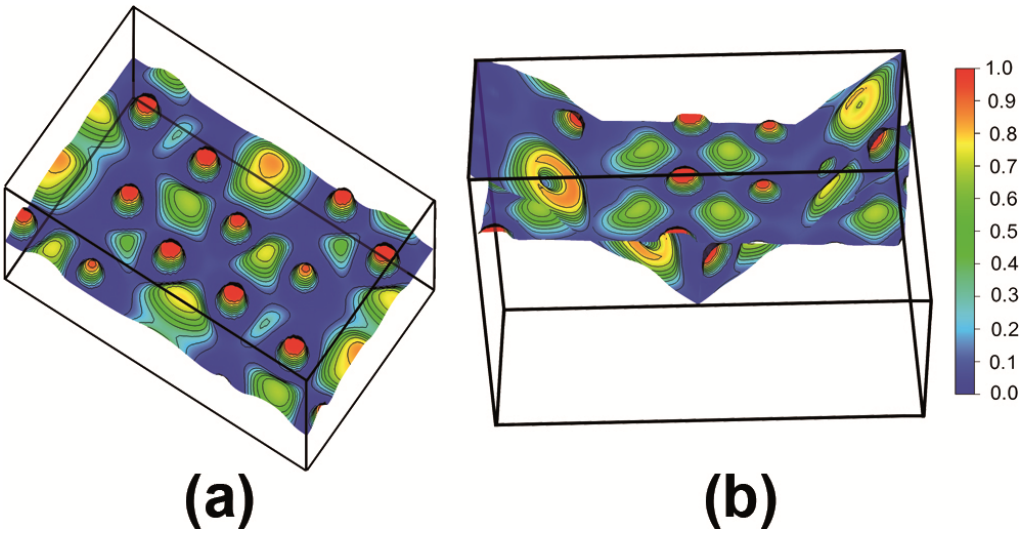

Figure S16. ELF contour plot with 0.15 increments, intersecting the Li atoms (seen as highly localized regions in red) within a chosen section of the unit cell of (a) $Li_{12}P_3N_9$ and (b) Li_4PN_3.

Figure S16 illustrate designated lattice planes of ELF intersecting the Li positions in both $Li_{12}P_3N_9$ and Li_4PN_3. The electron pair probability in terms of the ELF can be seen to be strongly localized solely around the Li atoms with no indication of contributions to covalent bonds between Li and N, corroborating chemical intuition of a strong ionic character. The P–N bonding situation for an ELF isovalue $\eta = 0.83$ reveals strong covalency within the $P_3N_9^{12-}$ and $PN_{2(2/2)}^{4-}$ units (Figure S17 and S18). The P–N bonds show strong N-polarization and free electron pairs of N^{3-} are found at terminal and bridging N atoms as expected from VSEPR considerations.

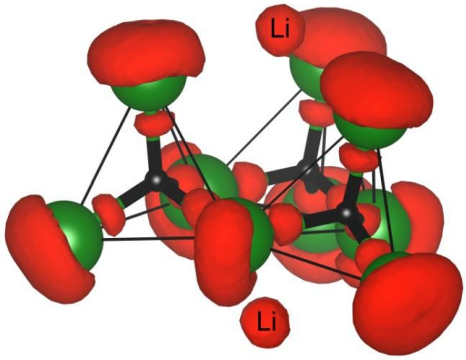

Figure S17. Isosurface of ELF (η = 0.83) for $Li_{12}P_3N_9$ in red. P: black; N: green; Li: gray.

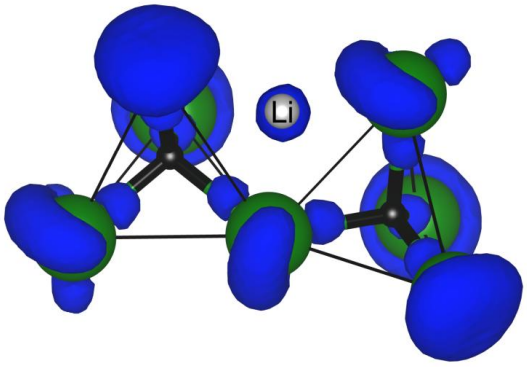

Figure S18. Isosurface of ELF (η = 0.83) for Li_4PN_3 in blue. P: black; N: green; Li: gray.

A.10. References

[1] K. Landskron, Doctoral Thesis, Universtiy of Munich, 2001.

[2] S. Pagano, M. Zeuner, S. Hug, W. Schnick, *Eur. J. Inorg. Chem.* **2009**, 1579–1584.

[3] S. Lupart, W. Schnick, *Z. Anorg. Allg. Chem.* **2012**, *638*, 2015–2019.

[4] S. Pagano, S. Lupart, S. Schmiechen, W. Schnick, *Z. Anorg. Allg. Chem.* **2010**, *636*, 1907–1909.

[5] M. Orth, W. Schnick, *Z. Anorg. Allg. Chem.* **1999**, *625*, 1426–1428.

[6] V. A. Blatov, *IUCr CompComm Newsl.* **2006**, *7*, 4–38.

[7] V. A. Blatov, *Crystallogr. Rev.* **2004**, *10*, 249–318.

[8] N. A. Anurova, V. A. Blatov, G. D. Ilyushin, O. A. Blatova, A. K. Ivanov-Schitz, L. N. Dem'yanets, *Solid State Ionics* **2008**, *179*, 2248–2254.

[9] V. A. Blatov, A. P. Shevchenko, V. N. Serezhin, *J. Appl. Crystallogr.* **2000**, *32*, 377–377.

[10] A. D. Becke, K. E. Edgecombe, *J. Chem. Phys.* **1990**, *92*, 5397–5403.

B. Supporting Information for Chapter 3

B.1. Additional crystallographic data for $Li_{18}P_6N_{16}$

Table S1. Fractional atomic coordinates, isotropic thermal displacement parameters, and site occupancies for $Li_{18}P_6N_{16}$.

Atom	Wyckoff Symbol	*x*	*y*	*z*	U_{iso} / Å^2	Occupancy
P1	2*i*	0.52929(11)	0.26103(8)	0.63851(6)		1
P2	2*i*	0.21417(11)	0.81732(8)	0.12234(6)		1
P3	2*i*	0.67764(10)	0.13016(8)	0.34642(6)		1
N1	2*i*	0.5378(4)	0.5458(3)	0.2802(2)		1
N2	2*i*	0.1937(4)	0.7549(3)	0.2709(2)		1
N3	2*i*	0.0674(4)	0.1841(3)	0.9530(2)		1
N4	2*i*	0.5579(4)	0.2597(3)	0.4746(2)		1
N5	2*i*	0.0540(4)	0.7286(3)	0.6628(2)		1
N6	2*i*	0.3196(4)	0.6681(3)	0.0072(2)		1
N7	2*i*	0.4415(4)	0.0468(3)	0.1844(2)		1
N8	2*i*	0.2788(4)	0.0635(3)	0.6212(2)		1
Li1	2*i*	0.1297(8)	0.0264(6)	0.4033(5)	0.0117(8)	1
Li2	2*i*	0.202(1)	0.2786(7)	0.7920(5)	0.0183(9)	1
Li3	2*i*	0.0785(10)	0.1228(8)	0.1450(6)	0.0219(10)	1
Li4	2*i*	0.3342(10)	0.3953(7)	0.3881(5)	0.0188(9)	1
Li5	2*i*	0.3710(11)	0.0989(8)	0.9653(6)	0.0247(11)	1
Li6	2*i*	0.6624(11)	0.3295(8)	0.1917(6)	0.0271(11)	1
Li7	2*i*	0.0638(13)	0.4199(9)	0.5862(7)	0.0328(13)	1
Li8	2*i*	0.392(3)	0.4440(17)	0.0551(14)	0.039(4)	0.6
Li9	2*i*	0.268(3)	0.4588(18)	0.0951(14)	0.030(5)	0.5
Li10	2*i*	0.130(5)	0.465(3)	0.113(2)	0.036(8)	0.35
Li11	2*i*	0.022(5)	0.429(3)	0.152(2)	0.066(7)	0.54

Table S2. Anisotropic displacement parameters occurring in $Li_{18}P_6N_{16}$.

Atom	U_{11} / Å^2	U_{22} / Å^2	U_{33} / Å^2	U_{12} / Å^2	U_{13} / Å^2	U_{23} / Å^2
P1	0.0042(2)	0.0038(2)	0.0030(2)	0.00149(18)	0.00122(18)	0.00130(18)
P2	0.0040(2)	0.0062(2)	0.0039(2)	0.00070(18)	0.00037(18)	0.00280(19)
P3	0.0030(2)	0.0035(2)	0.0033(2)	0.00094(18)	0.00064(18)	0.00092(18)
N1	0.0130(9)	0.0050(8)	0.0095(9)	0.0040(7)	0.0068(7)	0.0029(7)
N2	0.0039(8)	0.0081(8)	0.0044(8)	0.0016(6)	0.0009(6)	0.0037(7)
N3	0.0044(8)	0.0083(8)	0.0101(9)	0.0021(6)	-0.0001(7)	0.0039(7)
N4	0.0120(9)	0.0109(9)	0.0044(8)	0.0081(7)	0.0046(7)	0.0042(7)
N5	0.0047(8)	0.0050(8)	0.0103(9)	-0.0006(6)	0.0020(7)	0.0011(7)
N6	0.0108(9)	0.0059(8)	0.0074(8)	0.0039(7)	0.0060(7)	0.0033(7)
N7	0.0066(8)	0.0048(8)	0.0054(8)	-0.0008(6)	-0.0015(6)	0.0024(7)
N8	0.0046(8)	0.0044(8)	0.0062(8)	0.0014(6)	0.0000(6)	0.0022(6)

Table S3. List of interatomic distances / Å for $Li_{18}P_6N_{16}$.

P1—N1^{i}	1.588(2)	P1—N4	1.6456(19)	P1—N2^{i}	1.6733(19)
P1—N8	1.6764(19)	P2—N3^{iii}	1.583(2)	P2—N6	1.6164(19)
P2—N2	1.6850(19)	P2—N7^{iv}	1.6933(19)	P3—N5^{i}	1.6012(19)
P3—N8^{vi}	1.6541(19)	P3—N4	1.6678(19)	P3—N7	1.6955(19)
Li1—N8^{viii}	2.092(5)	Li1—N2^{x}	2.199(5)	Li1—N5^{iii}	2.516(5)
Li1—N8	2.071(5)	Li1—N4	2.358(5)	Li2—N1^{i}	2.051(5)
Li2—N2^{iii}	2.061(5)	Li2—N3	2.093(5)	Li2—N8	2.118(5)
Li3—N3^{viii}	2.073(6)	Li3—N3^{xi}	2.082(6)	Li3—N5^{iii}	2.207(6)
Li3—N7	2.199(6)	Li4—N1	2.033(5)	Li4—N4	2.026(5)
Li4—N4^{i}	2.379(5)	Li4—N5^{iii}	1.976(5)	Li5—N3	1.917(6)
Li5—N6^{i}	2.000(6)	Li5—N7^{vi}	2.110(6)	Li5—N7^{vii}	2.305(6)
Li6—N1	1.933(6)	Li6—N5^{i}	2.157(6)	Li6—N6^{ix}	1.984(6)
Li6—N7	2.130(6)	Li7—N1^{i}	2.247(7)	Li7—N2^{iii}	2.556(7)
Li7—N4^{xii}	2.583(7)	Li7—N5	2.224(7)	Li7—N5^{iii}	2.252(7)
Li8—N1	2.044(12)	Li8—N3^{xi}	2.084(12)	Li8—N6	2.005(12)
Li8—N6^{ix}	2.051(13)	Li9—N1	1.946(13)	Li9—N2	2.526(14)
Li9—N3^{xi}	1.984(12)	Li9—N6	2.009(12)	Li10—N1	2.34(2)
Li10—N2	2.144(19)	Li10—N3^{xi}	2.10(2)	Li10—N6	2.25(2)
Li10—N6^{v}	2.33(2)	Li11—N1	2.66(2)	Li11—N2	2.22(2)
Li11—N3^{xi}	2.33(2)	Li11—N5^{iii}	2.50(2)	Li11—N6^{v}	2.02(2)
Li8—Li8^{ix}	1.94(3)	Li8—Li9	0.847(17)	Li8—Li10	1.64(3)
Li8—Li11	2.35(3)	Li9—Li10	0.81(2)	Li9—Li11	1.52(3)
Li9—Li8^{ix}	2.65(2)	Li10—Li11	0.79(3)		

(i) 1-x, 1-y, 1-z; (ii) 1+x, y, z; (iii) -x, 1-y, 1-z; (iv) x, 1+y, z; (v) -x, 1-y, -z; (vi) 1-x, -y, 1-z; (vii) x, y, 1+z; (viii) -x, -y, 1-z; (ix) 1-x, 1-y, -z; (x) x, -1+y, z; (xi) x, y, -1+z; (xii) -1+x, y, z; (xiii) -x, -y, -z; (xiv) 1-x, -y, 2-z.

Table S4. List of bond angles / ° for $Li_{18}P_6N_{16}$.

N–P–N					
N1^{i}—P1—N4	107.65(10)	N3^{iii}—P2—N6	111.58(11)	N5^{i}—P3—N8^{vi}	111.59(10)
N1^{i}—P1—N2^{i}	114.63(10)	N3^{iii}—P2—N2	108.75(10)	N5^{i}—P3—N4	110.04(10)
N4—P1—N2^{i}	108.84(10)	N6—P2—N2	110.69(10)	N8^{vi}—P3—N4	111.44(10)
N1^{i}—P1—N8	107.81(10)	N3^{iii}—P2—N7^{iv}	111.04(10)	N5^{i}—P3—N7	109.87(10)
N4—P1—N8	110.75(10)	N6—P2—N7^{iv}	107.43(10)	N8^{vi}—P3—N7	108.49(9)
N2^{i}—P1—N8	107.16(9)	N2—P2—N7^{iv}	107.26(9)	N4—P3—N7	105.2(1)
P–N–P					
P1^{i}—N2—P2	115.79(11)	P1—N4—P3	133.55(12)	P2^{x}—N7—P3	119.84(11)
P1^{i}—N2—P2	115.79(11)	P1—N4—P3	133.55(12)	P2^{x}—N7—P3	119.84(11)
P3^{vi}—N8—P1	123.30(11)				

(i) 1-x, 1-y, 1-z; (ii) 1+x, y, z; (iii) -x, 1-y, 1-z; (iv) x, 1+y, z; (v) -x, 1-y, -z; (vi) 1-x, -y, 1-z; (vii) x, y, 1+z; (viii) -x, -y, 1-z; (ix) 1-x, 1-y, -z; (x) x, -1+y, z; (xi) x, y, -1+z; (xii) -1+x, y, z; (xiii) -x, -y, -z; (xiv) 1-x, -y, 2-z.

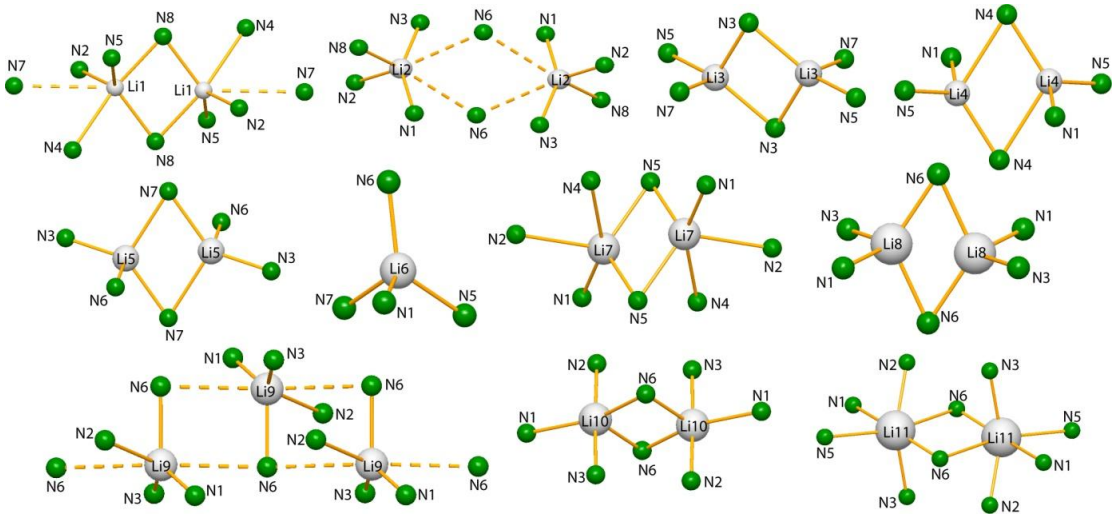

Figure S1. Coordination spheres of the Li^+ sites. Bond length up to 2.7 Å are shown by a continuous line and bond length from 2.7 to 3.0 Å are shown by dashed lines. Gray: Li, Green: N.

Depending on the adjustment of the bond length the Li^+ ions are coordinated by nitrogen forming $[LiN_4]$ and $[LiN_5]$ (bond length up to 2.7 Å) or $[LiN_4]$, $[LiN_5]$ and $[LiN_6]$ (bond length up to 3.0 Å) polyhedra which are sharing edges or corners. Assuming bond lengths Li–N ≤ 2.7 Å the atoms Li2 to Li6 and Li8 to Li9 are coordinated tetrahedrally. These distorted tetrahedra are all linked by corners, except Li8 and Li9 are furthermore linked by a common face. The polyhedron around Li7 is connected to the polyhedron of Li4 by an edge and the polyhedron of Li1 is connected with Li2 and Li4 by an edge each and additionally to the next Li1 by an edge. The polyhedrons of Li8 to Li11 are moreover edge sharing with the polyhedrons of Li3, Li4 and Li6.

B.2. Details of the Rietveld refinement

Table S5. Details of the Rietveld refinement of $Li_{18}P_6N_{16}$.

formula	**$Li_{18}P_6N_{16}$**
formula mass / g · mol^{-1}	534.9
crystal system / space group	triclinic $P\overline{1}$ (no. 2)
lattice parameters / Å, °	a = 5.42237(23)
	b = 7.53620(30)
	c = 9.86293(38)
	α = 108.4913(24)
	β = 99.3195(21)
	γ = 105.0244(21)
cell volume / Å^3	355.8
formula units per cell Z	1
X-ray density / g · cm^{-1}	2.49566(19)
linear absorption coefficient / cm^{-1}	73.79
radiation	Cu-$K_{\alpha 1}$ (λ = 1.540596 Å)
monochromator	Ge(111)
diffractometer	Stoe StadiP
detector	linear PSD
2θ-range / °	5.0-71.1
temperature / K	298 (2)
data points	4410
number of observed reflections	323
number of parameters	75
program used	TOPAS Academic
structure refinement	Rietveld method
profile function	fundamental parameters model
background function	shifted Chebyshev
R_{wp}	12.741
R_{exp}	8.606
R_p	9.999
R_{Bragg}	3.332
χ^2	1.480

B.3. Detailed Rietveld plot

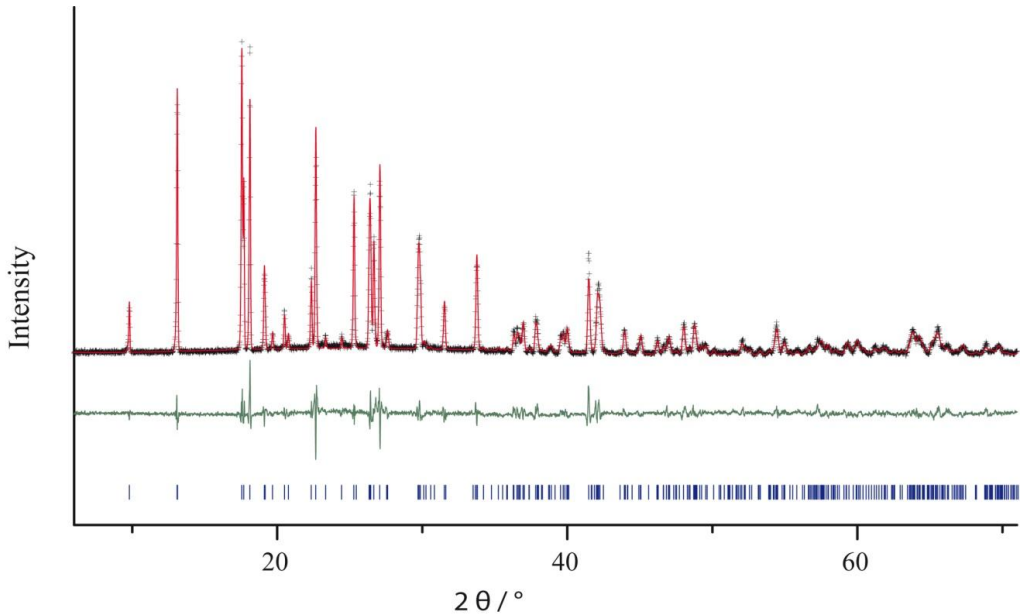

Figure S2. Observed (black crosses) and calculated (red line) powder diffraction pattern as well as difference profile (green) of the Rietveld refinement. Peak positions are marked by vertical blue bars.

Most probably the splitting of individual reflections (e.g. at $2\theta = 22.66$ $(1\ 0\ \overline{2})$ and $2\theta = 27.07$ $(1\ \overline{1}\ \overline{2})$ is due to different positions of the Li atoms in various crystals of the sample (figure S3). This variety of different Li^+ positions most likely is due to the mobility of the Li^+ ions which can be measured by impedance spectroscopy.

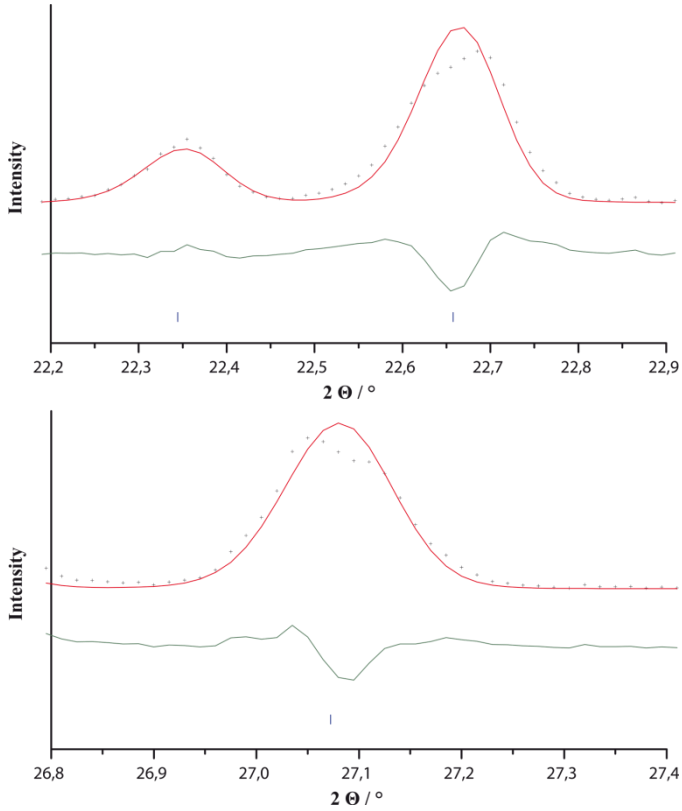

Figure S3. Rietveld refinement of $Li_{18}P_6N_{16}$ in the range of 22.2-27.4° 2θ.

B.4. ^{31}P and ^{7}Li solid state MAS NMR Spectroscopy

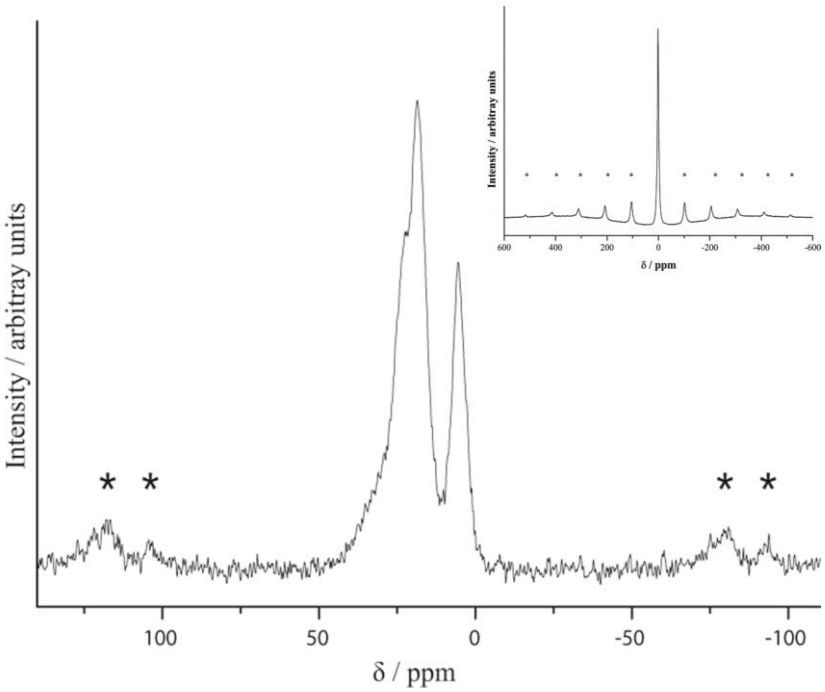

Figure S4. ^{31}P MAS NMR spectrum (left) and ^{7}Li MAS NMR spectrum (top right) of $Li_{18}P_6N_{16}$. Rotational sidebands are marked with asterisks.

The ^{31}P MAS NMR spectrum shows three strong resonances at 5.51, 18.57 and 22.24 ppm. These values correspond with those of other ternary nitridophosphates (−23.5 ppm for NaP_4N_7 to 54.6 ppm for Li_7PN_4).[1]

B.5. Details of scanning electron microscopy

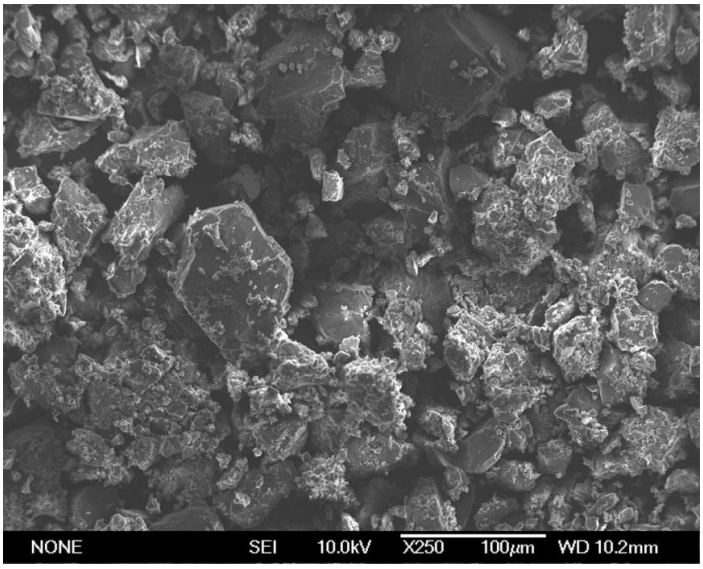

Figure S5. Scanning electron micrograph of a $Li_{18}P_6N_{16}$.

Table S6. EDX analysis of $Li_{18}P_6N_{16}$. Average of eight measuring points.

	N	**O**	**P**
EDX point 1[atom %]	65.53	9.77	22.70
EDX point 2[atom %]	63.73	10.31	25.96
EDX point 3[atom %]	71.57	9.86	18.57
EDX point 4[atom %]	64.52	14.86	20.62
EDX point 5[atom %]	73.05	7.05	19.91
EDX point 6[atom %]	70.42	8.11	21.48
EDX point 7[atom %]	68.56	9.27	22.17
EDX point 8[atom %]	65.35	11.74	22.91
Average	**68.09**	**10.12**	**21.79**
Calculated atom %	**72.7**	**0**	**27.3**

B.6. Temperature dependent powder X-ray diffraction

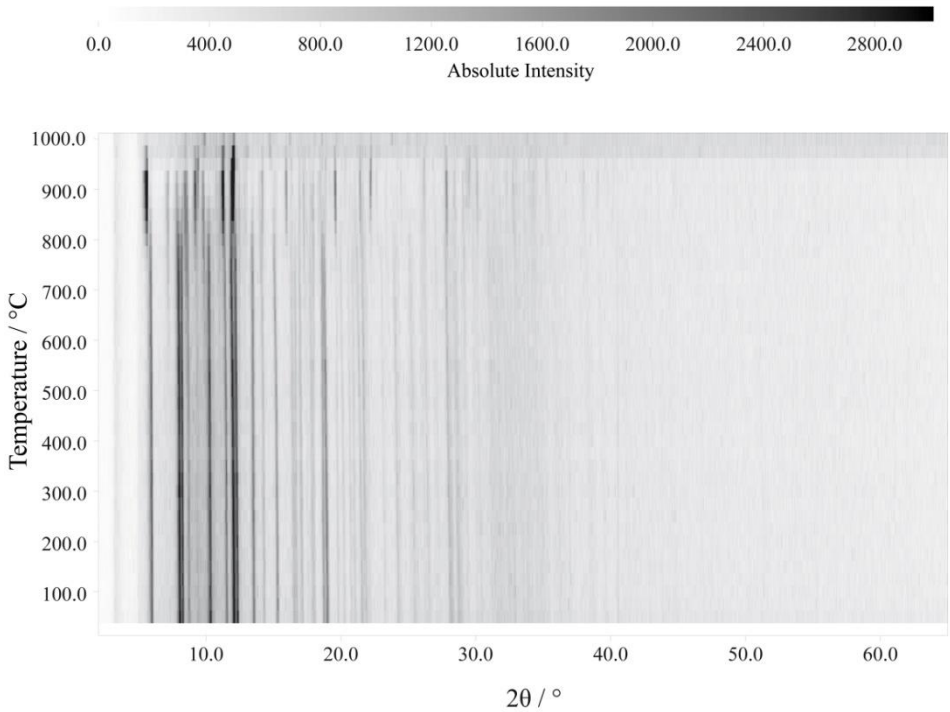

Figure S6. Temperature dependent powder X-ray diffractogram of $Li_{18}P_6N_{16}$.

B.7. FTIR spectrum

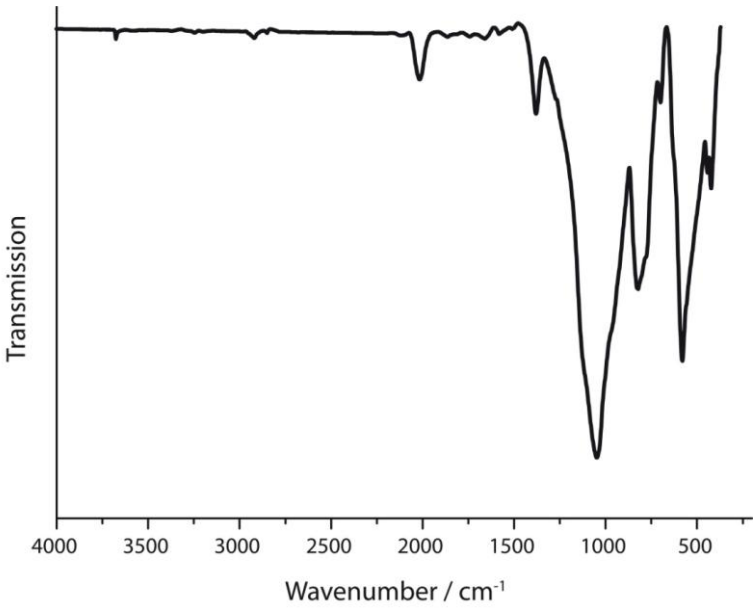

Figure S7. FTIR spectrum of $Li_{18}P_6N_{16}$.

Infrared spectroscopy measurements were performed on a Bruker FTIR-IFS 66v/S spectrometer. Before measurement in the range of 400-4000 cm^{-1} the sample was mixed with KBr in a glove box and cold-pressed into a pellet (Ø = 12 mm). The spectrum shows no significant valence vibrations in the region of 3000 cm^{-1}, where N–H vibrations are expected. A weak signal in that region can be explained by surface hydrolysis of the sample. Thus, the incorporation of stoichiometric amounts of hydrogen seems unlikely. Much more significant are the characteristic PN framework vibrations between 600 and 1500 cm^{-1}.

B.8. Structural Analysis of Possible Lithium Migration Pathways

Possible voids and migration pathways in $Li_{18}P_6N_{16}$ were analyzed with TOPOS.[2-5]

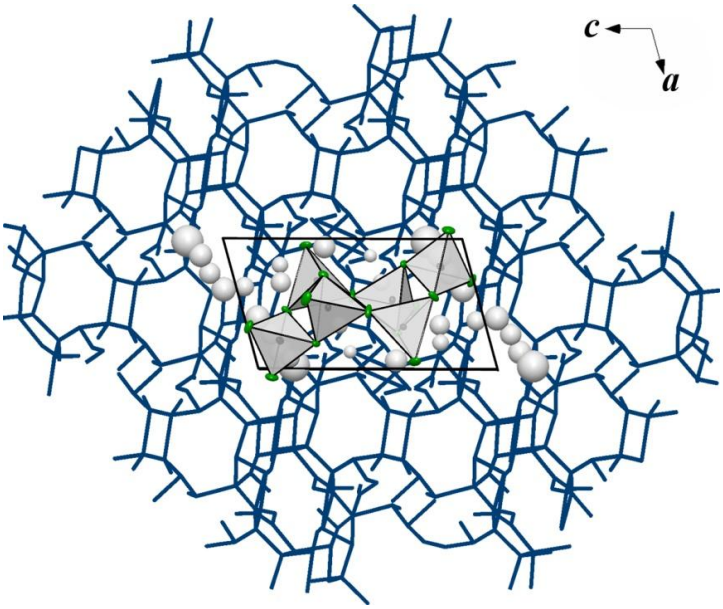

Figure S8. Calculated possible Li^+ pathways (black) according to the voids in the structure and unit cell of $Li_{18}P_6N_{16}$ viewing along *b*.

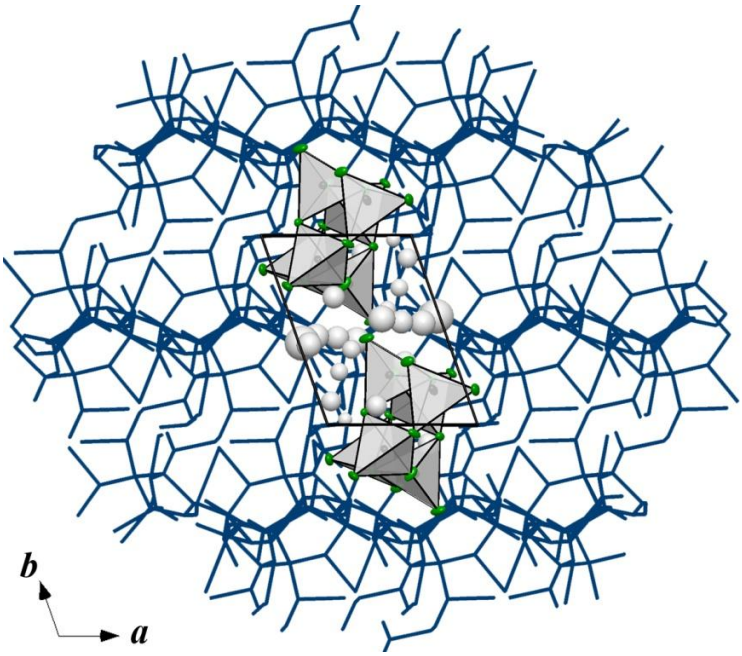

Figure S9. Calculated possible Li^+ pathways (black) according to the voids in the structure and unit cell of $Li_{18}P_6N_{16}$ viewing along *c*.

B.9. Details on the determination of the total conductivity of $Li_{18}P_6N_{16}$

Table S7. Impedance measurements of $Li_{18}P_6N_{16}$ at different temperatures.

Temperature / °C	**1/Temperature / K^{-1}**	**Raw. Res. / Ohm**	**Conductivity / S cm^{-1}**	**ln(conductivity · T^{-1})**
25	0.00337	$1.49 \cdot 10^{7}$	$7.70861 \cdot 10^{-8}$	-22.07258
35	0.00326	$8.61 \cdot 10^{6}$	$1.33132 \cdot 10^{-7}$	-21.55926
45	0.00315	$4.48 \cdot 10^{6}$	$2.55864 \cdot 10^{-7}$	-20.938
55	0.00306	$5.41 \cdot 10^{6}$	$4.75631 \cdot 10^{-7}$	-20.34904
65	0.00297	$1.34 \cdot 10^{6}$	$8.55425 \cdot 10^{-7}$	-19.79219
75	0.00288	$8.02 \cdot 10^{5}$	$1.42926 \cdot 10^{-6}$	-19.30811

Table S8. Data for Arrhenius plot.

equation	y = a + b · x		
weighting	no weighing		
Sum of the squares	0.00958		
Pearson R	-0.99914		
cor. R-square	0.99785		
		value	standard error
ln(conductivity)	interception of the y-axis	-2.58622	0.37626
ln(conductivity)	gradient	-5809.23796	120.69887

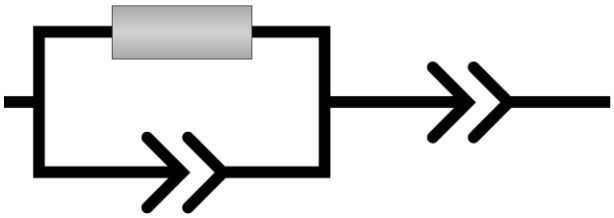

Figure S10. Equivalent circuit diagram used for the fits. The scare corresponds to the ohmic resistance and the arrows correspond to the constant phase elements.

B.10. References

[1] K. Landskron, Doctoral Thesis, University of Munich (LMU), 2001.

[2] Blatov, V. A. *IUCr CompComm Newsl.* **2006**, *7*, 4–38.

[3] Blatov, V. A. *Crystallogr. Rev.* **2004**, *10* (4), 249–318.

[4] Anurova, N. A.; Blatov, V. A.; Ilyushin, G. D.; Blatova, O. A.; Ivanov-Schitz, A. K.; Dem'yanets, L. N. *Solid State Ionics* **2008**, *179* (39), 2248–2254.

[5] Blatov, V. A.; Shevchenko, A. P.; Serezhin, V. N. *J. Appl. Crystallogr.* **2000**, *32*, 377-377.

C. Supporting Information for Chapter 4

C.1. Additional crystallographic data for β-$Li_{10}P_4N_{10}$

Due to the floating origin of the space group *R*3, the P1 position was not refined freely and therefore no error is given for P1.

Table S1. Fractional atomic coordinates, isotropic thermal displacement parameters, and site occupancies for β-$Li_{10}P_4N_{10}$ in space group *R*3 (no. 146).

Atom	Wyckoff position	*x*	*y*	*z*	U_{iso} / Å^2	Occupancy
P1	3*a*	0	0	0.89345	0.0074(2)	1
P2	9*b*	0.8866(5)	0.4372(5)	0.3365(5)	0.0074(2)	1
P3	3*a*	0	0	0.3066(2)	0.0074(2)	1
P4	9*b*	0.1180(5)	0.5558(6)	0.8635(5)	0.0074(2)	1
N1	9*b*	0.131(2)	0.574(2)	0.6921(8)	0.0043(5)	1
N2	9*b*	0.864(2)	0.4198(14)	0.2567 (8)	0.0043(5)	1
N3	3*a*	0	0	0.8182(14)	0.0043(5)	1
N4	9*b*	0.892(2)	0.789(2)	0.1743(8)	0.0043(5)	1
N5	9*b*	0.778(2)	0.240(2)	0.6098(9)	0.0043(5)	1
N6	3*a*	2/3	1/3	0.7130(13)	0.0043(5)	1
N7	9*b*	0.8900(12)	0.1491 (10)	0.5074(8)	0.0043(5)	1
N8	9*b*	0.1364(13)	0.8921(11)	0.6913(7)	0.0043(5)	1
Li1	9*b*	0.905(3)	0.159(3)	0.4168(11)	0.0199(18)	1
Li2	9*b*	0.850(4)	0.173(6)	0.2720(12)	0.0199(18)	1
Li3	3*a*	1/3	2/3	0.140(2)	0.0199(18)	1
Li4	9*b*	0.785(3)	0.211(4)	0.1305(10)	0.0199(18)	1
Li5	9*b*	0.155(3)	0.805(2)	0.3556(9)	0.0199(18)	1
Li6	9*b*	0.787(3)	0.191(4)	0.8688(9)	0.0199(18)	1
Li7	3*a*	0	0	0.7137(14)	0.0199(18)	1
Li8	3*a*	0	0	0.101(5)	0.0199(18)	1
Li9	9*b*	0.212(4)	1.018(6)	0.6158(14)	0.049(11)	2/3

Table S2. List of interatomic distances / Å for β-$Li_{10}P_4N_{10}$.

P1—N3	1.62(3)	P1—N2	1.63(2)	P2—N2	1.72(2)
P2—N1	1.70(2)	P2—N1	1.65(2)	P2—N8	1.60(2)
P3—N6	1.57(3)	P3—N5	1.68(2)	P4—N4	1.64(2)
P4—N4	1.724(14)	P4—N5	1.71(2)	P4—N7	1.54(2)
Li1—N7	1.95(3)	Li1—N1	2.05(3)	Li1—N6	2.10(3)
Li2—N5	2.00(4)	Li2—N2	2.12(6)	Li2—N1	2.15(4)
Li2—N4	2.26(4)	Li2—N5	2.28(6)	Li2—N2	2.44(4)
Li3—N6	2.01(5)	Li3—N7	2.10(2)	Li3—N7	2.10(2)
Li3—N7	2.10(2)	Li4—N3	1.87(4)	Li4—N4	1.88(4)
Li4—N8	2.28(3)	Li5—N8	2.17(2)	Li5—N8	2.19(3)
Li5—N5	2.04(3)	Li5—N6	2.70(3)	Li6—N2	1.96(4)
Li6—N7	2.00(3)	Li6—N7	2.13(3)	Li7—N8	1.910(12)
Li7—N8	1.910(12)	Li7—N8	1.91(2)	Li7—N3	2.24(4)
Li8—N1	2.23(6)	Li8—N1	2.23(6)	Li8—N4	2.24(6)
Li8—N1	2.23(7)	Li8—N4	2.24(6)	Li8—N4	2.24(6)
Li9—N2	2.33(6)	Li9—N5	2.01(3)	Li9—N8	1.88(4)
Li9—N7	2.43(4)				

Table S3. List of bond angles / ° for β-$Li_{10}P_4N_{10}$.

N–P–N					
N1—P2—N2	93.431(661)	N2—P1—N2	37.273(407)	N4—P4—N7	35.041(453)
N1—P2—N1	37.988(411)	N2—P1—N2	37.273(542)	N4—P4—N5	38.751(545)
N1—P2—N1	94.366(722)	N2—P1—N1	94.817(794)	N4—P4—N5	92.543(785)
N1—P2—N2	38.287(433)	N2—P1—N1	93.562(709)	N4—P4—N4	35.894(471)
N1—P2—N8	31.569(337)	N2—P1—N3	33.238(339)	N4—P4—N4	91.923(730)
N1—P2—N8	150.183(699)	N2—P1—N8	151.104(892)	N4—P4—N7	143.327(891)
N1—P2—N2	39.605(514)	N2—P2—N2	95.858(671)	N4—P4—N7	148.9(9)
N1—P2—N1	93.296(609)	N2—P2—N2	93.653(829)	N4—P4—N5	92.390(774)
N1—P2—N1	36.816(542)	N2—P2—N1	38.812(558)	N4—P4—N5	36.647(507)
N1—P2—N2	93.371(660)	N2—P2—N1	36.378(566)	N4—P4—N4	90.100(699)
N1—P2—N8	150.455(774	N2—P2—N3	151.895(935)	N4—P4—N4	33.868(449)
N1—P2—N8	31.323(356)	N2—P2—N8	32.418(511)	N4—P4—N7	29.544(404)
N5—P3—N4	94.865(828)	N5—P3—N6	32.355(332)	N5—P4—N5	91.192(816)
N5—P3—N7	147.424(912)	N5—P3—N4	91.246(739)	N5—P4—N5	92.979(722)
N5—P3—N5	36.919(490)	N5—P4—N4	36.79(59)	N5—P4—N6	147.327(102)
N5—P3—N5	36.919(417)	N5—P4—N7	32.476(573)	N5—P4—N4	36.928(593)

N3—P1—N2	33.522(345)	N7—P4—N4	37.683(433)	N8—P2—N1	32.685(388)
N3—P1—N2	33.522(358)	N7—P4—N5	36.691(508)	N8—P2—N2	35.289(455)
N3—P1—N2	33.522(360)	N7—P4—N4	33.525(461)	N8—P2—N1	33.421(468)
N6—P3—N5	35.041(400)				
N6—P3—N5	35.040(399)				
N6—P3—N5	35.040(388)				
P–N–P					
P1—N3—P2	144.796(173)	P2—N8—P2	145.310(429)	P3—N6—P4	145.388(186)
P1—N3—P2	144.796(184)	P2—N8—P2	146.728(514)	P3—N6—P4	145.385(191)
P1—N3—P2	144.796(184)	P2—N8—P1	141.957(520)	P3—N6—P4	145.388(191)
P1—N2—P2	31.602(443)	P2—N1—P2	86.562(497)	P3—N5—P4	86.032(557)
P1—N2—P2	85.641(589)	P2—N1—P2	30.999(620)	P3—N5—P4	32.810(573)
P1—N2—P2	87.734(588)	P2—N1—P1	86.081(643)	P3—N5—P4	87.742(603)
P1—N2—P2	85.641(507)	P2—N1—P2	30.095(438)	P3—N5—P4	87.742(553)
P1—N2—P2	87.734(571)	P2—N1—P2	85.773(637)	P3—N5—P4	86.032(604)
P1—N2—P2	31.602(570)	P2—N1—P1	85.306(625)	P3—N5—P4	32.810(565)
P1—N2—P2	87.734(502)	P2—N2—P2	84.180(465)	P3—N5—P4	32.810(489)
P1—N2—P2	31.602(548)	P2—N2—P2	86.165(654)	P3—N5—P4	87.742(612)
P1—N2—P2	85.641(573)	P2—N2—P1	29.685(577)	P3—N5—P4	86.032(615)
P4—N4—N4	110.238(735)	P4—N4—P4	32.121(476)	P4—N4—P4	88.143(573)
P4—N4—P4	89.826(536)	P4—N5—P4	88.718(521)	P4—N7—P4	148.950(431)
P4—N4—P4	34.013(576)	P4—N5—P4	87.011(628)	P4—N7—P4	141.283(503)
P4—N4—P3	88.294(648)	P4—N5—P3	32.187(645)	P4—N7—P3	142.970(527)
P4—N4—P3	86.713(619)				

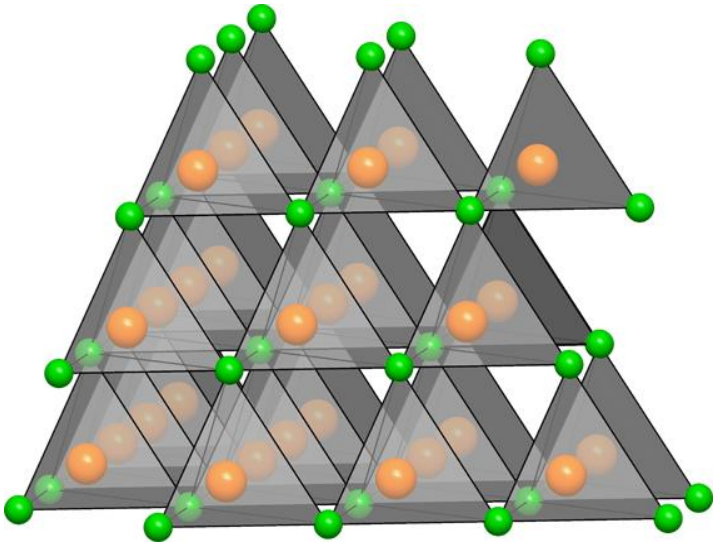

Figure S1. Packing of the AB_4 tetrahedra (A: centers of gravity of $[P_4N_{10}]^{10-}$ supertetrahedra of one orientation (orange), B: centers of gravity of the other orientation (green).

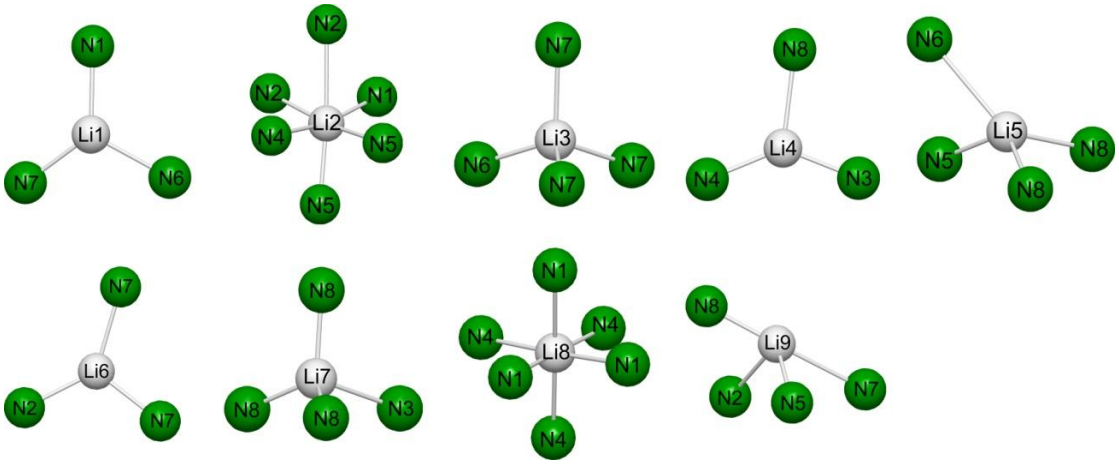

Figure S2. Coordination spheres of the Li^+ sites. Bond length up to 2.88 Å are shown by gray lines. Li: gray, N: green.

C.2. Additional crystallographic data for $Li_{13}P_4N_{10}Cl_3$

Table S4. Fractional atomic coordinates, isotropic thermal displacement parameters, and site occupancies for $Li_{13}P_4N_{10}Cl_3$ in space group $Fm\overline{3}m$ (no. 225).

Atom	Wyckoff position	*x*	*y*	*z*	U_{iso} / Å^2	Occupancy
P1	32*f*	0.8223(1)	0.8223(1)	0.3223(1)	0.05	1
N1	32*f*	0.3875(2)	0.6125(2)	0.6125(2)	0.05	1
N2	48*g*	1/4	3/4	0.1136(2)	0.05	1
Cl1	24*e*	0	1/2	0.3166(1)	0.05	1
Li1	24*e*	0	0	0.3582(6)	0.05	1
Li2	32*f*	0.1289(5)	0.8711(5)	0.8711(5)	0.05	1
Li3	48*i*	0.1841(5)	0.1841(5)	1/2	0.05	1

Table S5. List of interatomic distances / Å for $Li_{13}P_4N_{10}Cl_3$.

P1—N2	1.681(2)	P1—N1	1.573(3)		
Li1—N1	2.254(3)	Li2—N2	2.396(7)	Li3—N2	2.047(5)
Li1—Cl1	2.435(9)	Li2—Cl1	2.651(7)	Li3—N1	2.109(5)

Table S6. List of bond angles / ° for $Li_{13}P_4N_{10}Cl_3$.

N–P–N			
N2—P1—N2	106.11(10)	N1—P1—N2	112.65(15)
P–N–P			
P1—N2—P1	115.83(17)		

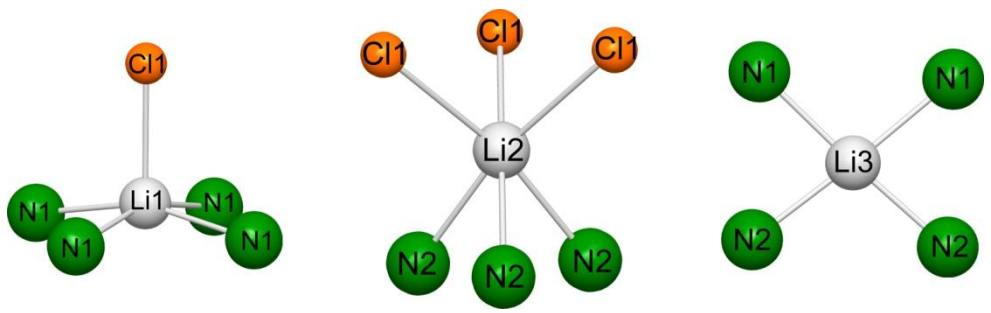

Figure S3. Coordination spheres of the Li^+ sites. Bond length up to 2.88 Å are shown by gray lines. Cl: orange, Li: gray, N: green.

C.3. Additional crystallographic data for $Li_{13}P_4N_{10}Br_3$

Table S7. Fractional atomic coordinates, isotropic thermal displacement parameters, and site occupancies for $Li_{13}P_4N_{10}Br_3$ in space group $Fm\overline{3}m$ (no. 225).

Atom	Wyckoff position	*x*	*y*	*z*	U_{iso} / Å^2	Occupancy
P1	32*f*	0.8213(1)	0.8213(1)	0.3213(1)	0.05	1
N1	32*f*	0.3847(2)	0.6153(2)	0.6153(2)	0.05	1
N2	48*g*	1/4	3/4	0.1158(3)	0.05	1
Br1	24*e*	0	1/2	0.3146(1)	0.05	1
Li1	24*e*	0	0	0.3665(11)	0.05	1
Li2	32*f*	0.1345(8)	0.8655(8)	0.8655(8)	0.05	1
Li3	48*i*	0.1817(7)	0.1817(7)	1/2	0.05	1

Table S8. List of interatomic distances / Å for $Li_{13}P_4N_{10}Br_3$.

P1—N1	1.549(3)	P1—N2	1.677(3)		
Li1—N1	2.315(3)	Li2—N2	2.320(12)	Li3—N1	2.098(6)
Li1—Br1	2.556(2)	Li2—Br1	2.778(11)	Li3—N2	2.128(7)

Table S9. List of bond angles / ° for $Li_{13}P_4N_{10}Br_3$.

N–P–N			
N2—P1—N2	105.97(12)	N1—P1—N2	112.78(18)
P–N–P			
P1—N2—P1	116.1(3)		

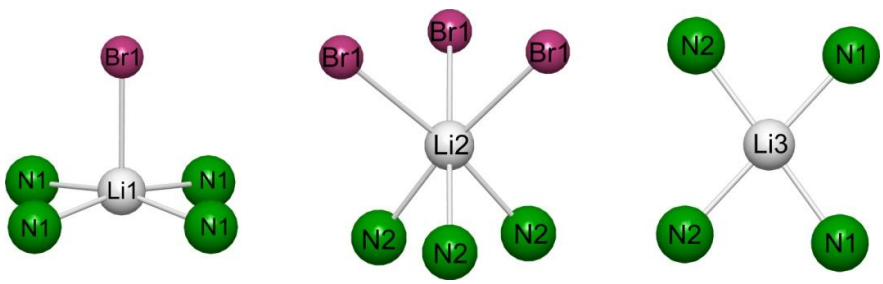

Figure S4. Coordination spheres of the Li^+ sites. Bond length up to 2.88 Å are shown by gray lines. Br: violet, Li: gray, N: green.

C.4. Detailed Rietveld plots

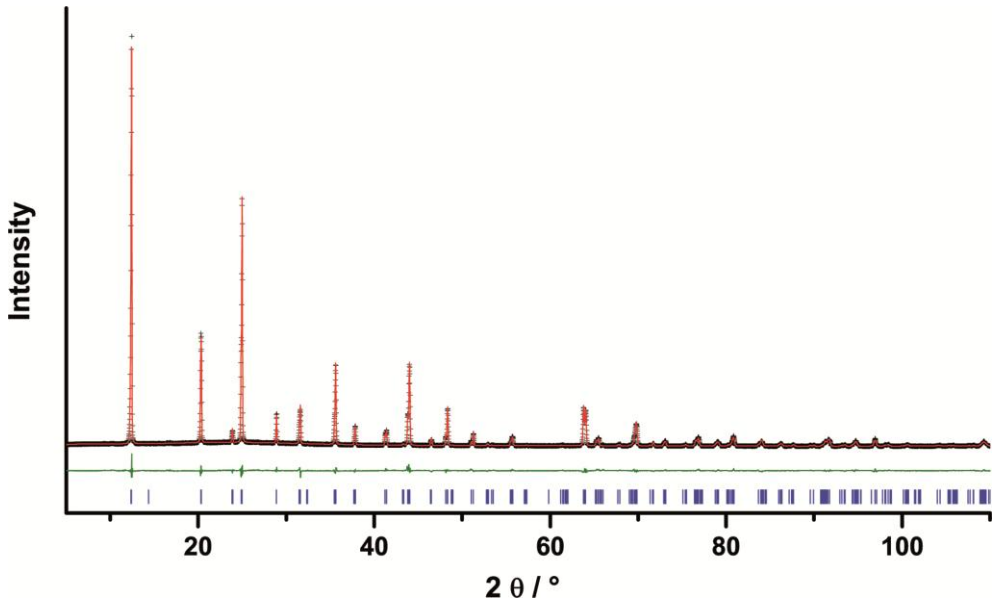

Figure S5. β-$Li_{10}P_4N_{10}$: Observed (black crosses) and calculated (red line) powder diffraction pattern as well as difference profile (green) of the Rietveld refinement in space group $R\bar{3}m$. Reflection positions are marked by vertical blue bars. It was measured with Cu-$K_{\alpha 1}$ radiation. (R_{wp} = 0.0578, R_{exp} = 0.0255, R_p = 0.0424, R_{Bragg} = 0.0209, *GooF* = *2.267* with 47 parameters)

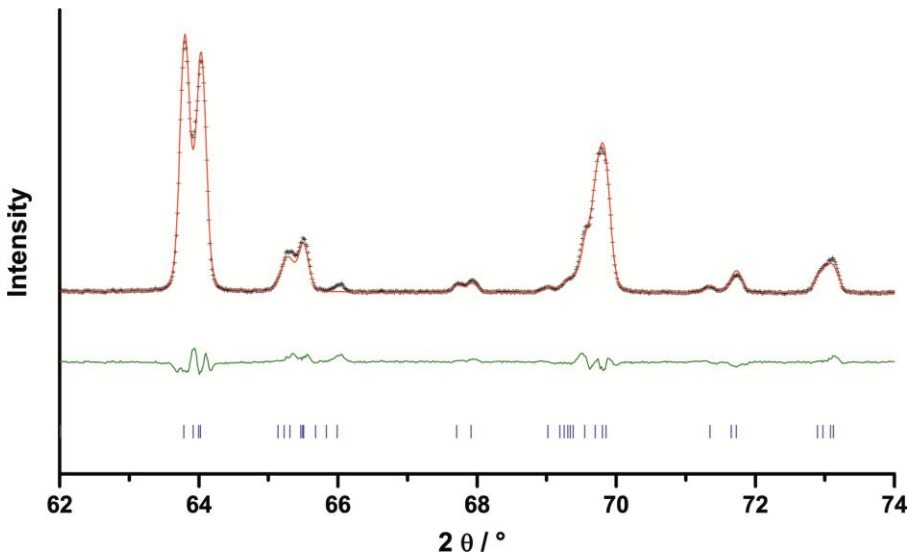

Figure S6. β-$Li_{10}P_4N_{10}$: Observed (black crosses) and calculated (red line) powder diffraction pattern as well as difference profile (green) of the Rietveld refinement in $R\bar{3}m$. Reflection positions are marked by vertical blue bars. It was measured with Cu-$K_{\alpha 1}$ radiation.

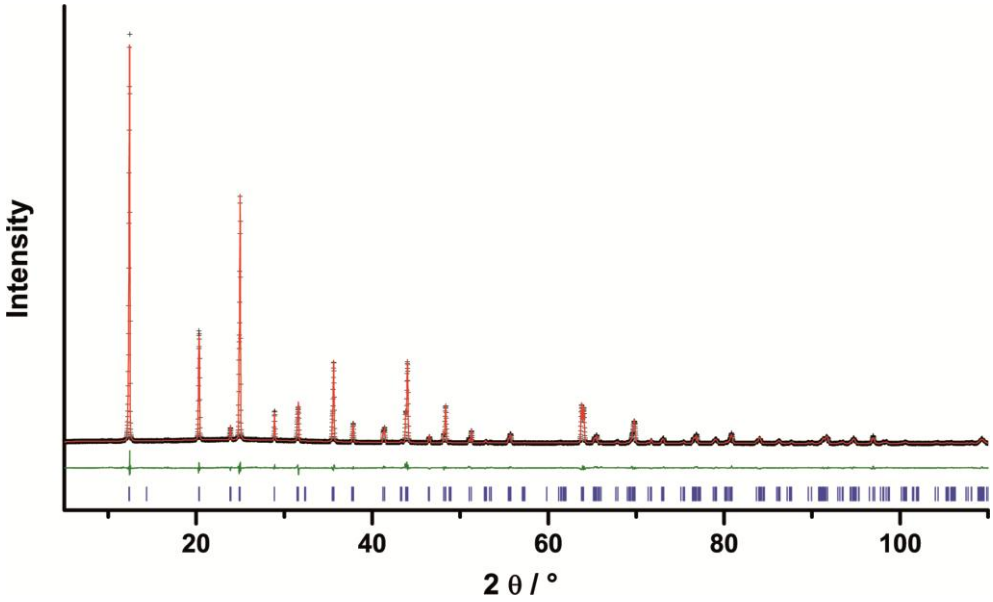

Figure S7. β-$Li_{10}P_4N_{10}$: Observed (black crosses) and calculated (red line) powder diffraction pattern as well as difference profile (green) of the Rietveld refinement in $R\overline{3}$. Reflection positions are marked by vertical blue bars. It was measured with Cu-$K_{\alpha 1}$ radiation. (R_{wp} = 0.0579, R_{exp} = 0.0255, R_p = 0.0425, R_{Bragg} = 0.0208, *GooF* = 2.270 with 46 parameters)

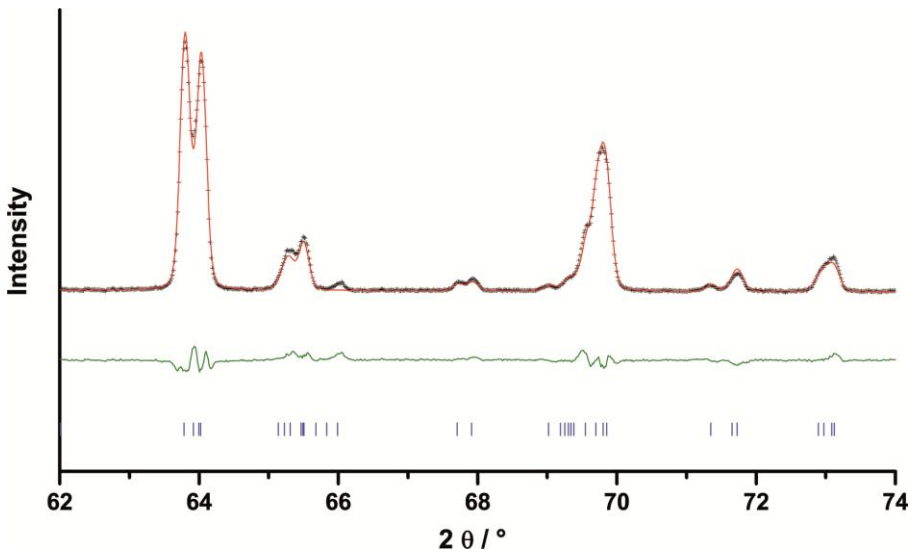

Figure S8. β-$Li_{10}P_4N_{10}$: Observed (black crosses) and calculated (red line) powder diffraction pattern as well as difference profile (green) of the Rietveld refinement in $R\overline{3}$. Reflection positions are marked by vertical blue bars. It was measured with Cu-$K_{\alpha 1}$ radiation.

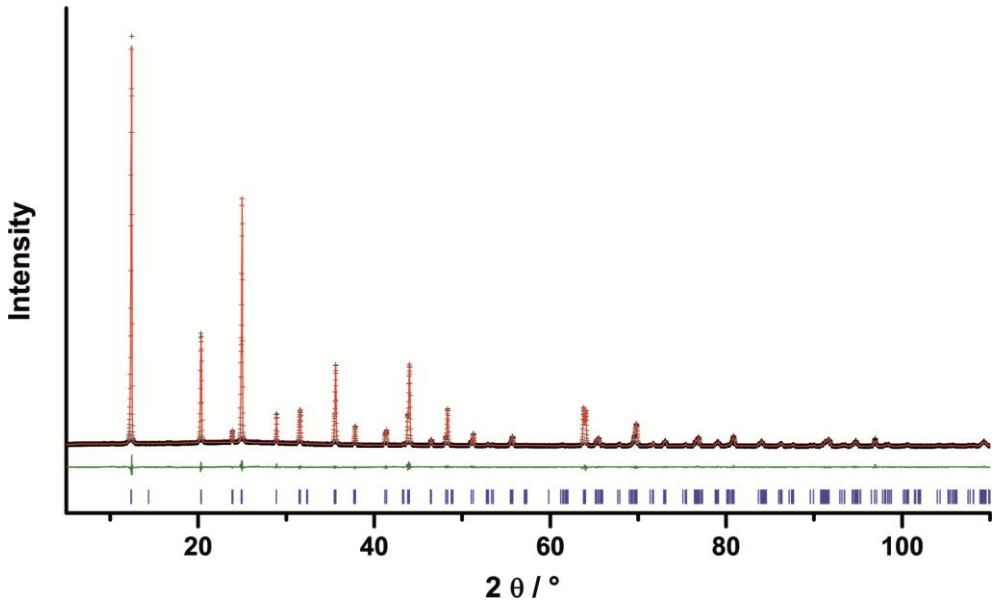

Figure S9. β-$Li_{10}P_4N_{10}$: Observed (black crosses) and calculated (red line) powder diffraction pattern as well as difference profile (green) of the Rietveld refinement in *R*3. Reflection positions are marked by vertical blue bars. It was measured with Cu-$K_{\alpha 1}$ radiation. (R_{wp} = 0.0493, R_{exp} = 0.0255, R_p = 0.0369, R_{Bragg} = 0.0146, *GooF* = 1.938 with 79 parameters)

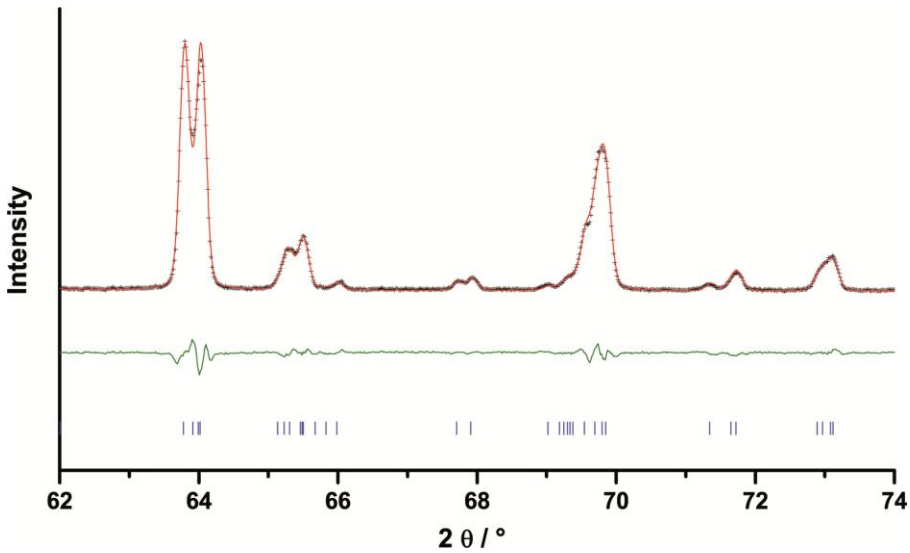

Figure S10. β-$Li_{10}P_4N_{10}$: Observed (black crosses) and calculated (red line) powder diffraction pattern as well as difference profile (green) of the Rietveld refinement in *R*3. Reflection positions are marked by vertical blue bars. It was measured with Cu-$K_{\alpha 1}$ radiation.

For comparison: β-$Li_{10}P_4N_{10}$ transforms to α-$Li_{10}P_4N_{10}$ at about 90 °C.

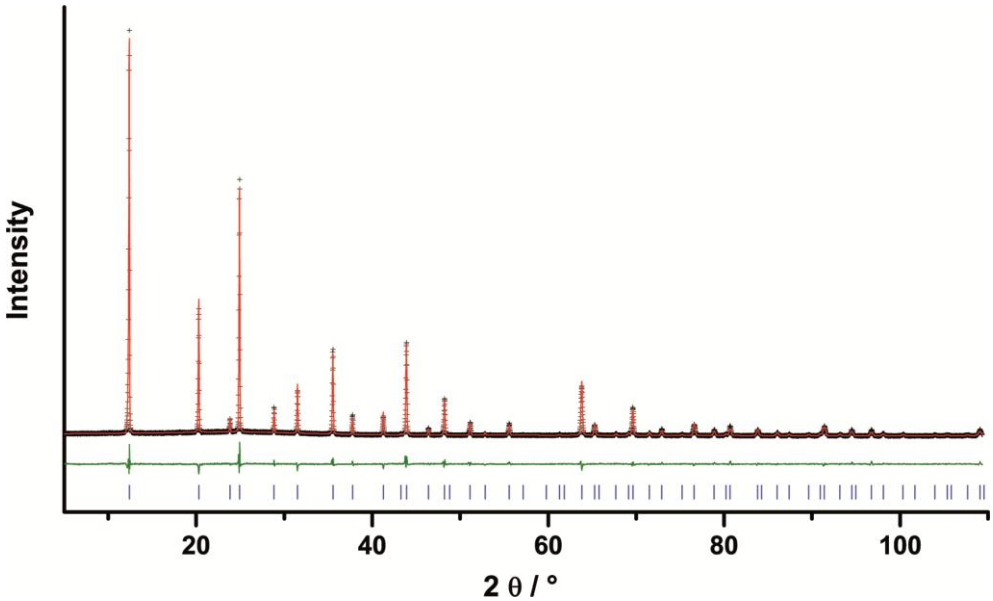

Figure S11. α-$Li_{10}P_4N_{10}$ at about 90 °C: Observed (black crosses) and calculated (red line) powder diffraction pattern as well as difference profile (green) of the Rietveld refinement in $Fd\bar{3}m$. Reflection positions are marked by vertical blue bars. It was measured with Cu-$K_{\alpha 1}$ radiation. (R_{wp} = 0.0835, R_{exp} = 0.0585, R_p = 0.0640, R_{Bragg} = 0.0361, *GooF* = 1.429 with 34 parameters)

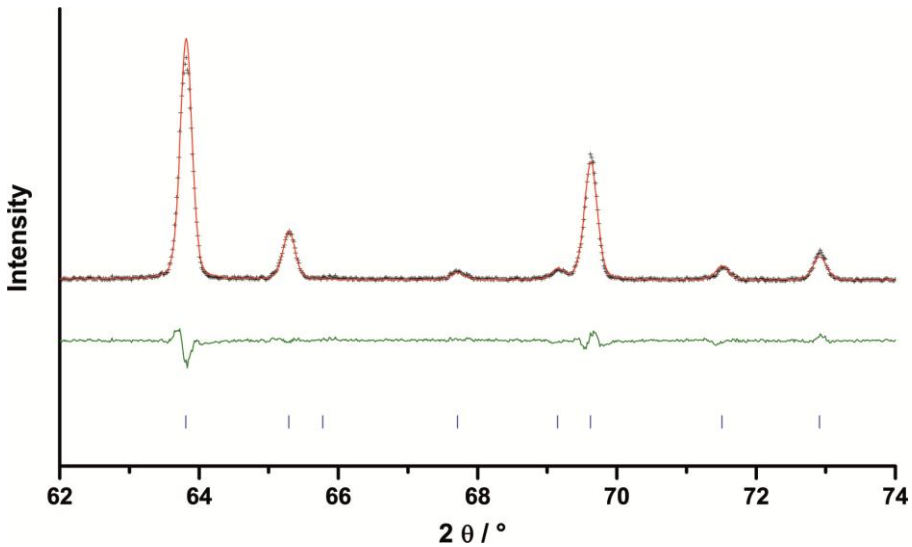

Figure S12. α-$Li_{10}P_4N_{10}$ at about 90 °C: Observed (black crosses) and calculated (red line) powder diffraction pattern as well as difference profile (green) of the Rietveld refinement in $Fd\bar{3}m$. Reflection positions are marked by vertical blue bars. It was measured with Cu-$K_{\alpha 1}$ radiation.

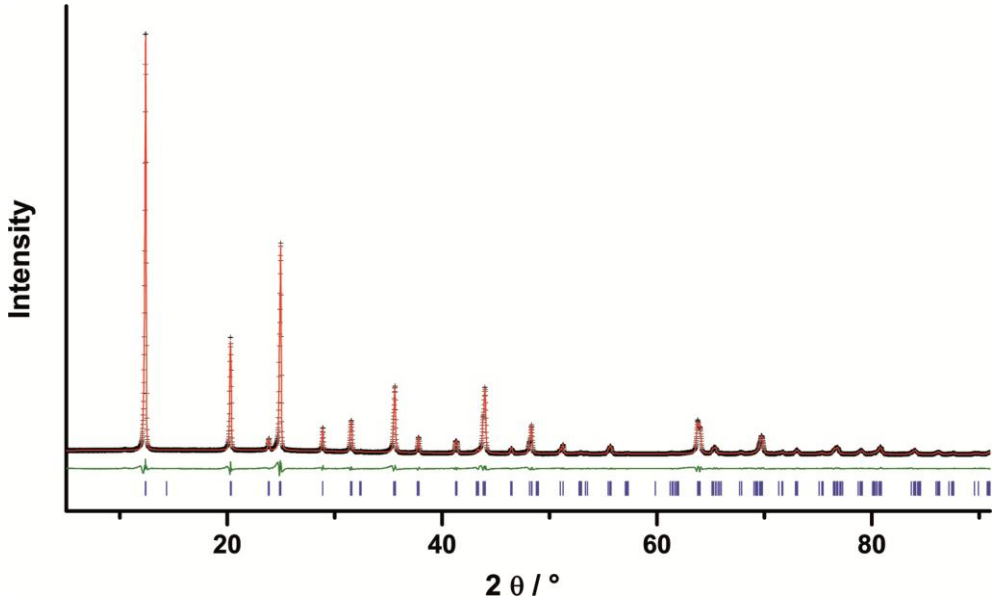

Figure S13. sintered β-$Li_{10}P_4N_{10}$ (190 °C): Observed (black crosses) and calculated (red line) powder diffraction pattern as well as difference profile (green) of the Rietveld refinement in *R*3. Reflection positions are marked by vertical blue bars. It was measured with Cu-$K_{\alpha 1}$ radiation. (R_{wp} = 0.0764, R_{exp} = 0.0198, R_p = 0.0501, R_{Bragg} = 0.0112, *GooF* = 3.867 with 79 parameters)

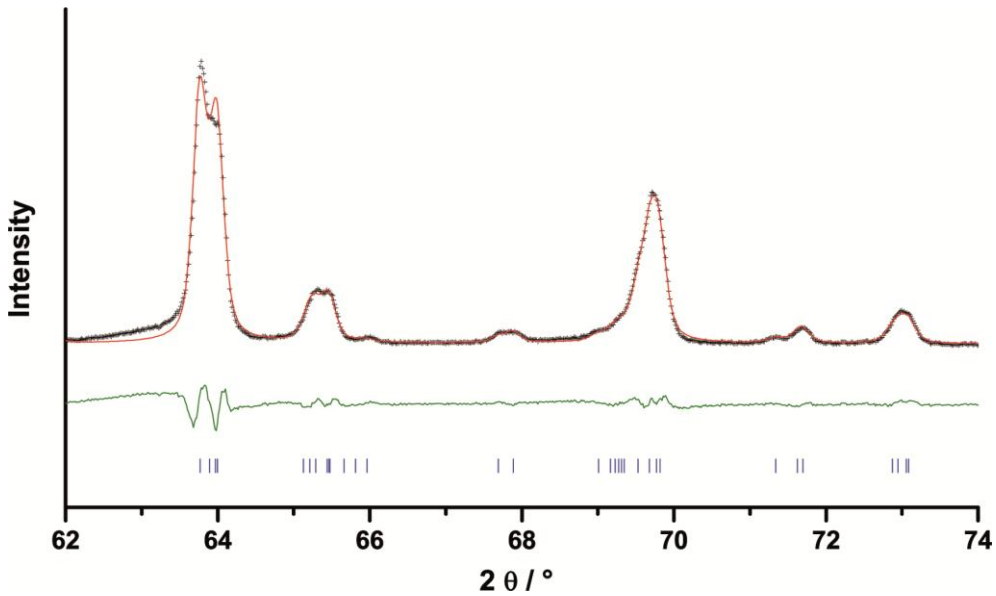

Figure S14. sintered β-$Li_{10}P_4N_{10}$ (190 °C): Observed (black crosses) and calculated (red line) powder diffraction pattern as well as difference profile (green) of the Rietveld refinement in *R*3. Reflection positions are marked by vertical blue bars. It was measured with Cu-$K_{\alpha 1}$ radiation.

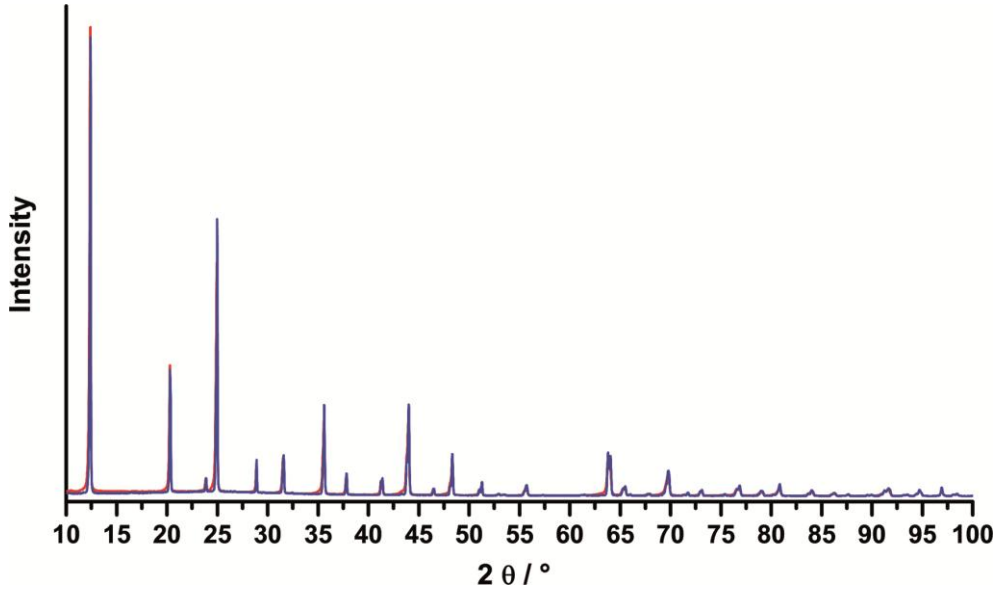

Figure S15. Comparison of the X-ray powder diffraction data of β-$Li_{10}P_4N_{10}$. Both diagrams were recorded at room temperature. Blue: after synthesis according to equation (1) and washing with EtOH; red: after sintering this sample at 190 °C.

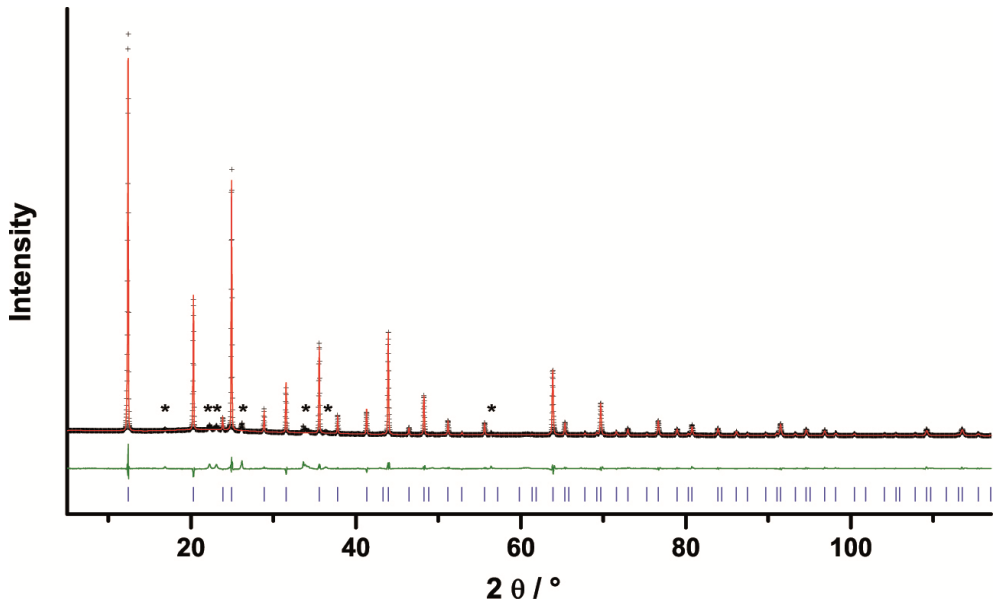

Figure S16. α-$Li_{10}P_4N_{10}$ after heating β-$Li_{10}P_4N_{10}$ to 600 °C: Observed (black crosses) and calculated (red line) powder diffraction pattern as well as difference profile (green) of the Rietveld refinement in $Fd\bar{3}m$. Reflection positions are marked by vertical blue bars. It was measured with Cu-$K_{\alpha 1}$ radiation. Reflections from an unknown side phase are marked with asterisks. (R_{wp} = 0.0934, R_{exp} = 0.0240, R_p = 0.0605, R_{Bragg} = 0.0336, *GooF* = 3.893 with 47 parameters)

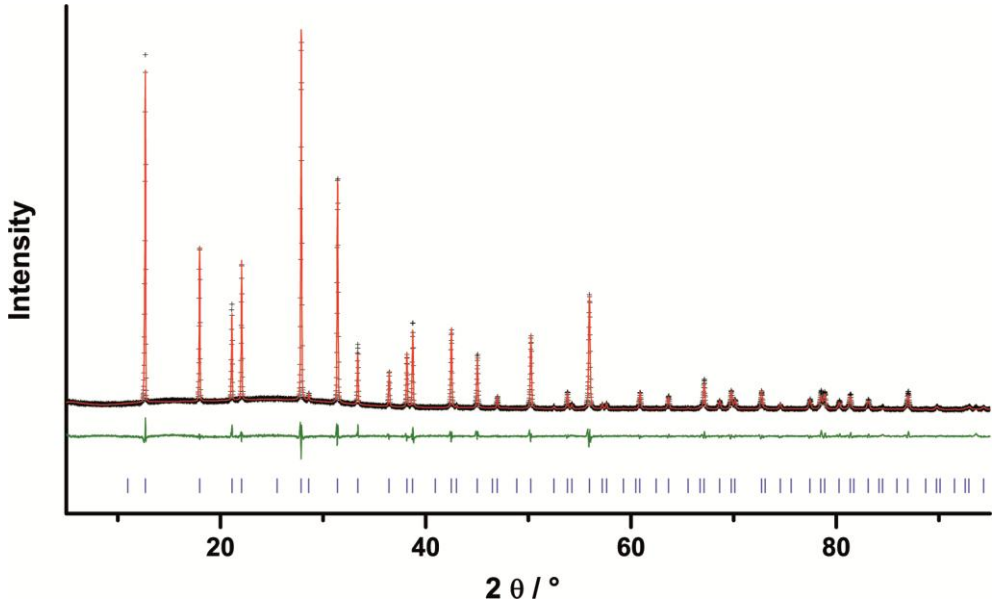

Figure S17. $Li_{13}P_4N_{10}Cl_3$: Observed (black crosses) and calculated (red line) powder diffraction pattern as well as difference profile (green) of the Rietveld refinement. Reflection positions are marked by vertical blue bars. It was measured with Cu-$K_{\alpha 1}$ radiation. (R_{wp} = 0.0670, R_{exp} = 0.0425, R_p = 0.0501, R_{Bragg} = 0.0187, *GooF* = 1.576 with 43 parameters)

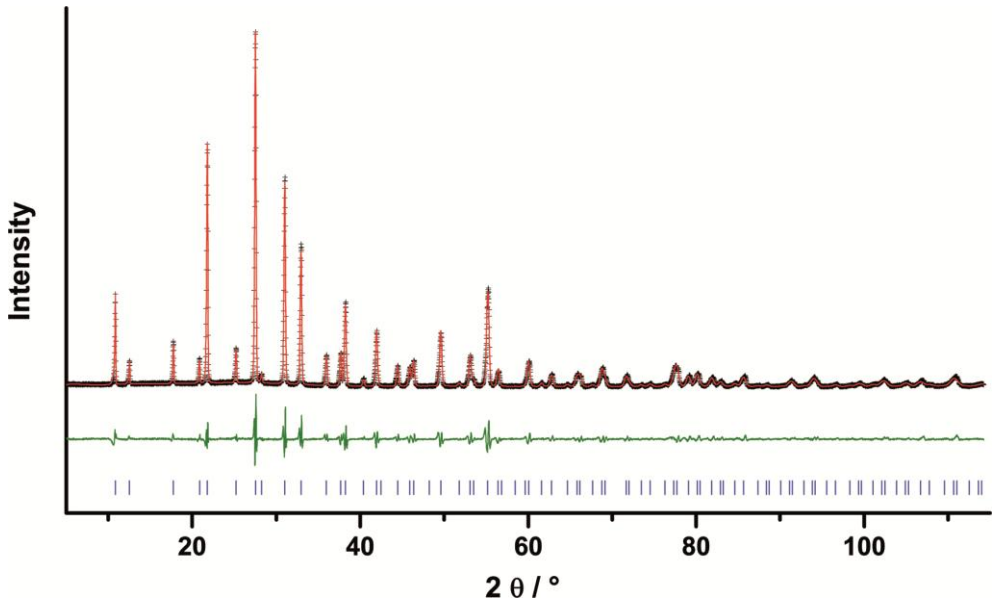

Figure S18. $Li_{13}P_4N_{10}Br_3$: Observed (black crosses) and calculated (red line) powder diffraction pattern as well as difference profile (green) of the Rietveld refinement. Reflection positions are marked by vertical blue bars. It was measured with Cu-$K_{\alpha 1}$ radiation. (R_{wp} = 0.1169, R_{exp} = 0.0499, R_p = 0.0873, R_{Bragg} = 0.0224, *GooF* = 2.234 with 42 parameters)

C.5. ^{31}P, ^{6}Li and ^{7}Li solid state MAS NMR spectroscopy

The ^{31}P MAS NMR spectra of β-$Li_{10}P_4N_{10}$, $Li_{13}P_4N_{10}Cl_3$, $Li_{13}P_4N_{10}Br_3$ show strong resonances between 15.4 and 4.71 ppm. The four signals in β-$Li_{10}P_4N_{10}$ correspond with four crystallographically independent P sites. $Li_{13}P_4N_{10}Cl_3$ and $Li_{13}P_4N_{10}Br_3$ have both one P site. The values for these compounds correspond with those of other ternary nitridophosphates.[1]

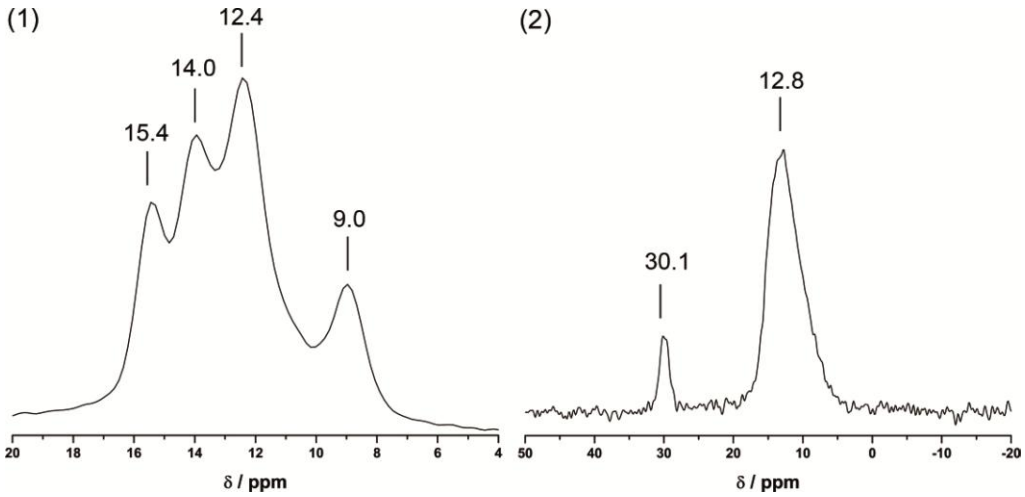

Figure S19. ^{31}P MAS NMR spectrum (1) β-$Li_{10}P_4N_{10}$ at room temperature rotated with 10 kHz. (2) α-$Li_{10}P_4N_{10}$ at room temperature rotated with 50 kHz.

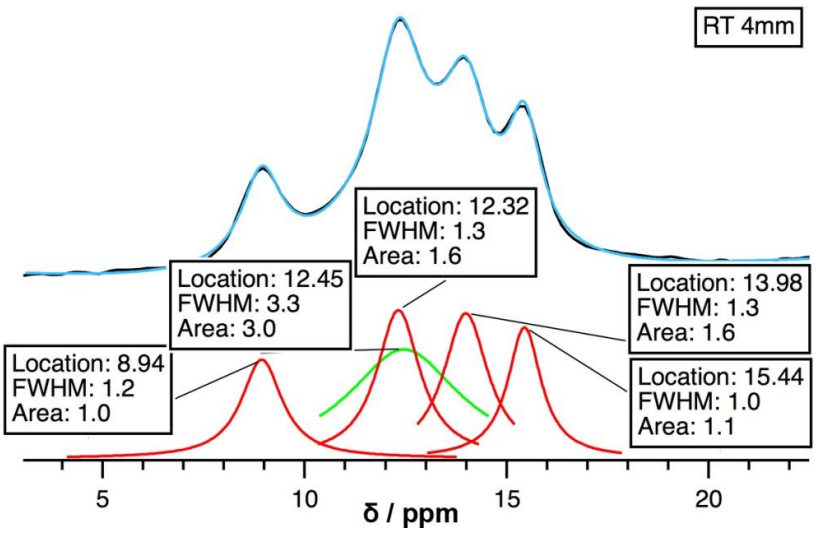

Figure S20. ^{31}P MAS NMR spectrum of β-$Li_{10}P_4N_{10}$ at room temperature rotated with 10 kHz. For integration the program IGOR PRO 7 (WaveMetrics) was used. Black: measured spectrum, blue: fitted spectrum, red: signals of β-$Li_{10}P_4N_{10}$ fitted by Lorentz, green: signal of α-$Li_{10}P_4N_{10}$ fitted by Lorenz.

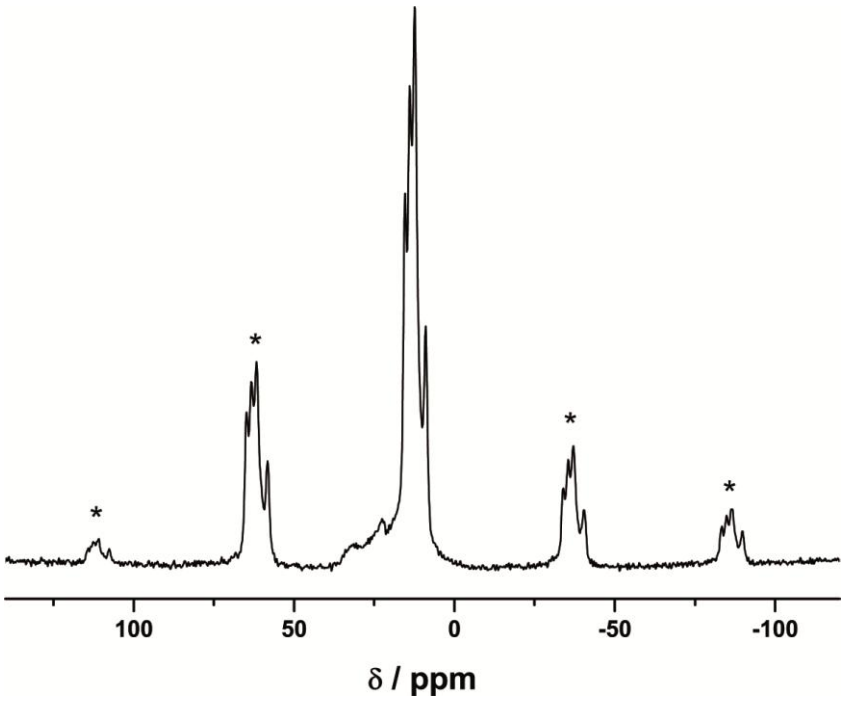

Figure S21. ^{31}P MAS NMR spectrum of β-$Li_{10}P_4N_{10}$ at room temperature rotated with 10 kHz with rotation with rotational sidebands (marked with asterisks).

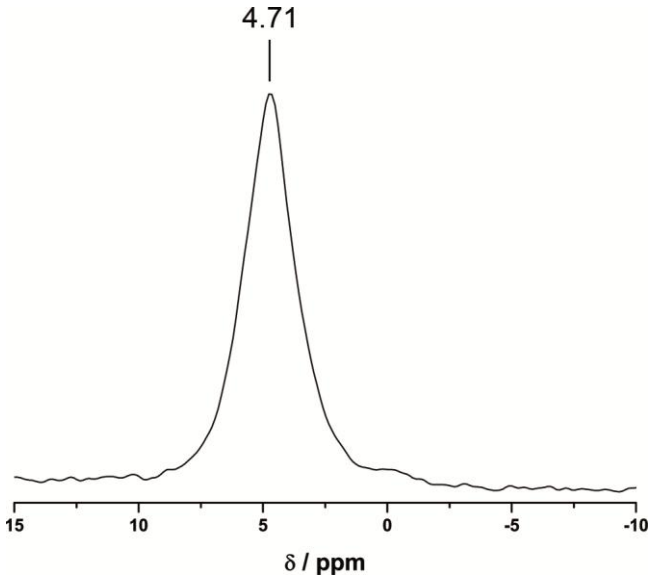

Figure S22. ^{31}P MAS NMR spectrum of $Li_{13}P_4N_{10}Cl_3$ at room temperature rotated with 20 kHz.

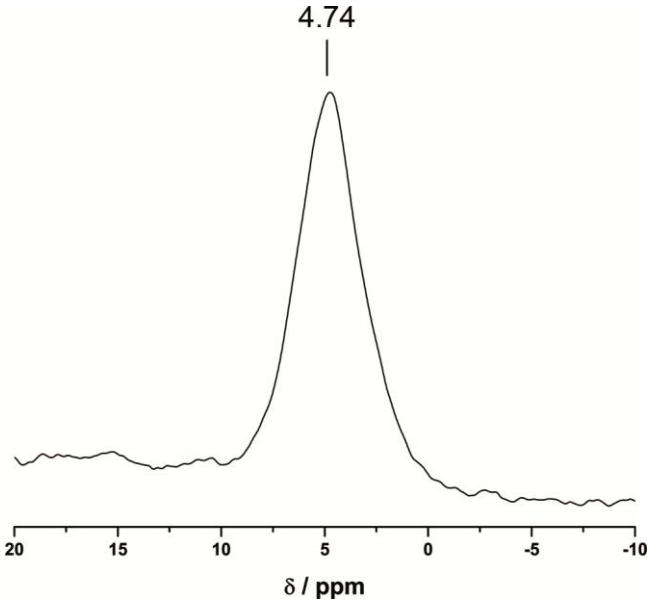

Figure S23. ^{31}P MAS NMR spectrum of $Li_{13}P_4N_{10}Br_3$ at room temperature rotated with 20 kHz.

The ^{6}Li MAS NMR spectrum shows strong resonances between 5.22 and 1.85 ppm. Due to the small chemical shift differences of the signals, the differentiation of the crystallographically independent sites cannot be observed in the spectra.

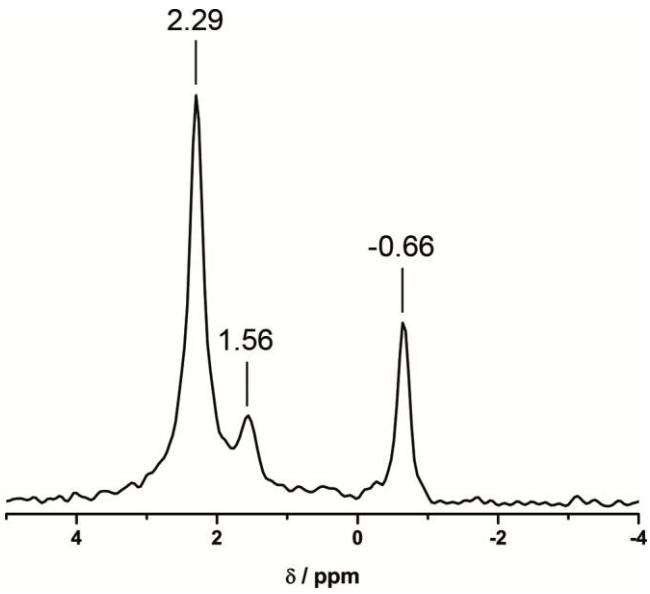

Figure S24. ^{6}Li MAS NMR spectrum of β-$Li_{10}P_4N_{10}$ at room temperature rotated with 20 kHz.

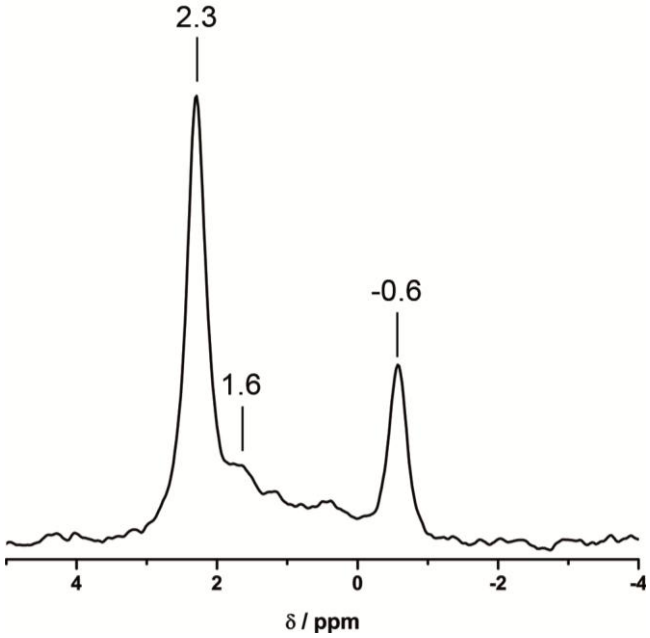

Figure S25. ^{6}Li MAS NMR spectrum of α-$Li_{10}P_4N_{10}$ at room temperature rotated with 50 kHz.

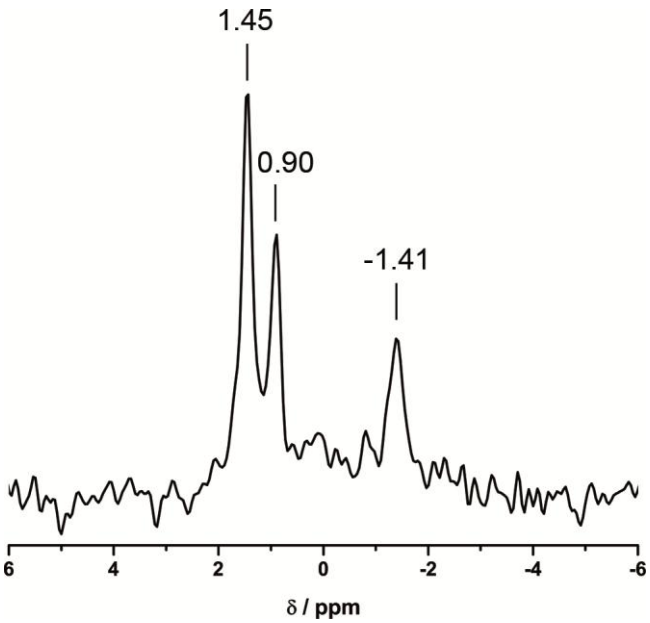

Figure S26. ^{6}Li MAS NMR spectrum of $Li_{13}P_4N_{10}Cl_3$ at room temperature rotated with 20 kHz.

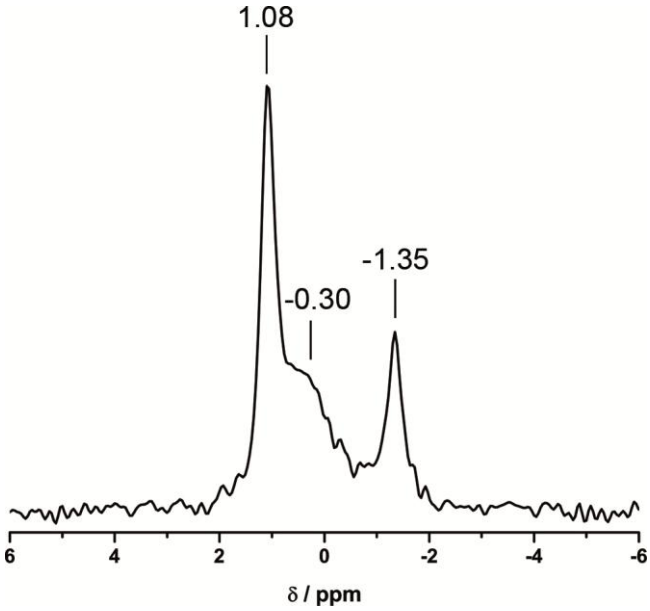

Figure S27. ^{6}Li MAS NMR spectrum of $Li_{13}P_4N_{10}Br_3$ at room temperature rotated with 20 kHz.

The ^{7}Li MAS NMR spectrum shows one strong resonances at 4.87 ppm. Due to the small chemical shift differences of the signals, no differentiation of the crystallographically independent sites can be observed in the spectrum. ^{7}Li MAS NMR spectra of different lithium nitridophosphates or silicates often show one resonance in this range.[2-5]

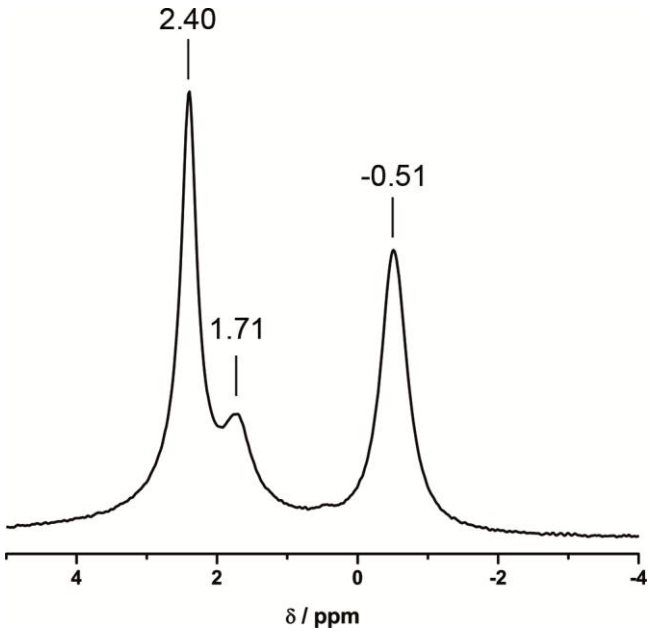

Figure S28. ^{7}Li MAS NMR spectrum of β-$Li_{10}P_4N_{10}$ at room temperature rotated with 20 kHz.

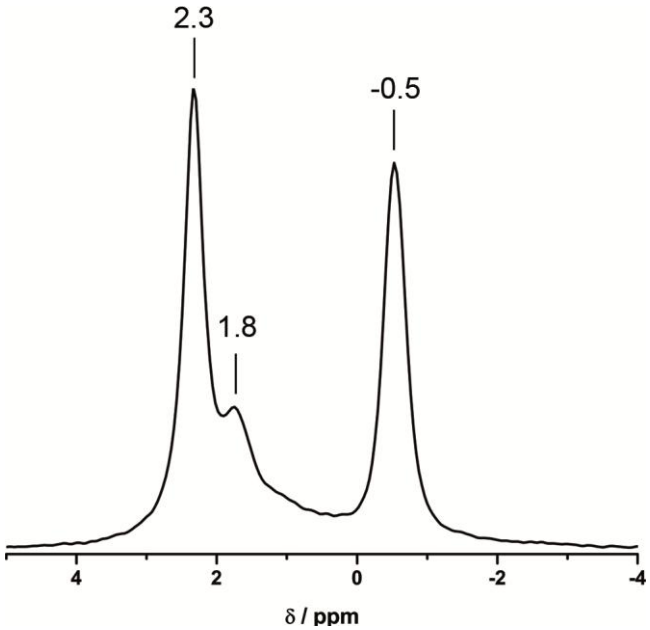

Figure S29. ^{7}Li MAS NMR spectrum of α-$Li_{10}P_4N_{10}$ at room temperature rotated with 50 kHz.

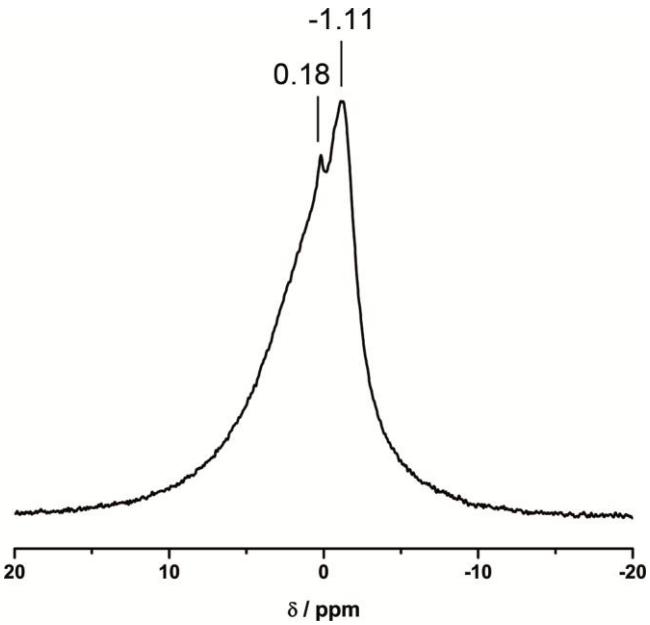

Figure S30. ^{7}Li MAS NMR spectrum of $Li_{13}P_4N_{10}Cl_3$ at room temperature rotated with 20 kHz.

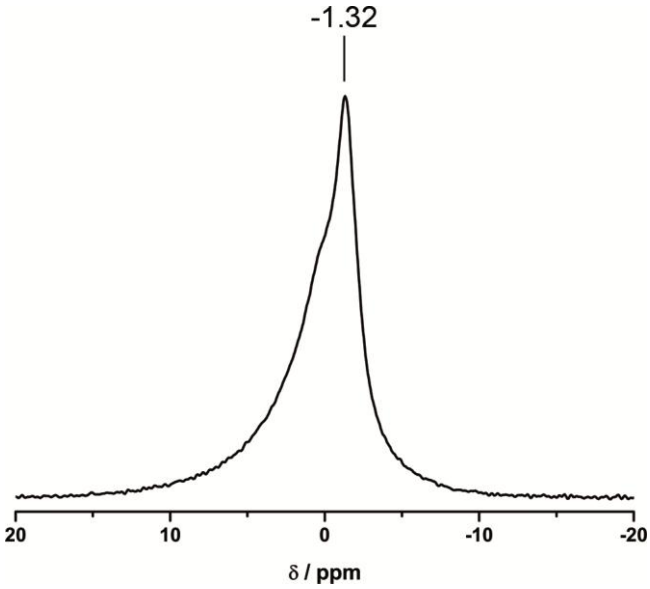

Figure S31. ^{7}Li MAS NMR spectrum of $Li_{13}P_4N_{10}Br_3$ at room temperature rotated with 20 kHz.

C.6. Details of scanning electron microscopy

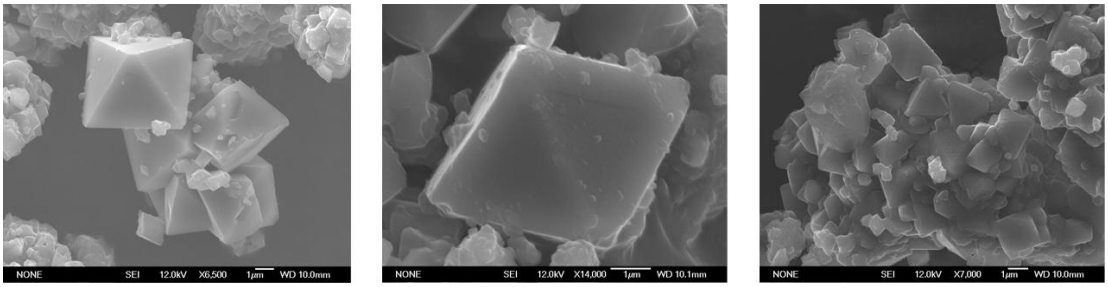

Figure S32. Scanning electron micrographs of β-$Li_{10}P_4N_{10}$.

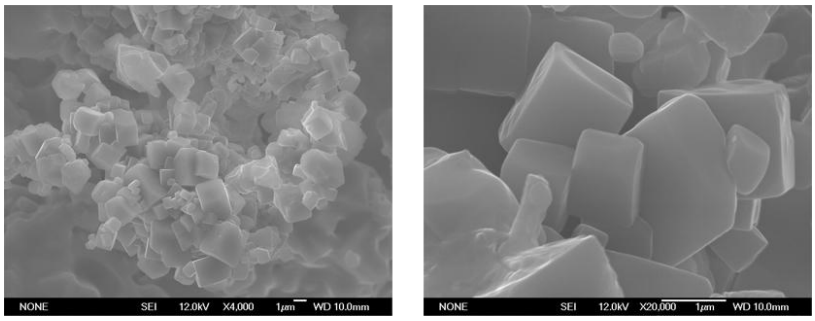

Figure S33. Scanning electron micrographs of $Li_{13}P_4N_{10}Cl_3$.

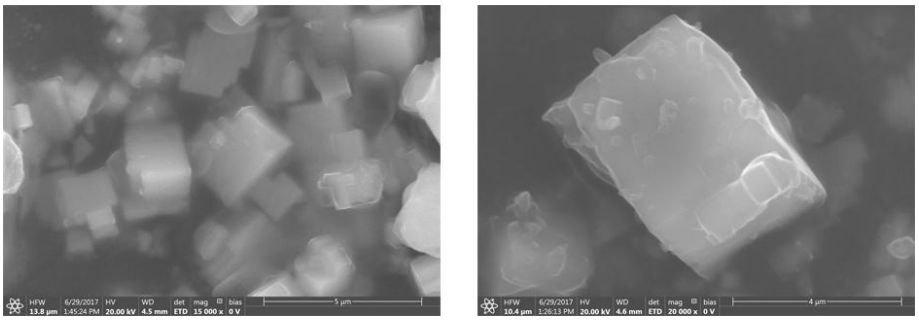

Figure S34. Scanning electron micrograph of $Li_{13}P_4N_{10}Br_3$.

Table S10. EDX analysis of β-$Li_{10}P_4N_{10}$.

	N	O	P
EDX point 1[atom %]	67.5	10.3	22.2
EDX point 2[atom %]	73.3	3.6	23.0
EDX point 3[atom %]	57.7	18.9	23.5
EDX point 4[atom %]	65.7	14.1	20.2
Average	**66.1**	**12.9**	**22.2**
Calculated atom %	**42.0**	**0**	**37.2**

Table S11. EDX analysis of $Li_{13}P_4N_{10}Cl_3$.

	N	O	P	Cl
EDX point 1[atom %]	65.2	5.0	16.8	13.0
EDX point 2[atom %]	58.6	3.2	21.3	17.0
EDX point 3[atom %]	65.7	6.3	15.8	12.1
Average	**63.2**	**4.8**	**18.0**	**14.0**
Calculated atom %	**33.3**	**0**	**13.3**	**10.0**

Table S12. EDX analysis of $Li_{13}P_4N_{10}Br_3$.

	N	O	P	Br
EDX point 1[atom %]	49.1	18.6	19.3	13.1
EDX point 2[atom %]	37.5	16.3	27.7	18.4
EDX point 3[atom %]	40.9	21.2	22.8	15.2
EDX point 4[atom %]	39.4	23.5	21.9	15.2
Average	**41.7**	**19.9**	**22.9**	**15.5**
Calculated atom %	**33.3**	**0**	**13.3**	**10.0**

Due to hydrolysis of the sample during mounting at air, oxygen was detected. It was observed that especially the crystals of $Li_{13}P_4N_{10}Br_3$ obtained an oxygen rich surface during mounting the sample at air which was also molten at some spots.

C.7. Temperature dependent powder X-ray diffraction

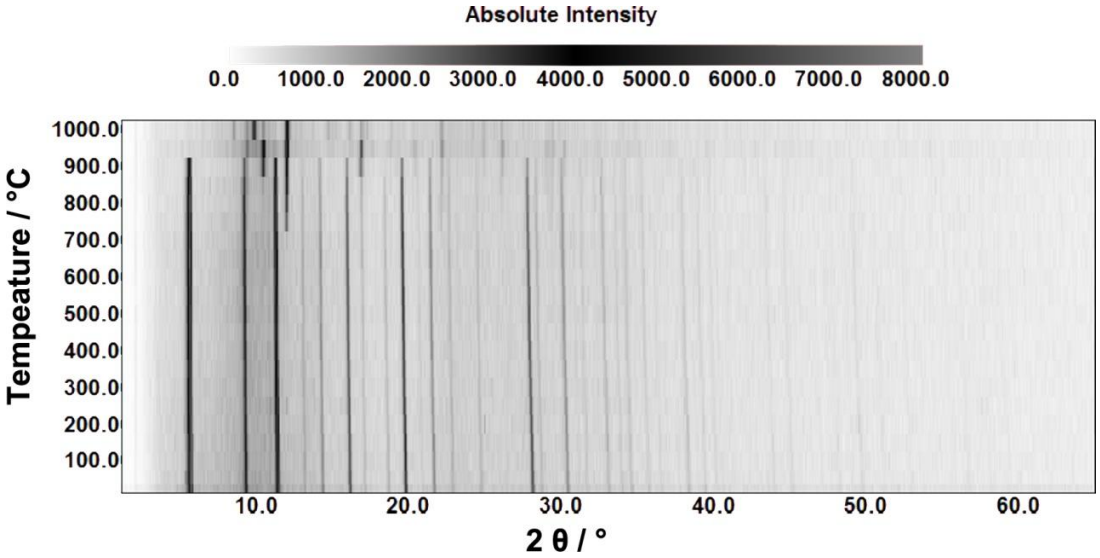

Figure S35. Temperature dependent powder X-ray diffraction of β-$Li_{10}P_4N_{10}$. It was measured with Mo-$K_{\alpha 1}$ radiation.

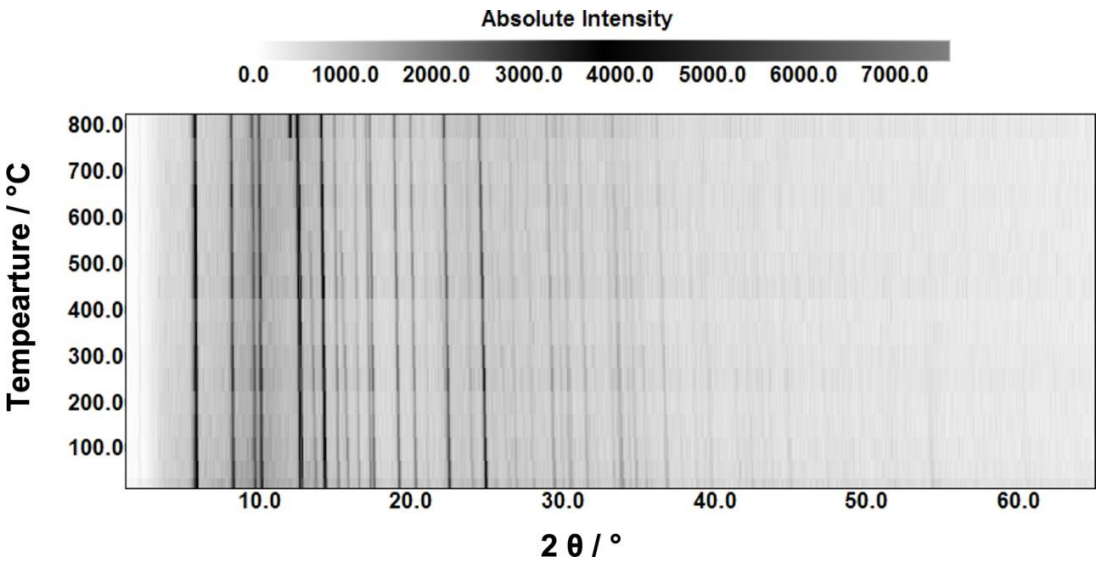

Figure S36. Temperature dependent powder X-ray diffraction of $Li_{13}P_4N_{10}Cl_3$. It was measured with Mo-$K_{\alpha 1}$ radiation.

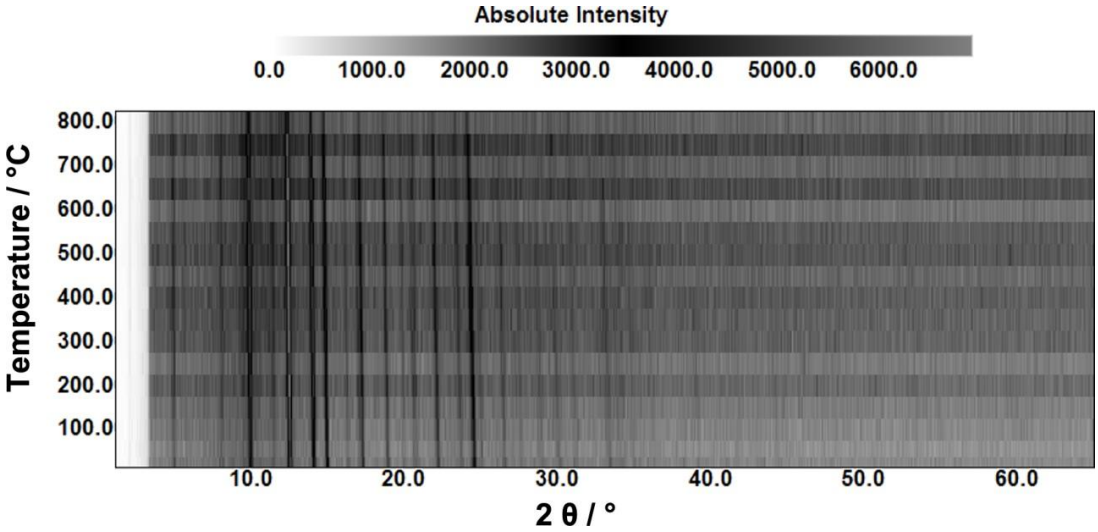

Figure S37. Temperature dependent powder X-ray diffraction of $Li_{13}P_4N_{10}Br_3$. It was measured with Mo-$K_{\alpha 1}$ radiation.

C.8. FTIR spectroscopy

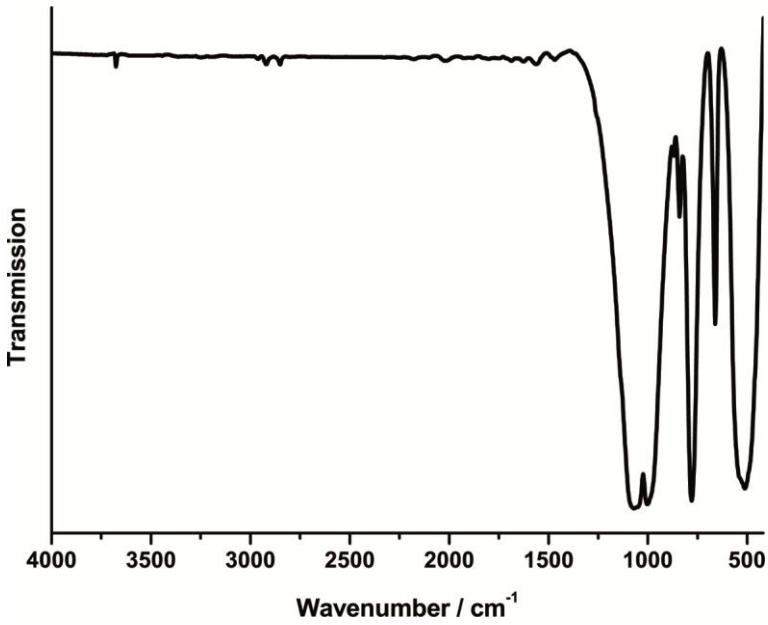

Figure S38. FTIR spectrum of β-$Li_{10}P_4N_{10}$.

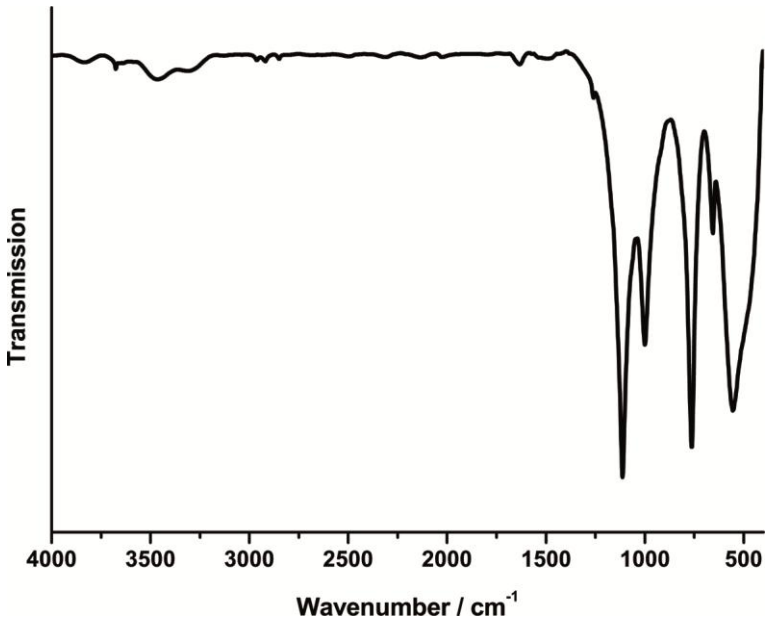

Figure S39. FTIR spectrum of $Li_{13}P_4N_{10}Cl_3$.

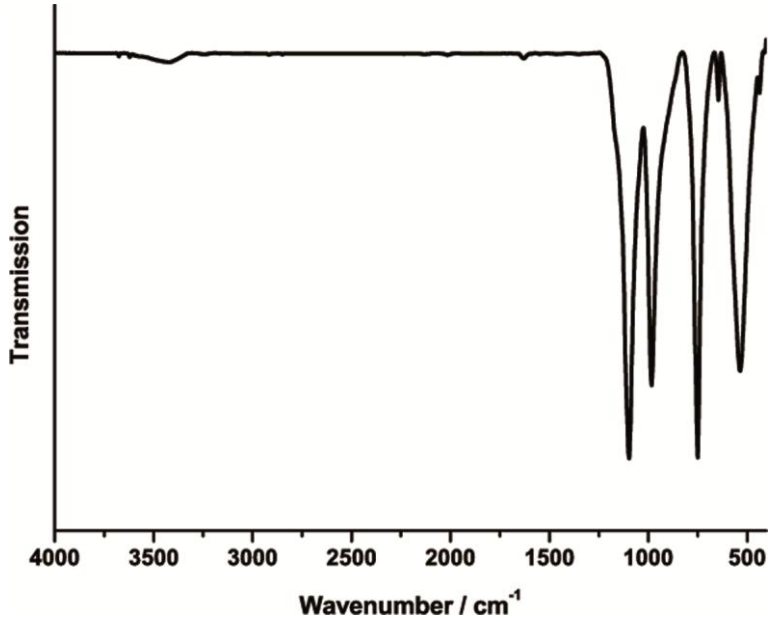

Figure S40. FTIR spectrum of $Li_{13}P_4N_{10}Br_3$.

Infrared spectroscopy measurements were performed on a Bruker FTIR-IFS 66v/S spectrometer. Before measurement in the range of 400-4000 cm^{-1} the sample was mixed with KBr in a glove box and cold-pressed into a pellet (Ø = 12 mm).The spectrum shows no significant valence vibrations in the region of 3000 cm^{-1}, where N–H vibrations are expected. A weak signal in that region can be explained by surface hydrolysis of the sample. Thus, the incorporation of stoichiometric amounts of hydrogen seems unlikely. Much more significant are the characteristic PN framework vibrations between 600 and 1500 cm^{-1}.

C.9. Structural Analysis of possible lithium migration pathways

Possible voids and migration pathways in β-$Li_{10}P_4N_{10}$, $Li_{13}P_4N_{10}Cl_3$ and $Li_{13}P_4N_{10}Br_3$ were analyzed with TOPOS.[6-9]

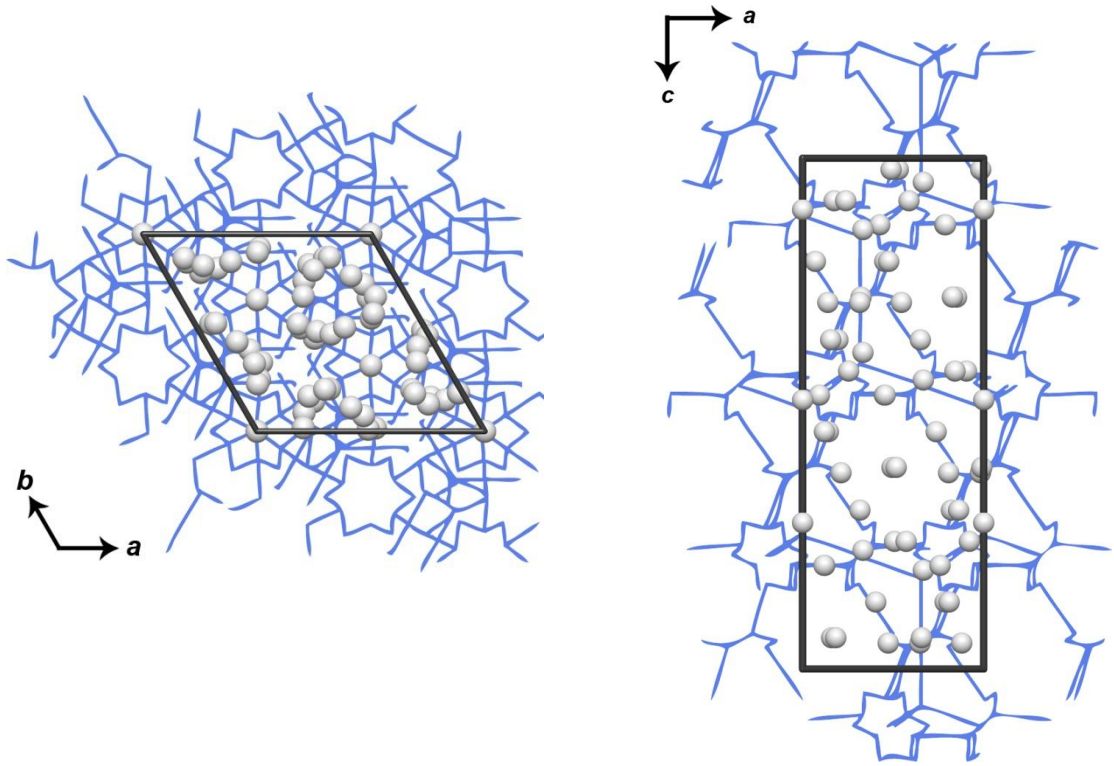

Figure S41. Calculated possible Li^+ pathways (blue) according to the voids in the structure and unit cell of β-$Li_{10}P_4N_{10}$.

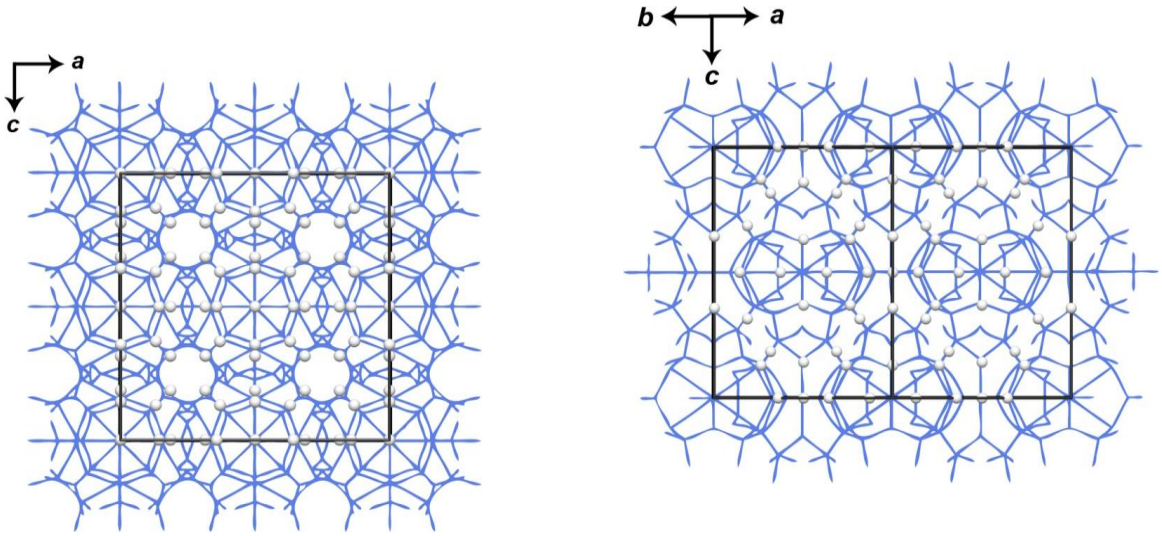

Figure S42. Calculated possible Li^+ pathways (blue) according to the voids in the structure and unit cell of $Li_{13}P_4N_{10}Cl_3$.

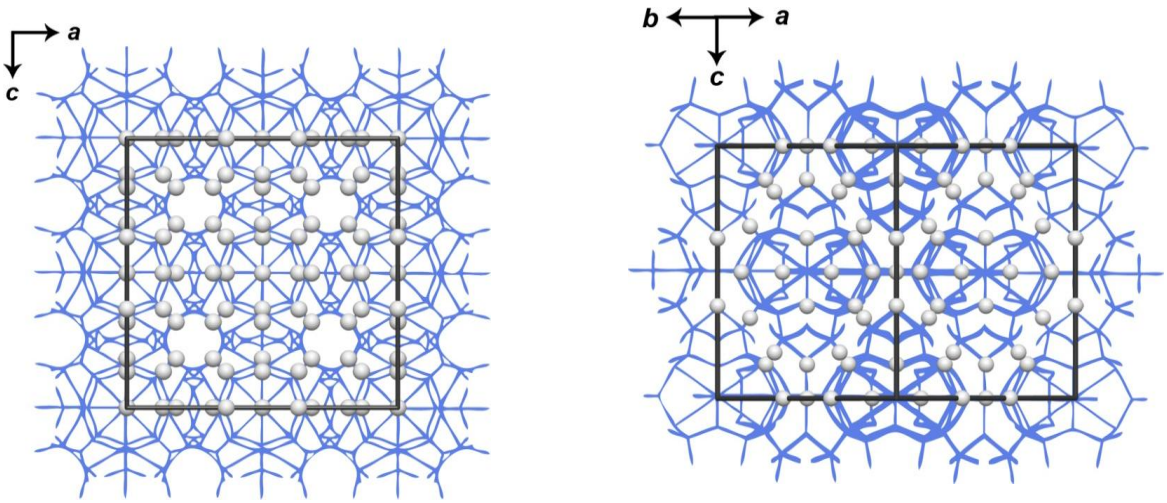

Figure S43. Calculated possible Li^+ pathways (blue) according to the voids in the structure and unit cell of $Li_{13}P_4N_{10}Br_3$.

C.10. Details of lithium ion conductivity

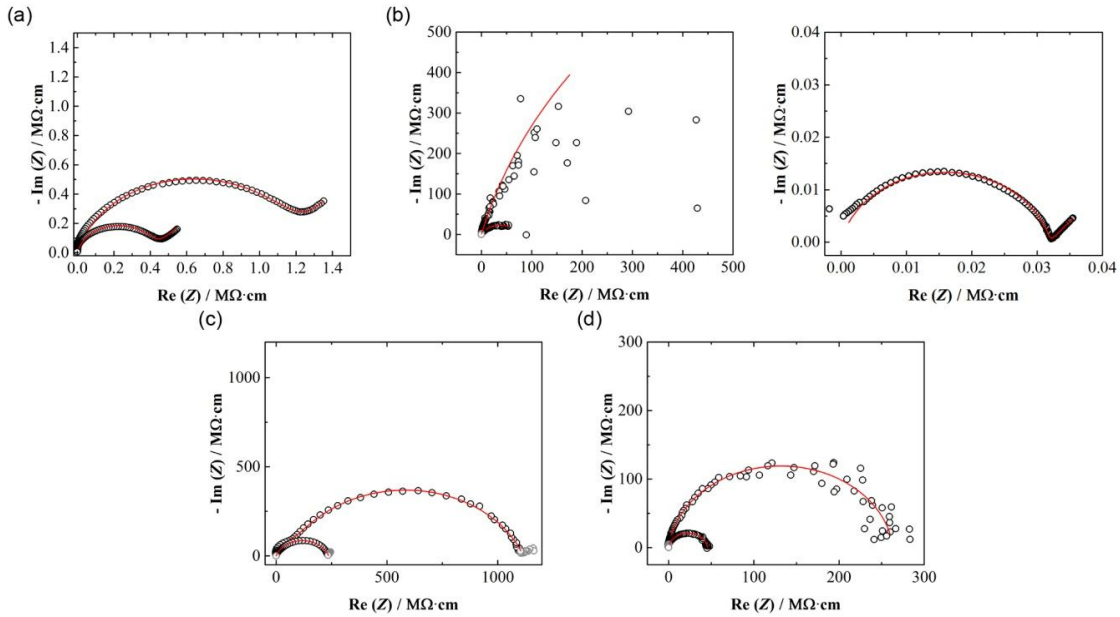

Figure S44. Normalized Nyquist plots of (a) $Li_{10}P_4N_{10}$ as prepared, (b) $Li_{10}P_4N_{10}$ (sintered), (c) $Li_{13}P_4N_{10}Cl_3$ and (d) $Li_{13}P_4N_{10}Br_3$ with curves observed at 25 °C (a-d), 45 °C (a-c), 50 °C (d) and 200 °C (b right), respectively. Samples b-d had been prior heated (before measurements) to 200 °C. Gray data points were excluded from the fitting (red line). Equivalent circuits and parameters are listed in table S13.

Table S13. Fitting parameter of Impedance measurements.

	Equivalent circuit	R_1 / MΩ	C_1 / nF	R_2 / MΩ	C_2 / nF
$Li_{10}P_4N_{10}$ as prepared (Z = 0.062 cm^{-1})					
25 °C	(R)(P)-P	$7.23 \cdot 10^{-2}$	0.651	-	-
45 °C	(R)(P)-P	$2.52 \cdot 10^{-2}$	0.689	-	-
$Li_{10}P_4N_{10}$ (Z = 0.062 cm^{-1})					
25 °C	(R)(P)	$1.43 \cdot 10^{2}$	0.743	-	-
45 °C	(R)(P)	4.68	1.16	-	-
$Li_{13}P_4N_{10}Cl_3$ (Z = 0.20 cm^{-1})					
25 °C	(R)(P)-(R)(P)*	$1.11 \cdot 10^{1}$	0.0111	$2.11 \cdot 10^{2}$	0.0233
45 °C	(R)(P)	$4.72 \cdot 10^{1}$	0.0252		
$Li_{13}P_4N_{10}Br_3$ (Z = 0.073 cm^{-1})					
25 °C	(R)(P)	6.99	0.148		
50 °C	(R)(P)	1.21	0.145		

*Resistivity listed in table S16 is given as the sum of R1 and R2.

Table S14. Impedance measurements of $Li_{10}P_4N_{10}$ as prepared at different temperatures.

Temperature / °C	**Raw. Res. / Ohm**	**Conductivity / S cm^{-1}**	**ln(conductivity · T)**	**C/nF**
25	$7.23 \cdot 10^{4}$	$8.56 \cdot 10^{-7}$	-8.27	0.651
35	$4.17 \cdot 10^{4}$	$1.48 \cdot 10^{-6}$	-7.69	0.665
45	$2.52 \cdot 10^{4}$	$2.46 \cdot 10^{-6}$	-7.15	0.696
55	$1.91 \cdot 10^{4}$	$3.23 \cdot 10^{-6}$	-6.85	0.747
65	$1.87 \cdot 10^{4}$	$3.30 \cdot 10^{-6}$	-6.80	0.833
70	$2.42 \cdot 10^{4}$	$2.56 \cdot 10^{-6}$	-7.04	0.921
74	$3.81 \cdot 10^{4}$	$1.62 \cdot 10^{-6}$	-7.48	1.06
78	$5.30 \cdot 10^{4}$	$1.17 \cdot 10^{-6}$	-7.80	1.2
84	$5.72 \cdot 10^{4}$	$1.08 \cdot 10^{-6}$	-7.86	1.38
90	$5.60 \cdot 10^{4}$	$1.34 \cdot 10^{-6}$	-7.62	1.49
100	$3.25 \cdot 10^{4}$	$1.90 \cdot 10^{-6}$	-7.25	1.68
125	$1.36 \cdot 10^{4}$	$4.55 \cdot 10^{-6}$	-6.31	1.84
150	$8.83 \cdot 10^{3}$	$7.00 \cdot 10^{-6}$	-5.82	1.37

Table S15. Impedance measurements of $Li_{10}P_4N_{10}$ (sintered) at different temperatures.

Temperature / °C	Raw. Res. / Ohm	Conductivity / S cm^{-1}	ln(conductivity · T)	C/nF
25	$1.43 \cdot 10^{8}$	$4.32 \cdot 10^{-10}$	-15.86	0.743
45	$1.94 \cdot 10^{7}$	$3.19 \cdot 10^{-9}$	-13.86	1.16
65	$3.79 \cdot 10^{6}$	$1.63 \cdot 10^{-8}$	-12.11	1.02
85	$1.03 \cdot 10^{6}$	$6.01 \cdot 10^{-8}$	-10.75	1.16
105	$2.74 \cdot 10^{5}$	$2.26 \cdot 10^{-7}$	-9.37	1.14
125	$7.83 \cdot 10^{4}$	$7.91 \cdot 10^{-7}$	-8.06	1.1
145	$2.66 \cdot 10^{4}$	$2.33 \cdot 10^{-6}$	-6.94	1.05
165	$9.82 \cdot 10^{3}$	$6.30 \cdot 10^{-6}$	-5.89	0.927
185	$3.61 \cdot 10^{3}$	$1.58 \cdot 10^{-5}$	-4.93	0.844
200	$1.96 \cdot 10^{3}$	$3.15 \cdot 10^{-5}$	-4.20	0.82

Table S16. Impedance measurements of $Li_{10}P_4N_{10}Cl_3$ at different temperatures.

Temperature / °C	Raw. Res. / Ohm	Conductivity / S cm^{-1}	ln(conductivity · T)	C/nF	C/nF (R2)
25	$2.27 \cdot 10^{8}$	$8.75 \cdot 10^{-10}$	-15.16	0.0111	0.0233
35	$1.04 \cdot 10^{8}$	$1.92 \cdot 10^{-9}$	-14.34	0.0208	
45	$4.77 \cdot 10^{7}$	$4.17 \cdot 10^{-9}$	-13.53	0.0252	
55	$2.26 \cdot 10^{7}$	$8.82 \cdot 10^{-9}$	-12.75	0.0229	
65	$1.07 \cdot 10^{7}$	$1.85 \cdot 10^{-8}$	-11.98	0.0196	
75	$5.14 \cdot 10^{6}$	$3.87 \cdot 10^{-8}$	-11.21	0.0185	
85	$2.41 \cdot 10^{6}$	$8.24 \cdot 10^{-8}$	-10.43	0.0169	

Table S17. Impedance measurements of $Li_{10}P_4N_{10}Br_3$ at different temperatures.

Temperature / °C	Raw. Res. / Ohm	Conductivity / S cm^{-1}	ln(conductivity · T)	C/nF
25	$6.71 \cdot 10^{6}$	$1.08 \cdot 10^{-8}$	-12.65	0.148
50	$1.20 \cdot 10^{6}$	$6.02 \cdot 10^{-8}$	-10.85	0.145
75	$2.66 \cdot 10^{5}$	$2.72 \cdot 10^{-7}$	-9.26	0.132
100	$7.54 \cdot 10^{4}$	$9.61 \cdot 10^{-7}$	-7.93	0.142
125	$2.47 \cdot 10^{4}$	$2.92 \cdot 10^{-6}$	-6.76	0.179
150	$9.15 \cdot 10^{3}$	$7.92 \cdot 10^{-6}$	-5.70	0.199
175	$3.61 \cdot 10^{3}$	$2.01 \cdot 10^{-6}$	-4.71	0.282
200	$1.50 \cdot 10^{3}$	$4.83 \cdot 10^{-5}$	-3.78	0.328

Table S18. Data for Arrhenius plot of $Li_{10}P_4N_{10}$ as prepared.

equation	y = a + b · x		
weighting	no weighing		
Sum of the squares	0.01422		
Pearson R	-0.99394		
cor. R-square	0.98188		
		value	standard error
ln(conductivity)	interception of the y-axis	7.69616	1.18819
ln(conductivity)	gradient	-4751.05526	371.46708

Table S19. Data for Arrhenius plot of $Li_{10}P_4N_{10}$ (sintered).

equation	y = a + b · x		
weighting	no weighing		
Sum of the squares	0.004471		
Pearson R	-0.99984		
cor. R-square	0.99963		
		value	standard error
ln(conductivity)	interception of the y-axis	15.41535	0.15866
ln(conductivity)	gradient	-9332.63958	59.48935

Table S20. Data for Arrhenius plot of $Li_{13}P_4N_{10}Cl_3$.

equation	y = a + b · x		
weighting	no weighing		
Sum of the squares	0.03123		
Pearson R	-0.9991		
cor. R-square	0.99783		
		value	standard error
ln(conductivity)	interception of the y-axis	12.86673	0.48901
ln(conductivity)	gradient	-8382.28648	159.57136

Table S21. Data for Arrhenius plot $Li_{13}P_4N_{10}Br_3$.

equation	y = a + b · x		
weighting	no weighing		
Sum of the squares	0.01768		
Pearson R	-0.99987		
cor. R-square	0.99969		
		value	standard error
ln(conductivity)	interception of the y-axis	11.14937	0.12736
ln(conductivity)	gradient	-7107.72634	47.46593

C.11. Details of XPS measurements

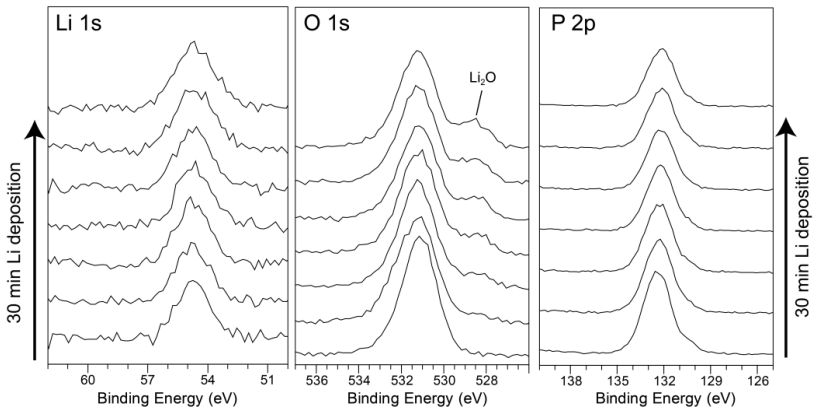

Figure S45. X-ray photoemission waterfall plots of β-$Li_{10}P_4N_{10}$ during stepwise exposure to lithium vapor.

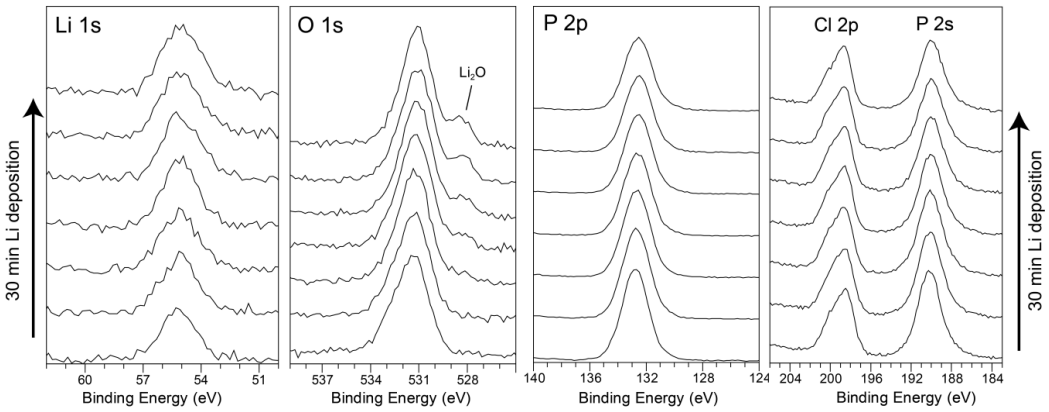

Figure S46. X-ray photoemission waterfall plots of $\mathbf{Li_{13}P_4N_{10}}Cl_3$ during stepwise exposure to lithium vapor.

On the surfaces of the samples small amounts of O (about 17 at% for β-$Li_{10}P_4N_{10}$ and 10 at% for $\mathbf{Li_{13}P_4N_{10}}Cl_3$) was detected beside Li, P and N (and Cl). For a signal in this area a layer of < 3 nm is sufficient. Such surface oxidation can derive from traces of oxygen or water in the UHV chamber, the glove box during sample preparation or during transfer of the sample.

C.12. References

[1] K. Landskron, Doctoral Thesis, Universtiy of Munich, 2001.

[2] S. Pagano, M. Zeuner, S. Hug, W. Schnick, *Eur. J. Inorg. Chem.* **2009**, 1579–1584.

[3] S. Lupart, W. Schnick, *Z. Anorg. Allg. Chem.* **2012**, *638*, 2015–2019.

[4] S. Pagano, S. Lupart, S. Schmiechen, W. Schnick, *Z. Anorg. Allg. Chem.* **2010**, *636*, 1907–1909.

[5] M. Orth, W. Schnick, *Z. Anorg. Allg. Chem.* **1999**, *625*, 1426–1428.

[6] V. A. Blatov, *IUCr CompComm Newsl.* **2006**, *7*, 4–38.

[7] V. A. Blatov, *Crystallogr. Rev.* **2004**, *10*, 249–318.

[8] N. A. Anurova, V. A. Blatov, G. D. Ilyushin, O. A. Blatova, A. K. Ivanov-Schitz, L. N. Dem'yanets, *Solid State Ionics* **2008**, *179*, 2248–2254.

[9] V. A. Blatov, A. P. Shevchenko, V. N. Serezhin, *J. Appl. Crystallogr.* **2000**, *32*, 377–377.

D. Supporting Information for Chapter 5

D.1. Additional crystallographic data for $Li_5P_2N_5$

Table S1. Fractional atomic coordinates, isotropic thermal displacement parameters, and site occupancies for $Li_5P_2N_5$.

Atom	Wyck. symbol	*x*	*y*	*z*	U_{iso} / Å^2	Occupancy
P1	8*f*	0.35644(7)	0.22823(6)	0.0530(2)		1
P2	8*f*	0.17597(7)	0.04753(6)	0.5596(2)		1
P3	8*f*	0.14635(7)	0.37020(6)	0.4444(2)		1
N1	8*f*	0.0875(2)	0.55895(19)	0.0212(8)		1
N2	8*f*	0.2422(2)	0.12046(19)	0.4786(8)		1
N3	4*c*	1/4	1/4	0		1
N4	8*f*	0.3798(2)	0.2097(2)	0.3892(8)		1
N5	8*f*	0.1228(2)	0.3518(2)	0.1089(8)		1
N6	8*f*	0.2917(2)	0.4714(2)	0.1122(8)		1
N7	8*f*	0.0726(2)	0.0710(2)	0.5086(8)		1
N8	8*f*	0.0820(3)	0.2035(2)	0.0332(8)		1
Li1	8*f*	0.0520(7)	0.4536(5)	0.096(2)	0.026(2)	1
Li2	4*e*	0	0.6312(9)	1/4	0.033(4)	1
Li3	8*f*	0.1216(10)	0.1813(8)	0.439(3)	0.058(4)	1
Li4	8*f*	0.2133(7)	0.1371(6)	0.035(2)	0.031(2)	1
Li5	8*f*	0.3221(7)	0.0330(6)	0.164(2)	0.025(2)	1
Li6	4*e*	0	0.2782(8)	1/4	0.022(3)	1
Li7	4*e*	0	0.0025(9)	1/4	0.021(2)	1
Li8	4*e*	0	0.1377(14)	1/4	0.066(6)	1
Li9	8*f*	0.4353(15)	0.4053(12)	0.050(5)	0.090(6)	1
Li10	4*d*	1/4	1/4	1/2	0.061(5)	1

Table S2. Anisotropic displacement parameters occurring in $Li_5P_2N_5$.

Atom	U_{11} / Å^2	U_{22} / Å^2	U_{33} / Å^2	U_{12} / Å^2	U_{13} / Å^2	U_{23} / Å^2
P1	0.0064(5)	0.0063(5)	0.0052(5)	0.0010(4)	0.0017(4)	0.0004(4)
P2	0.0051(5)	0.0046(5)	0.0042(5)	-0.0005(4)	-0.0003(4)	0.0002(4)
P3	0.0047(5)	0.0044(5)	0.0050(5)	0.0000(4)	0.0004(4)	0.0006(4)
N1	0.0075(16)	0.0074(16)	0.0104(19)	-0.0016(13)	0.0002(15)	-0.0011(15)
N2	0.0045(15)	0.0051(16)	0.0095(19)	-0.0004(12)	0.0001(14)	0.0002(15)
N3	0.009(2)	0.021(3)	0.020(3)	0.010(2)	-0.002(2)	0.000(3)
N4	0.0063(16)	0.0068(16)	0.0064(17)	-0.0017(13)	-0.0015(14)	0.0004(14)
N5	0.0096(17)	0.0084(17)	0.0053(17)	0.0029(14)	0.0004(14)	-0.0007(15)
N6	0.0098(17)	0.0067(15)	0.0054(17)	-0.0018(14)	0.0003(14)	0.0004(14)
N7	0.0054(15)	0.0111(17)	0.0114(19)	-0.0005(13)	-0.0017(15)	0.0028(16)
N8	0.0133(18)	0.0069(17)	0.013(2)	-0.0018(14)	0.0047(16)	0.0011(16)

Table S3. List of interatomic distances / Å for $Li_5P_2N_5$.

P1—N8^{i}	1.589(4)	P2—N7	1.589(4)	P3—N1^{ix}	1.591(4)
P1—N3	1.6263(11)	P2—N6^{iii}	1.675(4)	P3—N2^{iii}	1.677(4)
P1—N5^{i}	1.667(4)	P2—N6^{v}	1.678(4)	P3—N5	1.681(4)
P1—N4	1.684(4)	P2—N2	1.687(4)	P3—N4^{iii}	1.695(4)
Li1—N1^{ix}	2.116(11)	Li5—N6^{v}	2.327(11)	Li8—N8^{xv}	2.024(15)
Li2—N1^{xv}	2.174(10)	Li5—N1^{i}	2.329(11)	Li9—Li8^{i}	1.95(2)
Li2—N4^{xi}	2.389(10)	Li5—N5^{i}	2.602(11)	Li9—N8^{i}	2.00(2)
Li2—N5^{ix}	2.466(4)	Li6—N8^{xv}	2.120(9)	Li9—N7^{xxi}	2.09(2)
Li3—N4^{iii}	2.117(15)	Li6—N5^{xv}	2.371(8)	Li9—N7^{iii}	2.19(2)
Li4—N6^{i}	2.066(11)	Li6—N4^{iii}	2.436(4)	Li10—N4^{iii}	2.143(4)
Li4—N5^{i}	2.564(11)	Li7—N7^{xv}	2.020(11)	Li10—N2^{iii}	2.317(3)
Li5—N1^{v}	2.028(11)	Li7—N7^{xvii}	2.094(11)	Li10—N3^{vii}	2.4300(5)
Li5—N6^{i}	2.096(11)				

(i) 0.5-x, 0.5-y, -z; (ii) 0.5+x, -0.5+y, z; (iii) 0.5-x, 0.5-y, 1-z; (iv) x, y, -1+z; (v) 0.5-x, -0.5+y, 0.5-z; (vi) x, -y, 0.5+z; (vii) x, y, 1+z; (viii) -x, -y, 1-z; (ix) x, 1-y, 0.5+z; (x) -x, 1-y, 1-z; (xi) 0.5-x, 0.5+y, 0.5-z; (xii) x, 1-y, -0.5+z; (xiii) -x, 1-y, -z; (xiv) -0.5+x, 0.5-y, 0.5+z; (xv) -x, y, 0.5-z; (xvi) -0.5+x, 0.5+y, z; (xvii) x, -y, -0.5+z; (xviii) -0.5+x, 0.5-y, -0.5+z; (xix) -0.5+x, -0.5+y, z; (xx) -x, -y, -z; (xxi) 0.5+x, 0.5-y, -0.5+z; (xxii) 0.5+x, 0.5+y, z; (xxiii) 1-x, y, 0.5-z.

Table S4. List of bond angles / ° for $Li_5P_2N_5$.

N–P–N					
N8^{i}—P1—N3	109.69(15)	N7—P2—N6^{iii}	115.0(2)	N1^{ix}—P3—N2^{iii}	114.28(18)
N8^{i}—P1—N5^{i}	114.2(2)	N7—P2—N6^{v}	115.6(2)	N1^{ix}—P3—N5	107.2(2)
N3—P1—N5^{i}	109.32(14)	N6^{iii}—P2—N6^{v}	103.69(14)	N2^{iii}—P3—N5	112.6(2)
N8^{i}—P1—N4	108.4(2)	N7—P2—N2	108.89(18)	N1^{ix}—P3—N4^{iii}	114.57(19)
N3—P1—N4	110.22(14)	N6^{iii}—P2—N2	103.83(19)	N2^{iii}—P3—N4^{iii}	102.91(18)
N5^{i}—P1—N4	104.87(19)	N6^{v}—P2—N2	108.97(19)	N5—P3—N4^{iii}	104.94(18)
P–N–P					
P3^{iii}—N2—P2	126.8(2)	P1—N4—P3^{iii}	126.0(2)	P1^{i}—N5—P3	126.3(2)

(i) 0.5-x, 0.5-y, -z; (ii) 0.5+x, -0.5+y, z; (iii) 0.5-x, 0.5-y, 1-z; (iv) x, y, -1+z; (v) 0.5-x, -0.5+y, 0.5-z; (vi) x, -y, 0.5+z; (vii) x, y, 1+z; (viii) -x, -y, 1-z; (ix) x, 1-y, 0.5+z; (x) -x, 1-y, 1-z; (xi) 0.5-x, 0.5+y, 0.5-z; (xii) x, 1-y, -0.5+z; (xiii) -x, 1-y, -z; (xiv) -0.5+x, 0.5-y, 0.5+z; (xv) -x, y, 0.5-z; (xvi) -0.5+x, 0.5+y, z; (xvii) x, -y, -0.5+z; (xviii) -0.5+x, 0.5-y, -0.5+z; (xix) -0.5+x, -0.5+y, z; (xx) -x, -y, -z; (xxi) 0.5+x, 0.5-y, -0.5+z; (xxii) 0.5+x, 0.5+y, z; (xxiii) 1-x, y, 0.5-z.

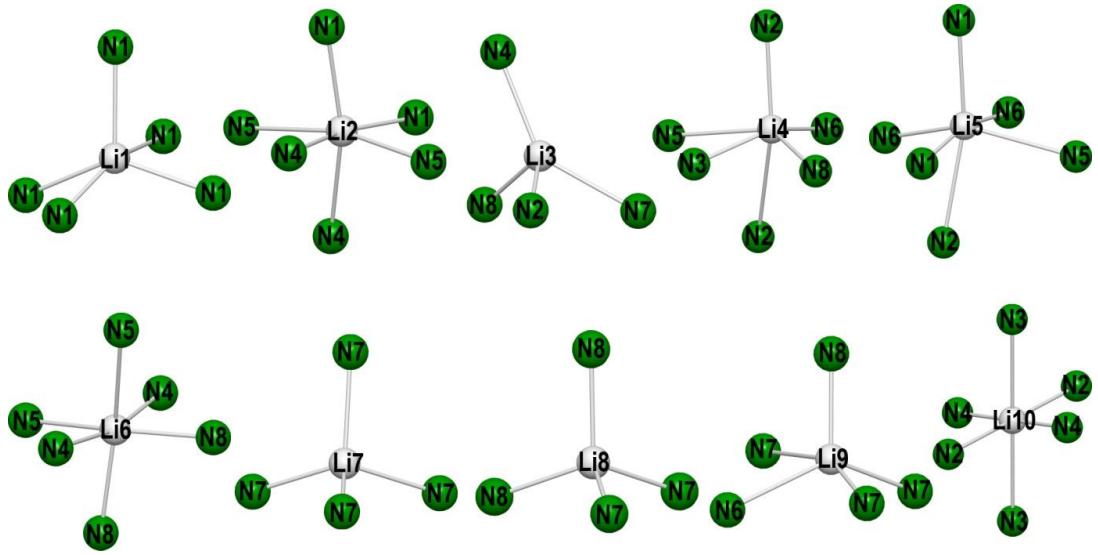

Figure S1. Coordination spheres of the Li^{+} sites. Bond length up to 2.88 Å are shown by a gray line. Gray: Li, Green: N.

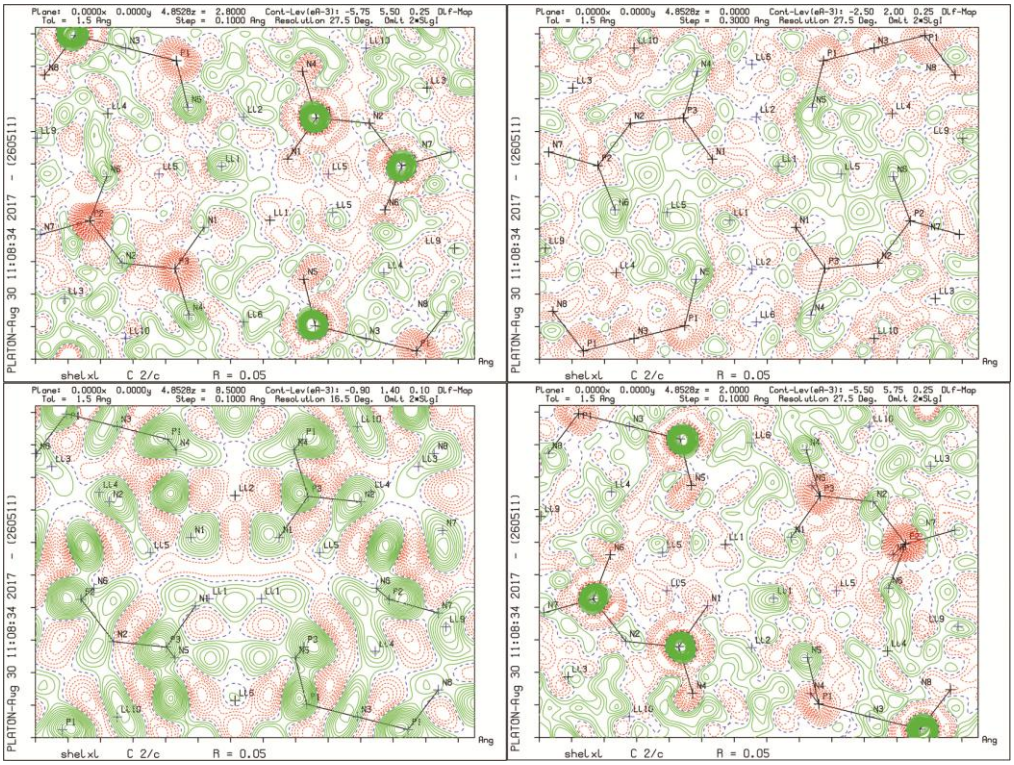

Figure S2. Different Difference Fourier maps of $Li_5P_2N_5$.

D.2. Details of the Rietveld refinement

Table S5. Details of the Rietveld refinement of $Li_5P_2N_5$.

formula	**$Li_5P_2N_5$**
formula mass / g · mol^{-1}	534.9
crystal system / space group	monoclinic *C* 2/*c* (no. 15)
lattice parameters / Å, °	*a* = 14.752(2)
	b = 17.802(2)
	c = 4.8479(5)
	β = 93.196(8)
cell volume / Å^3	1271.1(2)
formula units per cell *Z*	12
X-ray density / g · cm^{-3}	2.61305(49)
linear absorption coefficient / cm^{-1}	82.02(2)
radiation	Cu-$K_{\alpha 1}$ (λ = 1.540596 Å)
monochromator	Ge(111)
diffractometer	Stoe StadiP
detector	linear PSD
2*θ*-range / °	5.0-112.1
temperature / K	298 (2)
data points	7144
number of observed reflections	845
number of parameters	72
program used	TOPAS Academic
structure refinement	Rietveld method
profile function	fundamental parameters model
background function	shifted Chebyshev with 24 terms
R_{wp}	11.310
R_{exp}	2.041
R_p	7.614
R_{Bragg}	6.008
χ^2	5.542

D.3. Detailed Rietveld plot

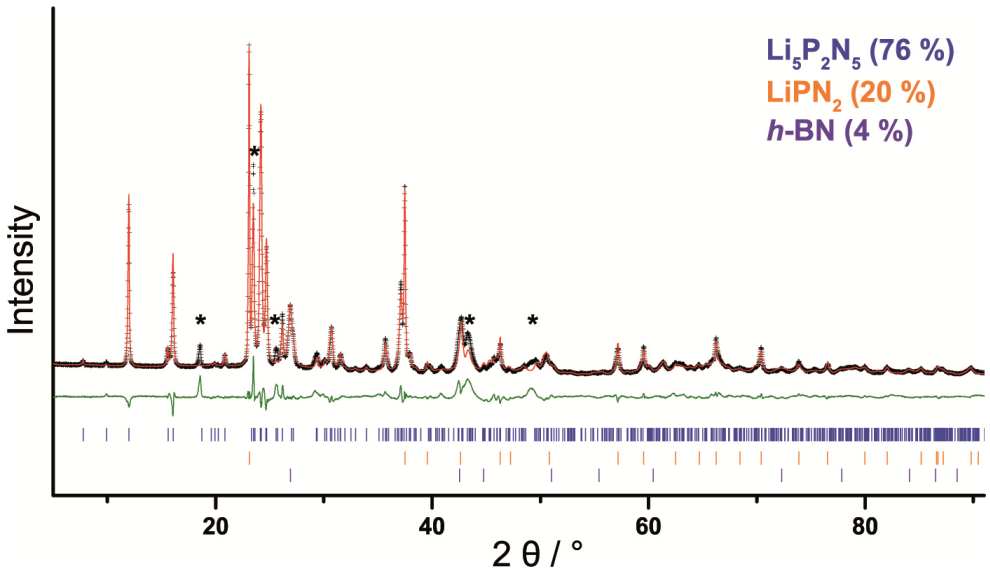

Figure S3. $Li_5P_2N_5$: Observed (black crosses) and calculated (red line) powder diffraction pattern as well as difference profile (green) of the Rietveld refinement. Reflection positions are marked by vertical blue bars. Peak positions of side phases are marked by vertical orange ($LiPN_2$) and violet (*h*-BN) bars.

The side phase *h*-BN can be traced back to the crucible material, which is difficult to remove from the sample. The difference of the peace profile of some peak positions is due to a further side phase, which could not be analyzed.

D.4. ^{31}P, ^{6}Li and ^{7}Li solid state MAS NMR Spectroscopy

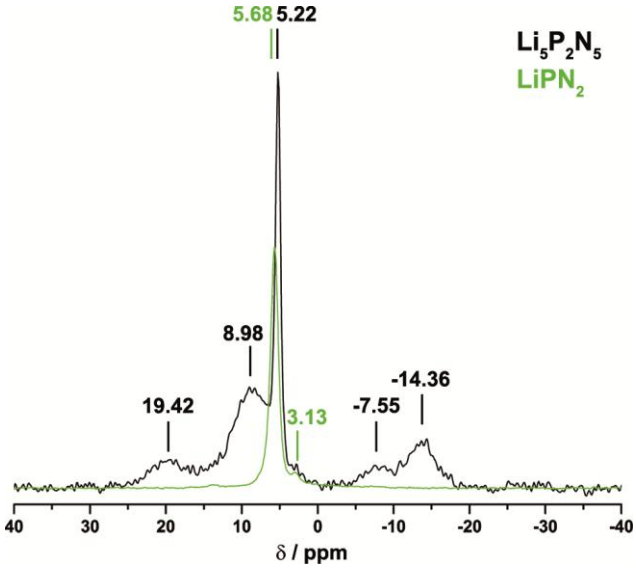

Figure S4. ^{31}P MAS NMR spectrum of $Li_5P_2N_5$ in black and the side phase $LiPN_2$ in green.

The ^{31}P MAS NMR spectrum of $Li_5P_2N_5$ is shown in black and shows one strong resonances at 5.22 ppm and further signals at 19.42, 8.98, −7.55 and −14.36 ppm. $Li_5P_2N_5$ has three crystallographically independent P sites, which all have approximately the same chemical surrounding and bond length to N atoms. The ^{31}P MAS NMR-spectrum of $LiPN_2$ is shown in green. The resonance at 5.68 ppm corresponds to one crystallographically independent P site. The resonance at 3.13 ppm assigned to little amount of side products in the starting material $LiPN_2$.

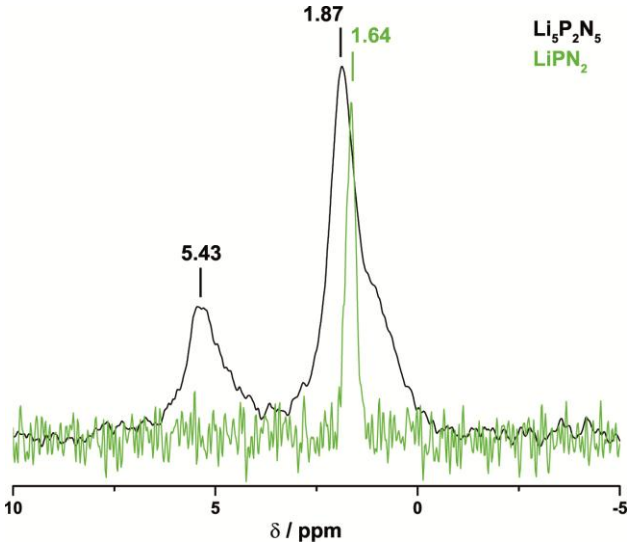

Figure S5. ^{6}Li MAS NMR spectrum of $Li_5P_2N_5$.

The ^{6}Li MAS NMR spectrum shows strong resonances between 5.43 and 1.87 ppm. Due to the small chemical shift differences of the signals, the differentiation of the 9 crystallographically independent sites cannot be observed in the spectrum.

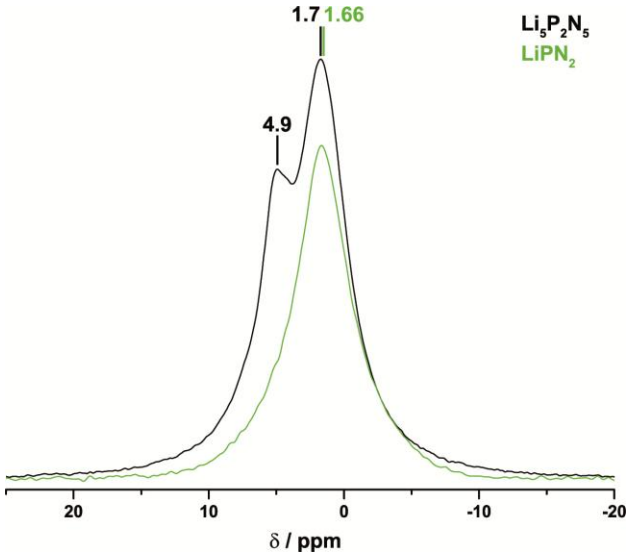

Figure S6. ^{7}Li MAS NMR spectrum of $Li_5P_2N_5$.

The ^{7}Li MAS NMR spectrum shows two strong resonances at 4.9 and 1.7 ppm. Due to the small chemical shift differences of the signals, no differentiation of the crystallographically independent sites can be observed in the spectrum.

D.5. Details of scanning electron microscopy

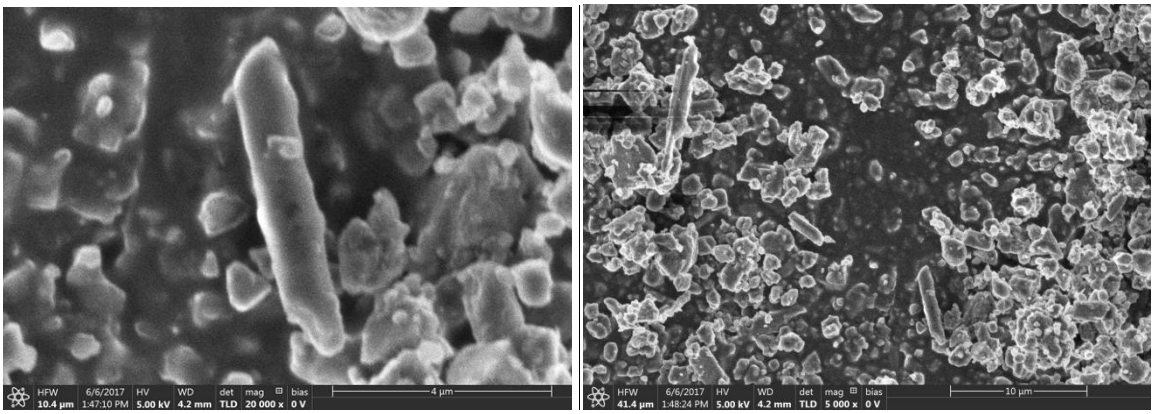

Figure S7. Scanning electron micrographs of $Li_5P_2N_5$.

Table S6. EDX analysis of $Li_5P_2N_5$.

	N	**O**	**P**
EDX point 1[atom %]	63.83	6.50	29.67
EDX point 2[atom %]	67.54	4.10	28.36
EDX point 3[atom %]	67.98	4.55	27.47
Average	**66.45**	**5.05**	**28.50**
Calculated atom %	**41.7**	**0**	**16.7**

Due to hydrolysis of the sample during mounting the sample at air, oxygen can be found in the sample

D.6. FTIR spectrum

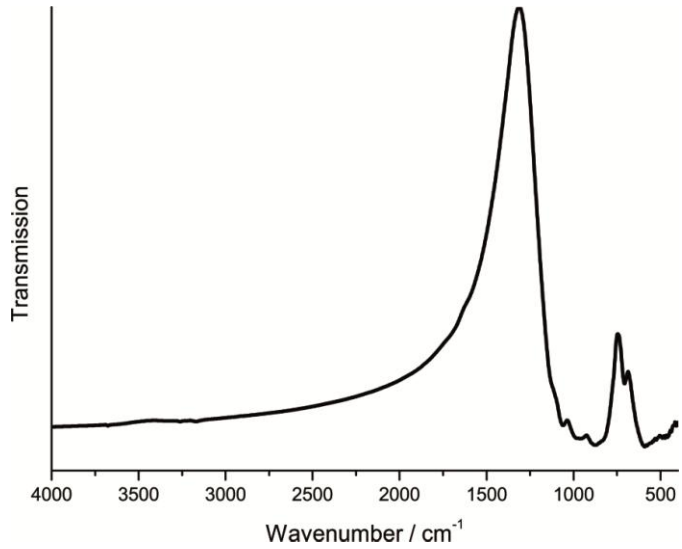

Figure S8. FTIR spectrum of $Li_5P_2N_5$.

Infrared spectroscopy measurements were performed on a Bruker FTIR-IFS 66v/S spectrometer. Before measurement in the range of 400-4000 cm^{-1} the sample was mixed with KBr in a glove box and cold-pressed into a pellet (Ø = 12 mm).The spectrum shows no significant valence vibrations in the region of 3000 cm^{-1}, where N–H vibrations are expected. A weak signal in that region can be explained by surface hydrolysis of the sample. Thus, the incorporation of stoichiometric amounts of hydrogen seems unlikely. Much more significant are the characteristic PN framework vibrations between 400 and 1500 cm^{-1}. The extreme background between 4000 and 1500 cm^{-1} is due to the brown side phases in the sample, which leads to a not transparent pellet.

D.7. Structural Analysis of Possible Lithium Migration Pathways

Possible voids and migration pathways in $Li_5P_2N_5$ were analyzed with TOPOS.[1-4]

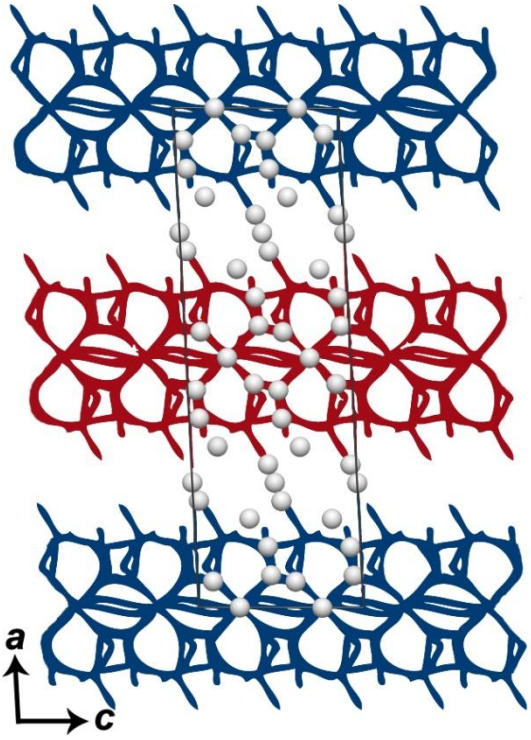

Figure S9. Calculated possible Li^+ pathways (blue and red) according to the voids in the structure and unit cell of $Li_5P_2N_5$. (Li: gray)

D.8. Density functional theory calculations

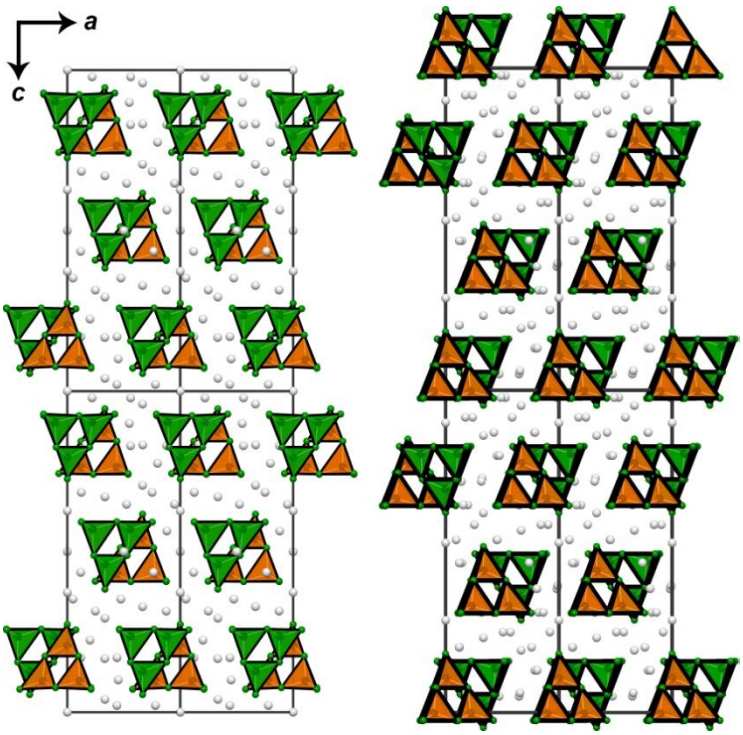

Figure S9. Left: unit cell of β-$Li_{10}P_4N_{10}$ with partially occupied Li position (Li9 is occupied by 2/3). Right: ordering model of β-$Li_{10}P_4N_{10}$ with fully occupied Li atoms (2/3 of Li9 positions were fully occupied), used for calculations. (P: black, N: green, Li: gray)

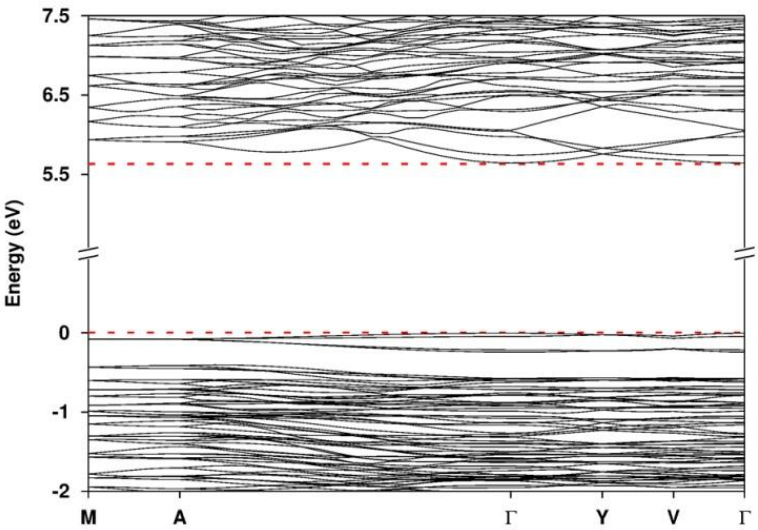

Figure S10. Electronic band structure along high-symmetry directions in the first Brillouin zone for $Li_5P_2N_5$.

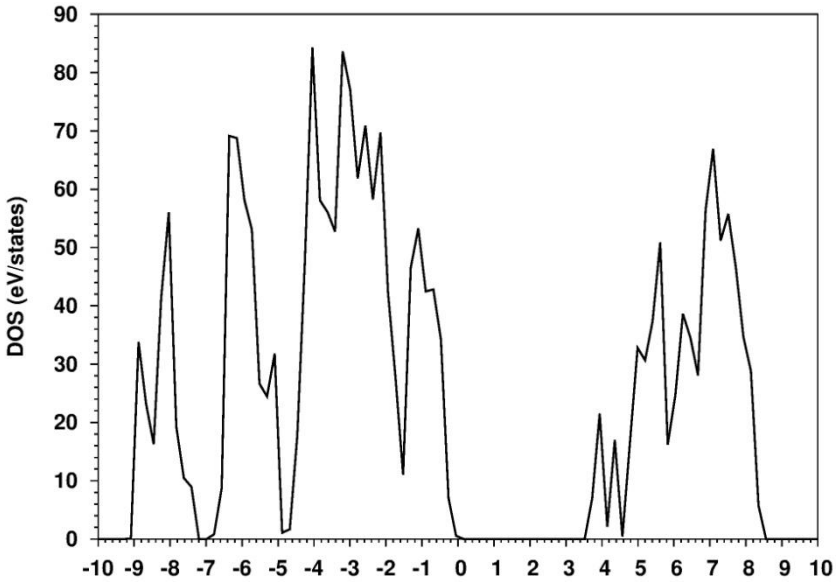

Figure S11. Density of states (DOS) for β-$Li_{10}P_4N_{10}$ (ordering model like in Figure S9). The band-gap estimated to 3.5 eV.

D.9. References

[1] V. A. Blatov, *IUCr CompComm Newsl.* **2006**, *7*, 4–38.

[2] V. A. Blatov, *Crystallogr. Rev.* **2004**, *10*, 249–318.

[3] N. A. Anurova, V. A. Blatov, G. D. Ilyushin, O. A. Blatova, A. K. Ivanov-Schitz, L. N. Dem'yanets, *Solid State Ionics* **2008**, *179*, 2248–2254.

[4] V. A. Blatov, A. P. Shevchenko, V. N. Serezhin, *J. Appl. Crystallogr.* **2000**, *32*, 377–377.

E. Supporting Information for Chapter 6

E.1. Experimental details of the Synthesis of $Li_{47}B_3P_{14}N_{42}$

P_3N_5. The binary starting material P_3N_5, was synthesized by reaction of P_4S_{10} (Sigma Aldrich, 99 %) according to the description of Stock and Grüneberg.[1] A quartz tube-type furnace and a quartz crucible were dried in vacuum for 2 h at 1273 K. The quartz crucible was loaded with P_4S_{10} and placed in the tube furnace. The sample was saturated with ammonia (Air-Liquide, 99.999) for 4 h. After saturation the furnace was heated to 1123 K with a ramp of 278 K/min , fired for 4 h and cooled down to room temperature. The orange product was isolated and washed with water, ethanol and acetone in order to eliminate side products. Phase purity of the product was confirmed by powder X-ray diffraction and FTIR spectroscopy. All further work steps were performed with strict exclusion of oxygen and moisture in an argon-filled glove box (Unilab, MBraun, Garching O_2 < 1 ppm, H_2O < 0.1 ppm).

$LiPN_2$ and Li_7PN_4. Both were prepared by reaction of Li_3N (Rockwood Lithium, 95%) and P_3N_5 in a sealed silica ampoules under N_2 atmosphere.[2,3] For $LiPN_2$ 1.2 equivalents of Li_3N were mixed with 1 equivalent P_3N_5 and for Li_7PN_4 7.2 equivalents of Li_3N with 1 equivalent of P_3N_5. After transformation into a Ta crucible, which was placed in a dried silica tube, the silica tube was sealed to an ampoule. Afterwards it was heated in a tube furnace at 1073 or 893 K for 90 h, respectively. $LiPN_2$ was washed with diluted hydrochloric acid, water and ethanol. Li_7PN_4 was not washed. Phase purity of the products was verified by powder X-ray diffraction and FTIR spectroscopy.

$Li_{47}B_3P_{14}N_{42}$. $Li_{47}B_3P_{14}N_{42}$ can be synthesized by two different approaches.

$$47\ Li_3N + 19\ P_3N_5 + 9\ BN \rightarrow Li_{47}B_3P_{14}N_{42} \quad (1)$$

According to equation 1, $Li_{47}B_3P_{14}N_{42}$ was synthesized by reaction of 48 equivalents Li_3N, 14 equivalents P_3N_5 and 9 equivalents *h*-BN in a Ta crucible in a sealed silica ampoule under N_2 atmosphere analogously to the synthesis of $LiPN_2$ and Li_7PN_4. The ampoule was fired at 1073 K for 42 h. The product was obtained as colorless crystals with brown contamination of Li_3P. The by-product could not be removed by washing ($Li_{47}B_3P_{14}N_{42}$ was not stabile in H_2O, EtOH, or DMF).

$$17\ LiPN_2 + 11\ Li_7PN_4 + 6\ BN \rightarrow Li_{47}B_3P_{14}N_{42} \quad (2)$$

According to equation 2 $Li_{47}B_3P_{14}N_{42}$ was synthesized by reaction of 5.95 equivalents $LiPN_2$, 8.05 equivalents Li_7PN_4 (in excess) and 0.7 equivalents *h*-BN (STERM, 99%) under high-pressure/high-temperature conditions using a modified Walker-type multi-anvil assembly in combination with a 1000 t press (Voggenreiter, Mainleus, Germany). The starting materials were thoroughly mixed and ground under inert conditions before they were packed in an h-BN crucible. The crucible was transferred in a specially prepared MgO octahedron (Ceramic Substrates & Components, Isle of Wight, UK) with an edge length of 18 mm. Additional details about the high-pressure setup might be found in literature.[4–8] The reaction was carried out at 3.5 GPa of pressure and 1273 K. The temperature was built up over 120 min, maintained for 240 min and ramped to room temperature in 100 min. The product was obtained as colorless crystals.

E.2. Information on data collection and structure elucidation of $Li_{47}B_3P_{14}N_{42}$

Single crystal X-ray diffraction of $Li_{47}B_3P_{14}N_{42}$ was performed with a D8 Venture diffractometer (Bruker, Billerica MA, USA) using Mo-K_α radiation from a fine-focused sealed tube X-ray source. The cell determination and integration was carried out using the Bruker program APEX2 and a multi-scan absorption correction. The space group was determined with Xprep[9] and structure solution was carried out with SHELXS-97 using direct methods and structure refinement with SHELXL-97.[10–12] Crystal structures were visualized using DIAMOND.[13]

X-ray powder diffraction for phase purity analysis and structure confirmation was executed on a StadiP diffractometer (Stoe & Cie, Darmstadt, Germany) in para-focussing Debye-Scherrer geometry using a Cu anode. With a Ge(111) single-crystal monochromator the Cu-$K_{\alpha1}$ radiation was selected from the raw X-ray spectrum. For detection a Mythen 1K Si-strip detector (Dectris, Baden, Switzerland) was used. Rietveld refinement was carried out using the TOPAS-Academic V4.1 program package.[14] The background was handled using a shifted-Chebychev function, and the peak shapes were described using the fundamental parameters approach.[15,16] Temperature dependent powder X-ray diffraction data (Mo-$K_{\alpha1}$ radiation, λ = 0.70930 Å) were recorded on a STOE StadiP diffractometer with a high-temperature graphite furnace, an image plate position sensitive detector and a Ge(111) monochromator. Diffraction patterns were collected up to a 1273 K with 25 K increments. With a rate of 5 K/min the temperature was increased between the measurements.

^{31}P, ^{6}Li, ^{7}Li and ^{11}B solid state MAS (Magnetic Angle Spinning) **NMR** (Nuclear Magnetic Resonance) spectra were recorded on a DSX Avance spectrometer (Bruker) with a magnetic field of 11.7 T. The ZrO_2 rotor (outer diameter of 2.5 mm) was spun at rotation frequency of 20 kHz. The experimental data were analyzed by device-specific software.

For **EDX measurements** a carbon coated sample was examined with a scanning electron microscope (SEM) type JSM-6500F (JEOL, Tokyo, Japan). Elemental analyses were carried out by an energy dispersive X-ray spectrometer type 7418 (Oxford Instruments, Abington, UK). The data was analyzed by INCA.[17]

Infrared spectroscopy was performed on a Bruker FTIR-IFS 66v/S spectrometer in a range of 400-4000 cm^{-1}. The sample was mixed with KBr and cold pressed into a pellet. The data were evaluated by OPUS.[18]

For determination of the **total conductivity** the single phase sample (synthesis according equation 2) was cold-pressed into a dense pellet (Ø = 5 mm, d = 1.27 mm) in a glove box. The pellets were coated with gold thin films blocking electrodes (150 nm thickness) by thermal evaporation (Ø = 4.5 mm, cell constant = 0.801 cm^{-1}). Impedance measurements were executed in the frequency range of 7 MHz to 100 mHz with an amplitude of 100 mV using a frequency response analyzer (BioLogic SP-300). The obtained conductivity values follow the Arrhenius equation in the measured temperature range between 253 and 358 K ($\sigma \cdot T = A \cdot \exp(-E_a/RT)$). To compare the measured conductivity of $Li_{47}B_3P_{14}N_{42}$ to that of $LiPN_2$ and Li_7PN_4 the conductivity was extrapolated to 400 K, assuming constant activation energy.

E.3. Details of single-crystal refinement

Table S1. Details of the single-crystal refinement of $Li_{47}B_3P_{14}N_{42}$. . For single-crystal structure analysis we used a product synthesized according to equation (2) by high-pressure/high-temperature synthesis.

formula	**$Li_{47}B_3P_{14}N_{42}$**
formula mass / g · mol^{-1}	4141.83
crystal system / space group	trigonal *P*3*c*1 (no. 158)
lattice parameters / Å	*a* = 19.3036(7)
	c = 18.0200(7)
cell volume / Å^3	5815.2(5)
formula units per cell Z	2
calculated density / g · cm^{-3}	2.365
F(000)	3960
diffractometer	Bruker D8 Venture
temperature / K	100
radiation	Mo-K$_\alpha$ (λ = 0.71073 Å), Goebel mirror
absorption correction	multi scan
θ-range / °	3.65-26.23
measured reflections	69567
independent reflections	29949
observed reflections	69567
refined parameters	335
GooF	0.917
R indices [$F_0^2 \geq 2\sigma (F_0^2)$]	R_1 = 0.0733, wR_2 = 0.1768
R indices (all data)	R_1 = 0.1767, wR_2 = 0.2228
max/min res. electron density / e Å^{-3}	2.107/ -1.197
R	0.1796
twin	plane and inversion
BASF	0.36852/ 0.22583/ 0.13121

$w = 1/[\sigma^2(F_o^2) + (0.0984 \cdot P)^2]$ where $P = (F_o^2 + 2\,F_c^2) / 3$.

E.4. Additional crystallographic data for $Li_{47}B_3P_{14}N_{42}$

Table S2. Fractional atomic coordinates, isotropic thermal displacement parameters, and site occupancies for $Li_{47}B_3P_{14}N_{42}$.

Atom	Wyckoff Symbol	*x*	*y*	*z*	U_{iso} / Å^2
P11	6d	0.3260(6)	0.3283(5)	0.2784(3)	0.0030(3)
P12	6d	0.3244(7)	0.2407(7)	0.1502(6)	0.0030(3)
P13	6d	0.2405(7)	0.3250(7)	0.1507(6)	0.0030(3)
P14	6d	0.4105(6)	0.4104(5)	0.1460(4)	0.0030(3)
N11	6d	0.3325(18)	0.3320(19)	0.3693(12)	0.007(3)
N21	6d	0.330(2)	0.164(2)	0.1285(17)	0.007(3)
N31	6d	0.163(2)	0.322(2)	0.1278(17)	0.007(3)
N41	6d	0.007(2)	0.5175(17)	0.1177(13)	0.007(3)
N12	6d	0.3225(18)	0.2425(17)	0.2427(16)	0.0032(8)
N13	6d	0.2455(18)	0.328(2)	0.2445(16)	0.0032(8)
N14	6d	0.4094(17)	0.4079(17)	0.2391(13)	0.0032(8)
N23	6d	0.2457(14)	0.2389(15)	0.1226(11)	0.0032(8)
N34	6d	0.321(2)	0.406(2)	0.1182(16)	0.0032(8)
N24	6d	0.4084(19)	0.327(2)	0.1195(16)	0.0032(8)
P21	6d	0.0844(7)	0.3401(7)	0.3950(5)	0.0030(3)
P22	6d	0.3408(7)	0.0852(7)	0.3939(5)	0.0030(3)
P23	6d	0.0008(9)	0.4261(6)	0.3931(4)	0.0030(3)
P24	6d	0.3390(6)	-0.0002(9)	0.2635(3)	0.0030(3)
N211	6d	0.2628(15)	0.002(2)	0.4245(12)	0.0032(8)
N212	6d	0.4193(18)	0.0769(18)	0.4219(16)	0.0032(8)
N213	6d	0.0826(19)	0.4212(18)	0.4244(15)	0.0032(8)
N214	6d	0.3437(19)	0.1640(19)	0.4234(16)	0.004(3)
N215	6d	0.0080(19)	0.5087(16)	0.4217(12)	0.004(3)
N216	6d	0.1619(18)	0.3370(19)	0.4273(15)	0.004(3)
N217	6d	0.0783(18)	0.3439(18)	0.3018(17)	0.0032(8)
N218	6d	0.005(2)	0.4209(16)	0.2967(13)	0.0032(8)
N219	6d	0.001(2)	0.3343(18)	0.1813(11)	0.004(3)
N220	6d	0.340(2)	0.0825(18)	0.3017(16)	0.0032(8)
P31	6d	0.1602(7)	0.1587(7)	0.4842(5)	0.0161(6)
B31	6d	0.078(2)	0.075(2)	0.0069(18)	0.004(2)
N311	2a	0	0	0.000(2)	0.004(3)
N312	6d	0.002(3)	0.230(2)	0.0236(12)	0.0143(15)
N313	6d	0.1505(19)	0.0805(19)	0.0093(18)	0.0039(11)

N314	6d	0.1642(18)	0.1583(19)	0.3947(15)	0.0143(15)
N315	6d	0.081(2)	0.157(2)	0.0139(16)	0.0039(11)
P41	6d	0.5091(7)	0.1747(7)	0.0540(7)	0.0161(6)
B41	6d	0.588(3)	0.334(3)	0.032(2)	0.004(2)
N411	6d	0.434(2)	0.098(2)	0.0252(17)	0.0143(15)
N412	6d	0.595(2)	0.1796(19)	0.0258(19)	0.0039(11)
N413	2c	2/3	1/3	0.030(3)	0.004(3)
N414	6d	0.514(2)	0.259(2)	0.0344(17)	0.0039(11)
N415	6d	0.5110(19)	0.170(2)	0.1478(19)	0.0143(15)
P81	6d	0.1750(7)	0.5088(7)	0.0546(7)	0.0161(6)
B81	6d	0.332(2)	0.591(3)	0.029(2)	0.004(2)
N811	6d	0.099(2)	0.433(2)	0.0209(17)	0.0143(15)
N812	6d	0.182(2)	0.591(2)	0.0295(19)	0.0039(11)
N813	2b	1/3	2/3	0.029(3)	0.004(3)
N814	6d	0.2570(18)	0.5150(19)	0.0281(17)	0.0039(11)
N815	6d	0.163(2)	0.4963(18)	0.1485(17)	0.0143(15)
P51	6d	0.0027(8)	0.0897(6)	0.2358(4)	0.0113(5)
N511	6d	0.1617(19)	0.003(3)	0.1960(13)	0.021(2)
N512	6d	0.1069(16)	0.0227(16)	0.3236(16)	0.021(2)
N513	6d	0.0821(18)	0.0817(17)	0.2186(13)	0.013(2)
P61	6d	0.5770(7)	0.3308(8)	0.3048(6)	0.0113(5)
N611	6d	0.5887(15)	0.2529(16)	0.3462(12)	0.013(2)
N612	6d	0.5077(19)	0.3348(19)	0.3568(17)	0.021(2)
N613	6d	0.5654(16)	0.3426(18)	0.2170(15)	0.021(2)
P71	6d	0.3307(7)	0.5760(7)	0.3066(6)	0.0113(5)
N711	6d	0.2508(18)	0.5883(18)	0.3223(16)	0.013(2)
N712	6d	0.321(2)	0.5013(19)	0.3479(17)	0.021(2)
N713	6d	0.3073(16)	0.5492(16)	0.2154(16)	0.021(2)
Li1	2a	0	0	0.137(6)	0.0319(16)
Li2	6d	0.457(4)	0.327(6)	0.030(4)	0.0319(16)
Li3	6d	0.070(5)	0.190(5)	0.405(5)	0.0319(16)
Li4	6d	0.219(4)	0.625(4)	0.218(3)	0.0319(16)
Li5	6d	0.061(5)	0.513(5)	0.016(3)	0.0319(16)
Li6	6d	0.092(3)	0.095(3)	0.343(3)	0.0319(16)
Li7	6d	0.099(4)	0.168(4)	0.138(4)	0.0319(16)
Li8	6d	0.159(4)	0.558(4)	0.408(4)	0.0319(16)
Li9	6d	0.530(3)	0.022(3)	0.308(3)	0.0319(16)
Li10	2c	2/3	1/3	0.414(6)	0.0319(16)
Li11	6d	0.247(4)	0.590(4)	0.199(3)	0.0319(16)
Li12	6d	0.374(5)	0.441(5)	0.421(5)	0.0319(16)

Li13	6d	0.212(3)	0.383(4)	0.319(3)	0.0319(16)
Li14	6d	0.192(4)	0.090(4)	0.119(3)	0.0319(16)
Li15	6d	0.461(4)	0.334(4)	0.254(4)	0.0319(16)
Li16	6d	0.144(5)	0.590(4)	0.145(4)	0.0319(16)
Li17	6d	0.195(5)	0.201(5)	0.023(2)	0.0319(16)
Li18	6d	0.227(4)	0.281(4)	0.417(3)	0.0319(16)
Li19	6d	0.191(4)	0.183(4)	0.277(2)	0.0319(16)
Li20	6d	0.468(5)	0.133(5)	0.302(4)	0.0319(16)
Li21	6d	0.150(5)	0.480(5)	0.302(4)	0.0319(16)
Li22	6d	0.333(5)	0.338(6)	0.017(3)	0.0319(16)
Li23	6d	0.201(5)	0.090(5)	0.417(4)	0.0319(16)
Li24	6d	0.377(3)	0.070(3)	0.049(3)	0.0319(16)
Li25	6d	0.436(3)	0.018(3)	0.033(2)	0.0319(16)
Li26	6d	0.478(4)	0.261(4)	0.148(4)	0.0319(16)
Li27	6d	0.386(4)	0.183(5)	0.026(3)	0.0319(16)
Li28	6d	0.032(4)	0.256(4)	0.133(3)	0.0319(16)
Li29	6d	0.215(4)	0.012(4)	0.297(3)	0.0319(16)
Li30	6d	0.392(4)	0.105(4)	0.140(3)	0.0319(16)
Li31	6d	0.320(4)	0.462(5)	0.021(4)	0.0319(16)
Li32	6d	0.103(3)	0.279(4)	0.228(3)	0.0319(16)
Li33	6d	0.308(3)	0.031(3)	0.052(3)	0.0319(16)
Li34	6d	0.250(4)	0.465(5)	0.145(4)	0.0319(16)
Li35	6d	0.585(4)	0.128(4)	0.142(4)	0.0319(16)
Li36	6d	0.010(6)	0.337(4)	0.0009(18)	0.0319(16)
Li37	2b	1/3	2/3	0.429(6)	0.0319(16)
Li38	6d	0.128(4)	0.341(4)	0.025(3)	0.0319(16)
Li39	6d	0.415(3)	0.023(3)	0.108(3)	0.0319(16)
Li40	6d	0.595(4)	0.265(4)	0.187(3)	0.0319(16)
Li41	6d	0.256(3)	0.456(3)	0.440(3)	0.0319(16)
Li42	6d	0.294(4)	0.225(4)	0.399(3)	0.0319(16)
Li43	6d	0.341(4)	0.476(4)	0.274(3)	0.0319(16)
Li44	6d	0.574(4)	0.153(4)	0.417(3)	0.0319(16)
Li45	6d	0.439(4)	0.363(5)	0.406(4)	0.0319(16)
Li46	6d	0.120(5)	0.271(5)	0.024(3)	0.0319(16)
Li47	6d	0.381(4)	0.230(4)	0.334(3)	0.0319(16)
Li48	6d	0.488(4)	0.231(5)	0.417(4)	0.0319(16)
Li49	6d	0.251(3)	0.068(3)	0.069(3)	0.0319(16)

Table S3. List of interatomic distances / Å for $Li_{47}B_3P_{14}N_{42}$.

P11	N11	1.6416(223)	N14	Li43	2.3670(1003)	N411	Li36	2.1209(734)
P11	N13	1.6670(402)	N23	Li17	1.9996(496)	N411	Li33	2.1624(592)
P11	N14	1.7265(244)	N23	Li7	2.4685(717)	N411	Li45	2.2010(805)
P11	N12	1.7463(372)	N23	Li14	2.5221(781)	N411	Li30	2.2505(695)
P12	N23	1.5823(330)	N23	Li22	2.6262(699)	N411	Li27	2.252(118)
P12	N21	1.5864(459)	N34	Li31	2.0634(889)	N412	Li44	2.0110(643)
P12	N12	1.6680(308)	N34	Li34	2.2293(1147)	N412	Li2	2.1520(1252)
P12	N24	1.7347(286)	N34	Li22	2.3252(975)	N412	Li35	2.2851(813)
P13	N31	1.5248(444)	N34	Li16	2.5374(706)	N413	Li10	2.0903(1209)
P13	N34	1.6652(292)	N24	Li2	1.8658(854)	N414	Li2	2.0939(1306)
P13	N13	1.6924(308)	N24	Li35	2.3211(675)	N414	Li27	2.1576(705)
P13	N23	1.7876(350)	N24	Li26	2.3246(1040)	N414	Li26	2.1684(807)
P14	N41	1.5495(258)	N24	Li22	2.4257(940)	N414	Li48	2.1702(794)
P14	N24	1.6602(429)	N24	Li15	2.6051(796)	N415	Li40	1.8755(619)
P14	N14	1.6782(245)	N211	Li17	2.1645(711)	N415	Li35	1.9664(1042)
P14	N34	1.7596(433)	N211	Li22	2.1946(909)	N415	Li30	1.9972(718)
P21	N216	1.6340(411)	N211	Li3	2.4130(871)	N415	Li26	2.1472(1030)
P21	N213	1.6695(412)	N211	Li29	2.5190(666)	N415	Li39	2.5966(554)
P21	N217	1.6877(321)	N211	Li23	2.5206(1251)	N415	Li20	2.8857(794)
P21	N211	1.6895(251)	N212	Li2	2.1515(800)	N811	Li36	1.8253(713)
P22	N214	1.5857(419)	N212	Li22	2.3617(699)	N811	Li12	1.9343(993)
P22	N211	1.6530(263)	N212	Li20	2.3889(769)	N811	Li5	2.0158(1255)
P22	N220	1.6621(302)	N212	Li48	2.5827(920)	N811	Li38	2.1135(1027)
P22	N212	1.6791(419)	N212	Li44	2.5878(737)	N811	Li25	2.1397(741)
P23	N215	1.6142(360)	N213	Li31	2.0155(746)	N811	Li41	2.2930(676)
P23	N212	1.645(27)	N213	Li22	2.2808(708)	N811	Li39	2.6023(652)
P23	N213	1.7233(436)	N213	Li8	2.3111(707)	N811	Li33	2.8501(509)
P23	N218	1.7442(248)	N213	Li21	2.5237(763)	N812	Li5	2.0652(818)
P24	N219	1.4848(207)	N214	Li42	1.9053(1027)	N812	Li16	2.2037(839)
P24	N217	1.6188(277)	N214	Li47	1.9544(645)	N812	Li31	2.2131(1177)
P24	N218	1.6455(425)	N214	Li27	2.0092(620)	N812	Li8	2.2613(815)
P24	N220	1.7297(417)	N214	Li23	2.3889(883)	N813	Li37	1.8020(1209)
P31	N312	1.5199(330)	N214	Li48	2.4171(759)	N814	Li41	1.9429(579)
P31	N314	1.6148(285)	N215	Li5	1.9323(630)	N814	Li31	1.9458(1148)
P31	N313	1.6884(415)	N215	Li12	1.9610(876)	N814	Li34	2.2928(835)
P31	N315	1.6959(442)	N215	Li9	2.1273(596)	N815	Li11	1.9483(611)
P41	N411	1.5546(294)	N215	Li45	2.3164(1122)	N815	Li16	2.0183(1062)
P41	N414	1.6211(444)	N215	Li25	2.4392(574)	N815	Li34	2.0504(1104)

P41	N412	1.6911(439)	N215	Li8	2.5863(826)	N815	Li4	2.4947(732)
P41	N415	1.6941(365)	N215	Li44	2.6964(718)	N815	Li21	2.7810(783)
P81	N811	1.5860(296)	N216	Li38	2.0006(690)	N511	Li28	2.0010(961)
P81	N812	1.5894(439)	N216	Li18	2.0349(1038)	N511	Li14	2.0262(782)
P81	N814	1.5995(403)	N216	Li46	2.1061(788)	N511	Li29	2.0549(672)
P81	N815	1.7085(330)	N216	Li41	2.1109(503)	N511	Li7	2.1559(684)
P51	N511	1.5643(571)	N216	Li13	2.1619(592)	N511	Li32	2.2717(1018)
P51	N512	1.6440(302)	N216	Li3	2.5153(827)	N511	Li49	2.7605(571)
P51	N513	1.6449(423)	N217	Li32	2.0403(825)	N512	Li6	1.5982(763)
P51	N513	1.7069(256)	N217	Li21	2.2763(873)	N512	Li6	2.1463(472)
P61	N613	1.6298(302)	N217	Li13	2.3192(676)	N512	Li29	2.2490(942)
P61	N612	1.6664(412)	N217	Li29	2.388(67)	N512	Li23	2.3367(773)
P61	N611	1.7858(236)	N218	Li9	2.0041(795)	N512	Li3	2.4228(1096)
P61	N611	1.7912(371)	N218	Li20	2.3319(831)	N512	Li19	2.8093(690)
P71	N712	1.5486(400)	N218	Li21	2.4397(956)	N513	Li7	2.1090(819)
P71	N711	1.6438(266)	N219	Li30	1.9251(748)	N513	Li1	2.1591(773)
P71	N711	1.6975(430)	N219	Li39	1.9277(717)	N513	Li6	2.2536(588)
P71	N713	1.7143(303)	N219	Li28	2.0748(960)	N513	Li19	2.2890(567)
N11	Li42	1.8894(795)	N219	Li33	2.5200(574)	N513	Li14	2.7217(795)
N11	Li45	1.9472(837)	N219	Li24	2.6679(591)	N611	Li10	1.9575(708)
N11	Li18	1.9623(714)	N219	Li32	2.7976(896)	N611	Li48	2.1825(829)
N11	Li12	2.0619(958)	N220	Li29	2.0971(716)	N611	Li44	2.2090(794)
N11	Li36	2.3779(400)	N220	Li20	2.1556(964)	N611	Li20	2.4551(719)
N11	Li47	2.6460(1009)	N220	Li47	2.6113(833)	N611	Li40	2.8759(583)
N21	Li49	2.0207(541)	N311	Li1	2.4687(1140)	N612	Li45	1.8876(1047)
N21	Li30	2.0336(1054)	N312	Li33	1.4383(883)	N612	Li44	1.9358(627)
N21	Li27	2.0780(672)	N312	Li49	1.4465(616)	N612	Li15	2.0568(817)
N21	Li14	2.3154(729)	N312	Li46	2.0030(1073)	N612	Li48	2.1388(993)
N21	Li26	2.5381(679)	N312	Li36	2.0343(1015)	N612	Li47	2.3012(620)
N21	Li33	2.7535(706)	N312	Li28	2.0452(589)	N613	Li40	1.8407(670)
N21	Li24	2.7954(790)	N312	Li18	2.1630(597)	N613	Li40	1.9283(983)
N31	Li38	2.0665(725)	N312	Li38	2.3013(668)	N613	Li15	2.0491(894)
N31	Li32	2.0807(603)	N312	Li24	2.5331(920)	N613	Li26	2.0533(664)
N31	Li46	2.0832(648)	N312	Li42	2.6071(727)	N613	Li35	2.1380(916)
N31	Li28	2.1920(746)	N312	Li14	2.7976(634)	N711	Li21	2.0549(730)
N31	Li34	2.4291(835)	N313	Li23	1.868(80)	N711	Li8	2.1979(797)
N31	Li7	2.5932(790)	N313	Li17	2.0522(968)	N711	Li4	2.2014(752)
N41	Li5	2.1315(788)	N313	Li14	2.1062(664)	N711	Li11	2.2239(614)
N41	Li39	2.1982(678)	N313	Li49	2.3339(760)	N711	Li37	2.4725(884)
N41	Li35	2.3029(773)	N314	Li6	1.6126(528)	N712	Li43	1.5328(750)

N41	Li25	2.3075(580)	N314	Li23	1.8278(1230)	N712	Li41	1.9991(595)
N41	Li16	2.3438(878)	N314	Li18	2.0904(730)	N712	Li13	2.2602(570)
N12	Li47	2.0767(775)	N314	Li42	2.1716(726)	N712	Li12	2.3082(1174)
N12	Li19	2.2868(739)	N314	Li19	2.1787(460)	N712	Li8	2.416(66)
N12	Li15	2.3636(663)	N314	Li3	2.1973(1225)	N712	Li4	2.8112(647)
N12	Li42	2.8572(615)	N315	Li17	1.9292(967)	N713	Li4	1.1523(650)
N13	Li13	2.0085(824)	N315	Li46	1.9457(994)	N713	Li11	1.7261(1005)
N13	Li32	2.4388(653)	N315	Li3	2.0842(926)	N713	Li34	1.9175(775)
N13	Li19	2.5179(795)	N315	Li7	2.2568(775)	N713	Li11	2.0549(590)
N13	Li43	2.5644(678)	N411	Li24	1.0450(609)	N713	Li43	2.1105(921)
N14	Li9	1.8999(538)	N411	Li25	1.5703(782)	N713	Li16	2.3161(1001)
N14	Li15	2.1261(1020)	N411	Li39	1.9814(657)	N713	Li4	2.7464(1018)
B31	N313	1.3503(581)	B41	N412	1.4090(778)	B81	N813	1.4489(609)
B31	N311	1.4828(275)	B41	N414	1.4389(492)	B81	N814	1.4576(432)
B31	N315	1.5599(602)	B41	N413	1.5264(649)	B81	N812	1.4864(647)

Table S4. List of bond angles / ° for $Li_{18}P_6N_{16}$.

	P-N-P						
P11	N11	P13	148.012(875)	P21	N216	P22	142.785(1557)
P11	N11	P12	144.233(863)	P21	N216	P23	145.612(1556)
P11	N11	P14	142.507(840)	P21	N216	P24	145.123(1302)
P11	N13	P13	33.392(1207)	P21	N213	P22	88.983(1386)
P11	N13	P12	88.132(1125)	P21	N213	P23	33.906(1234)
P11	N13	P14	88.212(1105)	P21	N213	P24	89.452(1116)
P11	N14	P13	87.712(947)	P21	N217	P22	86.127(1319)
P11	N14	P12	85.660(906)	P21	N217	P23	83.687(1307)
P11	N14	P14	31.802(906)	P21	N217	P24	29.148(1087)
P11	N12	P13	86.168(1084)	P21	N211	P22	31.587(1200)
P11	N12	P12	32.439(1004)	P21	N211	P23	86.634(1280)
P11	N12	P14	87.672(1014)	P21	N211	P24	87.407(935)
P12	N23	P13	35.828(1163)	P22	N214	P21	145.842(1338)
P12	N23	P14	91.071(1068)	P22	N214	P23	143.552(1474)
P12	N23	P11	89.615(927)	P22	N214	P24	144.354(1278)
P12	N21	P13	150.300(1564)	P22	N211	P21	32.369(1189)
P12	N21	P14	142.826(1388)	P22	N211	P23	86.808(1338)
P12	N21	P11	140.076(1369)	P22	N211	P24	88.361(951)
P12	N12	P13	87.691(1322)	P22	N220	P21	88.845(1137)
P12	N12	P14	90.509(1088)	P22	N220	P23	88.609(1397)
P12	N12	P11	34.166(1029)	P22	N220	P24	33.235(1029)
P12	N24	P13	88.714(1423)	P22	N212	P21	85.251(1162)
P12	N24	P14	32.466(1144)	P22	N212	P23	30.614(1342)
P12	N24	P11	87.773(1114)	P22	N212	P24	86.752(1111)
P13	N31	P12	144.608(1794)	P23	N215	P21	141.382(1298)
P13	N31	P11	140.839(1570)	P23	N215	P22	148.40(112)
P13	N31	P14	147.140(1781)	P23	N215	P24	144.072(1024)
P13	N34	P12	90.297(1480)	P23	N212	P21	85.842(1422)
P13	N34	P11	90.283(1195)	P23	N212	P22	31.318(1101)
P13	N34	P14	34.958(1327)	P23	N212	P24	86.987(1107)
P13	N13	P12	89.055(1394)	P23	N213	P21	32.712(1347)
P13	N13	P11	32.828(1036)	P23	N213	P22	87.456(1117)
P13	N13	P14	88.875(1383)	P23	N213	P24	88.298(1021)
P13	N23	P12	31.207(951)	P23	N218	P21	85.520(1246)

P13	N23	P11	87.004(844)	P23	N218	P22	87.454(959)
P13	N23	P14	86.879(1055)	P23	N218	P24	31.051(810)
P14	N41	P12	149.913(1177)	P24	N219	P22	143.603(870)
P14	N41	P13	141.971(1346)	P24	N219	P21	143.181(868)
P14	N41	P11	142.919(1094)	P24	N219	P23	148.348(882)
P14	N24	P12	34.118(1198)	P24	N217	P22	86.518(1173)
P14	N24	P13	89.131(1444)	P24	N217	P21	30.517(1131)
P14	N24	P11	88.403(1108)	P24	N217	P23	83.623(1205)
P14	N14	P12	87.046(1041)	P24	N218	P22	88.994(967)
P14	N14	P13	87.662(1235)	P24	N218	P21	86.196(950)
P14	N14	P11	32.830(838)	P24	N218	P23	33.145(1092)
P14	N34	P12	87.574(1177)	P24	N220	P22	31.779(1044)
P14	N34	P13	32.835(1402)	P24	N220	P21	86.481(1066)
P14	N34	P11	86.385(1066)	P24	N220	P23	86.634(1113)

N-P-N

N11	P11	N14	35.643(718)	N217	P21	N213	37.801(937)
N11	P11	N13	32.971(802)	N217	P21	N220	93.305(1606)
N11	P11	N12	35.191(793)	N217	P21	N211	36.481(859)
N21	P12	N12	38.002(1100)	N217	P21	N216	31.336(903)
N21	P12	N23	32.701(1125)	N218	P24	N217	39.233(1173)
N21	P12	N24	36.515(1135)	N218	P24	N219	30.517(803)
N31	P13	N13	38.145(1265)	N218	P24	N220	36.908(996)
N31	P13	N34	35.598(1434)	N218	P24	N212	91.658(1252)
N31	P13	N23	36.249(1301)	N218	P24	N213	94.358(1223)
N41	P14	N14	36.355(911)	N218	P24	N215	147.804(1518)
N41	P14	N34	37.975(1045)	N218	P23	N217	93.078(1500)
N41	P14	N24	33.318(1167)	N218	P23	N219	146.291(1355)
N12	P12	N21	35.844(993)	N218	P23	N220	90.796(1222)
N12	P12	N23	35.632(856)	N218	P23	N212	34.941(813)
N12	P12	N13	92.807(1550)	N218	P23	N213	37.418(807)
N12	P12	N24	36.524(951)	N218	P23	N215	32.016(691)
N12	P12	N14	89.636(1303)	N219	P24	N217	35.167(880)
N12	P12	N11	145.976(1629)	N219	P24	N218	34.246(759)
N12	P11	N21	148.934(1751)	N219	P24	N220	36.991(847)

N12	P11	N23	94.760(1318)	N220	P22	N219	145.994(1652)
N12	P11	N13	36.223(1050)	N220	P22	N214	33.51(92)
N12	P11	N24	90.509(1393)	N220	P22	N212	36.725(964)
N12	P11	N14	36.929(873)	N220	P22	N211	35.756(842)
N12	P11	N11	32.803(820)	N220	P22	N217	91.532(1440)
N13	P11	N31	147.562(2050)	N220	P22	N218	93.029(1558)
N13	P11	N34	93.684(1507)	N220	P24	N219	31.098(819)
N13	P11	N12	38.246(1213)	N220	P24	N214	148.481(1761)
N13	P11	N14	36.835(1179)	N220	P24	N212	91.569(1367)
N13	P11	N11	32.407(941)	N220	P24	N211	92.692(1403)
N13	P11	N23	90.117(1350)	N220	P24	N217	35.149(994)
N13	P13	N31	33.815(990)	N220	P24	N218	34.840(1049)
N13	P13	N34	35.673(943)	N312	P31	N315	40.088(1439)
N13	P13	N12	90.370(1584)	N312	P31	N314	32.721(943)
N13	P13	N14	90.792(1555)	N312	P31	N313	35.118(1118)
N13	P13	N11	146.185(1658)	N314	P31	N313	38.933(1016)
N13	P13	N23	37.860(854)	N314	P31	N512	119.830(1589)
N14	P14	N41	33.185(748)	N314	P31	N312	30.581(798)
N14	P14	N24	37.057(854)	N314	P31	N315	35.324(948)
N14	P14	N13	92.642(1392)	N411	P41	N415	37.533(1174)
N14	P14	N34	37.726(862)	N411	P41	N412	35.635(1262)
N14	P14	N12	92.767(1271)	N411	P41	N414	32.634(1121)
N14	P14	N11	149.013(1364)	N412	P41	N414	145.088(2503)
N14	P11	N41	148.138(1537)	N412	P41	N413	90.156(1424)
N14	P11	N24	94.597(1283)	N412	P41	N415	37.624(1246)
N14	P11	N13	35.371(1044)	N412	P41	N414	34.947(1315)
N14	P11	N34	90.961(1217)	N412	P41	N411	32.383(1286)
N14	P11	N12	37.427(890)	N414	P41	N412	152.830(2114)
N14	P11	N11	33.649(783)	N414	P41	N413	92.417(1571)
N23	P12	N12	37.888(1037)	N414	P41	N415	37.841(1141)
N23	P12	N21	32.797(1221)	N414	P41	N412	36.696(1233)
N23	P12	N24	36.680(1202)	N414	P41	N411	31.141(1077)
N23	P12	N31	143.196(1905)	N415	P41	N411	33.990(1052)
N23	P12	N13	92.076(1393)	N415	P41	N414	35.947(1066)
N23	P12	N34	92.517(1446)	N415	P41	N412	37.547(1140)
N23	P13	N12	92.043(1267)	N415	P41	N613	118.297(1852)

N23	P13	N21	145.737(1680)	N811	P81	N815	39.369(1123)
N23	P13	N24	90.490(1437)	N811	P81	N814	34.027(1213)
N23	P13	N31	30.289(1005)	N811	P81	N812	33.571(1121)
N23	P13	N13	35.523(888)	N812	P81	N814	37.802(1266)
N23	P13	N34	34.395(928)	N812	P81	N813	94.301(1619)
N34	P13	N31	32.211(1177)	N812	P81	N814	150.154(2090)
N34	P13	N41	144.932(2131)	N812	P81	N811	33.489(1112)
N34	P13	N13	36.348(1035)	N812	P81	N815	35.848(1108)
N34	P13	N14	90.881(1638)	N814	P81	N812	37.521(1386)
N34	P13	N24	91.105(1914)	N814	P81	N813	93.793(1512)
N34	P13	N23	37.332(981)	N814	P81	N812	148.651(2403)
N34	P14	N31	144.409(2363)	N814	P81	N811	33.701(1320)
N34	P14	N41	32.809(1193)	N814	P81	N815	35.569(1210)
N34	P14	N13	91.716(1639)	N815	P81	N811	36.073(1014)
N34	P14	N14	35.702(986)	N815	P81	N812	33.011(1026)
N34	P14	N24	34.358(1220)	N815	P81	N713	110.155(1674)
N34	P14	N23	88.806(1479)	N815	P81	N814	32.995(1008)
N24	P14	N14	37.527(948)	N511	P51	N512	35.727(994)
N24	P14	N41	30.841(945)	N511	P51	N513	36.857(1345)
N24	P14	N23	93.499(1570)	N511	P51	N513	32.213(1279)
N24	P14	N21	146.214(1953)	N512	P51	N513	45.888(969)
N24	P14	N12	93.315(1483)	N512	P51	N314	133.607(1617)
N24	P14	N34	36.738(1172)	N512	P51	N511	33.753(841)
N24	P12	N14	91.970(1479)	N512	P51	N513	32.051(823)
N24	P12	N41	144.221(1872)	N513	P51	N512	108.379(1798)
N24	P12	N23	33.015(1005)	N513	P51	N511	155.220(2271)
N24	P12	N21	32.968(1031)	N513	P51	N513	94.426(1526)
N24	P12	N12	34.909(962)	N513	P51	N513	35.972(1240)
N24	P12	N34	89.842(1597)	N513	P51	N511	30.460(1333)
N211	P22	N212	38.583(1140)	N513	P51	N512	32.032(1028)
N211	P22	N213	94.712(1607)	N513	P51	N512	43.752(972)
N211	P22	N220	35.984(930)	N513	P51	N511	33.348(1293)
N211	P22	N214	32.482(1037)	N513	P51	N513	34.477(903)
N211	P22	N217	90.834(1384)	N513	P51	N513	92.989(1736)
N211	P22	N216	149.763(1927)	N513	P51	N511	151.486(2003)
N211	P21	N212	92.361(1594)	N513	P51	N512	106.277(1584)

N211	P21	N213	36.737(1099)	N611	P61	N612	38.874(1174)
N211	P21	N220	93.416(1400)	N611	P61	N611	94.999(1353)
N211	P21	N214	148.526(1917)	N611	P61	N611	42.299(1069)
N211	P21	N217	36.436(926)	N611	P61	N612	147.381(1840)
N211	P21	N216	33.738(1026)	N611	P61	N613	30.925(880)
N212	P23	N211	95.163(1860)	N611	P61	N612	150.327(1754)
N212	P23	N213	38.69(101)	N611	P61	N611	42.141(923)
N212	P23	N220	94.799(1622)	N611	P61	N611	94.866(1481)
N212	P23	N214	150.473(2014)	N611	P61	N612	36.276(1059)
N212	P23	N218	37.393(928)	N611	P61	N613	95.554(1323)
N212	P23	N215	31.125(1040)	N612	P61	N611	42.266(1221)
N212	P22	N211	37.876(1202)	N612	P61	N613	33.716(1008)
N212	P22	N213	94.656(1608)	N612	P61	N611	39.494(1181)
N212	P22	N220	36.294(1114)	N613	P61	N612	34.579(951)
N212	P22	N214	32.434(1207)	N613	P61	N415	120.903(1603)
N212	P22	N218	92.595(1617)	N613	P61	N611	34.270(853)
N212	P22	N215	149.188(2170)	N711	P71	N713	113.490(1792)
N213	P21	N217	38.289(996)	N711	P71	N712	157.138(2051)
N213	P21	N212	91.099(1833)	N711	P71	N711	36.991(1017)
N213	P21	N211	37.252(1037)	N711	P71	N711	95.736(1857)
N213	P21	N215	147.615(1973)	N711	P71	N712	29.836(1104)
N213	P21	N216	33.725(1114)	N711	P71	N713	32.540(965)
N213	P21	N218	89.954(1486)	N711	P71	N713	42.930(1141)
N213	P23	N217	89.222(1558)	N711	P71	N712	32.795(1234)
N213	P23	N212	36.635(1247)	N711	P71	N711	94.426(1586)
N213	P23	N211	91.023(1475)	N711	P71	N711	35.638(1233)
N213	P23	N215	34.296(1190)	N711	P71	N712	153.308(2195)
N213	P23	N216	147.096(2217)	N711	P71	N713	111.464(1752)
N213	P23	N218	37.953(990)	N712	P71	N713	38.768(1072)
N214	P22	N220	35.358(1028)	N712	P71	N711	36.421(1187)
N214	P22	N211	34.044(1073)	N712	P71	N711	31.878(1037)
N214	P22	N212	34.604(1158)	N713	P71	N711	42.410(1021)
N215	P23	N213	36.981(1094)	N713	P71	N712	34.448(959)
N215	P23	N212	31.788(914)	N713	P71	N815	127.124(1668)
N215	P23	N218	34.950(831)	N713	P71	N711	31.049(887)
N216	P21	N213	34.559(1243)	N313	P31	N315	153.824(2230)

N216	P21	N211	35.048(1190)	N313	P31	N311	92.262(1765)
N216	P21	N217	32.490(1064)	N313	P31	N314	36.943(1054)
N217	P24	N218	40.007(1288)	N313	P31	N312	31.187(1215)
N217	P24	N219	31.890(946)	N313	P31	N315	37.067(1072)
N217	P24	N213	98.826(1580)	N315	P31	N313	143.688(2494)
N217	P24	N220	37.962(1269)	N315	P31	N312	35.249(1549)
N217	P24	N211	94.213(1473)	N315	P31	N311	88.243(1447)
N217	P24	N216	151.426(2016)	N315	P31	N313	36.877(1296)
N217	P21	N218	97.710(1631)	N315	P31	N314	33.407(1069)
	N-B-N						
N311	B31	N313	144.714(1862)	N413	B41	N414	29.524(2054)
N311	B31	N313	25.693(1864)	N413	B41	N414	149.332(2282)
N311	B31	N313	93.908(1592)	N413	B41	N412	147.418(2033)
N311	B31	N315	30.771(1870)	N413	B41	N412	27.529(2251)
N311	B31	N315	149.174(1861)	N413	B41	N412	92.651(2418)
N311	B31	N315	88.659(1593)	N413	B41	N414	149.415(2549)
N311	B31	N313	93.908(1677)	N413	B41	N414	90.363(2116)
N311	B31	N313	144.714(1663)	N413	B41	N414	29.543(2557)
N311	B31	N313	25.693(1499)	N413	B41	N412	92.693(2111)
N311	B31	N315	88.659(1714)	N413	B41	N412	147.312(2536)
N311	B31	N315	30.771(1648)	N413	B41	N412	27.490(2554)
N311	B31	N315	149.174(1497)	N414	B41	N412	30.446(2286)
N311	B31	N313	25.693(1654)	N414	B41	N413	31.539(2422)
N311	B31	N313	93.908(1762)	N414	B41	N415	111.356(2494)
N311	B31	N313	144.714(1497)	N414	B41	N412	90.236(2960)
N311	B31	N315	149.174(1672)	N414	B41	N411	150.012(2934)
N311	B31	N315	88.659(1725)	N812	B81	N814	90.216(2564)
N311	B31	N315	30.771(1504)	N812	B81	N813	29.978(2072)
N313	B31	N315	35.686(2310)	N812	B81	N814	30.000(2191)
N313	B31	N311	28.432(2022)	N812	B81	N811	151.448(2862)
N313	B31	N314	108.589(2626)	N812	B81	N815	114.084(2464)
N313	B31	N312	144.947(3275)	N813	B81	N812	30.883(2144)
N313	B31	N315	88.710(2302)	N813	B81	N812	89.161(2213)
N315	B31	N313	30.329(1773)	N813	B81	N812	150.860(2142)
N315	B31	N312	146.934(2691)	N813	B81	N814	29.360(2106)
N315	B31	N311	29.10(142)	N813	B81	N814	90.664(2175)

N315	B31	N313	85.467(2370)	N813	B81	N814	149.377(2107)
N315	B31	N314	103.545(2222)	N813	B81	N812	150.947(2120)
N412	B41	N414	31.163(2579)	N813	B81	N812	30.905(2124)
N412	B41	N413	29.985(2193)	N813	B81	N812	89.074(2087)
N412	B41	N415	104.581(2654)	N813	B81	N814	90.708(2070)
N412	B41	N414	87.758(3174)	N813	B81	N814	149.268(2109)
N412	B41	N411	147.877(3226)	N813	B81	N814	29.316(2097)
N413	B41	N414	29.565(2268)	N813	B81	N812	89.119(2084)
N413	B41	N414	149.438(2051)	N813	B81	N812	150.837(2123)
N413	B41	N414	90.406(2398)	N813	B81	N812	30.860(2118)
N413	B41	N412	27.510(2042)	N813	B81	N814	149.357(2096)
N413	B41	N412	92.737(2324)	N813	B81	N814	29.339(2108)
N413	B41	N412	147.335(2273)	N813	B81	N814	90.620(2067)
N413	B41	N414	90.448(2372)				

B-N-B

B31	N313	B31	95.849(2423)	B81	N813	B81	29.977(1587)
B31	N313	B31	155.786(3303)	B81	N813	B81	30.023(1617)
B31	N311	B31	30.348(1074)	B81	N814	B81	91.539(2930)
B31	N311	B31	30.348(1202)	B81	N814	B81	151.533(3467)
B31	N315	B31	149.581(2415)	B81	N812	B81	149.116(3477)
B31	N315	B31	89.904(2261)	B81	N812	B81	89.118(2786)
B41	N412	B41	92.729(3629)	N814	B81	N812	89.117(2728)
B41	N412	B41	152.390(3919)	N814	B81	N813	29.147(2094)
B41	N414	B41	148.872(3851)	N814	B81	N812	30.656(2258)
B41	N414	B41	88.916(3503)	N814	B81	N811	150.534(2936)
B41	N413	B41	30.048(1935)	N814	B81	N815	112.563(2494)
B41	N413	B41	30.007(1930)				

E.5. Details of the crystal structure

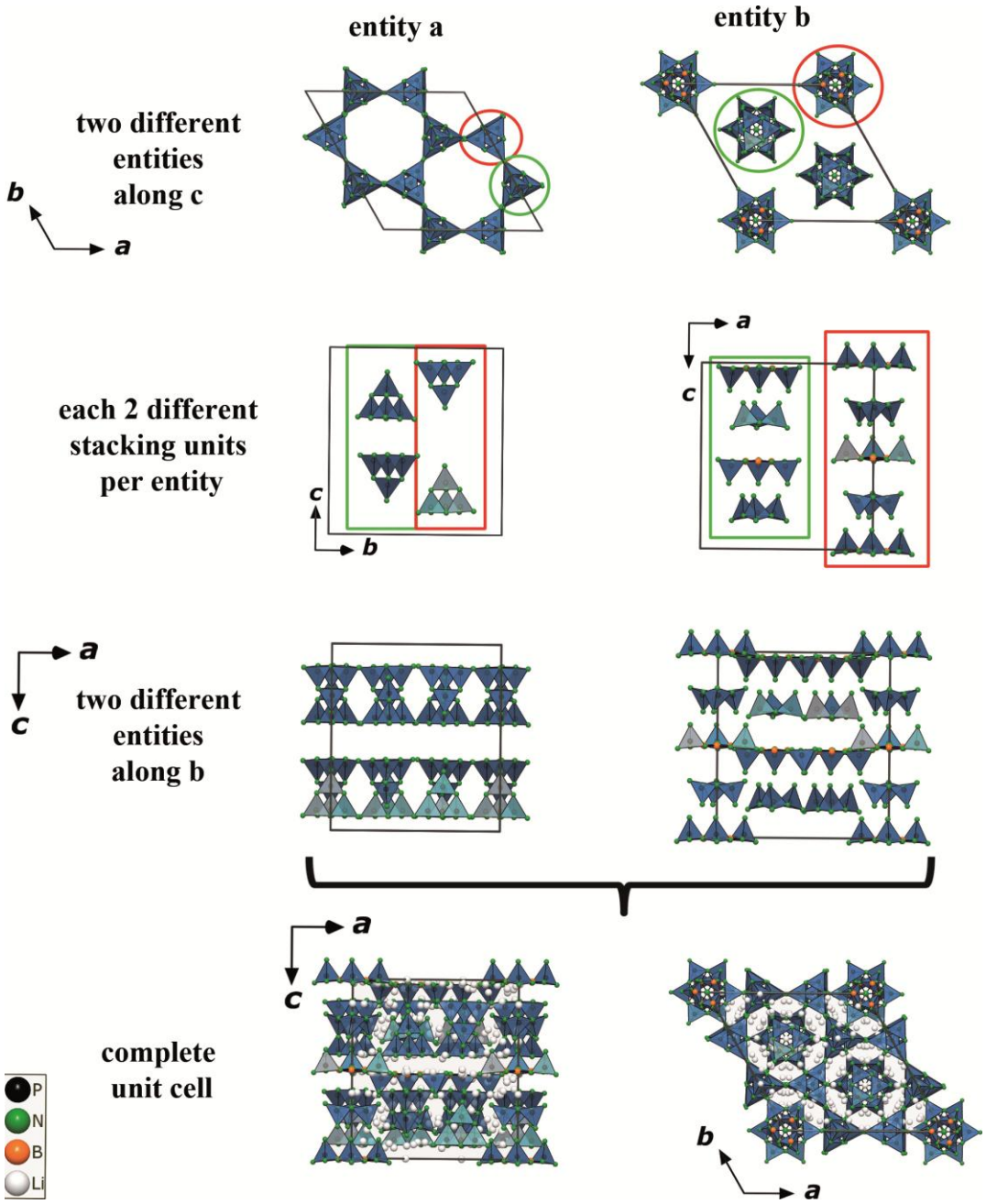

Figure S1. Visualization of $Li_{47}B_3P_{14}N_{42}$ with 2 different entities and 2 different stacking orders each.

E.6. Details of the Rietveld refinement

Table S5. Details of the Rietveld refinement of $Li_{47}B_3P_{14}N_{42}$.

formula	**$Li_{47}B_3P_{14}N_{42}$**
formula mass / g · mol^{-1}	4141.83
crystal system / space group	trigonal *P*3*c*1 (no. 158)
lattice parameters / Å, °	*a* = 19.36271(37)
	c = 18.07075(57)
cell volume / Å^3	5867.31(29)
formula units per cell Z	2
X-ray density / g · cm^{-1}	2.392
linear absorption coefficient / cm^{-1}	0.690
radiation	Cu-$K_{\alpha 1}$ (λ = 1.540596 Å)
monochromator	Ge(111)
diffractometer	Stoe StadiP
detector	linear PSD
2θ-range / °	5.0-83.6
temperature / K	298 (2)
data points	5243
number of observed reflections	1350
number of parameters	207
program used	TOPAS Academic
structure refinement	Rietveld-Method
profile function	fundamental parameters model
background function	shifted Chebyshev
R_{wp}	10.533
R_{exp}	7.505
R_p	8.533
R_{Bragg}	4.547
χ^2	1.458

E.7. Detailed Rietveld plot

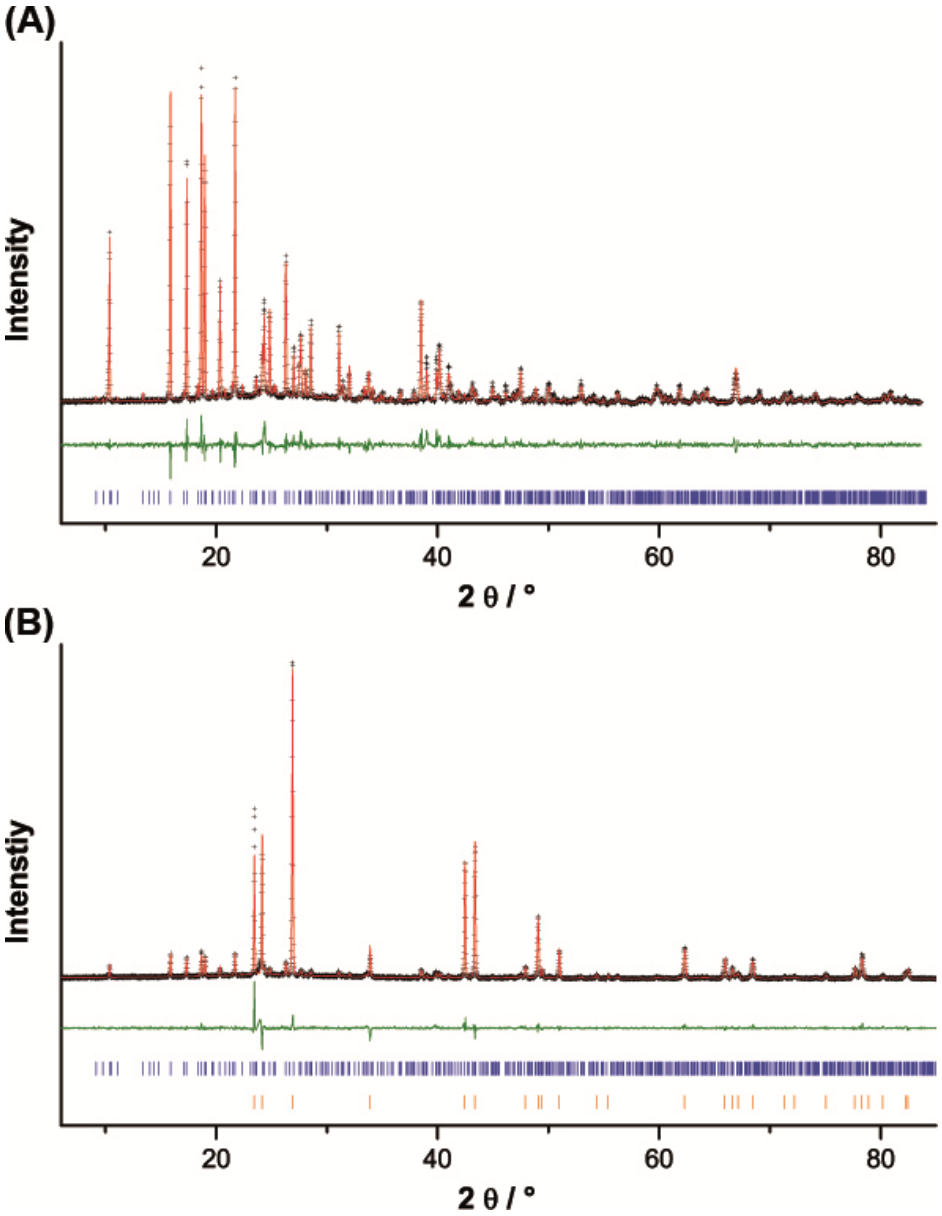

Figure S2. Rietveld refinement of $Li_{47}B_3P_{14}N_{42}$ in the 2θ range of 5-85° measured with Cu-$K_{\alpha 1}$ (λ = 1.540596 Å) radiation. Observed (black crosses) and calculated (red line) powder diffraction pattern. The theoretical reflection positions for $Li_{47}B_3P_{14}N_{42}$ (blue vertical bars) and Li_3P (orange vertical bars) and the difference plot (green line) are displayed below the refinement. (A) Product synthesized according to equation (2) by high-pressure/high-temperature synthesis. (B) Product synthesized according to equation (1) by ampoule synthesis with Li_3P as side phase (about 59 %).

E.8. Solid-state MAS NMR spectroscopy

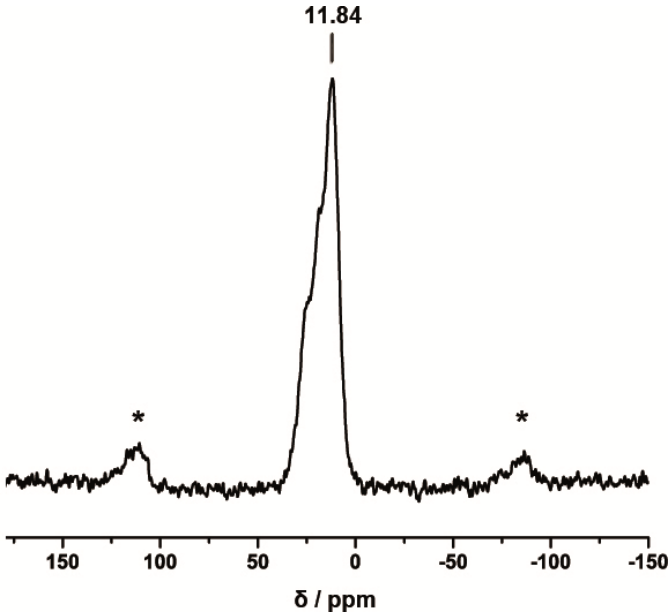

Figure S3. ^{31}P solid-state MAS NMR spectrum of a $Li_{47}B_3P_{14}N_{42}$. For this spectrum we used a product synthesized according to equation (2) by high-pressure/high-temperature synthesis.

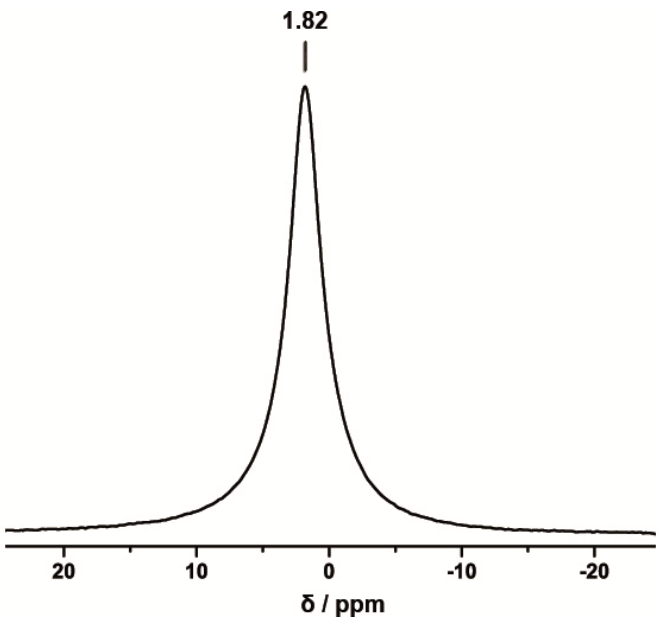

Figure S4. ^{7}Li solid-state MAS NMR spectrum of a $Li_{47}B_3P_{14}N_{42}$. For this spectrum we used a product synthesized according to equation (2) by high-pressure/high-temperature synthesis.

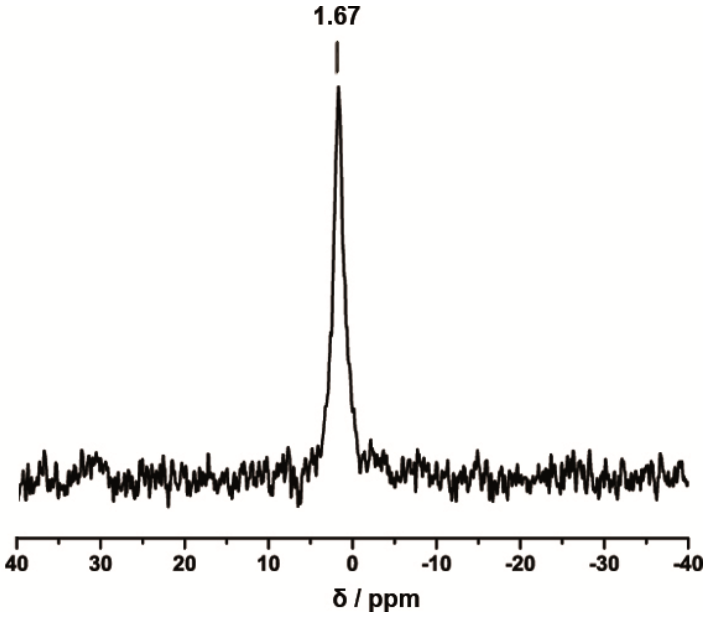

Figure S5. ^{6}Li solid-state MAS NMR spectrum of a $Li_{47}B_3P_{14}N_{42}$. For this spectrum we used a product synthesized according to equation (2) by high-pressure/high-temperature synthesis.

E.9. Details of scanning electron microscopy

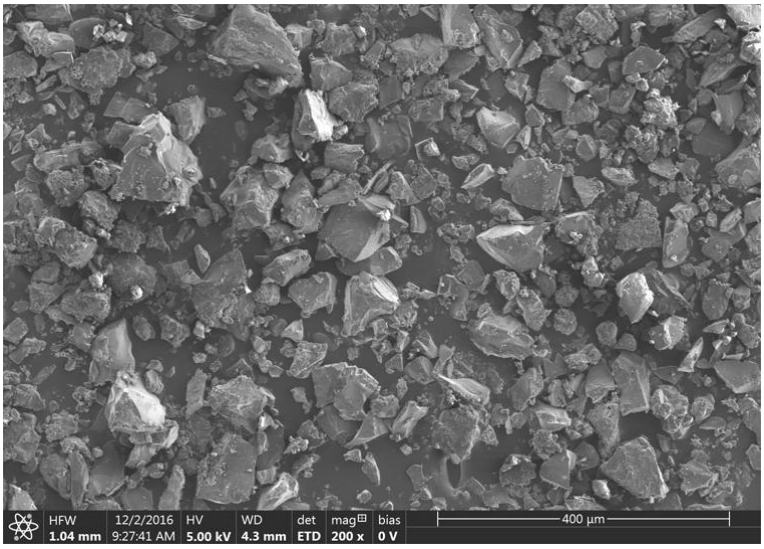

Figure S6. Scanning electron micrograph of $Li_{47}B_3P_{14}N_{42}$. For this investigation we used a product synthesized according to equation (2) by high-pressure/high-temperature synthesis.

Table S6. EDX analysis of $Li_{47}B_3P_{14}N_{42}$. For this investigation we used a product synthesized according to equation (2) by high-pressure/high-temperature synthesis.

	N	**O**	**P**	**B**
EDX point 1[atom %]	66.61	4.11	22.91	6.36
EDX point 2[atom %]	64.33	4.16	25.32	6.18
EDX point 3[atom %]	60.70	5.73	28.01	5.56
EDX point 4[atom %]	56.61	7.04	30.36	5.99
Average	**62.06**	**5.26**	**26.65**	**6.02**
Calculated atom %	**71.2**	**0**	**23.7**	**5.1**

The observation of oxygen can be explained by partial hydrolysis of the compound during contact of the sample with air. Li could not be detected by EDX measurements. No other elements than B, P, N and O were found.

E.10. Temperature dependent powder X-ray diffraction

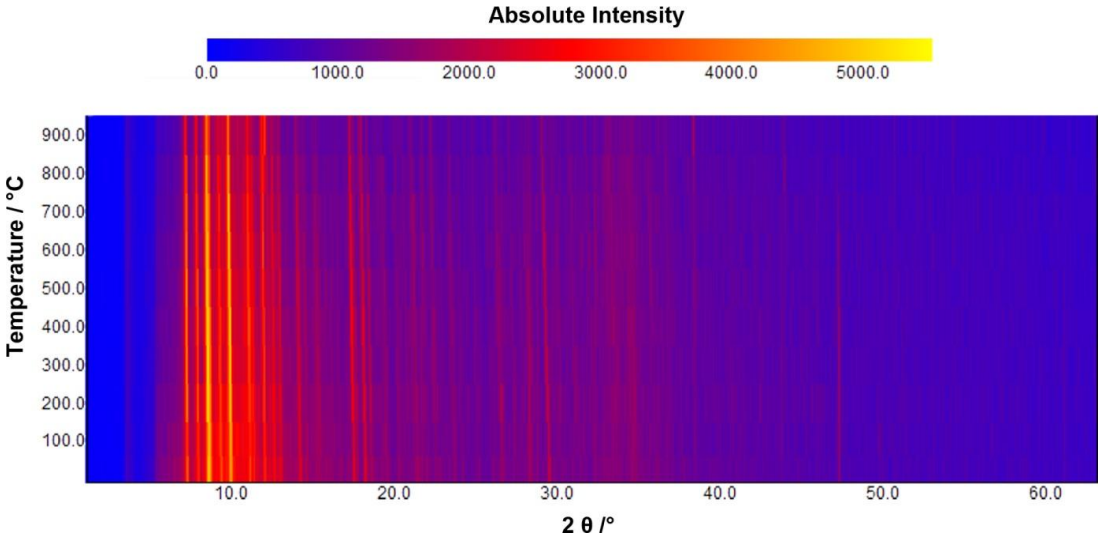

Figure S7. Temperature dependent powder X-ray diffractogram of $Li_{47}B_3P_{14}N_{42}$. For this investigation we used a product synthesized according to equation (2) by high-pressure/high-temperature synthesis.

E.11. FTIR spectrum

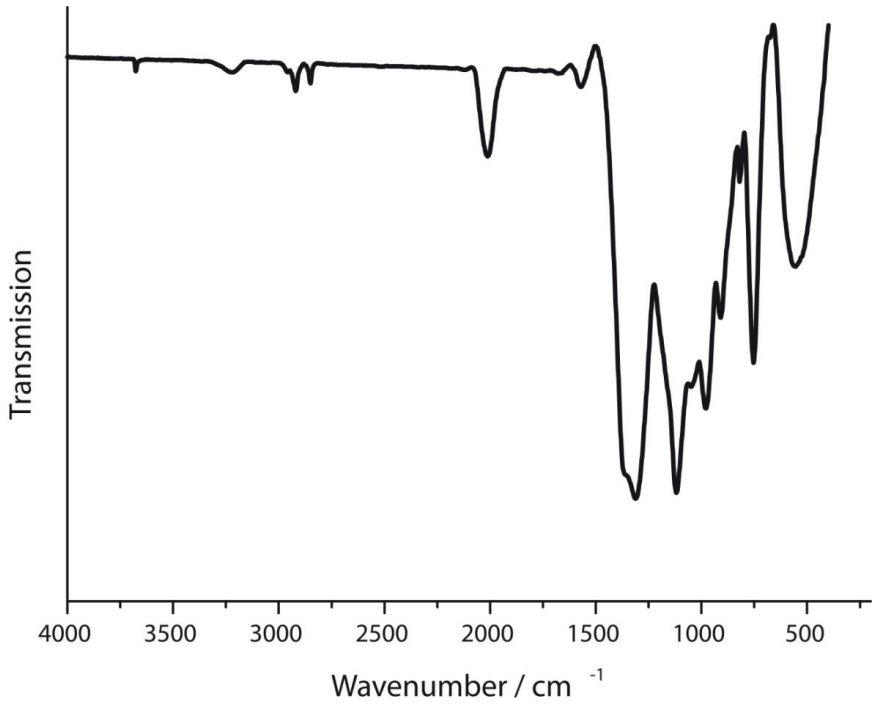

Figure S8. FTIR spectrum of $Li_{47}B_3P_{14}N_{42}$. For this spectrum we used a product synthesized according to equation (2) by high-pressure/high-temperature synthesis.

Infrared spectroscopy measurements were performed on a Bruker FTIR-IFS 66v/S spectrometer. Before measurement in the range of 400-4000 cm^{-1} the sample was mixed with KBr in a glove box and cold-pressed into a pellet (Ø = 12 mm). The FTIR spectrum shows no significant valence vibrations in the region of 3000 cm^{-1}, where N-H absorption bands are expected. We explain the weak signal by surface hydrolysis of the sample. The presence of stoichiometric amounts of hydrogen in the structure would lead to much more intense and characteristic N-H absorptions bands.[19,20] In the region of 600-1500 cm^{-1} the characteristic PN framework vibrations can be identified.

E.12. Structural Analysis of Possible Lithium Migration Pathways

Possible voids and migration pathways in $Li_{47}B_3P_{14}N_{42}$ were analyzed with TOPOS.[21–24]

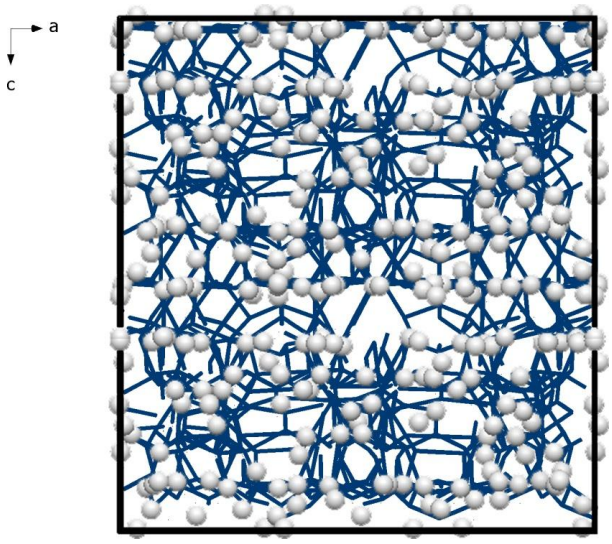

Figure S9. Calculated possible Li^+ pathways (blue) according to the voids in the structure and Li^+ ions of $Li_{47}B_3P_{14}N_{42}$ viewing along *b* after single-crystal structure analysis. For single-crystal structure analysis we used a product synthesized according to equation (2) by high-pressure/high-temperature synthesis.

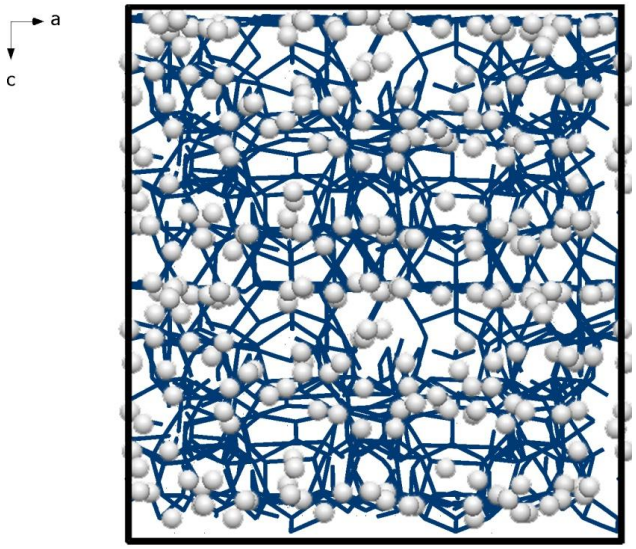

Figure S10. Calculated possible Li^+ pathways (blue) according to the voids in the structure and Li^+ ions of $Li_{47}B_3P_{14}N_{42}$ viewing along *c* after Rietveld refinement. For Rietveld refinement we used a product synthesized according to equation (2) by high-pressure/high-temperature synthesis.

E.13. Details on the determination of the total conductivity of $Li_{47}B_3P_{14}N_{42}$

Table S7. Impedance measurements of $Li_{47}B_3P_{14}N_{42}$ at different temperatures (cell constant = 0.801 cm^{-1}). For the conductivity measurement we used a product synthesized according to equation (2) by high-pressure/high-temperature synthesis.

Temperature / °C	**Raw. Res. / Ohm**	**Conductivity / S cm^{-1}**	**ln(conductivity · T)**	**Capacitance / nF**
25	$7.76 \cdot 10^6$	$1.03 \cdot 10^{-7}$	-10.39	0.07
30	$6.72 \cdot 10^6$	$1.19 \cdot 10^{-7}$	-10.23	0.03
40	$3.72 \cdot 10^6$	$2.16 \cdot 10^{-7}$	-9.60	0.04
50	$2.07 \cdot 10^6$	$3.88 \cdot 10^{-7}$	-8.98	0.03
60	$1.19 \cdot 10^6$	$6.71 \cdot 10^{-7}$	-8.41	0.03
70	$7.13 \cdot 10^5$	$1.12 \cdot 10^{-6}$	-7.86	0.03
80	$4.40 \cdot 10^5$	$1.82 \cdot 10^{-6}$	-7.35	0.03
90	$2.78 \cdot 10^5$	$2.89 \cdot 10^{-6}$	-6.86	0.03
25	$7.82 \cdot 10^6$	$1.03 \cdot 10^{-7}$	-10.40	0.03

Table S8. Data for Arrhenius plot.

equation	y = a + b · x		
weighting	no weighing		
Sum of the squares	0.03333		
Pearson R	-0.99886		
cor. R-square	0.99739		
		value	standard error
ln(conductivity)	interception of the y-axis	9.46704	0.33271
ln(conductivity)	gradient	-5946.09332	107.47186

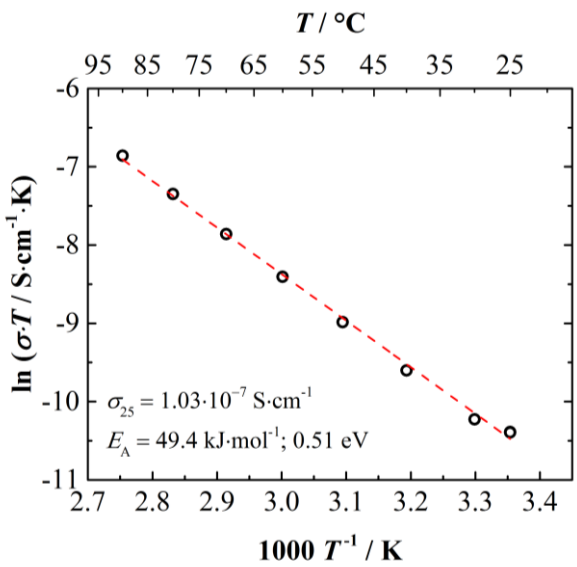

Figure S11. Arrhenius plot of the measurements at different temperature from 25 to 90 °C.

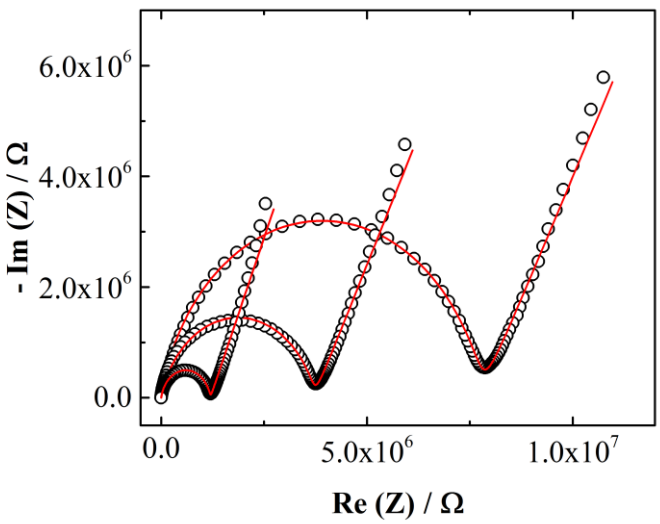

Figure S12. Nyquist plots of the measurements at different temperature (25, 40 and 60 °C ,right to left).

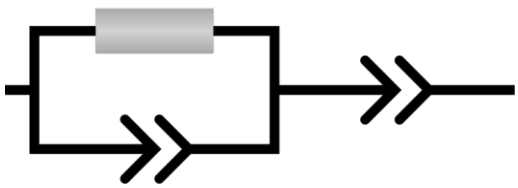

Figure S13. Equivalent circuit diagram used for the fits. The rectangle represents the ohmic resistance and the arrows represent constant phase elements.

E.14. References

[1] A. Stock, H. Grüneberg, *Ber. Dtsch. Chem. Ges.* **1907**, *40*, 2573–2578.

[2] W. Schnick, J. Lücke, *Z. Anorg. Allg. Chem.* **1990**, *588*, 19–25.

[3] W. Schnick, J. Luecke, *J. Solid State Chem.* **1990**, *87*, 101–106.

[4] N. Kawai, S. Endo, *Rev. Sci. Instrum.* **1970**, *41*, 1178–1181.

[5] D. Walker, M. A. Carpenter, C. M. Hitch, *Am. Mater.* **1990**, *75*, 1020–1028.

[6] D. Walker, *Am. Mater.* **1991**, *76*, 1092–1100.

[7] D. C. Rubie, *Phase Transitions* **1999**, *68*, 431–451.

[8] H. Huppertz, *Z. Kristallogr.* **2004**, *219*, 330–338.

[9] *XPREP Reciprocal Space Exploration, Vers. 6.12*, Bruker-AXS, Karlsruhe, **2001**.

[10] G. M. Sheldrick, *Acta Crystallogr., Sect. A Found. Crystallogr.* **2008**, *64*, 112–122.

[11] L. J. Farrugia, *J. Appl. Crystallogr.* **1999**, *32*, 837–838.

[12] G. M. Sheldrick, *SHELXS*, University of Göttingen, **1997**.

[13] K. Brandenburg, **2005**.

[14] A. Coelho, *TOPAS-Academic* **2007**.

[15] R. W. Cheary, A. A. Coelho, *J. Appl. Crystallogr.* **1992**, *25*, 109–121.

[16] R. W. Cheary, A. A. Coelho, *J. Res. Natl. Inst. Stand. Technol.* **2007**, *109*, 1–25.

[17] *INCA, Version 4.02*, OXFORD Instruments**.**

[18] *OPUS/IR*, Bruker Analytik GmbH, **2000**.

[19] D. Baumann, W. Schnick, *Inorg. Chem.* **2014**, *53*, 7977–7982.

[20] A. Marchuk, V. R. Celinski, J. Schmedt Auf Der Günne, W. Schnick, *Chem. Eur. J.* **2015**, *21*, 5836–5842.

[21] V. A. Blatov, *IUCr Comp Comm Newsl.* **2006**, *7*, 4–38.

[22] V. A. Blatov, *Crystallogr. Rev.* **2004**, *10*, 249–318.

[23] N. A. Anurova, V. A. Blatov, G. D. Ilyushin, O. A. Blatova, A. K. Ivanov-Schitz, L. N. Dem'yanets, *Solid State Ionics* **2008**, *179*, 2248–2254.

[24] V. A. Blatov, A. P. Shevchenko, V. N. Serezhin, *J. Appl. Crystallogr.* **2000**, *33*, 1193–1193.

F. Miscellaneous

The results complied in this thesis were published in scientific journals as detailed in following list.

F.1. List of Publications Within this Thesis

1. **$Li_{12}P_3N_9$ with Non-Condensed $[P_3N_9]^{12-}$ Rings and its High-Pressure Polymorph Li_4PN_3 with Infinite Chains of PN_4-Tetrahedra**

   Eva-Maria Bertschler, Robin Niklaus, Wolfgang Schnick

   published in: *Chem. Eur. J.* **2017**, *23*, 9592-9599. DOI: 10.1002/chem.201700979

   Writing the main parts of the manuscript, creation of graphical material, literature research, synthesis of the sample, structure elucidation and topological analysis were performed by Eva-Maria Bertschler. Solid-state MAS NMR and EDX/REM spectroscopy were carried out by Christian Minke, FTIR spectroscopy by Marion Sokoll and single-crystal X-ray diffraction by Peter Mayer and all were evaluated by Eva-Maria Bertschler. DFT calculations and evaluation of them were performed by Robin Niklaus. Wolfgang Schnick directed and supervised the work. All authors revised the manuscript.

2. **$Li_{18}P_6N_{16}$ – A Lithium Nitridophosphate with Unprecedented Tricyclic $[P_6N_{16}]^{18-}$ Ions**

   Eva-Maria Bertschler, Christian Dietrich, Jürgen Janek, Wolfgang Schnick

   published in: *Chem. Eur. J.* **2017**, *23*, 2185-2191. DOI: 10.1002/chem.201605316

Literature research, creation of graphical material, writing the main part of the manuscript, synthesis of the samples, structure elucidation, topological analysis, Rietveld refinement and evaluation of spectroscopic data were performed by Eva-Maria Bertschler. The spectroscopic data were measured by Christian Minke (solid-state MAS NMR, EDX/REM), Marion Sokoll (FTIR) and Peter Mayer (single-crystal X-ray diffraction). Impedance measurements and evaluation were performed by Christian Dietrich with supervision of Jürgen Janek. Wolfgang Schnick directed and supervised the work. All authors revised the manuscript.

3. Li^+ Ion Conductors with Adamantane-type Nitridophosphate Anions – β-$Li_{10}P_4N_{10}$ and $Li_{13}P_4N_{10}X_3$ with X = Cl, Br

Eva-Maria Bertschler, Christian Dietrich, Thomas Leichtweiß, Jürgen Janek, Wolfgang Schnick

published in: *Chem. Eur. J.* **2018**, *24*, 196-205. DOI: 10.1002/chem.201704305

For this contribution, writing the main part, literature screening, imaging, as well as the determination of the structures and their topological analysis were performed by Eva-Maria Bertschler. Solid-state MAS NMR and EDX/REM spectroscopy were carried out by Christian Minke and FTIR spectroscopy by Marion Sokoll and all were evaluated by Eva-Maria Bertschler. Impedance measurements and evaluation were performed by Christian Dietrich. XPS measurements and evaluation of the data were performed by Thomas Leichtweiß. Both were supervised by Jürgen Janek. Wolfgang Schnick directed and supervised the work. All authors also revised the manuscript.

4. Reversible Polymerization of Adamantane-type $[P_4N_{10}]^{10-}$ Anions to Honeycomb-type $[P_2N_5]^{5-}$ Layers under High-Pressure

Eva-Maria Bertschler, Robin Niklaus, Wolfgang Schnick

published in: *Chem. Eur. J.* **2018**, *24*, 736-742. DOI: 10.1002/chem.201704975

For this publication, literature research, writing the manuscript, creation of most graphical material, synthesis of the samples, structure elucidation, Rietveld refinement, evaluation of spectroscopic data and topological analysis were performed by Eva-Maria Bertschler. The spectroscopic data were measured by Christian Minke (solid-state MAS NMR, EDX/REM), Marion Sokoll (FTIR) and Peter Mayer (single-crystal X-ray diffraction). DFT calculations and evaluation of them were performed by Robin Niklaus. Wolfgang Schnick directed and supervised the work. All authors revised the manuscript.

5. $Li_{47}B_3P_{14}N_{42}$ – A Lithium Nitridoborophosphate with $[P_3N_9]^{12-}$, $[P_4N_{10}]^{10-}$ and the Unprecedented $[B_3P_3N_{13}]^{15-}$Ion

Eva-Maria Bertschler, Thomas Bräuniger, Christian Dietrich, Jürgen Janek, Wolfgang Schnick

published in: *Angew. Chem. Int. Ed.* **2017**, *56*, 4806-4809. DOI: 10.1002/anie.201701084

published in: *Angew. Chem.* **2017**, *129*, 4884-4887. DOI: 10.1002/ange.201701084

Writing the main parts of the manuscript, literature research, synthesis of the sample, structure elucidation from single crystal data, Rietveld refinement and topological analysis were performed by Eva-Maria Bertschler. Solid-state MAS NMR and EDX/REM spectroscopy were carried out by Christian Minke, FTIR spectroscopy by Marion Sokoll and single-crystal X-ray diffraction by Peter Mayer. Solid-state MAS NMR spectroscopy was elucidated by Thomas Bräuniger and Eva-Maria Bertschler in strong collaboration. EDX/REM, FTIR spectroscopy were evaluated by Eva-Maria Bertschler. Impedance measurements and evaluation were performed by Christian Dietrich with supervision of Jürgen Janek. Wolfgang Schnick directed and supervised the work. All authors revised the manuscript.

F.2. Contributions to Conferences

1. **Schneekristallartige Anion-Strukturen in Lithium Nitridophosphaten** (oral presentation)

   E.-M. Bertschler, W. Schnick

   2. Obergurgl-Seminar on Solid State Chemistry **2016**, Obergurgl, Austria

2. **Surprising Anion Topologies in Lithium Nitridophosphates** (poster presentation)

   E.-M. Bertschler, C. Dietrich, J. Janek, W. Schnick

   European conference on solid state chemistry **2015**, Vienna, Austria

3. **$Li_{18}P_6N_{16}$ - a Novel Lithium Nitridophosphate Opening a Field of Potential Ion Conductors** (poster presentation)

   E.-M. Bertschler, C. Dietrich, J. Janek, W. Schnick

   EuCheMS Chemistry Congress **2016**, Seville, Spain

4. **Li_4PN_3: A High-Pressure Polymorph of $Li_{12}P_3N_9$** (poster presentation)

   E.-M. Bertschler, W. Schnick

   18. Vortragstagung der FG Festkörperchemie und Materialforschung **2016**, Innsbruck, Austria

5. **Ungewöhnliche Anion-Strukturen in Lithium Nitridophosphaten** (oral presentation)

   E.-M. Bertschler, W. Schnick

   Hirschegg-Seminar on Solid State Chemistry **2017**, Hirschegg, Austria

F.3. Deposited Crystallographic Data

Crystallographic data for the compounds synthesized as part of this work were deposited at the Fachinformationszentrum (FIZ) Karlsruhe, Germany (fax: +49-7247-808-666, e-mail: crysdata@fizkarlsruhe.de) and are available on quoting the following CSD depository numbers.

Compound	**CSD-Number**
$Li_{12}P_3N_9$	432590
Li_4PN_3	432591
$Li_{18}P_6N_{16}$	431316
β-$Li_{10}P_4N_{10}$	433514
$Li_{13}P_4N_{10}Cl_3$	433515
$Li_{13}P_4N_{10}Br_3$	433516
$Li_5P_2N_5$	433592
$Li_{47}B_3P_{14}N_{42}$	432318